Continuous crystallization - Contribution to the implementation of the Pasteurian resolution of racemic Ibuprofen in a Couette-Taylor crystallizer

Laureline Marc

Normandie Université

THÈSE

Pour obtenir le diplôme de doctorat

Spécialité CHIMIE

Préparée au sein de l'Université de Rouen Normandie

Continuous crystallization - Contribution to the implementation of the Pasteurian resolution of racemic Ibuprofen in a Couette-Taylor crystallizer

Présentée et soutenue par
LAURELINE MARC

Thèse soutenue le 25/11/2022 devant le jury composé de		
MME BEATRICE BISCANS	DIRECTEUR DE RECHERCHE, UNIVERSITE TOULOUSE 3 PAUL SABATIER	Rapporteur du jury
M. WOO SIK KIM	PROFESSEUR DES UNIVERSITES, Université Kyung Hee	Rapporteur du jury
MME VALÉRIE DUPRAY	MAITRE DE CONFERENCES, Université de Rouen Normandie	Membre du jury
M. SAMUEL PETIT	PROFESSEUR DES UNIVERSITES, Université de Rouen Normandie	Membre du jury
M. GÉRARD COQUEREL	PROFESSEUR DES UNIVERSITES, Université de Rouen Normandie	Directeur de thèse
M. JEAN-MARIE SCHNEIDER	DOCTEUR, Seqens Porcheville	Co-directeur de thèse

Thèse dirigée par GÉRARD COQUEREL (SCIENCES ET METHODES SEPARATIVES) et JEAN-MARIE SCHNEIDER (SEQENS PORCHEVILLE)

UNIVERSITÉ DE ROUEN NORMANDIE

ED 591 PSIME

SMS Sciences et Méthodes Séparatives

Normandie Université

PH. D. thesis

Physics

Continuous crystallization - Contribution to the implementation of the Pasteurian resolution of racemic Ibuprofen in a Couette-Taylor crystallizer

Defended by

Laureline MARC

Public defense on November 25th, 2022

Jury composed of:

Dr. Béatrice BISCANS	CNRS Senior Researcher Université de Toulouse	Reviewer
Prof. Woo-Sik KIM	Professor Kyung Hee University	Reviewer
Dr. Valérie DUPRAY	Assistant Professor – HDR Université de Rouen Normandie	Examiner
Prof. Samuel PETIT	Professor Université de Rouen Normandie	Examiner
Prof. Gérard COQUEREL	Professor Université de Rouen Normandie	Co-director
Dr. Jean-Marie SCHNEIDER	R&D Manager Seqens Porcheville	Co-director

Ph. D. thesis directed by Prof. Gérard COQUEREL (Lab. SMS, Université de Rouen Normandie) and Dr. Jean-Marie Schneider (Seqens Porcheville).

UNIVERSITÉ DE ROUEN NORMANDIE

ED PSIME

SMS Sciences et Méthodes Séparatives

SEQENS

“If I had an hour to solve a problem and my life depended on the solution, I would spend the first 55 minutes determining the proper question to ask, for once I know the proper question, I could solve the problem in less than five minutes.”

Albert Einstein

“L’essentiel est invisible pour les yeux”

“Les étoiles sont éclairées pour que chacun puisse un jour retrouver la sienne.”

Antoine de Saint-Exupéry

A Olivier.

Acknowledgements

This work was funded by Seqens, through a CIFRE convention.

First of all, I would like to warmly thank Prof. Gérard COQUEREL, for having given me the opportunity to achieve this Ph. D. in the SMS laboratory. Thank you for your constructive guidance throughout these last three (and a little more) years. Your passion for crystallization and sciences in general is communicative, and I am really happy to have been able to exchange with you on so many different subjects. I have often been challenged by your ability to think outside the box, which has pushed me further in many skills, and I am truly grateful to you. Thank you for giving me this incredible opportunity to partly understand the depth of the unknown in scientific knowledge, opening the field to all possibilities.

Then, I would like to give a special thanks to Dr. Jean-Marie SCHNEIDER, my Ph. D. co-director. You have followed my evolution from the 5th academic year internship until the end of my Ph. D. with great kindness. Your wise advice has accompanied the development of this thesis work, as well as your much appreciated support.

I am grateful to Dr. Béatrice BISCANS and Prof. Woo-Sik KIM as reviewers, and Dr. Valérie DUPRAY and Prof. Samuel PETIT as examiners for having accepted to review this work. I look forward to your comments, which will certainly lead to interesting discussions during the defense.

I would also like to address a thanks to the companies with which I have been in contact during my thesis, especially for the development of the continuous set-up: Cole-Parmer, Sulzer and SKF.

Finally, I could not write these acknowledgements without mentioning my amazing colleagues from the SMS laboratory, and from the site of Seqens Porcheville. Many moments are running through my mind right now, and I think I'm going to need more time to properly put my thanks down on paper. To be continued…

Table of contents

Introduction

Traditionally, API (Active Pharmaceutical Ingredient) production is realized through batch mode. However, in the past years, the use of the batch mode has shown some economical and technical limitations. Conversely, the continuous mode is more cost effective and can also ensure a production with a more constant product quality.

Racemic Ibuprofen (rac-Ibu) is an API contained in drugs ranking among the most sold in the world. However, its enantiomer *S* has been proved to have a greater therapeutic effect than the racemic mixture. Therefore, the development of the continuous chiral resolution of rac-Ibu to produce its more efficient single enantiomer *S*-Ibu presents a great interest.

The development of continuous crystallization, as well as flow chemistry, has attracted an increased attention in the past decades. Among the different continuous crystallizers designed over the years, Couette-Taylor (CT) crystallizers are constituted of two concentric cylinders, and provide a unique flow motion, thanks to the rotation of its internal one. Previous results obtained on deracemization quasi-isothermal processes seemed favorable in view of the implementation of chiral resolution by crystallization processes in CT crystallizers.

Thus, the goal of the work presented in this manuscript was to transfer an optimized process of the Pasteurian resolution of rac-Ibu to the continuous mode.

Chapter I describes the generalities about the main topics broached in this work. After some essential notions about crystallization in solution, chiral resolution by crystallization is presented, with a focus on Pasteurian resolution. Finally, the continuous crystallization and the CT reactor are introduced.

Chapter II is the first experimental chapter; it presents the preliminary investigations realized on the system to be resolve. Firstly, solubility measurements were determined, aiming at designing a robust chiral resolution process. Then, the phase diagram between the two diastereomers formed by the Pasteurian resolution was studied and updated after evidencing the presence of a partial solid solution on the side of the desired diastereomer. The crystals of this partial solid solution domain exhibit a surprising fibrous aspect, prone to form biphasic fluid inclusions under certain process conditions. The fibrous nature as well as the fluid inclusions formation are finally addressed in this chapter.

Chapter III is dedicated to the preparation of the continuous set-up. This latter was carefully examined prior to the beginning of the continuous experimental part. The upstream part of the installation was investigated in order to be properly designed for the further experiments. The environment of the CT crystallizer was also modified to improve its efficiency.

Chapter IV focuses on the continuous and batch work performed on the Pasteurian resolution of rac-Ibu. The batch work served the process optimization, and also enabled the generation of data to compare the two modes. The continuous mode was rationalized through a Design of Experiments approach, to study simultaneously the impact of different factors on the process results.

Finally, a general conclusion and some perspectives are discussed, according to the results presented in the different chapters.

Nomenclature

Abbreviations

<pss>	Partial solid solution (solid)
<pss*R*>	Partial solid solution which main enantiomer is the *R* one (solid)
<pss*S*>	Partial solid solution which main enantiomer is the *S* one (solid)
<*R*>	Single *R*-enantiomer (solid)
<*S*>	Single *S*-enantiomer (solid)
<*SR*>	Racemic compound (solid)
<sss>	Complete solid solution by means of substitution (solid)
ADNC	Automated Direct Nucleation Control
API	Active Pharmaceutical Ingredient
BFDH (model)	Bravais-Friedel-Donnay-Harker model
CFC	Continuous Filtration Carousel
COBC	Continuous Oscillatory Baffled Crystallizers
CSD	Crystal Size Distribution
CT	Couette-Taylor
DoE	Design of Experiments
DSC	Differential Scanning Calorimetry
FBRM (probe)	Focused Beam Reflectance Measurement
FDA	(USA) Food and Drug Administration
GRAS	Generally Regarded As Safe
HPLC	High Performance Liquid Chromatography
MSMPR	Mixed-Suspension, Mixed-Product Removal
PC	Preferential Crystallization
PFC	Plug Flow Crystallizer
PSD	Particle Size Distribution
PVM (probe)	Particle Vision and Measurement
R-Ibu-*S*-αMBA	Diastereomer *R*-Ibuprofen-*S*-(-)-α-Methylbenzylamine
RA	Resolving Agent
Rac-Ibu	Racemic Ibuprofen
RS-Ibu-*S*-αMBA	Mixture of diastereomers *S*-Ibu-*S*-αMBA and *R*-Ibu-*S*-αMBA
S-αMBA	*S*-(-)-α-Methylbenzylamine
S-Ibu	Enantiomer *S*-Ibuprofen
S-Ibu-*S*-αMBA	Diastereomer *S*-Ibuprofen-*S*-(-)-α-Methylbenzylamine
SCXRD	Single Crystal X-Ray Diffraction
SEM	Scanning Electron Microscopy
SM-PFC	Simulated Moving Plug Flow Crystallizer
SOAT	Second-Order Asymmetric Transformation
ss-*S*-Ibu-*S*-αMBA	(Partial) solid solution of *S*-Ibuprofen-*S*-(-)-α-Methylbenzylamine
XRPD	X-Ray Powder Diffraction

Variables

β	[-]	Supersaturation ratio or degree
γ	[J.m^{-2}]	Surface tension
ΔC	Molar or mass fraction (also: [g/L], [mol/L], [g/g]…)	Absolute supersaturation
Δde	[-]	Difference between the diastereomeric excess between of the last fraction and that of the first one
$\Delta H_{f,A}$	[J.mol^{-1}]	Enthalpy of fusion of pure component A
ΔP	[Pa]	Difference of pressure between the interior and the exterior of the bubble of gas
ΔT	[°C] or [K]	Temperature difference
$\lvert\Delta T\rvert$	[°C] or [K]	Absolute temperature difference
$\Delta T_{lm\text{-}counter}$	[K]	Logarithmic mean temperature difference for counter-current flow
η	[Pa.s]	Fluid dynamic viscosity
η_r	[-]	Radius ratio
λ	[-]	Supersaturation ratio related to the mass fraction of the solid
λ_{fluid}	[W.m^{-1}.K^{-1}]	Thermal conductivity of the fluid
λ_w	[W.m^{-1}.K^{-1}]	Thermal conductivity of the glass wall
μ	[-]	Ratio between the rotation speeds of the outer and inner CT cylinders
ν	[m².s^{-1}]	Kinematic viscosity
ρ	[kg.m^{-3}]	Fluid density
σ	[-]	Relative supersaturation
Φ	[J.s^{-1}]	Heat flow
Φ_c	[J.s^{-1}]	Heat flow in the cold part
Φ_h	[J.s^{-1}]	Heat flow in the hot part
Φ_w	[J.s^{-1}]	Heat flow in the glass wall
Ω	[rad.s^{-1}] or [rpm]	Rotation speed
Ω_i	[rad.s^{-1}] or [rpm]	Rotation speed of the inner cylinder
Ω_o	[rad.s^{-1}] or [rpm]	Rotation speed of the outer cylinder
$[A]$	Molar or mass fraction (also: [g/L], [mol/L], [g/g]…)	Concentration of compound A
b_i	[-]	Principal effect of the factor X_i
$b_{i,i}$	[-]	Quadratic (or curvature) effect of X_i
$b_{i,j}$	[-]	Interaction effect between X_i and X_j

C	Molar or mass fraction (also: [g/L], [mol/L], [g/g]…)	Concentration
C^*	Molar or mass fraction (also: [g/L], [mol/L], [g/g]…)	Solubility
C_i	Molar or mass fraction (also: [g/L], [mol/L], [g/g]…)	Initial concentration
Cp	[$J.kg^{-1}.K^{-1}$]	Heat capacity
Cp_c	[$J.kg^{-1}.K^{-1}$]	Heat capacity of the cold part
Cp_h	[$J.kg^{-1}.K^{-1}$]	Heat capacity of the hot part
D_{pipe}	[m]	Pipe diameter
d	[m]	Gap width between the two cylinders
de	[-]	Diastereomeric excess
D_h	[m]	Hydraulic diameter
e	[m]	Glass wall thickness
H	[$W.m^{-2}.K^{-1}$]	Global heat transfer
h	[$W.m^{-2}.K^{-1}$]	Convection coefficient
h_c	[$W.m^{-2}.K^{-1}$]	Convection coefficient in the cold part
h_h	[$W.m^{-2}.K^{-1}$]	Convection coefficient in the hot part
L_{pipe}	[m]	Length of the pipe
$\dot{m}$	[$kg.h^{-1}$]	Mass flow
$\dot{m}_c$	[$kg.h^{-1}$]	Mass flow of the cold part
$m_{collected}$	[g]	Mass of solid collected in one batch or in one fraction
$m_{expected}$	[g]	Expected mass to be collected from one batch or from one fraction
$\dot{m}_h$	[$kg.h^{-1}$]	Mass flow of the hot part
$m_{remaining\ solid}$	[g]	Mass of remaining solid recovered from sampling the supernatant of a suspension for solubility measurement by gravimetric method
$m_{sampled\ supernantant}$	[g]	Mass of the sample of supernatant of a suspension for solubility measurement by gravimetric method
$m_{solvent\ 1\ fraction}$	[g]	Mass of solvent that goes through the CT reactor during one residence time t
Nu	[-]	Nusselt number
Pr	[-]	Prandtl number
Q_v	[$m^3.s^{-1}$]	Volume flow rate
R	[$J.mol^{-1}.K^{-1}$]	Gas constant (8.314)

r	[m]	Radius of the bubble
R_c	[$W.K^{-1}$]	Resistance to the heat transfer due to the boundary layer of the cold part
Re	[-]	Reynolds number
Re_z	[-]	Axial Reynolds number
R_h	[$W.K^{-1}$]	Resistance to the heat transfer due to the boundary layer of the hot part
r_i	[m]	Radius of the inner cylinder
r_o	[m]	Outer cylinder radius
R_{pipe}	[m]	Pipe radius
R_t	[$W.K^{-1}$]	Total resistance to the heat transfer
R_w	[$W.K^{-1}$]	Resistance to the heat transfer due to the glass wall
S	[m^2]	Exchange area
S_a	[m^2]	Average of S_h and S_c
S_c	[m^2]	Surface between the glass wall and the cold part
S_h	[m^2]	Surface between the hot part and the glass wall
$S_{section}$	[m^2]	Pipe section
t	[min]	Residence time
T_1	[K]	Temperature of the hot fluid
T_2	[K]	Temperature at the hot wall
T_3	[K]	Temperature at the cold wall
T_4	[K]	Temperature of the cold fluid
$T1$	[°C]	Set temperature of the thermostat of the inner cylinder
$T2$	[°C]	Set temperature of the thermostat of the outer cylinder
Ta	[-]	Taylor number
Ta^*_c	[-]	Critical Taylor number in presence of the axial flow
$Ta^*_c(Re_z=0)$	[-]	Critical Taylor number without the axial flow
$T_{c,i}$	[K]	Temperature of the cold fluid at the inlet
$T_{c,o}$	[K]	Temperature of the cold fluid at the outlet
$t_{collection}$	[min]	Duration of one fraction, equivalent to the residence time t
T_e	[K]	Temperature of the eutectic invariant
$T_{f,A}$	[K]	Melting point of pure component A
$T_{h,i}$	[K]	Temperature of the hot fluid at the inlet
$T_{h,o}$	[K]	Temperature of the hot fluid at the outlet

T_j	[°C]	Jacket temperature, i.e. set temperature of the thermostat
T_{ref}	[°C]	Target temperature within the CT crystallizer, with $T_{ref} = \frac{T1+T2}{2}$
U_m	[m.s^{-1}]	Fluid velocity
V	[mL]	Volume of suspension collected
V_m	[m.s^{-1}]	Mean axial linear velocity
$\bar{x}$	[x]	Average
x_A	Mass or molar fraction	Composition in component A
X_i	[factor]	DoE factor
x_i	[x]	Value of x
Y	[Y]	DoE response

Chapter I. Generalities

I.1. Essentials of crystallization in solution

A crystalline solid is a material in which components (atoms, molecules or ions) are organized through a periodic long-range order in three independent directions[1–3]. Such arranged material can be obtained thanks to a crystallization operation starting from different mediums like vapors or melts[4]. Nevertheless, when dealing with organic solids, the most used process remains crystallization in solution. This step has the advantage of being able to combine the isolation and the purification of the product, which is not negligeable in the fine chemistry field.

The principle of crystallization in solution leans on supersaturation, its driving force[5], described in the next sections.

I.1.1. Solubility

Before introducing supersaturation, solubility must be defined. The solubility is the amount of a compound that can be dissolved in a specific solvent system, at given temperature and pressure. The system is then in the thermodynamic equilibrium.

The solubility can be written C^* and is expressed in mass or mole fraction. The units g/L, mol/L, or mg/g can also be found.

An example of solubility curve is given in Figure I- 1. When the concentration of the solute is inferior to the solubility, the solution is undersaturated. It becomes saturated when concentration equals the solubility, by means of evaporation or cooling for example (see section I.1.3). When the concentration of the solute exceeds the saturation, crystallization is supposed to take place. However, crystallization does not always occur as predicted; the system is then in a metastable state called supersaturation.

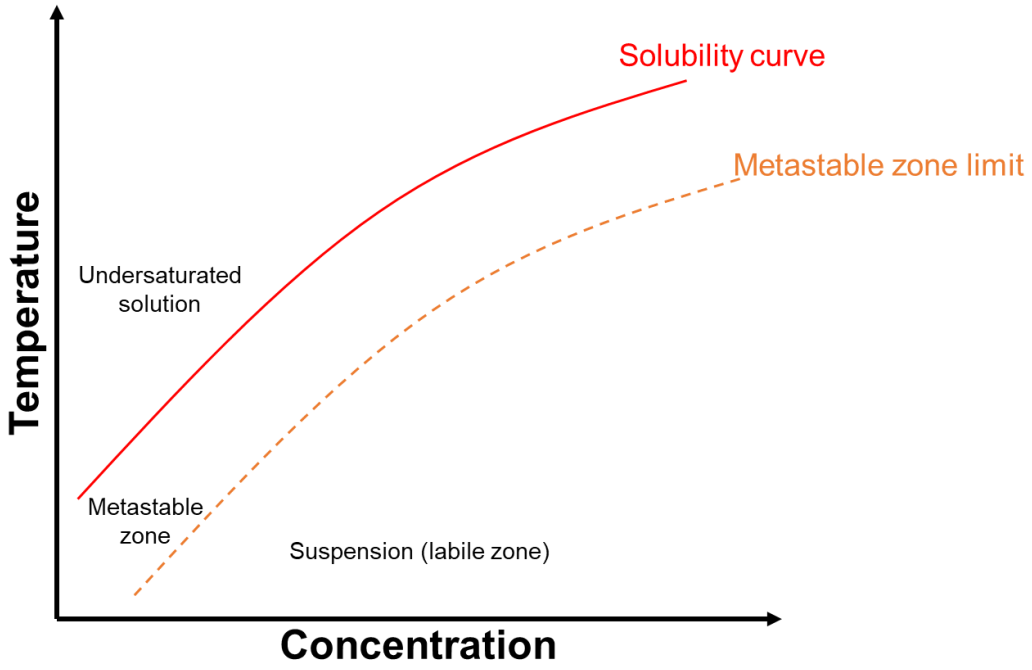

Figure I- 1: Representation of the solubility curve (red curve), delimiting the undersaturated solution zone, and of the metastable zone limit (orange curve), separating the metastable zone and the labile zone.

I.1.2. Supersaturation

As seen in the previous section, a supersaturated solution is a solution where the solute is dissolved at a higher concentration C than the solubility C*[3,4]. The system is then out of thermodynamic equilibrium, in the metastable zone (Figure I- 1). In this zone, the probability of crystallization occurrence increases when coming closer to the metastable zone limit. This limit is system-dependent and characterizes the boundary of metastability, i.e., the curve of spontaneous crystallization.

When crystallization occurs, it will last until the system gets back from the metastable supersaturated state to the thermodynamic equilibrium, i.e., the concentration of solute returns to the solubility value. That is why supersaturation is called the driving force of a crystallization process in solution.

Supersaturation can be expressed as[3,5]:

- Supersaturation ratio or degree β (dimensionless): $\beta = \frac{C}{C^*}$,
- Absolute supersaturation ΔC (same unit as C and C*): $\Delta C = C - C^*$,
- Relative supersaturation σ (dimensionless): $\sigma = \frac{C-C^*}{C} = \beta - 1$,
- A fourth interesting equation can be used[6], λ, which gives directly the mass fraction of solid that can be retrieved for a mass unit of the system: $\lambda = \frac{C-C^*}{1-C^*}$ (dimensionless).

Supersaturation can be induced with different methods; the principal ones are described in the next section.

I.1.3. Main methods of crystallization in solution

In crystallization processes in solution, three main techniques are used: variation of the temperature, evaporation, and addition of an antisolvent. The two first methods are illustrated in Figure I- 2, and the third one is displayed in Figure I- 3.

(1) *Crystallization induced by variation of temperature:* starting from the initial point A, in the present case of direct solubility, the temperature is decreased until point B, which is on the metastable zone limit. Spontaneous nucleation will occur at point B, the solution will desaturate and follow one pathway from B to C. At point C, the system is in equilibrium: the concentration in solution equals the solubility value.

(2) *Crystallization induced by evaporation:* starting from the initial system state in point A, evaporation at constant temperature is performed. When reaching point D, on the metastable zone limit, the spontaneous nucleation occurs. Crystallization will consume the excess of solute, lowering the solution concentration until the solubility value (point E). The system is now in the thermodynamic equilibrium.

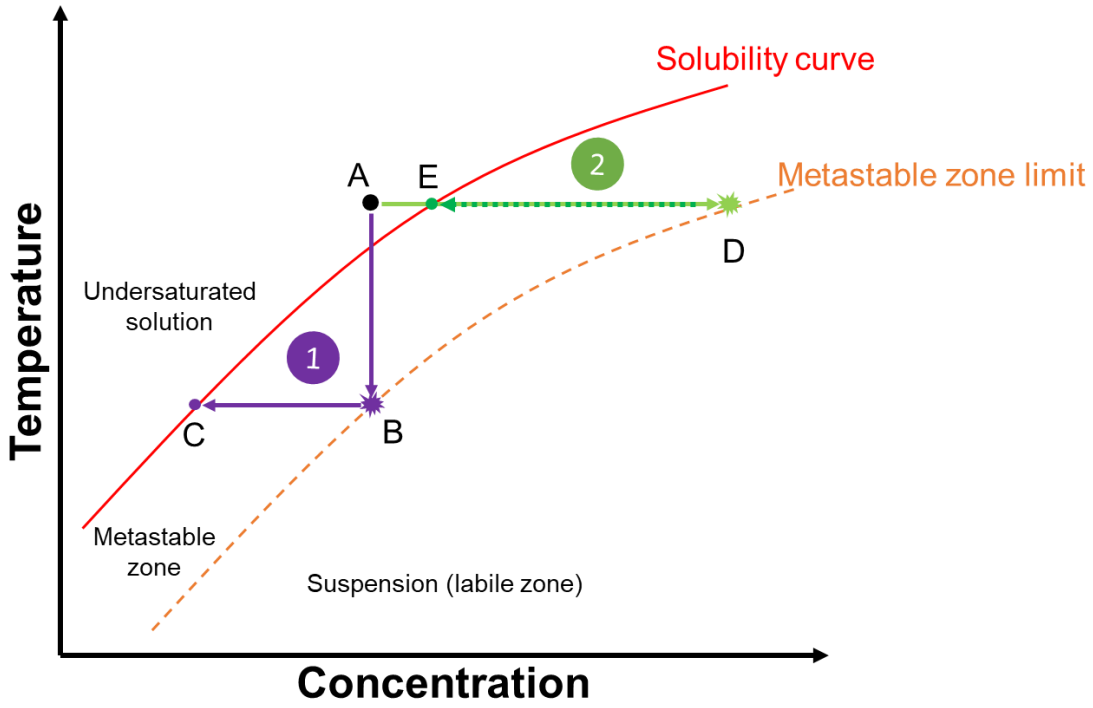

Figure I- 2: Pathways of crystallization induced by cooling (purple elements) and by evaporation (green elements).

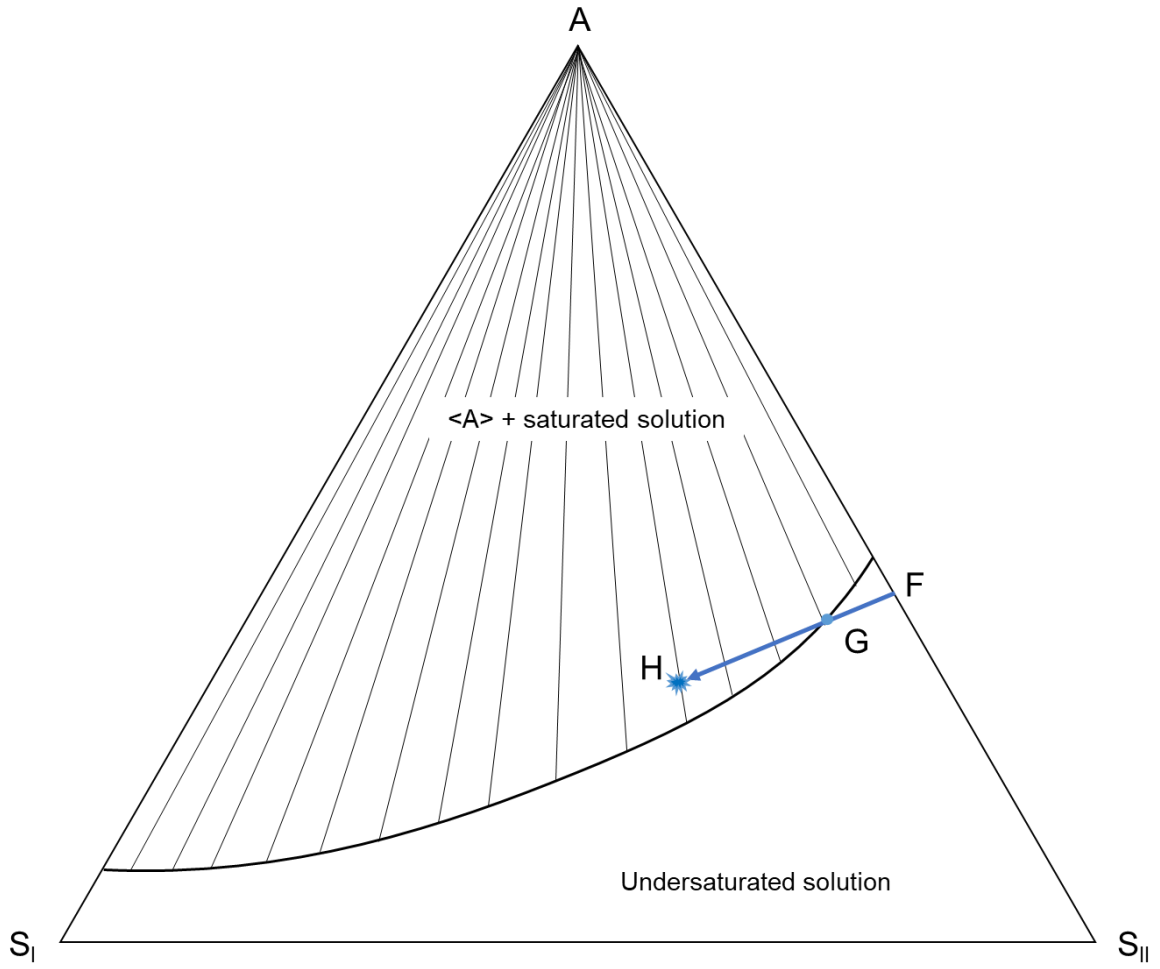

Figure I- 3: Ternary isotherm depicting crystallization by antisolvent addition, with solute A, solvent S_I (bad solvent or anti-solvent), and solvent S_{II} (good solvent).

(3) *Crystallization induced by addition of an antisolvent:* by definition, the solubility of a solute in an 'antisolvent' is low. The addition of the antisolvent changes the order of the system, therefore, the description of this method goes through a ternary isotherm, as displayed in Figure I- 3, with the solute A, the bad or antisolvent S_I, and the good solvent S_{II}.

Antisolvent S_I is gently added to the system of A dissolved in S_{II} starting from point F. At a specific solvent ratio, the solubility curve (black bold line) is crossed in point G. The system enters then in the biphasic domain of "<A> + saturated solution", where the excess of A (regarding thermodynamics) should crystallize. The system is able to accept supersaturation until point H, where spontaneous nucleation occurs.

It is noteworthy to mention that in case of a fast antisolvent addition, a phenomenon of oiling out between the two solvents can be observed[6].

The crystallization pathway involving variation of temperature is the simplest to implement and to control. This method should be favored. However, when the solubility varies poorly with temperature[3], solvent evaporation or addition of an antisolvent are good alternatives. Also, this latter method has the advantage of giving an access to heterosolvates[7].

The control of the crystallization process is mandatory to ensure the physical quality specifications of a process. General quality requirements concern the yield, the purity, the polymorphism, the morphology, the particle size distribution (PSD)[3,8–10]…

In addition to the choice of the technique among the three aforementioned, the control and robustness of a crystallization process can be guaranteed by a seeding procedure. In this case, the nucleation will no longer occur spontaneously, but it will be induced by the inoculation of seeds meeting the process specifications. The system then follows other pathways than described above, according to the crystallization method used.

Crystallization allows chemists to isolate a product most of the time, associated with its purification. Purification here refers to chemical purity, but the crystallization step can also be the cradle of "enantio-purification", i.e., chiral resolution. One of the simplest methods of chiral resolution by crystallization is the formation of diastereomeric salts, also called Pasteurian resolution[11]. This is presented in the next section.

I.2. Chiral resolution by diastereomeric salt formation

Before introducing chiral resolution by diastereomeric salt formation, the notion of enantiomers and their associate phase equilibria must be addressed.

I.2.1. Enantiomers

Enantiomers are stereoisomer molecules that are mirror images of each other, thus non superimposable (e.g., a pair of hands)[12]. The chirality of such molecules has a great importance in pharmaceutical industry since enantiomers of chiral drugs can have very different properties with respect to their pharmacological and toxicological effects[13]. Thalidomide is a striking example of these differences: the *R*-enantiomer has a sedative effect on pregnant women, while the *S*-enantiomer causes birth defects[14]. Commonly, only one enantiomer (eutomer) of a chiral drug provides the best therapeutic effect and/or less side effects. The other enantiomer (distomer) is generally less/not efficient, or even harmful[15]. In some specific cases, the two enantiomers can have two distinct biological activities[12].

When one of the two enantiomers is toxic, the separation of the two entities is mandatory. When the distomer is only less active, the chiral resolution can be interesting in order to minimize the Active Pharmaceutical Ingredient (API) amount in the drug dose[12]. Thus, separation of enantiomers, or chiral resolution, appears to be a key point in many pharmaceutical industry processes, especially knowing that 80 % of the marketed drugs approved by the USA Food and Drug Administration (FDA) contain a chiral center[16].

There are different ways to access pure chiral molecules, such as stereoselective synthesis, chromatography, biocatalytic synthesis, membranes, or crystallization. Chromatography techniques are the most convenient in the majority of cases, but it is quite expensive and present limitations regarding productivity, hence inapplicable for large scale production[17]. Conversely, resolution by crystallization ranks as the oldest and most readily applicable operation in chemical processing[10].

To elaborate the best crystallization strategy to separate the two enantiomers, the phase equilibria between the enantiomers needs to be investigated.

I.2.2. Phase equilibria between enantiomers

There are two main phase equilibria between two non-racemizable enantiomers[13,18]:

(1) *Racemic compound forming systems:* this type of phase equilibria is depicted in Figure I- 4 (a), and represents 90-95 % of the cases of racemic mixtures crystallization[18]. A racemic compound is a stoichiometric compound with equivalent proportions of *S* and *R*-enantiomer in the same single crystal. Thus, the separation of the two enantiomers is not possible as such, as shown on the phase diagram of Figure I- 4 (a).

(2) *Conglomerate forming systems:* this kind of equilibria is represented in Figure I- 4 (b). In such case, the chiral discrimination is spontaneous, as the two enantiomers crystallize in separated crystal lattices.

A third type of equilibria can be mentioned: the systems exhibiting a complete solid solution by means of substitution <sss>, as shown in Figure I- 4 (c). This is induced by a total miscibility of the two enantiomers in the solid state: each enantiomer can substitute the other[13].

Hybrid cases are possible[18], like the one presented in Figure I- 4 (d): the conglomerate forming system exhibits partial solid solutions <pss> of each enantiomer. The access to the enantiopure compounds is then compromised, as each stereoisomer crystal lattice accept a small amount of the other one.

As mentioned before, conglomerate forming systems give a direct access to enantiopure compounds, through preferential crystallization (PC), Second-Order Asymmetric Transformation (SOAT) or deracemization for example[10,17–23]. Associated with a fast racemization in the liquid state, such methods can lead to the recovery of 100 % of the desired enantiomer[18].

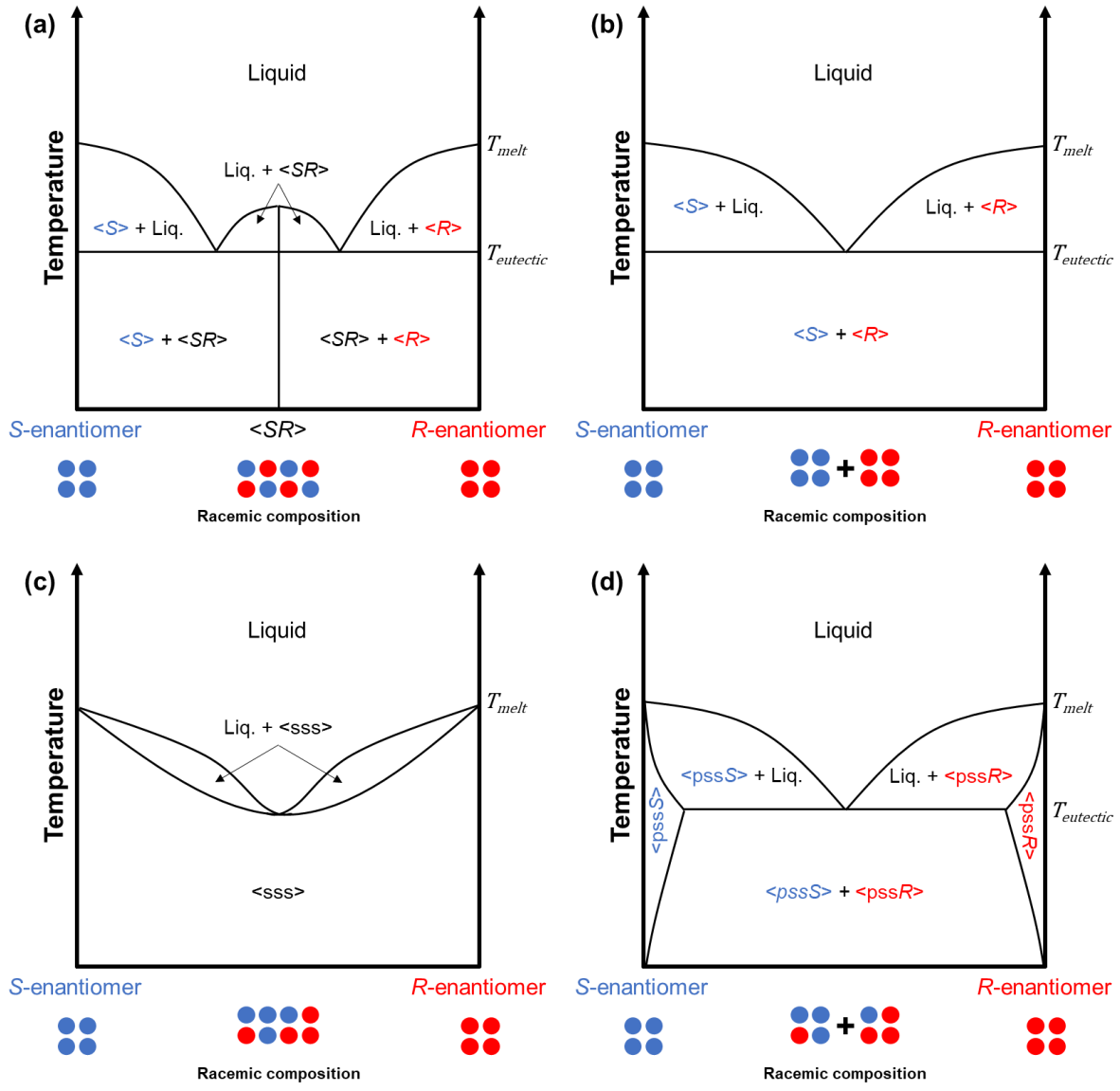

Figure I- 4: Schematic representation of four examples of phase equilibria between two non-racemizable enantiomers, and their racemic composition organization at the molecular scale: (a) racemic compound <SR> system, (b) conglomerate forming system, (c) system with a complete solid solution formed by substitution <sss>, (d) conglomerate forming system with partial solid solutions <pssS> and <pssR>. N.B.: the compounds are stable at fusion.

If the system to resolve do not form conglomerate, it needs to be modified in order to recover the eutomer by crystallization. When the knowledge on the enantiomers is poor, the choice of the method to use for their separation can be rationalized with the decision tree presented by Ciriani *et al.*[16].

One of the easiest techniques to implement and to scale up, is the chiral resolution by diastereomeric salt formation[11], or Pasteurian resolution. In this method, the enantiomers are transformed in diastereomers, which are easier to separate.

I.2.3. Pasteurian resolution

The Pasteurian resolution is based on the work of Louis Pasteur on tartaric acid[24]. This widely used technique is seen as the classical resolution method[10,11,17,19,20].

I.2.3.1. Principle

This chiral resolution method deals with the formation and separation of diastereomers[11,17,19,20]. By reacting a single enantiomer of a chiral resolving agent (RA) on the enantiomers to resolve, a pair of diastereomeric salts is formed. This reaction is often based on an opposite acid-base character between the enantiomers and the RA.

After salt formation, the formed diastereomers are separated: unlike enantiomers, diastereomers have different physical properties, such as solubility. Therefore, it is easier to separate diastereomers than enantiomers[18,25].

This method is suitable to scale-up and is already used in some large-scale processes[11]. To ensure its robustness, the conditions must be carefully examined.

I.2.3.2. Choice of the conditions

Resolving agent

One of the main burning topics of the Pasteurian resolution is to choose the proper RA[17,20]. In the literature, a lot of RAs are listed; nevertheless, the first compounds to consider are those with a structure similar to that of the racemate being resolved[17,19,20]. Also, the interactions between the enantiomers to resolve and the RA should preferably be noncovalent, to ensure an easy recovery of the pure enantiomer by salting out[10]. Therefore, the formation of diastereomeric salts is generally preferred. It is noteworthy to mention that the molar ratio between the RA and the enantiomers is not restricted to 1:1 or 2:1, it can be 4:1 or even 6:1[11,17,20].

In 2008, Faigl *et al.* detailed the parameters influencing the choice of the chiral RA and its good enantiomer, such as the resolvability parameter S (based on thermodynamic and structural parameters) or the structural similarity around the stereogenic center[20].

Moreover, to secure the resolution process at production scale, the chosen RA should be inexpensive, and has to be readily available in large quantities, with a high chiral purity[10].

Solvent

According to Siedlecka (2013), the efficiency of a resolution procedure strongly depends on the nature of the solvent (protic, aprotic, dielectric constant, polarity…) in some cases, such

as the resolution of mandelic acid[17]. For example, studies have demonstrated that one enantiomer of a chiral selector can recognize both enantiomers of a target molecule in different solvent systems with different dielectric constants. The phenomenon is termed “dielectrically controlled resolution”[26].

The solvent can also induce a preferred configuration of the molecule or the formation of solvates[20]. This latter case must be cautiously studied because it can be favorable or unfavorable.

Solvent mixtures should not be forgotten; it can be preferred to pure solvents[19], but the composition must be optimized carefully[20].

The choice of the RA and of the solvent(s) covers the most influent parameters of the Pasteurian resolution, but attention must be paid to the potential role played by temperature and by pH[20].

Once the conditions are determined, the formation of the diastereomeric pair of salts can be carried out. The next step is the procedure of separation of the formed diastereomers.

I.2.3.3. Separation of the diastereomers

Classical separation in chiral resolution by diastereomer salt formation processes is based on the difference in solubility between the formed diastereomers[11,17,19]. This characteristic emphasizes the importance of the choice of the solvent. Thus, the efficiency of the separation is determined by the extent of the difference in solubility of the two diastereomers.

Separation is usually done by cristallization[17], but it can also be performed by a supercritical fluid extraction or by distillation[20].

The stability difference between the less and more soluble diastereomeric salt depends mostly on the existence/magnitude of intermolecular interactions, such as hydrogen bonds, CH/π interactions and van der Waals interactions[17,20]. The separation is also influenced by the diastereomer conformational rigidity[17].

Separation is followed by the removal of the RA, generally by salting out, to recover the pure enantiomer alone.

In some cases, to improve its efficiency, the classical diastereomeric salt formation method can be modified by putting additives[17,20].

I.2.3.4. Variations of the classical diastereomeric salt formation method

The following sections deal with the two main variations of the diastereomeric salt formation method, one developed by Pope and Peachey, and another one which is called the Dutch resolution.

Pope and Peachey procedure

The resolution method of Pope and Peachey consists in incorporating an optically inactive reagent, which completes the optically active RA of the classical procedure[27,28]. Figure I- 5 shows a schematic comparison between the typical procedure of the chiral resolution by diastereomeric salt formation and Pope and Peachey method in the ideal cases.

In favorable cases, the optically inactive reagent will react selectively and completely with one enantiomer, while the optically active RA reacts completely with the other enantiomer. The achiral reagent may also play the role of inhibitor for the nucleation of the undesired enantiomer[17].

This method is also called the “half-equivalent” method of resolution[19], because only half equivalent of the chiral RA is needed, the other half equivalent is replaced by the optically inactive reagent[20], as shown on Figure I- 5. Therefore, it can be quite suitable if the optically active RA is expensive.

According to Wilen *et al.* (1969), the main advantage of the Pope and Peachey procedure consists in avoiding the majority or even all the recrystallizations often needed in typical chiral resolutions[27]. Indeed, in the classical chiral resolution by diastereomeric salt formation, the extent of the resolution is limited by usually small solubility differences between the two diastereomers produced. In the Pope and Peachey procedure, this dependence, even though existing, should be less restrictive, as the products are not diastereomers[27].

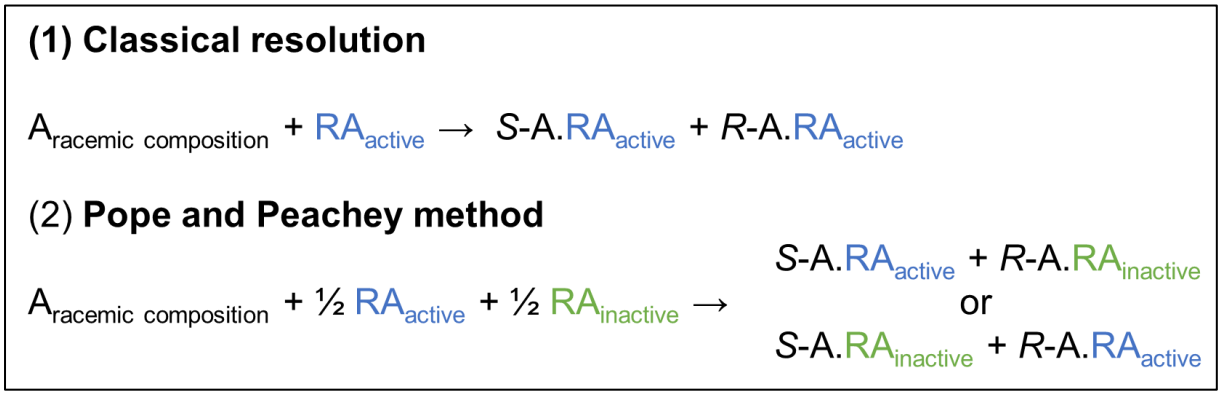

Figure I- 5: Schematic comparison between (1) the classical chiral resolution by diastereomeric salt formation and (2) the Pope and Peachey method. $A_{racemic\ composition}$ stands for the racemic mixture, RA_{active} (blue) for the optically active RA and $RA_{inactive}$ (green) for the optically inactive reagent.

The major difficulty in the Pope and Peachey method is the selection of a good optically inactive reagent. It must be selective of one enantiomer, and inert regarding the optically active RA. It is generally the burning topic regarding chiral resolution[17,20].

A technique close to that developed by Pope and Peachey can by mentioned: the Marckwald’s procedure[29], which consists in reducing the amount of the optically active RA, without compensating it.

Dutch resolution method (or family resolution)

The Dutch resolution technique is another variation of the diastereomeric salt formation method. It consists in adding a mixture of RAs to the enantiomeric system to resolve[19,20]. The used RAs must have analogous structure and the same configuration.

Fogassy *et al.* (2006) noticed an interesting fact: the ratio of RAs in the precipitated salt is not necessarily similar to that in the solution[19].

The use of the Dutch resolution method is rarely reported, probably because of two principal drawbacks. First, the constant change of the proportions of liquid and solid can be challenging. Secondly, no successful rationalization could be elaborated.

These variations offer additional possibilities to the classical method of chiral resolution by diastereomeric salt formation. This also shows to what extent this latter has been studied. In 2013, Wang and Chen even proposed a rationalization of this optical resolution method[11].

I.2.3.5. Pasteurian resolution rationalization

The diastereomer system formed with the classical resolution method can be put in equations[11], from which conditions, such as the volume of solvent, the pH or the number of RA equivalent needed, can be determined. These equations can also permit to calculate the theoretical yield and to determine the separation efficiency.

In their published work, Wang and Chen (2013) also proposed a practical workflow for chiral resolution screening by diastereomeric salt formation (Figure I- 6), based on their own experience. They specified that this workflow must be coupled with X-Ray Powder Diffraction (XRPD) and/or Differential Scanning Calorimetry (DSC) analyses.

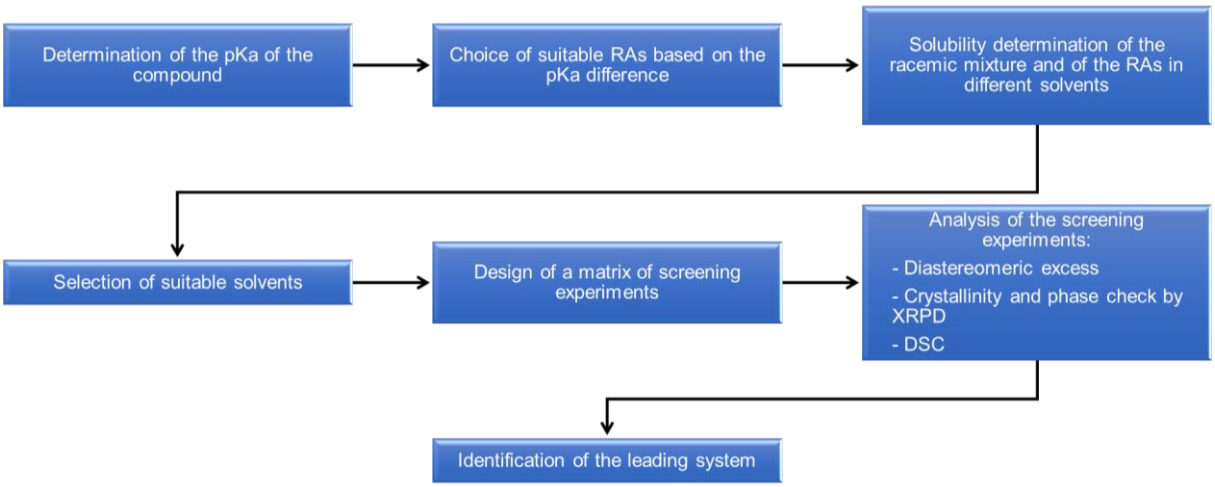

Figure I- 6: Schematic diagram of the practical workflow proposed by Wang and Chen for the screening of the conditions for chiral resolution by diastereomeric salt formation.

With a proper design, such workflow promises to perform a large number of screening experiments with a small amount of material (≈500 mg) and a high rate of success.

It is noteworthy to mention that an optimization is generally needed with respect to temperature, pH and molar ratio of the RA[11].

The diastereomeric salt formation resolution method is a quite complete procedure, which crucial points are related to the choice of the RA(s) and of the process conditions. Thanks to its simplicity, its excellent results, and its reliability, this technique can easily be implemented at an industrial scale[10].

Traditionally, the Pasteurian resolution is performed in batch mode. However, since the majority of the chiral drugs approved by the USA FDA are single enantiomers[12,16], the transfer of such chiral resolution method to continuous mode should be considered.

I.3. Continuous crystallization

If flow chemistry is used since decades in the petrochemical and bulk chemical industry, its development in the pharmaceutical industry is more recent[30–32].

As mentioned before, API production is usually performed through batch processes[8,10,16,33]. However, batch facilities age and are eventually decommissioned, giving the opportunity for companies to invest in continuous systems[34].

I.3.1. Comparison between batch and continuous modes

In the past years, the use of the batch mode has shown some economical limitations, especially due to high requirements of human intervention and high operating costs[8,16,35]. Conversely, the continuous mode is more cost effective: despite its initial expensive implementation, it offers lower operating cost and space requirement[16,30,32,35,36]. In addition, the development period to pilot and/or to commercial production can be significantly reduced[37,38].

On the technical aspect, the batch production mode can be subject to batch-to-batch product quality variation[8,16,34–36,38,39]. In opposition, optimized continuous processes guarantee a constant product quality, or at least less variation, thanks to the steady state functioning, which enables a better process control[8,10,30,31,33–39].

In continuous device, the heat and mass transfers are achieved more efficiently[30,31,33,40,41]. These characteristics serve a more effective mixing, and a better control of temperature and residence times. As a consequence, with the help of process optimization, the side-product production is limited, and the productivity is enhanced.

In summary, continuous mode offers an improvement in process efficiency, leading to better process results, such as an improved and more constant product quality/purity, an enhanced selectivity and a higher yield[30–35,40,41].

Batch mode can also be restrictive regarding the feasibility and scale-up of some processes[34]. Due to its enhanced robustness, continuous mode has been shown to ease the scale-up and to be more predictable than batch mode[33,40]. These attributes offer adaptative manufacturing.

In the cases of chemical processes difficult or impossible to implement in batch mode (not viable economically, extreme temperatures and/or pressures, short contact times, mixing regimes, heat removal, etc.), the transfer to flow chemistry can be a clear beneficial solution; it also gives an access to ‘greener’ and safer process conditions[16,30,31,34,39–41].

In flow processes, the bottleneck is generally located at the isolation steps: crystallization and filtration[9]. More than 90 % of APIs are isolated as crystalline products[16], thus, crystallization is a critical stage in pharmaceutical processes, as it governs the API purity and physical properties[39].

I.3.2. Continuous crystallization

Since the continuous mode seems to improve the product and process features, its application to crystallization has attracted an increased attention in the two past decades,

especially in the fine chemistry and pharmaceutical industry[8,10,33,35–40]. However, such implementation is challenging, as crystallization processes and formation of impurities are sensitive to temperature, mixing and residence time[40].

I.3.2.1. Challenges

In the continuous mode, the main technical difficulties are encrustation, fouling and blockage[3,8,35,38,40,42–44]. The risk of such phenomenon is even higher when the continuous operation is the crystallization step. The principal origins of clogging issues are the heterogeneous nucleation induced by insufficient heat transfer, or by equipment material differences between scales, the small size of the production lines and the use of low flowrates[33,38]. If these process parameters cannot be modified, the implementation of preventive periodic temperature cycling can be a solution to avoid these issues[8,44].

Also, literature reports troubles in improving the yield of continuous crystallization processes[8,33], but it can largely be counterbalanced by an increased productivity[38].

More generally, according to Zhang *et al.* (2017), the two main obstacles to the development of crystallization operations in continuous mode are: the ability to choose the appropriate design for the production of the desired crystals and the ability to determine the suitable continuous crystallization process[8]. In addition, the fundamentals of crystallization (nucleation, growth, polymorphism, crystal structure-property relationships) are not always well-understood, which is why continuous crystallization has not been as studied as flow chemistry[39].

To implement continuous crystallization processes, specific reactors were designed and studied in the past years. Some of them are presented in the next section.

I.3.2.2. Continuous crystallizers

Continuous crystallizers are divided in two main categories: mixed-suspension, mixed-product removal (MSMPR) crystallizers and plug flow crystallizers (PFCs).

Because of their easy handling, MSMPR crystallizers are the most used ones, especially in API process development[8,9,33,35]. They are particularly suitable for long residence time processes[8–10,35]. Nevertheless, issues can be encountered with such device, like difficulty in controlling the crystal shape and size distribution, and a complicated scale-up[8,33].

In opposition, PFCs can be easily scaled up and offer a higher efficiency than MSMPR reactors of the same volume[8,33,38]. Their use is more appropriate for short residence time processes[8,10,33,35]. Nonetheless, the risk of fouling or blockage is higher and the equipment is more complex[8,33,35].

To date, no study has been published to compare directly PFCs and MSMPR crystallizers, but the yield should be theoretically better in PFC-based systems[33].

Besides these two main types of continuous crystallizers, other designs have also been developed: continuous oscillatory baffled crystallizers (COBCs), fluidized bed crystallizers or continuous laminar shear crystallizers[33,35,36,39]. Couette-Taylor (CT) crystallizers belong to this last group.

I.3.3. Couette-Taylor crystallizer

I.3.3.1. Continuous laminar shear crystallizers

Continuous laminar shear crystallizers are more rarely cited in the literature than the other categories presented in the previous section. Such reactors are constituted by two concentric cylinders; thanks to the rotation of one of the cylinders, or of both of them[45,46], a shear force is applied to the flow going through the gap between the two cylinders.

Maurice Couette was the first to run experiments on the fluid flow between two concentric cylinders in 1890[47]. Thanks to his apparatus, with the external cylinder rotating, he was able to show that at low rotation speed, the torque varies linearly with the rotation speed[48]. He also noticed that above a certain rotation speed, a hydrodynamic instability occurs with a sudden increase of the torque.

Thirty years later, G. I. Taylor (1923) studied and described the nature of this instability, by demonstrating the appearance of specific vortices when the rotation speed is sufficient[49]. The cause of the occurrence of these vortices is the sudden predominance of the centrifugal forces over viscous forces[50,51]. It is a dissipative structure.

This specific flow motion has been studied theoretically and/or experimentally by many groups afterwards, with different apparatus size and design, and with various configuration regarding the rotating cylinder(s): external rotating cylinder like Couette; internal rotating cylinder as Taylor; both cylinders rotating, in the same or opposite direction[45,46,52–55]. During their study, Kataoka (1986) and Maron and Cohen (1991) have identified the potential of using a device with such characteristic fluid flow as a chemical reactor, considering it as a series of micro-stirred tanks.

The Couette-Taylor (CT) crystallizers belong to the category of continuous laminar shear crystallizers, with the internal cylinder rotating, the outer cylinder being at rest, like the device used by Taylor in 1923.

I.3.3.2. Concept of the Couette-Taylor crystallizer

Continuous CT crystallizers have been developed based on the flow characteristics described in the previous section. At low rotation speed, the fluid motion follows Couette observations, and above a certain rotation speed, the flow changes into radial vortex combined with small axial dispersion, as explained by Taylor[35,50,56–58].

The Couette-Taylor flow within a CT crystallizer is displayed in Figure I- 7: a stratified Couette flow coupled with Taylor vortices.

The azimuthal fluid motion resulting from the rotation of the inner cylinder of CT crystallizers creates periodic toroidal vortex flow patterns[56,59]. This specific flow motion gives the CT device an ability for a very effective and homogeneous mixing[56–58,60]. Thanks to this highly efficient mixing, the CT fluid motion exhibits enhanced heat and mass transfer rates in comparison with turbulent flow of batch tanks or even other continuous crystallizers[50,51,55,56,61,62].

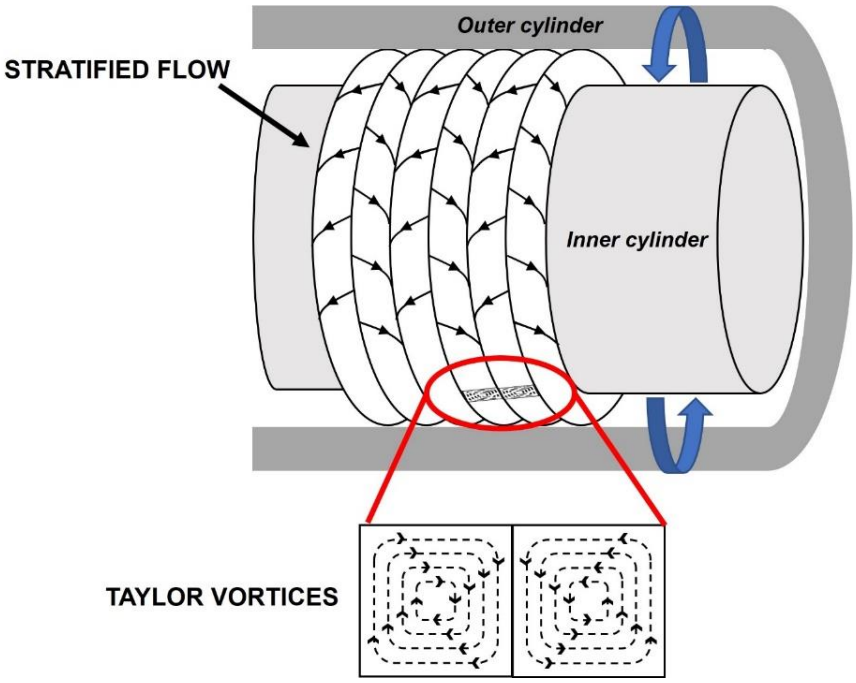

Figure I- 7: Visualization of the Taylor vortices in a CT crystallizer[63].

The crystal properties are dependent on the operating conditions of the crystallization process, hence on the hydrodynamics. Thereby, CT crystallizers seem suitable for the implementation of continuous crystallization processes[35,51,57].

I.3.3.3. Determination of the critical rotation speed

As mentioned previously, to ensure the occurrence of the unique vortex flow of the CT reactors, a certain rotation speed must be reached. This critical rotation speed, at which the flow instability occurs, can be retrieved from the critical Taylor number[49]. This dimensionless number can be described as the ratio of centrifugal forces to viscous forces[50,51]. It is given by Equation I- 1, where Ω_i is the rotation speed of the inner cylinder in rad.s^{-1}, r_i the radius of the inner cylinder (m), d the gap width between the two cylinders (m), and ν the kinematic viscosity (m².s^{-1}):

$$Ta = \frac{\Omega_i^2 r_i d^3}{\nu^2}$$ *Equation I- 1*

As shown in Equation I- 1, the Taylor number, thus the critical Taylor number Ta^*_c, depends mainly on the kinematic viscosity and on the system geometry. This latter is characterized by the ratio $\frac{d}{r_i}$, or by the radius ratio $\eta_r = \frac{r_i}{r_o}$, with r_o the outer cylinder radius[45,56].

The value of the critical Taylor number can be found in the literature, since various research groups have determined it analytically and experimentally over the years, with different geometries and rotation configuration (choice of the rotating cylinder(s))[45,46,52–55,64–73].

However, in many cases, this critical Taylor number does not consider the presence of an axial flow. This lack leads to the correction of the critical Taylor number value, given by Equation I- 2[55]:

$$Ta^*_c = Ta^*_c(Re_z = 0) + 26.5 {Re_z}^2$$ *Equation I- 2*

In Equation I- 2, Ta^*_c is the critical Taylor number in presence of the axial flow and $Ta^*_c(Re_z=0)$ the critical Taylor number without the axial flow. Re_z, the axial Reynolds number, is defined in Equation I- 3, with V_m the mean axial linear velocity ($m.s^{-1}$):

$$Re_z = \frac{dV_m}{\upsilon} \qquad \textit{Equation I- 3}$$

The critical rotation speed can then be calculated thanks to Equation I- 1.

The extensive work done on the Couette-Taylor flow has shown that it can be divided in different flow regimes, with specific rotation speed ranges.

I.3.3.4. Couette-Taylor flow regimes

At some specific critical Taylor number 'multiples', the initial axisymmetric Taylor vortex flow goes through other flow regimes up to a fully developed turbulent flow[51,54,55]. It is presented in Table I- 1.

Ta/Ta^*_c	Flow regime
Ta/Ta^*_c <1	Laminar Couette flow
1< Ta/Ta^*_c <9	Laminar periodic Taylor vortex flow
9< Ta/Ta^*_c <176.89	Singly periodic wavy vortex flow
176.89< Ta/Ta^*_c <324	Doubly periodic wavy vortex flow
324< Ta/Ta^*_c <1089	Weakly turbulent wavy vortex flow
1089< Ta/Ta^*_c <25600	Turbulent vortex flow
25600< Ta/Ta^*_c	Turbulent aperiodic flow

Table I- 1: The different flow regimes reachable within a CT crystallizer and their critical Taylor number range.

The crystallization process is influenced by the flow regime[50]. The switch from one flow regime to another is strongly facilitated within a CT crystallizer, by only changing the rotation speed[35].

In addition to the interesting inherent features of the CT reactors, modifications of the initial design can be implemented, in order to meet specific requirements.

I.3.3.5. Modifications of the initial Couette-Taylor device

In the past decade, the original CT crystallizer design has been adapted for new research studies, especially in the group of Professor Kim in South Korea. In particular, experiments were run with a multiple-feeding mode, or by implementing an independent temperature regulation for each cylinder, in order to generate a temperature gradient between the two cylinders[50,59,62]. This last modification has shown its efficiency in controlling crystal size distribution (CSD), and has also been identified as "especially appropriate for cooling crystallization"[74].

The use of the CT crystallizer has been proved to impact CSD[51,62,74], crystal morphology, agglomeration[58] and polymorphism[57,59,60,75]. Recently, the temperature gradient implementable between the two cylinders of the CT reactor has enabled the acceleration of deracemization processes[61,76]. This technology has also been used for *mechanical* continuous chiral resolution[77–79], but to date, no other examples of continuous chiral resolution in CT crystallizer can be found in the literature.

I.3.4. Continuous chiral resolution by crystallization

The use of continuous mode for chiral resolution by crystallization is rarely reported. Most of the published examples deal with PC implementation in MSMPR crystallizers and in fluidized bed crystallizers[8,10,15,16,35,38]. Two reasons can explain this lack of study: continuous crystallization processes are subject to clogging issues[40], and the yield of continuous chiral resolution by crystallization processes is generally low[8].

However, the unique flow provided by the CT crystallizers and previous results obtained on deracemization processes are promising regarding the implementation of chiral resolution by crystallization processes in CT crystallizers. Such operation can be really interesting in the cases of compounds produced at large scale, like Ibuprofen.

Chapter II. Chiral resolution of racemic Ibuprofen: Presentation of the system

The present work focuses on the chiral resolution by diastereomeric salt formation of racemic Ibuprofen (rac-Ibu) with *S*-(-)-α-Methylbenzylamine (*S*-αMBA). This second chapter is a general introduction to the studied system.

In the first place, after an introduction on Ibuprofen, the solubility measurements of rac-Ibu and of the desired diastereomer *S*-Ibu-*S*-αMBA are reported. Then, the diastereomeric couple is presented through its revised phase diagram, and a study of the surprising fibrous nature of the less soluble salt. Due to this latter, the recovered particles trend to exhibit fluid inclusions, which formation was investigated and is discussed here.

II.1. Presentation of Ibuprofen

Ibuprofen is an API marketed since the 1960s as an anti-inflammatory and analgesic agent[80]. This nonsteroidal anti-inflammatory drug (NSAID) is commercialized in its racemic form, i.e., a 1:1 mixture of *S*-(+)-Ibuprofen and *R*-(-)-Ibuprofen (Figure II- 1).

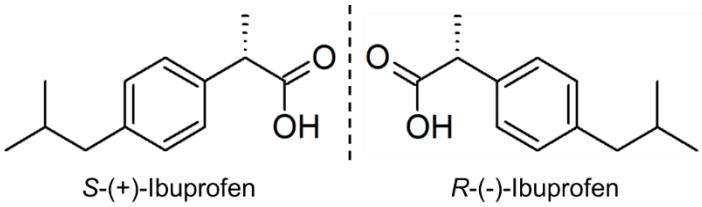

Figure II- 1: Enantiomers of Ibuprofen.

In this chiral drug, the *S* enantiomer is responsible of the therapeutic effect, while the *R* enantiomer is nontoxic and inefficient. In addition, a significant amount of the distomer *R* can be inverted into the eutomer *S* within the body, which is why it can be marketed in its racemic form[12,80].

Nevertheless, it has been proved that the eutomer has a higher efficiency than the racemic mixture[80]. This is probably due to the presence of the distomer, which chiral inversion is not instantaneous. Furthermore, in a general way, there are many benefits in using a single enantiomer of a chiral drug, such as the reduction of the metabolic burden and the diminished risk of pharmacokinetic interactions with other drugs[12,80].

Classically, the resolution of racemic Ibuprofen can be performed through a diastereomeric salt formation with *S*-(+)-Lysine. The formed diastereomers can then be separated by PC or temperature selective diastereo-recognition[81,82]. The *S*-Ibuprofen (*S*-Ibu) is then recovered after the removal of the *S*-(+)-Lysine.

The use of *S*-(-)-α-Methylbenzylamine (*S*-αMBA) as resolving agent (RA) can also be interesting, because of its ability to recognize efficiently acidic enantiomers in the solid state[83]. However, the *S*-αMBA is not a GRAS (Generally Regarded As Safe) substance, thus, it must be carefully removed when it is used to resolve chiral drugs. Its elimination can be easily performed with the addition of an acid to the diastereomeric salt dissolved in ethanol. Despite this inconvenience, *S*-αMBA remains a remarkable resolving agent of carboxylic acids, thanks to its predictable intermolecular interaction with such molecular function[83].

In the present work, racemic Ibuprofen (rac-Ibu) is resolved through a diastereomeric salt formation with *S*-αMBA (Scheme II- 1) in a mixture of ethanol and water, with different ratios.

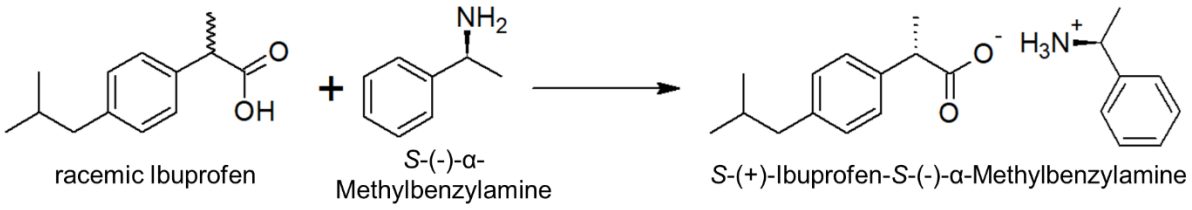

Scheme II- 1: Chiral resolution by diastereomeric salt formation of racemic Ibuprofen with S-α-Methylbenzylamine.

Drugs containing rac-Ibu rank among the most sold in the world. Therefore, the development of its continuous chiral resolution to produce the more efficient single enantiomer *S*-Ibu presents a great interest.

The continuous or semi continuous chiral resolution of rac-Ibu has already been successfully performed with enzyme resolution techniques in a packed bed reactor, operating as a plug-flow reactor[84], or in an enzymatic membrane reactor, considered as a continuous stirred tank reactor[85]. The continuous PC of the diastereomer (±)-Ibuprofen-S-Lysine through a sequential coupled-batch operation[86] was also successfully carried out.

Regarding the efficiency of the heat and mass transfer rates in CT device (see Chapter I section I.3.3), there is a strong interest in evaluating the transfer of the rac-Ibuprofen chiral resolution process by diastereomeric salt formation with *S*-αMBA from batch mode to continuous mode in a CT crystallizer.

In order to design a robust process, solubility measurements were performed on the system to be resolved.

In the first place, they were measured for rac-Ibu, the molecule to resolve. Secondly, the solubility of the desired diastereomer ss-*S*-Ibu-*S*-αMBA was evaluated at different temperatures and in different ratios of ethanol/water. The results are presented in the next section.

II.2. Solubility of the racemic Ibuprofen and of the *S*-diastereomer

II.2.1. Racemic Ibuprofen

After a first estimation at the ambient temperature (see Appendix A section A.3.1) of 785 $mg.mL_{solvent}^{-1}$, i.e. 0.50 $g.g_{saturated\ solution}^{-1}$, the solubility measurement of rac-Ibu in technical ethanol[1] (EtOH) was performed in the Crystal 16 (see Appendix A section A.3.2). The four tested concentrations are described in Table II- 1.

Vial n°	Calculated concentration ($g.g_{saturated\ solution}^{-1}$)	Real concentration ($g.g_{saturated\ solution}^{-1}$)
1	0.47	0.463
2	0.50	0.510
3	0.53	0.534
4	0.56	0.556

Table II- 1: Concentration values of rac-Ibu in technical EtOH tested in the Crystal 16.

The temperature program used is shown in Figure II- 2: three temperature cycles between 5 °C and 70 °C, with stages of 1 h at 5 °C and 30 min at 70 °C.

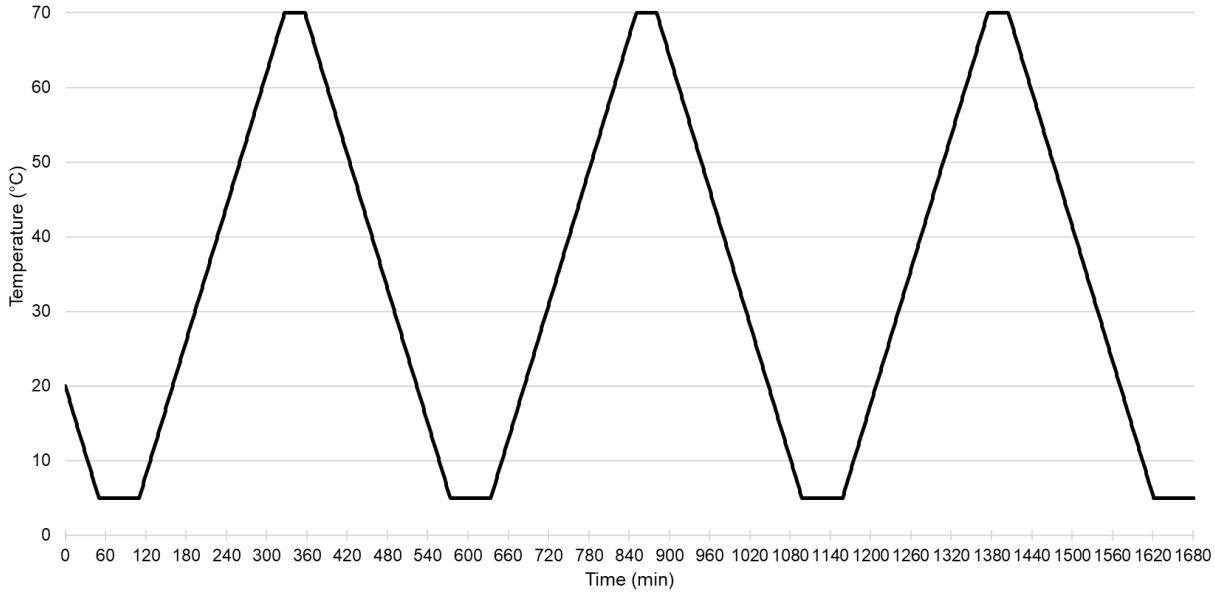

Figure II- 2: Temperature program of the solubility measurements of rac-Ibu in technical EtOH in the Crystal 16.

The results of the solubility measurements of rac-Ibu in technical ethanol are presented in Figure II- 3. The blue points show the measured values, and the orange curve is the fitted curve given by the software Crystal Clear, based on the van't Hoff regression, with a correlation

[1] Technical ethanol is at the azeotropic composition, i.e., EtOH/H_2O 96/4 V/V. This gives a mass composition of 95/5 w/w.

coefficient R^2 of 0.94. This coefficient is correct but would be better with more data to fit. Nevertheless, regarding the really high solubility of rac-Ibu in technical EtOH, there is no need in obtaining more precise data, since the initial concentration of rac-Ibu in the developed process is much lower than the solubility.

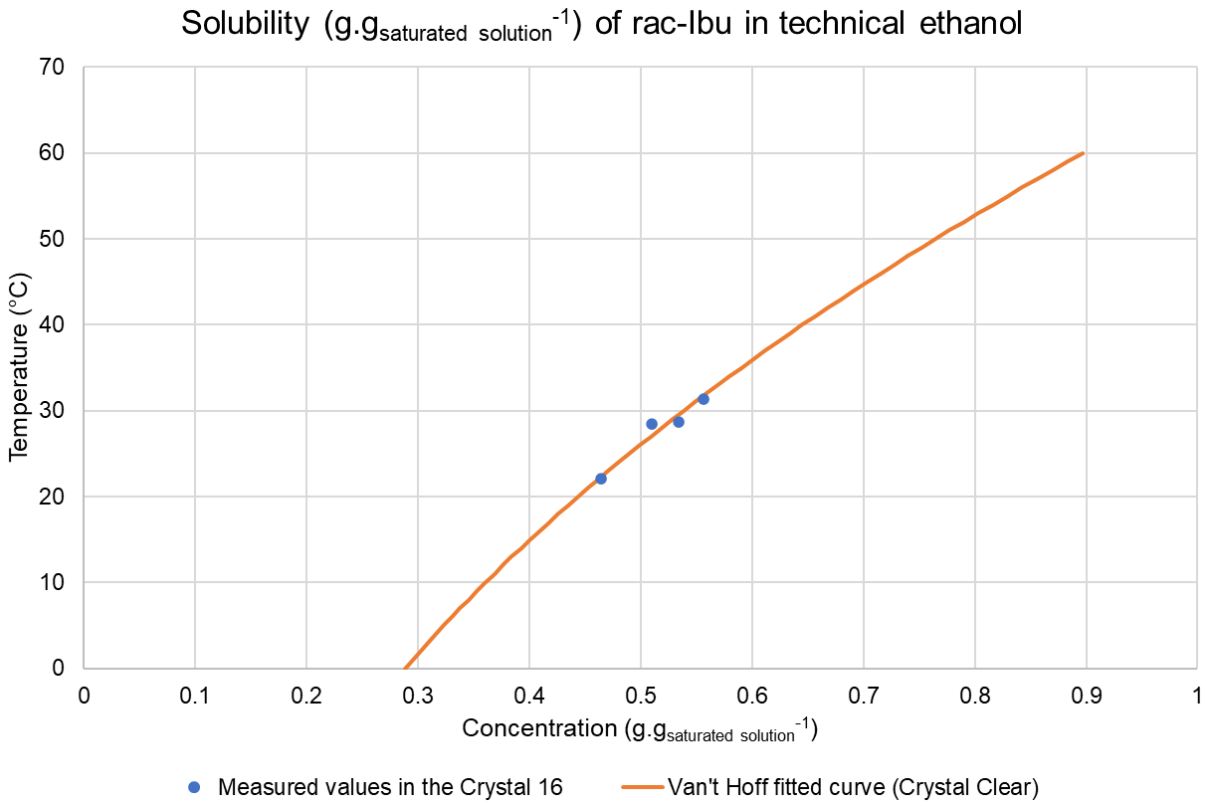

Figure II- 3: Solubility ($g.g_{saturated\ solution}^{-1}$) of rac-Ibu in technical EtOH: in blue the points measured by the Crystal 16 and in orange the fitted curve based on van't Hoff regression determined with the software Crystal Clear.

After being realized on rac-Ibu, solubility measurements were done for *S*-Ibu-*S*-αMBA in different ratios of EtOH/H_2O.

II.2.2. *S*-Ibuprofen-*S*-α-MethylBenzylAmine

Initially, the chiral resolution of rac-Ibu with *S*-αMBA was performed in pure technical EtOH (see Chapter IV section IV.1). Nevertheless, during the process optimization, the addition of water to ethanol has proved its benefic effect on the crystal morphology (see section IV.2). Therefore, the solubility of the diastereomeric salt *S*-Ibu-*S*-αMBA has been determined in different ratios of [technical EtOH]/H_2O.

The initial ratios were thought regarding the amount of technical ethanol versus that of water. However, as mentioned before, technical ethanol being at the azeotropic composition, it already contains 5 %w of water. Table II- 2 gives the conversion of the initial chosen mass proportions of [technical EtOH]/H_2O into the real mass proportions of EtOH/H_2O. For the sake of precision, the ratios presented in the next sections are those of the real proportions of EtOH/H_2O.

Solubility of *S*-Ibu-*S*-αMBA was measured by gravimetric method (see Appendix A section A.3.3) in the ratios mentioned above, and in pure ethanol, at six temperatures: 10, 20, 30, 40, 50 and 60 °C.

Initial mass proportions of [technical EtOH]/H_2O	Real mass proportions of EtOH/H_2O
100/0	95/5
95/5	90/10
90/10	86/14
80/20	76/24
70/30	67/33
50/50	48/52

Table II- 2: Conversion table of mass proportions [technical EtOH]/H_2O into real mass proportions of EtOH/H_2O.

The results of the solubility measurements were exploited with Excel: the results are presented in Figure II- 4, with the concentration (%w) as a function of temperature. The polynomial regression curves are depicted in this figure, with good correlation coefficients (R^2). The first observation of these curves is that the solubility variation is not linear with the water amount.

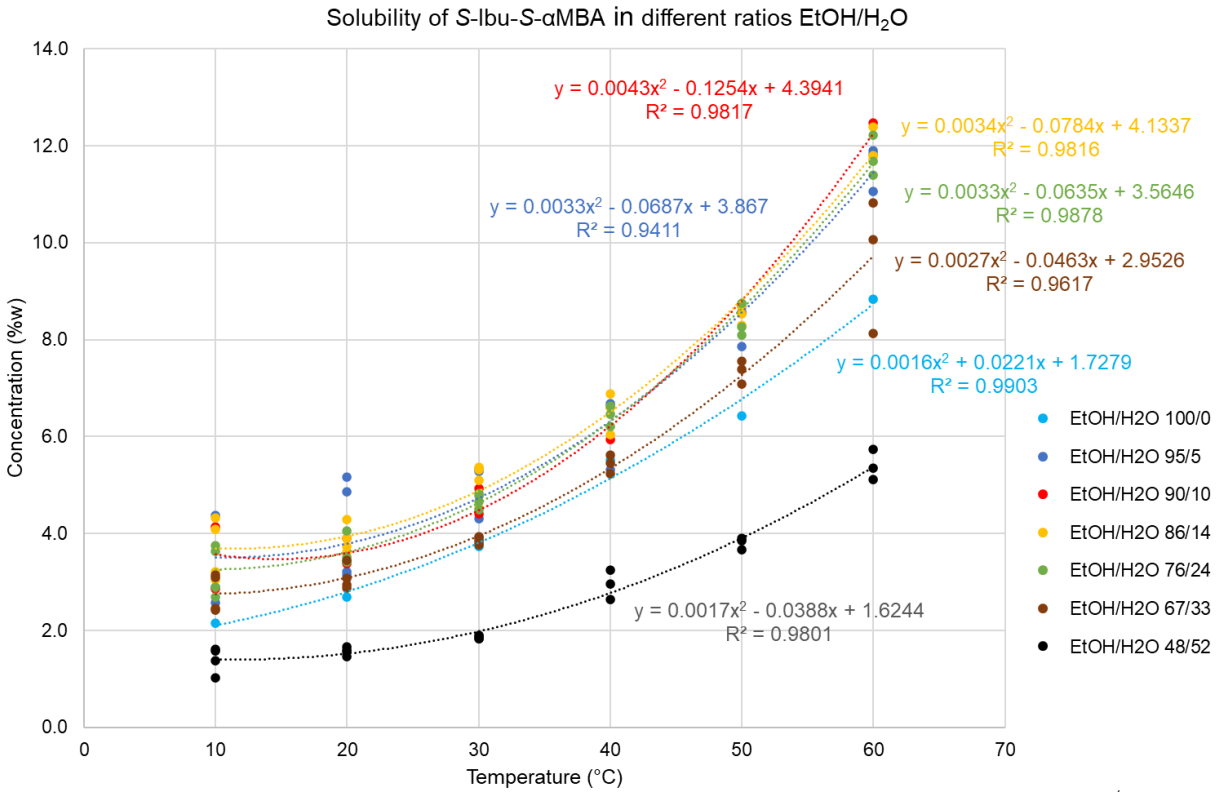

Figure II- 4: Solubility curves and polynomial trendlines of the diastereomer S-Ibu-S-αMBA in different ratios EtOH/H_2O. Representation with concentration (%w) as a function of temperature (°C). Light blue ratio 100/0 w/w; dark blue ratio 95/5 w/w; red ratio 90/10 w/w; yellow ratio 86/14 w/w; green ratio 76/24 w/w; brown ratio 67/33 w/w; black ratio 48/52 w/w.

The same data are represented in Figure II- 5 with the concentration as a function of the amount of water. At each temperature, the curve presents a belt shape, with a maximum between 10 and 15 %w of water.

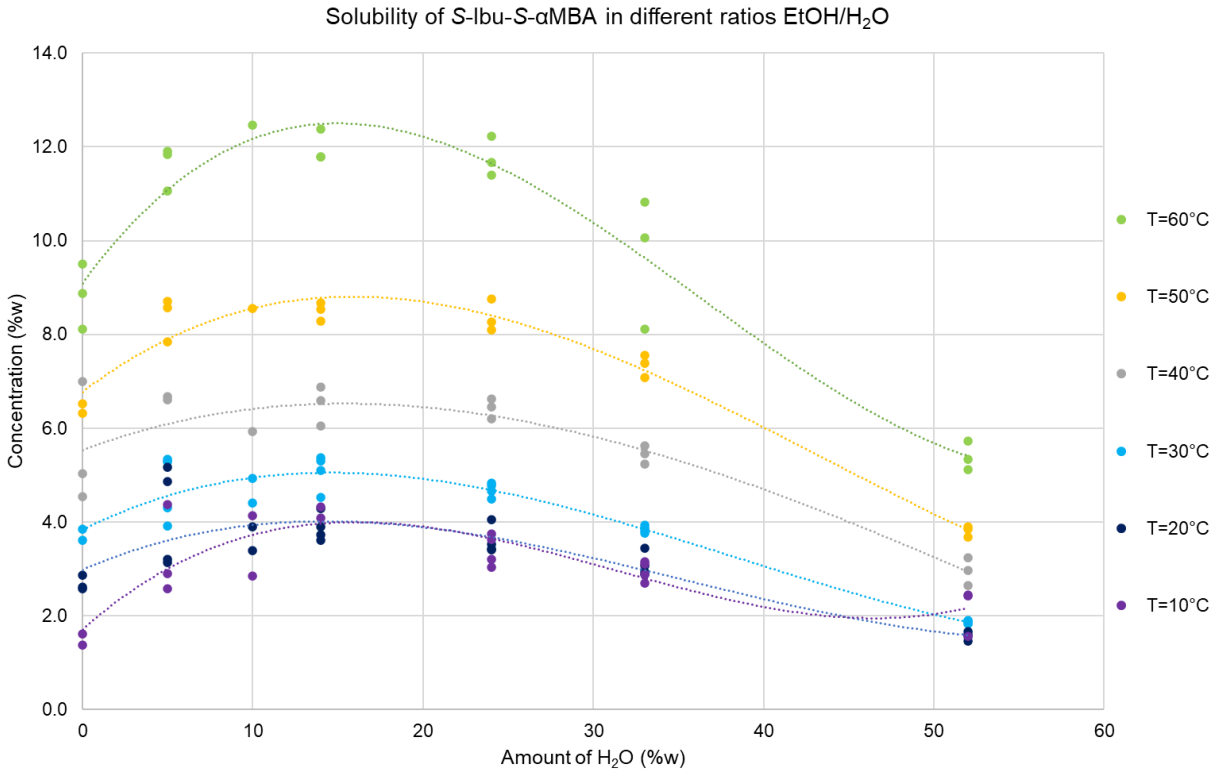

Figure II- 5: Solubility curves and polynomial trendlines of the diastereomer S-Ibu-S-αMBA in different ratios EtOH/H₂O. Representation with concentration (%w) as a function of the amount of water (%w). Green T = 60 °C; yellow T = 50 °C; grey T = 40 °C; light blue T = 30 °C; dark blue T = 20 °C; purple T = 10 °C.

The Excel regression exploitation was compared with two others: van't Hoff plots and Dynochem, a simulation tool working as an Excel add-in (see Appendix A section A.10). To discriminate the different solubility models, the results of the equations given by each one were compared to the measured values. In the end, the results of the equations given by the Excel exploitation appeared to be the closest to the experimental data. Therefore, this model was chosen for the calculation of solubility for further work.

Another aspect regarding solubility was addressed: the influence of the chiral purity. Indeed, according to its diastereomeric excess, the solubility of the *S*-Ibu-*S*-αMBA salt can change. This effect was studied and is presented in the next section.

Effect of the product chiral purity

One of the parameters that can represent the process effectiveness in separating two diastereomers is the diastereomeric excess (de). The diastereomeric excess defines the amount of eutomer recovered 'alone', i.e., the chiral purity of the obtained product. It can be calculated as:

$$de = \frac{[Eutomer] - [Distomer]}{[Eutomer] + [Distomer]}$$ *Equation II- 1*

As the *S*-Ibu-*S*-αMBA products were analyzed by chiral High Performance Liquid Chromatography (HPLC, see Appendix A section A.4), the diastereomeric excess is the direct difference of the two calculated percentages, as described in Equation II- 2.

$$de = \%_{S-\text{Ibu}-S-\alpha\text{MBA}} - \%_{R-\text{Ibu}-S-\alpha\text{MBA}} \qquad \textit{Equation II- 2}$$

The solubility measurements presented in the previous sections were made with a product with a $\mathrm{de} = 0.61$. This value is the average de of *S*-Ibu-*S*-αMBA obtained from batch mode.

Solubility was measured by gravimetric method on two other products, with a different de: one with $\mathrm{de} = 0.35$ and one with $\mathrm{de} = 0.72$. Figure II- 6 shows the solubility in a mixture EtOH/H_2O 76/24 w/w of *S*-Ibu-*S*-αMBA products with these three chiral purities.

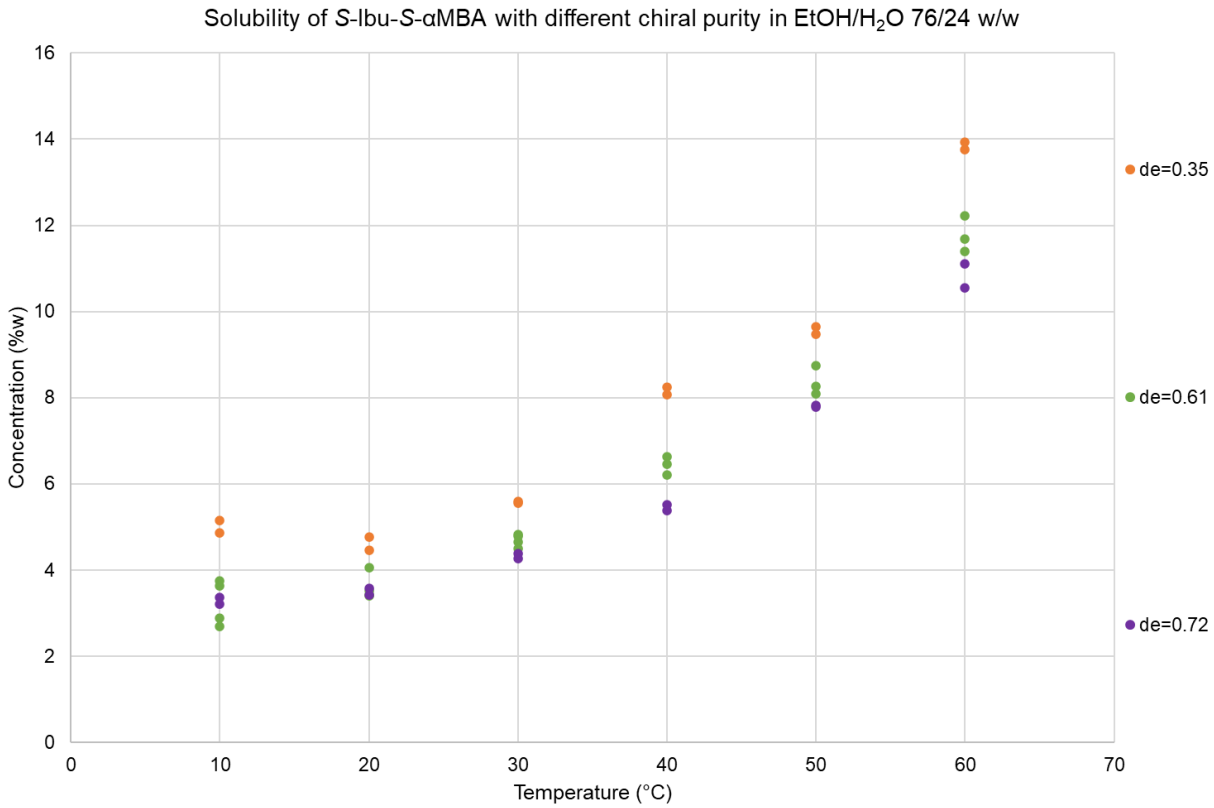

Figure II- 6: Comparison between the solubility curves of S-Ibu-S-αMBA products with different chiral purities: de=0.35 (orange), de=0.61(green) and de=0.72 (purple).

On Figure II- 6, it can clearly be observed that as chiral purity increases, solubility decreases. This behavior was expected.

As explained in Appendix A section A.3, the remaining solid of the solubility measurements was analyzed by X-Ray Powder Diffraction (XRPD; see Appendix A section A.5), to check that the phase did not change in the studied solvent(s). If all the recovered solids globally exhibit the same pattern than the initial product, small peak shifts were sometimes observed. Such behavior is characteristic of the presence of a partial solid solution (see Chapter I section I.2.2). Nevertheless, when reviewing the literature, the binary system between the two diastereomers *S*-Ibu-*S*-αMBA and *R*-Ibu-*S*-αMBA only exhibits a simple eutectic at 150 °C[87]. The part of the phase diagram close to pure *S*-Ibu-*S*-αMBA was then investigated.

II.3. Revised binary phase diagram

II.3.1. Existence of a partial solid solution enriched in *S*-Ibu-*S*-αMBA

To refine the reported binary phase diagram between the diastereomers *S*-Ibu-*S*-αMBA and *R*-Ibu-*S*-αMBA, investigations were made by using Differential Scanning Calorimetry (DSC; see Appendix A section A.6) analysis.

In the first place, the analyses were performed by using crucible with pierced lids.

II.3.1.1. DSC analyses in crucibles with pierced lids

For this first series of DSC analyses, different compositions in *S*-Ibu-*S*-αMBA / *R*-Ibu-*S*-αMBA w/w were prepared from *RS*-Ibu-*S*-αMBA and pure *S*-Ibu-*S*-αMBA: 95/5, 90/10, 85/15, 80/20, 70/30, 60/40 and 50/50. Two preparation methods were used: dry grinding of the two raw powders, and cooling crystallization in pure ethanol. It appeared that the technique does not affect the product purity.

The DSC thermograms of the different compositions are displayed in Figure II- 7.

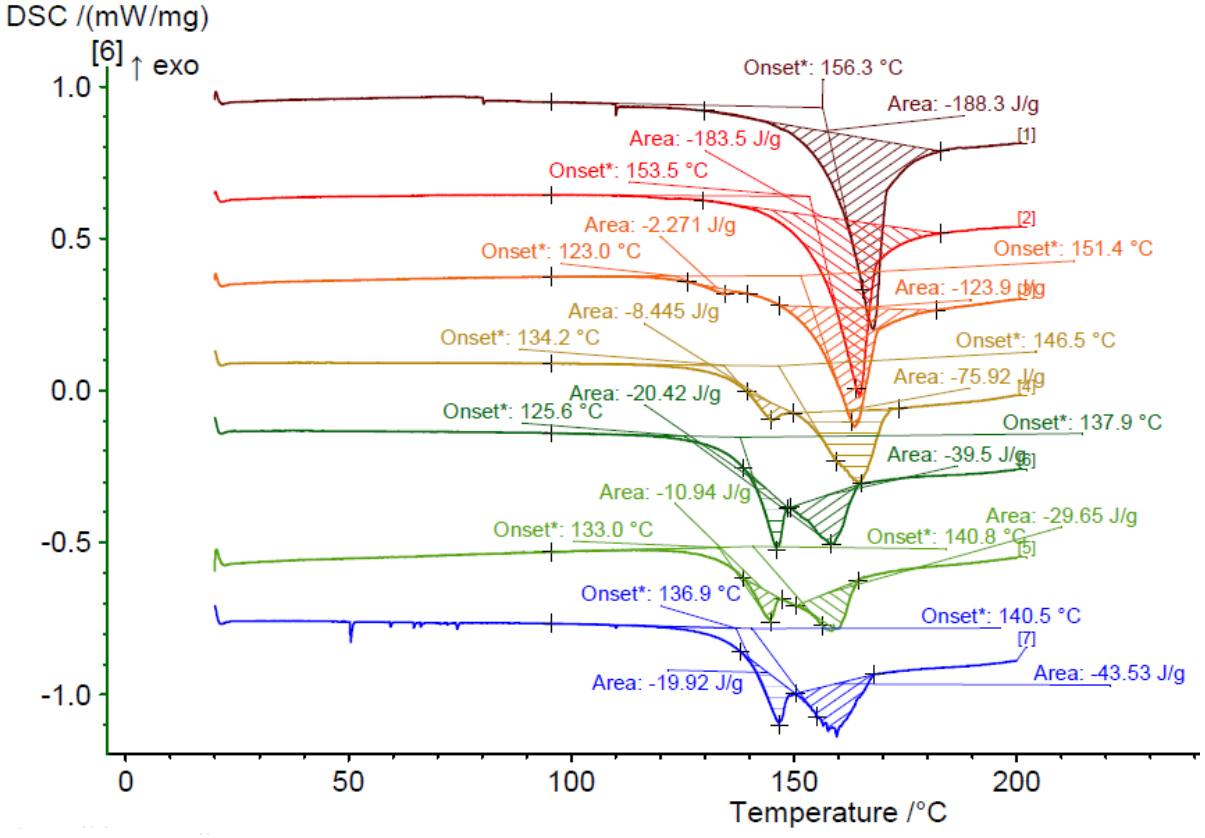

Figure II- 7: DSC thermograms obtained in crucibles with pierced lids at different compositions in S-*Ibu*-S-*αMBA /* R-*Ibu*-S-*αMBA. Samples were heated from 20 °C to 200 °C at a rate of 2 K.min^{-1}. From top to bottom: composition 95/5 w/w (dark red); composition 90/10 w/w (red); composition 85/15 w/w (orange); composition 80/20 w/w (yellow); composition 70/30 w/w (dark green); composition 60/40 w/w (green); composition 50/50 w/w (blue).*

In Figure II- 7, the endothermic peak at the highest temperature corresponds to the fusion. Its temperature decreases as the amount of *R*-Ibu-*S*-αMBA increases, which is an expected behavior.

The second endothermic peak observed for the compositions *S*-Ibu-*S*-αMBA / *R*-Ibu-*S*-αMBA 85/15, 80/20, 70/30, 60/40 and 50/50 w/w should correspond to the eutectic invariant. As it is not present in the thermograms of the compositions 95/5 and 90/10 w/w, this would mean that the eventual partial solid solution has a limit comprised between 10 %w and 15 %w of *R*-Ibu-*S*-αMBA.

However, the apparent eutectic temperature is below the one reported by Ebbers *et al.*[87]. Also, the fusion peak is not sharp, and the following baseline is not flat. This is due to the sublimation of the salt. It has been confirmed by collecting the vapors above a Köfler bench at approximately 140 °C. Regarding this deviation, another series of DSC analyses was performed, in sealed crucibles.

II.3.1.2. DSC analyses in sealed crucibles

In this second series of DSC analyses, the same compositions than these of the previous section were prepared. Their DSC thermograms are depicted in Figure II- 8. The fusion peaks resolution is improved in sealed crucible, and the following baseline is flatter.

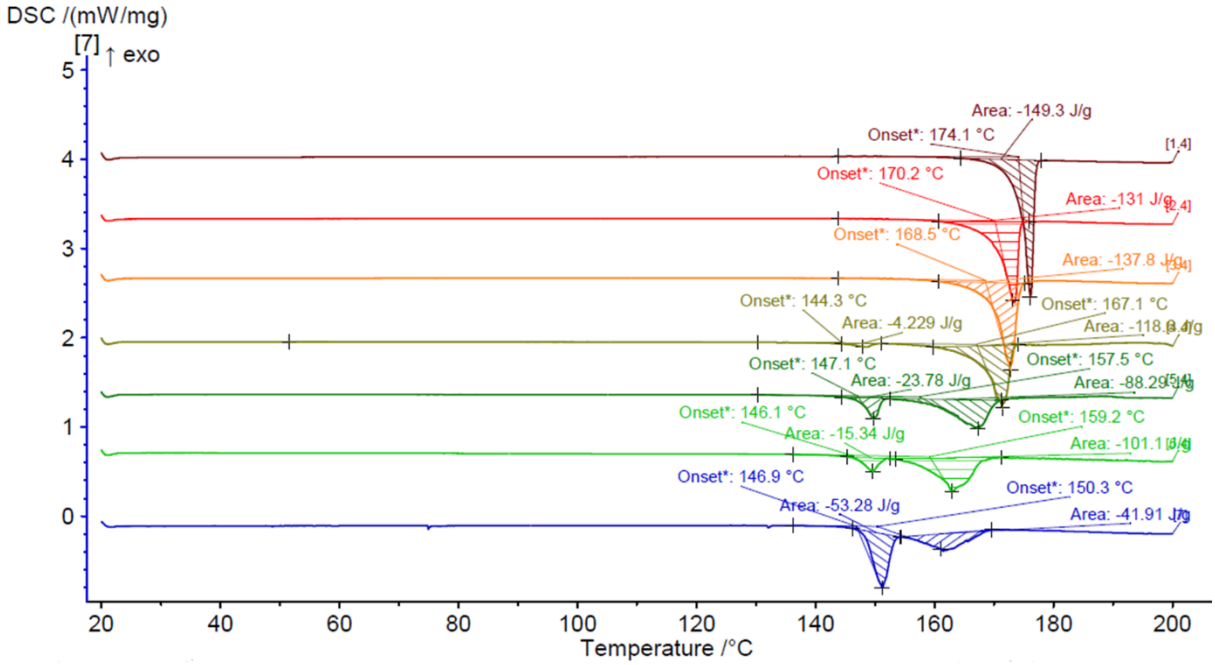

Figure II- 8: DSC thermograms obtained in sealed crucibles at different compositions in S-Ibu-S-αMBA / R-Ibu-S-αMBA. Samples were heated up to 130 °C, with a heating rate of 2 K.min^{-1}, maintained at 130 °C for 2 h, then cooled down to 20 °C at 5 K.min^{-1} and finally heated up to 200 °C at a rate of 2 K.min^{-1}. From top to bottom: composition 95/5 w/w (dark red); composition 90/10 w/w (red); composition 85/15 w/w (orange); composition 80/20 w/w (yellow); composition 70/30 w/w (dark green); composition 60/40 w/w (green); composition 50/50 w/w (blue).

To evaluate the two DSC analysis series, the eutectic temperature and composition of the data of each series can be compared with the literature information. The temperature of the eutectic invariant is given by the DSC analysis. Assuming that there is no solid solution, its composition can then be estimated with the simplified Schröder - van Laar equation[88] (Equation

II- 3), with x_A the composition in component A (molar fraction), $\Delta H_{f,A}$ the enthalpy of fusion of pure A (J.mol^{-1}), R the gas constant (8.314 J.mol^{-1}.K^{-1}), $T_{f,A}$ the melting point of pure component A (K) and T_e the temperature of the eutectic invariant (K).

$$\ln(x_A) = \frac{\Delta H_{f,A}}{R}\left[\frac{1}{T_{f,A}} - \frac{1}{T_e}\right] \qquad \textit{Equation II- 3}$$

By taking the data measured in DSC analysis, the different parameters can be estimated. The comparison between the calculated values and the literature data is presented in Table II- 3, for the two series of DSC analysis.

In the literature[87], the eutectic invariant is given with a temperature of 150 °C and a composition of 0.34 %mol$_{S\text{-Ibu-}S\text{-}\alpha MBA}$. It is clear that the results from DSC measurements in sealed crucibles are closer to the reported data.

	$\Delta H_{f,$ *S*-Ibu-*S*-αMBA (J.mol-1)	$T_{f,$ *S*-Ibu-*S*-αMBA (K)	T_e (K)	T_e (°C)	$x_{S\text{-Ibu-}S\text{-}\alpha MBA,\ eutectic}$ (%mol)	T_e (K) with the literature $x_{S\text{-Ibu-}S\text{-}\alpha MBA,\ eutectic}$ = 0.34%mol
Pierced pans	40834	439	407	134	0.418	400
Sealed pans	54039	449	418	145	0.346	418

Table II- 3: Calculation of the eutectic composition $x_{S\text{-Ibu-}S\text{-}\alpha MBA,\ eutectic}$ with DSC measurements in pierced lid pans and in sealed pans. Comparison between the eutectic temperature measured by DSC analysis for both series, and that calculated with Schröder – van Laar equation with the eutectic composition given in the literature[87]: 0.34 %mol.

Nevertheless, contrarily to the first series of analyses in pierced pans, the first endotherm is not present for the composition *S*-Ibu-*S*-αMBA / *R*-Ibu-*S*-αMBA 85/15 w/w, suggesting that the partial solid solution limit would be comprised between 10 %w and 15 %w of *R*-Ibu-S-αMBA. Anyway, both DSC analysis series show that the partial solid solution exists[89]. The presence of this partial solid solution was also confirmed by X-Ray Diffraction.

II.3.1.3. X-Ray Diffraction

Analysis of powder

XRPD analysis with internal calibration (quartz) was performed on two products of partial solid solution of *S*-Ibu-*S*-αMBA (ss-*S*-Ibu-*S*-αMBA) compared with pure *S*-Ibu-*S*-αMBA. This is shown in Figure II- 9: the peak at 24.3 °2θ clearly shows a shift in Bragg angle consistent with the partial solid solution.

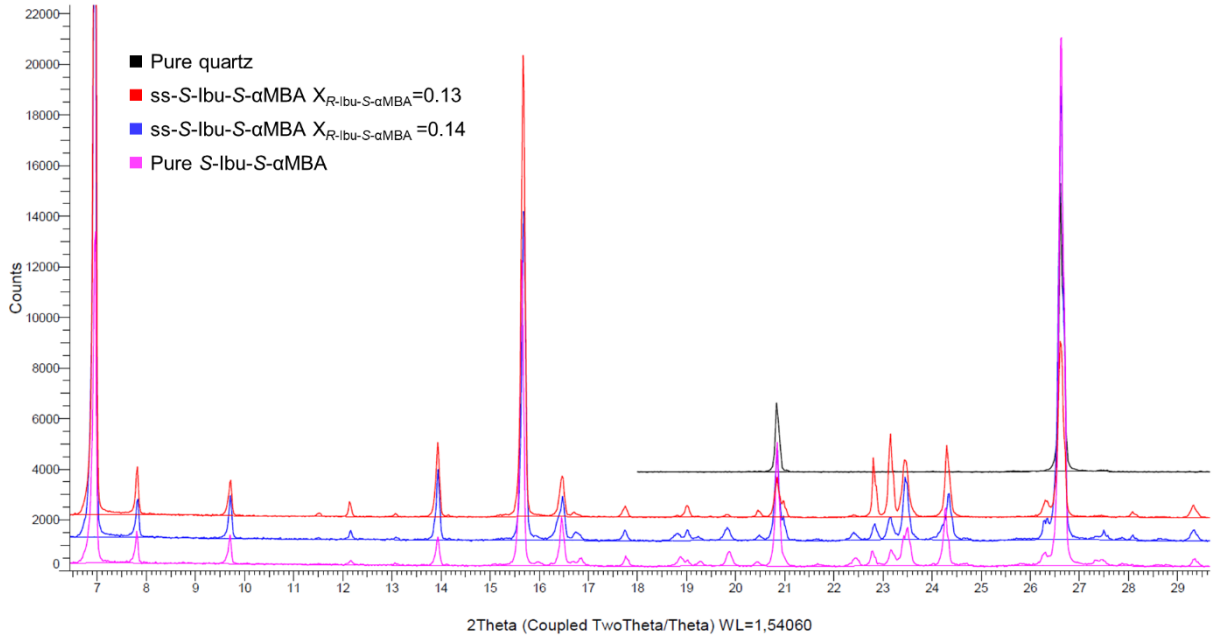

Figure II- 9: XRPD overlay of two products of partial solid solution of S-Ibu-S-αMBA (ss-S-Ibu-S-αMBA) with the highest chiral purity obtained by chiral resolution of rac-Ibu, compared with pure S-Ibu-S-αMBA. Quartz was added in the sample preparation to ensure an internal calibration of the diffractograms on the peak 26.6 °2θ.

Structure resolution by Single Crystal X-Ray Diffraction (SCXRD; see Appendix A section A.7) was also performed; it is presented in the next section.

Analysis of a single crystal

Despite the fibrous nature of the ss-*S*-Ibu-*S*-αMBA crystals (see section 0), and several unsuccessful attempts, a 'twinned' crystal of ss-*S*-Ibu-*S*-αMBA was finally picked up and roughly resolved at room temperature by selecting a unique set of spots. The evaluation of the existence of the solid solution from the single crystal analysis point of view is discussed in the supplementary information of Marc *et al*. (2021)[89].

The crystallographic parameters of ss-*S*-Ibu-*S*-αMBA and of pure *S*-Ibu-*S*-αMBA were determined at room temperature; they appeared to be consistent with literature[83,90]. Both groups determined that the salt crystallizes in an orthorhombic system with a space group space group $P2_12_12_1$. The obtained lattice parameters are compared with parameters calculated from powder diffraction with the software Material Studio in Table II- 4.

Structure	Origin	Nature and purity	a (Å)	b (Å)	c (Å)
1	Powder diffraction	ss-*S*-Ibu-*S*-αMBA $x_{R\text{-Ibu-}S\text{-αMBA}} = 0.14$	5.96 ± 0.01	15.32 ± 0.03	22.53 ± 0.05
2	Single crystal diffraction	ss-*S*-Ibu-*S*-αMBA $x_{R\text{-Ibu-}S\text{-αMBA}} \approx 0.18$	5.962(1)	15.354(2)	22.543(3)
		Difference with 1 (Å)	0	-0.03	-0.01
		Difference with 1 (%)	0	-0.20	-0.04
3	Powder diffraction	Pure *S*-Ibu-*S*-αMBA	5.93 ± 0.01	15.33 ± 0.03	22.62 ± 0.05
		Difference with 1 (Å)	-0.03	+0.01	-0.91
		Difference with 1 (%)	-0.51	+0.07	+4.02

Table II- 4: Comparison between lattice parameters of the ss-S-Ibu-S-αMBA with a composition of $x_{R\text{-Ibu-S-αMBA}} = 0.14$, the single crystal ($x_{R\text{-Ibu-S-αMBA}} \approx 0.18$) and the pure salt S-Ibu-S-αMBA. Data obtained from the software Material Studio.

It appears that the parameter along c-axis increases more than the others. Indeed, the C*-CH_3 covalent bond and the c-axis are 19.3° only apart (Figure II- 10), which is consistent with the existence of a partial substitution of *S*-Ibu by *R*-Ibu by means of inversion between both the methyl and the hydrogen in the alpha of the stereogenic carbon.

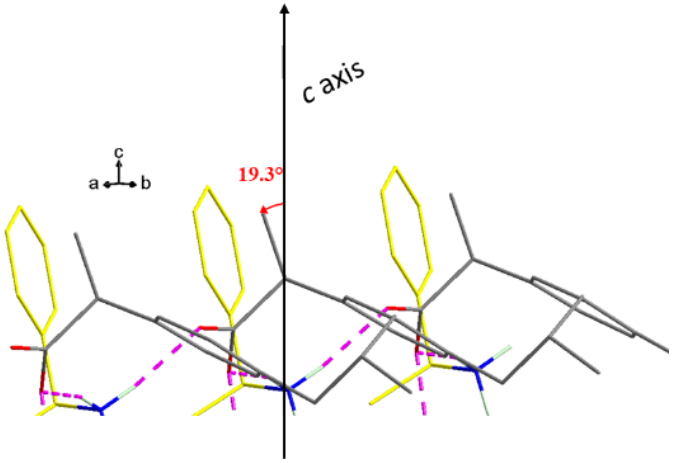

Figure II- 10: Inclination of the bond C-C with reference to the c-axis.*

Figure II- 11b shows a projection of the structure along the 'a' axis. The polar periodic bond chains propagate along the 'a' axis, forming a polar column (Figure II- 11a). The rest of the crystal structure is definitively hydrophobic.

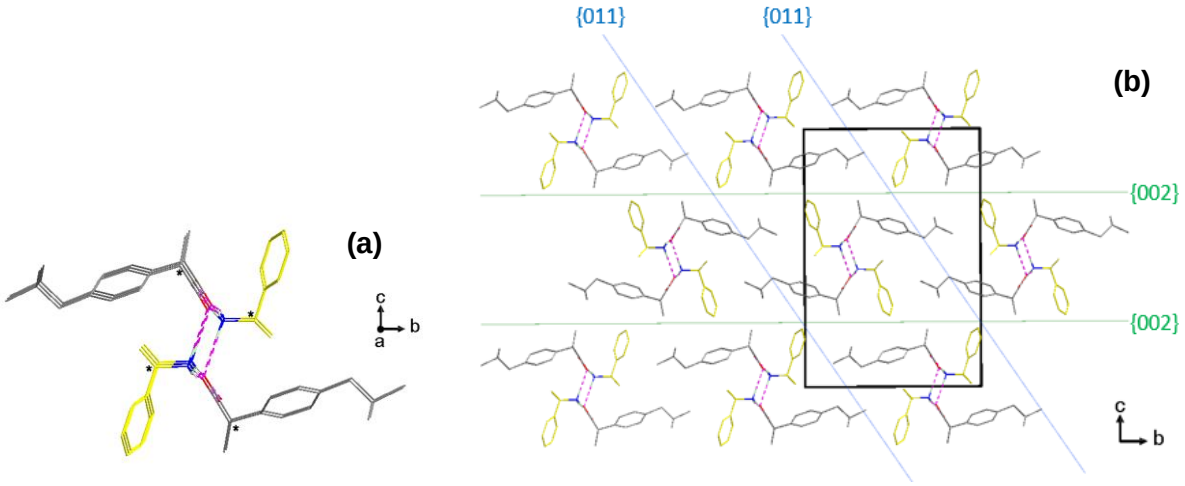

Figure II- 11: Molecular chain of S-Ibu-S-α-MBA spreading along the 'a' axis. The carbon atoms are displayed in yellow for S-αMBA and in grey for S-Ibu. Chiral carbon for both molecules is highlighted with an asterisk. (b) Projection along the 'a' axis of the S-Ibu-S-α-MBA crystal structure. The slices {002} and {011} are shown; their surfaces are clearly hydrophobic.

In the partial solid solution domain, the substitution of one enantiomer of Ibuprofen by the other alters the quality of the single crystals but not that much the crystal lattice. It is likely that the *R* enantiomer existing in the matrix of the ss-*S*-Ibu-*S*-αMBA results from the inversion of the methyl moiety by the hydrogen atom, minimizing the steric hindrance.

Now that the existence of the partial solid solution has been proved, it is interesting to determine its limit in composition, as this will also condition the maximum chiral purity reachable by chiral resolution of rac-Ibu.

II.3.2. Partial solid solution composition limit

The presence of a partial solid solution enriched in the wanted diastereomer *S*-Ibu-*S*-αMBA physically means that a solid phase mainly composed of *S*-Ibu-*S*-αMBA can accept the unwanted diastereomer *R*-Ibu-*S*-αMBA. Within the domain of this partial solid solution, the improvement of the chiral purity is uneasy. Thus, as mentioned before, this induces a limit of chiral purity reachable after a single crystallization step. This is why it is important to determine the composition range of ss-*S*-Ibu-*S*-αMBA domain.

The limit of miscibility in the solid state of *R*-Ibu-*S*-αMBA at the temperature of the eutectic has been estimated by plotting the enthalpies of the eutectic invariant given by the DSC analysis as a function of the composition in mass fraction (in this particular application, mass fraction equals molar fraction). This representation is called a Tammann graph. The Tammann graph of the samples analyzed in sealed pans is shown in Figure II- 12. The intersection between the regression trendline and the abscissa axis gives the eutectic composition: $x_{R\text{-Ibu-}S\text{-}\alpha\text{MBA, eutectic}} = 0.17$.

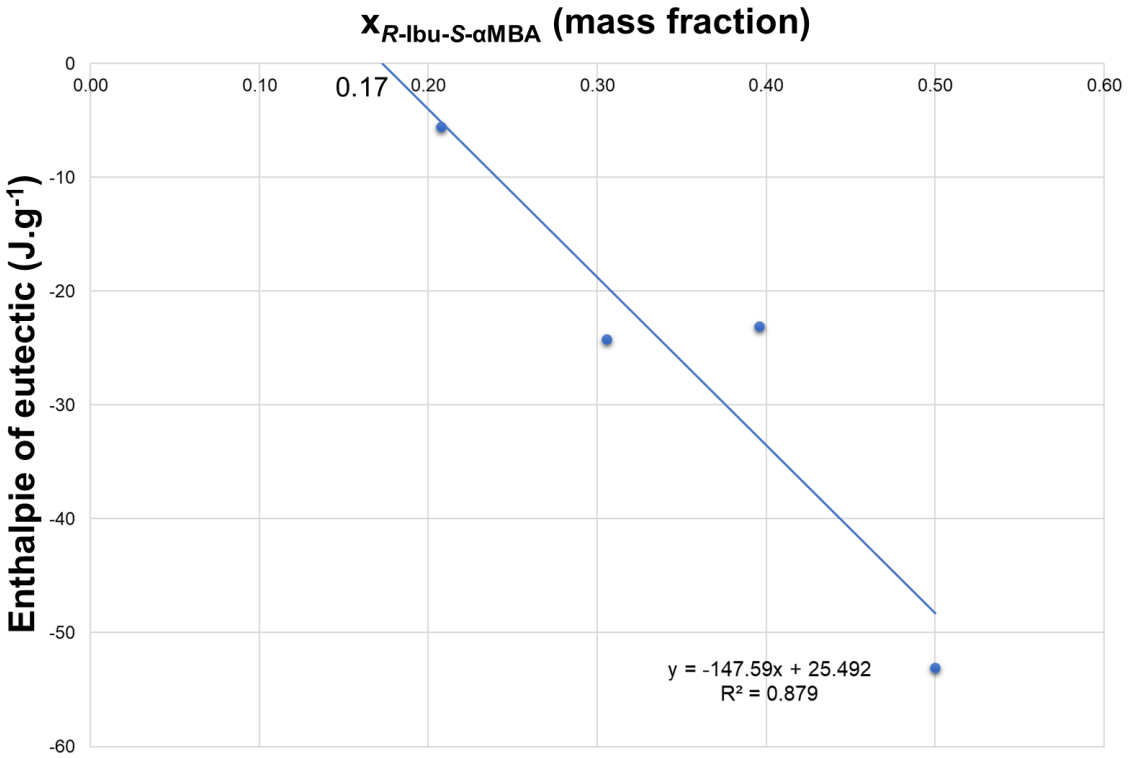

Figure II- 12: Tammann graph obtained with the DSC measurements in closed pans.

The collected data served the drawing of the binary phase diagram on the side of *S*-Ibu-*S*-αMBA, which is quite relevant, as the system presents a partial solid solution[11,13,91]. It is depicted in Figure II- 13. The blue curve represents the liquidus, and the black one stands for the eutectic invariant. The dotted lines represent the estimated limits of the partial solid solution ss-*S*-Ibu-*S*-αMBA. The limit of the partial solid solution at 20 °C was estimated at $x_{R\text{-Ibu-}S\text{-}\alpha MBA} = 0.13$, thanks to the production in batch mode.

It is noteworthy to mention that all the phases have been verified by XRPD analysis.

The phase diagram drawn is that obtained from DSC measurements in sealed pans, which means that it is not the representation of the domains at atmospheric pressure. Indeed, as the crucibles are sealed, the pressure inside will increase with the temperature. However, when the DSC analysis is performed in pierced or open pans, sublimation occurs. Therefore, in both cases, the obtained data do not correspond to the 'true' phase diagram under ambient pressure. Nevertheless, the representation given in Figure II- 13 is probably the closest one, as no matter is lost during the DSC analysis.

Thanks to the different analyses performed, the construction of the revised phase diagram between *S*-Ibu-*S*-αMBA and *R*-Ibu-*S*-αMBA was possible. This revision from the previous published data[87] was necessary because of the detection of the partial solid solution ss-*S*-Ibu-*S*-αMBA, and was reported in 2021[89].

This identified limit of miscibility in the solid state of ss-*S*-Ibu-*S*-αMBA restricts the diastereomeric excess reachable after the first resolution step. Therefore, the maximum chiral purity achievable is restraint by heterogeneous equilibria: if the access to a composition within the partial solid solution domain is possible, this composition will not be adaptable easily once reached. Nevertheless, the unique flow motion of CT crystallizers can be effective in achieving a good chiral purity.

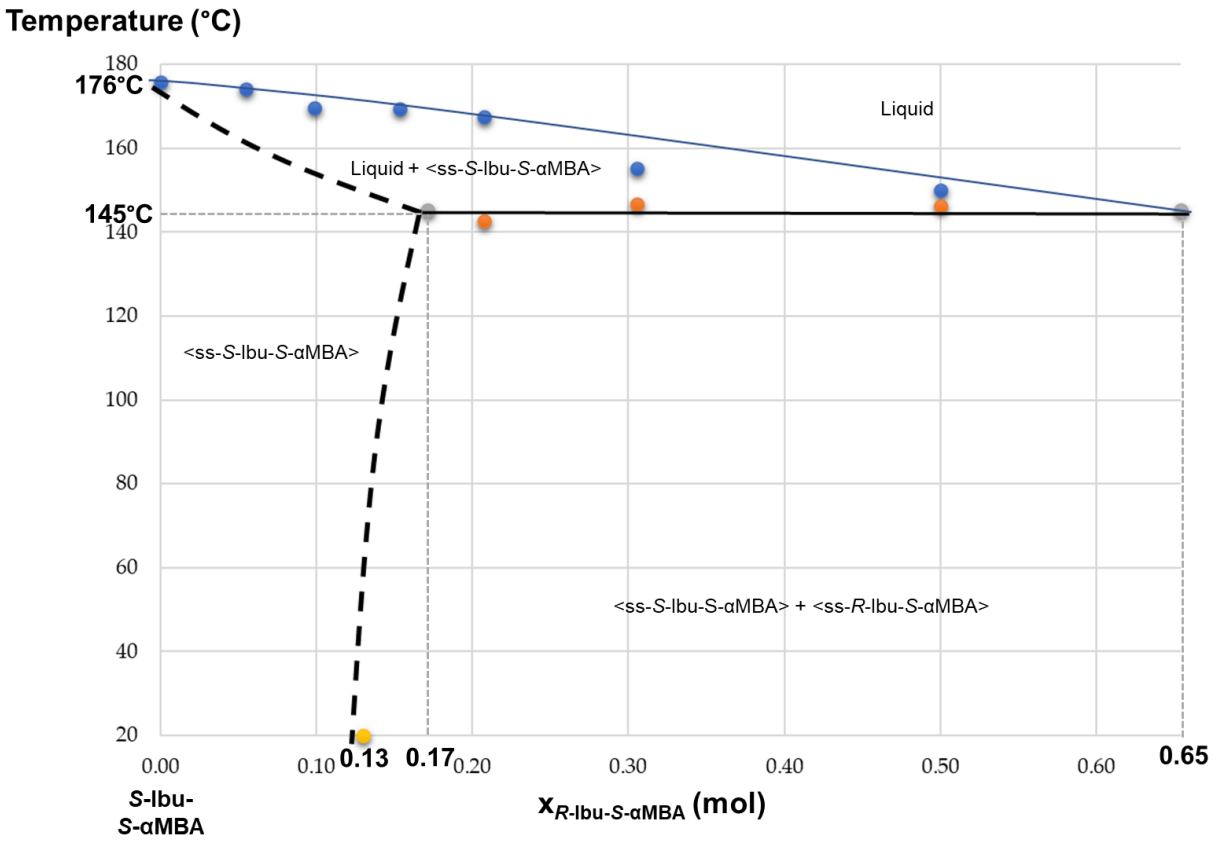

Figure II- 13: Revised binary system between S-Ibu-S-αMBA and R-Ibu-S-αMBA; focus on the part close to S-Ibu-S-αMBA, the desired diastereomeric salt. Binary phase diagram obtained with DSC measurements in sealed pans. Blue curve = liquidus; black line = eutectic; dotted lines = limits of the partial solid solution. The solvus has been extrapolated with the following points: (T = 145 °C; $x_{R\text{-}Ibu\text{-}S\text{-}\alpha MBA}$ = 0.17) and (T = 20 °C; $x_{R\text{-}Ibu\text{-}S\text{-}\alpha MBA}$ = 0.13). NB: the presence of a partial solid solution close to R-Ibu-S-αMBA is highly suspected, which is why the second component of the biphasic domain is labelled ss-R-Ibu-S-αMBA.

During the study presented in this section, aiming at proving the existence of a partial solid solution, single crystals of ss-*S*-Ibu-*S*-αMBA were sought, in view of analyzing them by SCXRD. At a macroscopic scale (circa 0.5 mm scale), some particles looked like classical single crystals. However, at microscopic scale, the single particles appear more like fibrous crystals, which could be defined as a collection of well-aligned fibers with an external shape resembling that of a single crystal. This was evidenced by Scanning Electron Microscopy (SEM; see Appendix A section A.8) analysis, as shown in Figure II- 14.

Such 'fibers association' was already experienced in the laboratory when trying to prepare a single crystal of sodium divalproate (unpublished results). SCXRD on several of those fibrous crystals lead to an undefined reciprocal space. Difficulties in obtaining suitable single crystals with such crystals assembly were also reported in the literature[92].

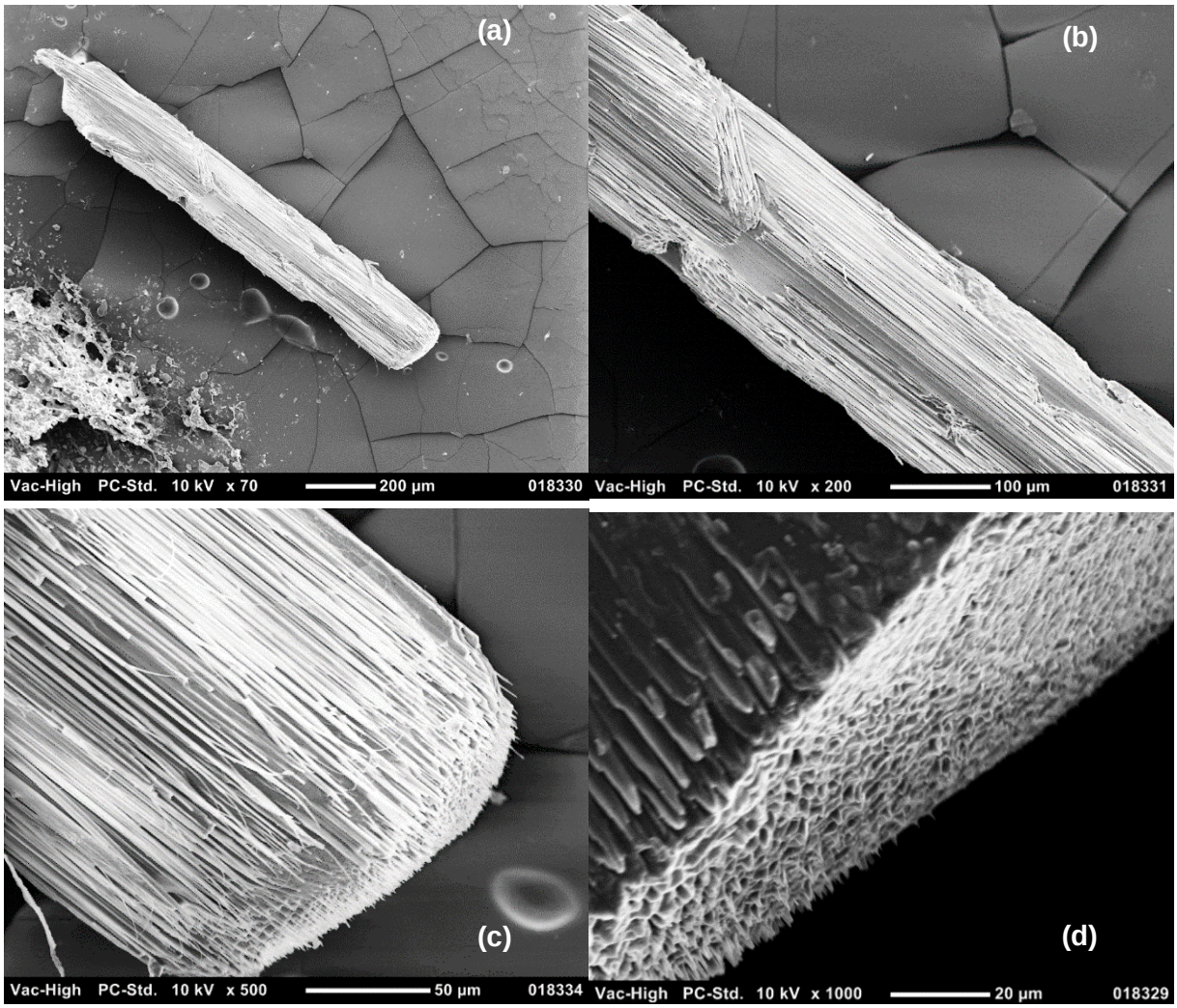

Figure II- 14: SEM photographs of ss-S-Ibu-S-αMBA exhibiting the fibrous nature of the crystals of the partial solid solution. The magnifications are (a) 70, (b) 200, (c) 500 and (d) 1000.

This surprising crystal aspect was investigated. The work and reflections about the fibrous nature of the crystals of ss-*S*-Ibu-*S*-αMBA is presented in the next section.

II.4. Fibrous nature of the ss-*S*-Ibu-*S*-αMBA crystals

II.4.1. Characterization of the fibrous nature

To begin with, crystals of pure *S*-Ibu-*S*-αMBA were analyzed by SEM. Figure II- 15 shows a comparison between SEM photographs of particles obtained in EtOH/H_2O 76/24 w/w.

Figure II- 15a-c exhibit crystals representative of the population for the pure *SS* diastereomeric salt, and Figure II- 15d-f for the phase at the limit of the partial solid solution ss-*S*-Ibu-*S*-αMBA. Pure salt is smooth and has a regular shape, whereas the salt with solid solution is rough due to a visible association of fibers. Some cracks are observed on the two samples. Therefore, the fibrous nature seems to be characteristic of the ss-*S*-Ibu-*S*-αMBA phase. Thus, it can be inferred that the miscibility in the solid state is responsible for the rather 'bad' crystallographic quality of the fibrous crystals.

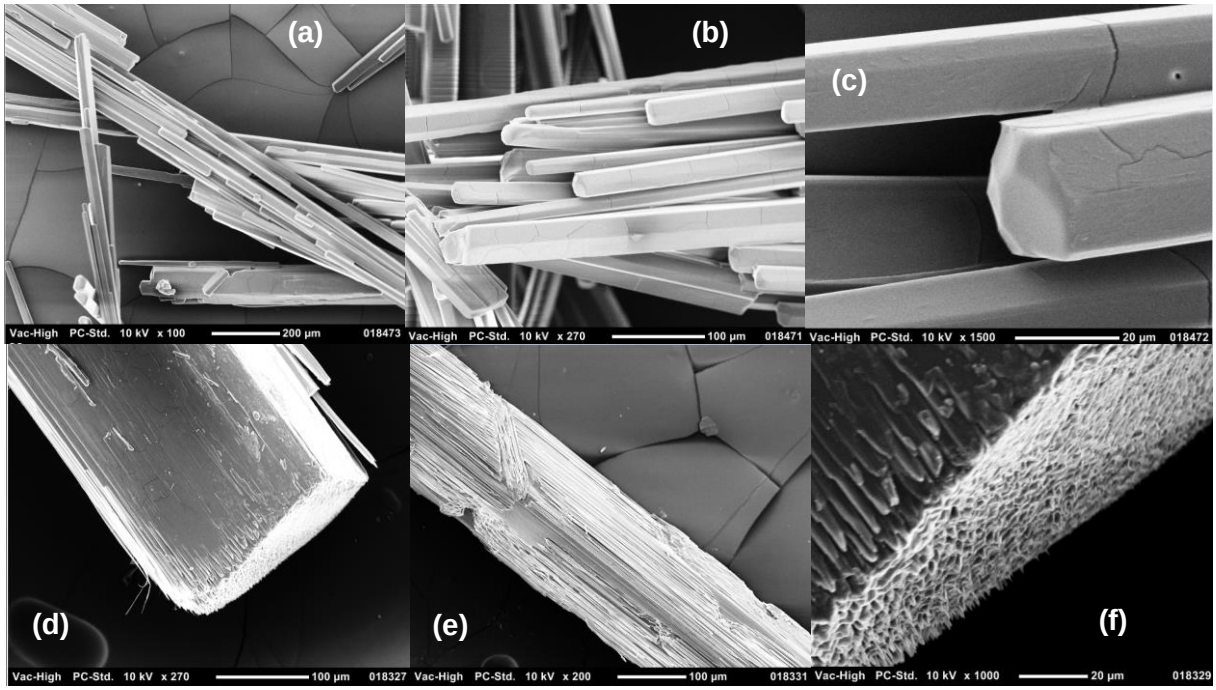

Figure II- 15: (a–c) SEM photographs of pure S-*Ibu*-S-*αMBA. (d–f) SEM photographs of ss*-S-*Ibu*-S-*αMBA at the limit of the solid solution ($X_{R\text{-}Ibu\text{-}S\text{-}\alpha MBA}$ = 14%).*

These fibrous crystals mimic pretty well 'classical' single crystals inasmuch as their macroscopic habit looks the same: with external faces for which simple Miller indices could be assigned. Figure II- 16a displays the calculated morphology, with the classical BFDH model, with distance to the central point inversely proportional to the d-spacing (1/d). The large discrepancy with the actual morphology of the fibrous crystals is obvious.

A much better variant of the model is obtained when the distance between the central point and the (hkl) face is proportional to exp(-Ad) (Figure II- 16b)[93]. In this refined model, A = 0.4 is the upper limit, so that {002} appears (i.e., it appears for k < 0.4). The two sets of planes {002} and {011} delineate the morphology of the particles.

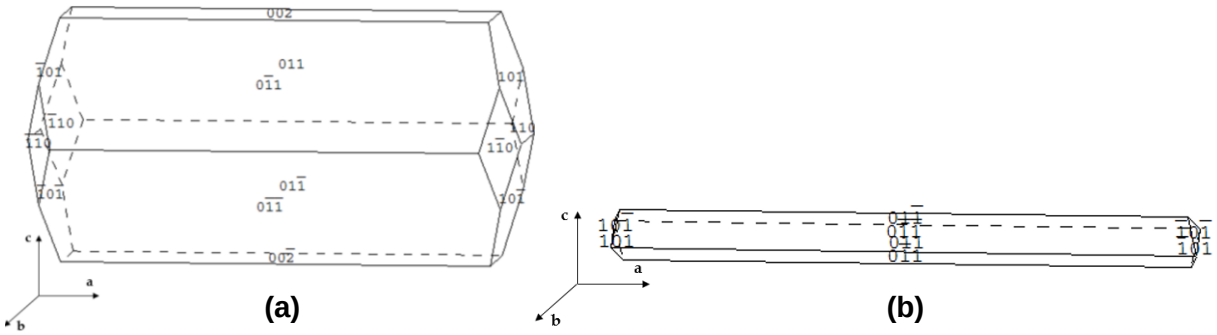

Figure II- 16: Calculated morphologies with BFDH model. (a) BFDH with distance to the central point inversely proportional to the d-spacing (1/d). (b) Variant of the BFDH model with distance to the central point proportional to exp(-Ad) with A = 0.4. Growth rate of {101} could be much faster resulting in a more extreme needle shape.

Since the presence of the undesired diastereomer in the crystal lattice of *S*-Ibu-*S*-αMBA leads to fibrous crystals, a hypothesis arose: do both diastereomers crystallize in the same fibers or in separated ones? To answer it, as *R*-Ibu-*S*-αMBA is more soluble than the *SS* diastereomeric salt, preferential dissolution tests were performed.

A particle of ss-*S*-Ibu-*S*-αMBA (from the same batch than those observed in Figure II- 14 and Figure II- 15d-f) was placed in a solution of EtOH/H_2O 76/24 w/w saturated in ss-*S*-Ibu-*S*-αMBA. Figure II- 17 shows the particle habit at the beginning of the first test (a) and after seven days in the saturated solution (b). If an inhomogeneous dissolution can be observed along the 'a' axis, leading to a rougher surface, no conclusions can be assured. SEM analysis confirmed the non-homogeneity of the particle dissolution, but no specific fiber dissolution was noted. Another test was run, in a solution saturated with pure *S*-Ibu-*S*-αMBA; the observations were identical.

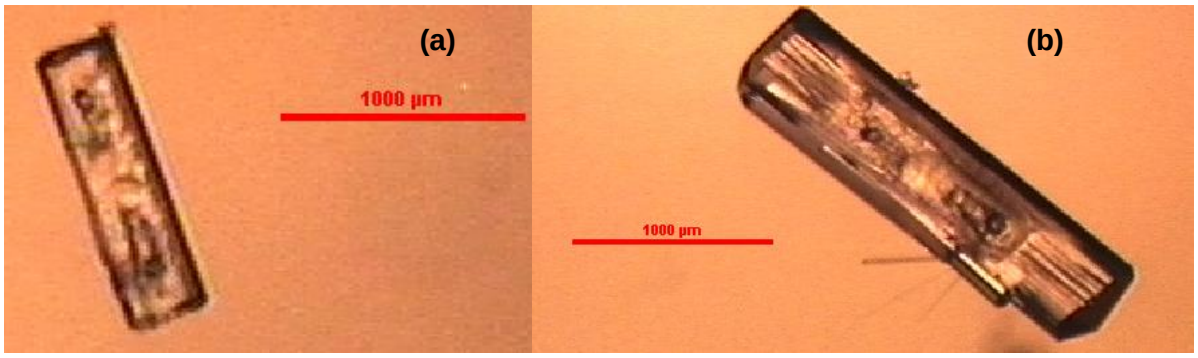

Figure II- 17: Optical microscopy (see Appendix A section A.9) photographs of the first preferential dissolution test, (a) at the beginning of the experiment (magnification 35) and (b) after seven days (magnification 40), taken with a binocular optical microscopy.

Therefore, the assembled fibers of the particles of ss-*S*-Ibu-*S*-αMBA would be constituted of compound of the same composition. This is consistent with a partial solid solution which is a monophasic domain

Nevertheless, since the diastereomer at the limit of the partial solid solution seems organized as a fiber assembly, the qualification as 'single crystals' can be discussed.

II.4.2. Discussion about the qualification of 'single crystals'

Particles of ss-*S*-Ibu-*S*-αMBA respect the definition of what is a crystalline material, given in Chapter I section I.1, i.e.: an organization through a periodic long-range order in three independent directions[1–3]. However, when searching for single crystals in view of analyzing them by SCXRD, the SEM analysis of some apparent good candidates clearly evidenced their fibrous nature (Figure II- 14). Indeed, the first attempts of SCXRD lead to an undefined reciprocal space. Therefore, the qualification of ss-*S*-Ibu-*S*-αMBA particles as single crystals can be questionable.

Nevertheless, after several trials, the SCXRD analysis of one fibrous crystal of ss-*S*-Ibu-*S*-αMBA was successful. The results were presented in Table II- 4 (section II.3.1.3). These differences of results from one 'single crystal' to another highlights the question of the mosaicity of single crystals. Indeed, the particles of ss-*S*-Ibu-*S*-αMBA are an assembly of fibers: each fiber has its proper degree of intrinsic order, but this degree can vary from one fiber to another. It can also be linked with lattice mismatch[92].

More generally, the structure resolution by SCXRD of partial solid solution particles is tricky[94], because of their general bad crystallinity. However since it was finally possible, it means that there is probably a sort of 'gradient of order' among the crystals of ss-*S*-Ibu-*S*-αMBA.

The same concern was encountered by Polyzois *et al.* (2022)[92], with the metastable form III of oxcarbazepine, exhibiting a morphology of twisted crystalline aggregates. Their decision was to use the terms of (polycrystalline) aggregate or fibers to refer to the multiple intertwined crystals. Likewise ss-*S*-Ibu-*S*-αMBA, the access to single crystals suitable for SCXRD analysis appeared to be challenging. Also, regarding their troubles in observing the direct aggregation of the crystals, they suspect that the self-assembly of the fibers "occurs during the early onset of crystallization"[92]. Such hypothesis could probably apply to the present case too.

Finally, according to Polyzois *et al.* (2022), the self-assembly and aggregation depend upon the medium around the needles (fibers), thus on the growth conditions[92]. This would be consistent with the differences of morphology observed between pure *S*-Ibu-*S*-αMBA et ss-*S*-Ibu-*S*-αMBA in Figure II- 15.

Moreover, further examination of the ss-*S*-Ibu-*S*-αMBA particles revealed that they are actually constituted of two or more parts, connected by a zone roughly perpendicular to the main axis 'a' of the elongated particles. It is shown in Figure II- 18. It is not clear if this is a kind of twin or resulting from the initial seed which grew towards dual opposite sides.

The 'connecting zone' was observed by optical microscopy. As shown in Figure II- 19, the delimitation between the parts is clear, as well as the fibrous aspect of the crystals. It seems from (b) that the zone can be damaged. This observation and the 'T-particle' observed in Figure II- 18 suggest that at some point of the growth phenomenon, some parts may leave.

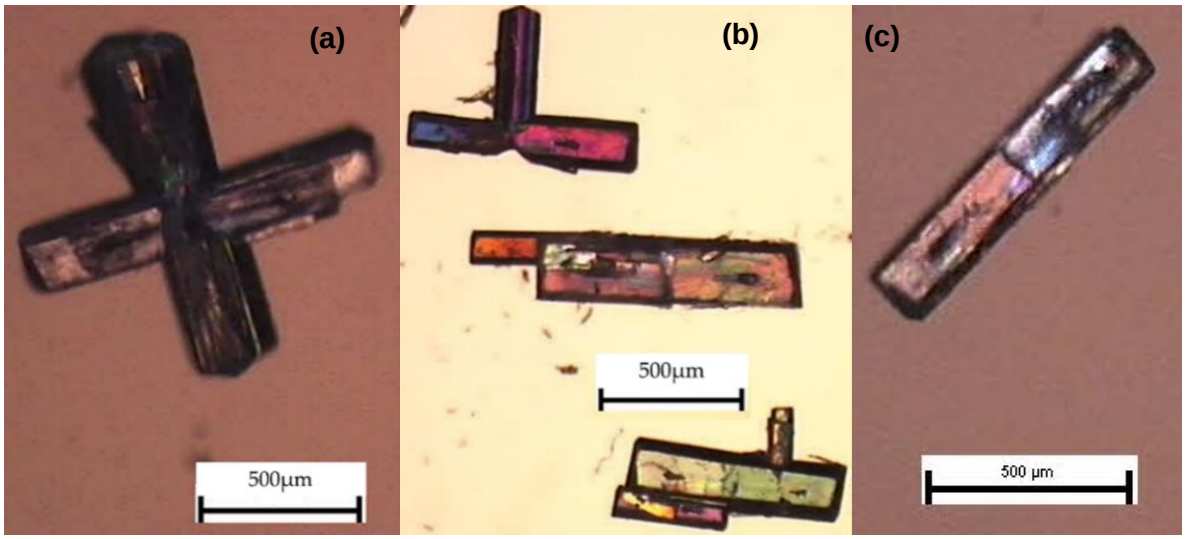

Figure II- 18: Photographs taken by binocular polarized light microscopy of the observed 'parts' of the ss-S-Ibu-S-αMBA crystals. They seem connected by a zone roughly perpendicular to the main axis 'a' of the elongated particles. (a) Particle with four visible parts; (b) and (c) particles with two or three visible parts.

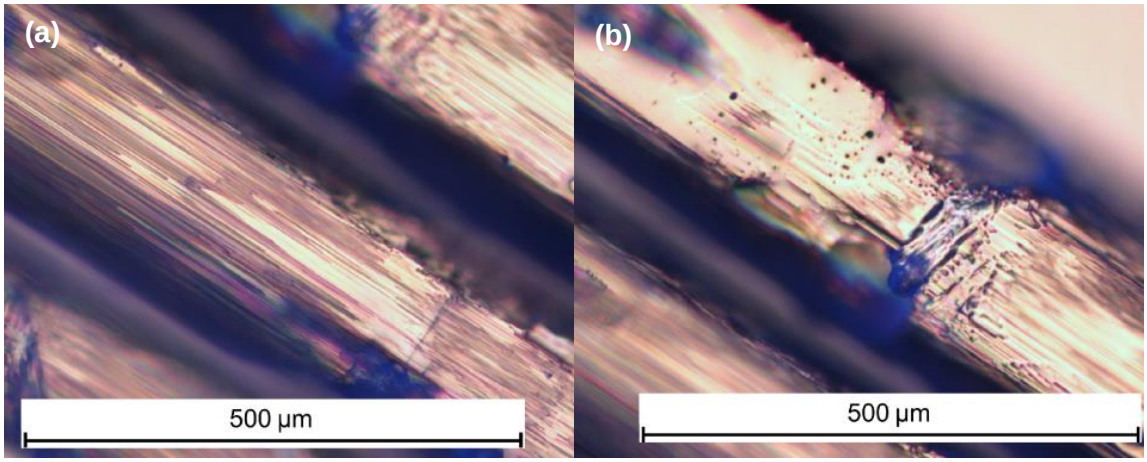

Figure II- 19: Micrographs of the connecting zone between the particle parts taken by a binocular optical microscope.

To conclude, the qualification of the fibrous particles of ss-*S*-Ibu-*S*-αMBA as single crystals can be questioned. Indeed, they seems to exhibit an acicular mosaicity, where the degree of microscopic order may vary from one fiber to another. The previous observations tend towards naming them as fibrous crystals, polycrystalline aggregates or fibers assembly.

The results of the different tests realized on the fibrous crystals, in addition to the specific particle aspect, and to its proneness to form fluid inclusions, let us reconsider the question of the growth mechanism.

II.4.3. Growth mechanism

In view of the observations and conclusions of the previous sections, Figure II- 20 shows a proposition for the growth mechanism of the particles of ss-*S*-Ibu-*S*-αMBA. The product is supposed to be arranged as molecular chains when nucleation occurs, and these chains would be assembled together (step 1). This arrangement is supposed to occur during the early onset

of crystallization[92]. Then, according to the observed particles, the growth would be faster along one of the three axes (step 2). Such polycrystalline arrangement probably stabilizes the particle, by reducing the surface energy[92].

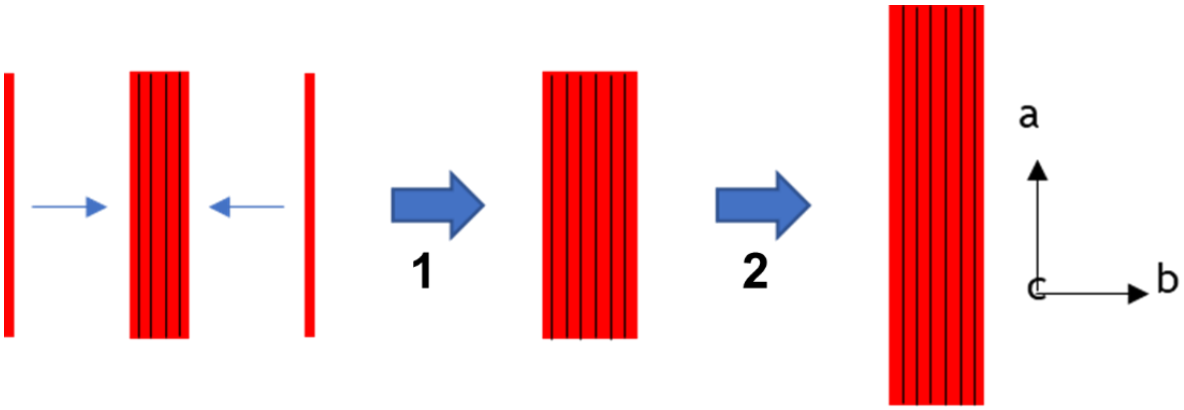

Figure II- 20: Proposition of growth mechanism for the particles of ss-S-Ibu-S-αMBA. Step 1: oriented molecular chain assembly. Step 2: Growth along the 'a' axis (main axis).

To probate the proposed mechanism, specific experiments were set-up, with a temperature-controlled jacket placed under the binocular optical microscope. The prepared solution was slightly supersaturated ($\beta = 1.06$), in order to observe growth and to avoid nucleation. The supersaturated solution was then seeded with the crystal of ss-*S*-Ibu-*S*-αMBA to be grown. Different seeding particles were tested: initial, cleaved, and grinded. In every case, the correct observation of the growth phenomenon was not possible. Firstly, nucleation occurred, despite the low supersaturation level. Secondly, the initial crystal moves too much during the experiment video recording.

The same kind of experiments were attempted in a hot/cold stage chamber Linkam THMS 600. The volume being smaller in this device, the issues encountered in the temperature-controlled jacket were supposed to be reduced or even eliminated. Unfortunately, despite experiment fine tuning in terms of supersaturation, solvent evaporation and observation field, the same problems occurred.

Nevertheless, the last series of experiments permitted the observation of a surprising phenomenon. This is shown in Figure II- 21: after a step of 'healing' (a to c), the particle of ss-*S*-Ibu-*S*-αMBA grows, mainly along one axis (b to c), but the final phase of growth led to the appearance of rough surface at both ends of the crystal (d). The supersaturation was not high enough for the growth to continue, but the left end of the particle seems to exhibit the start of the formation of an inclusion. Therefore, it seems that the ss-*S*-Ibu-*S*-αMBA particles need to have a certain shape before growing. This habit can be reached after a 'self-healing' step.

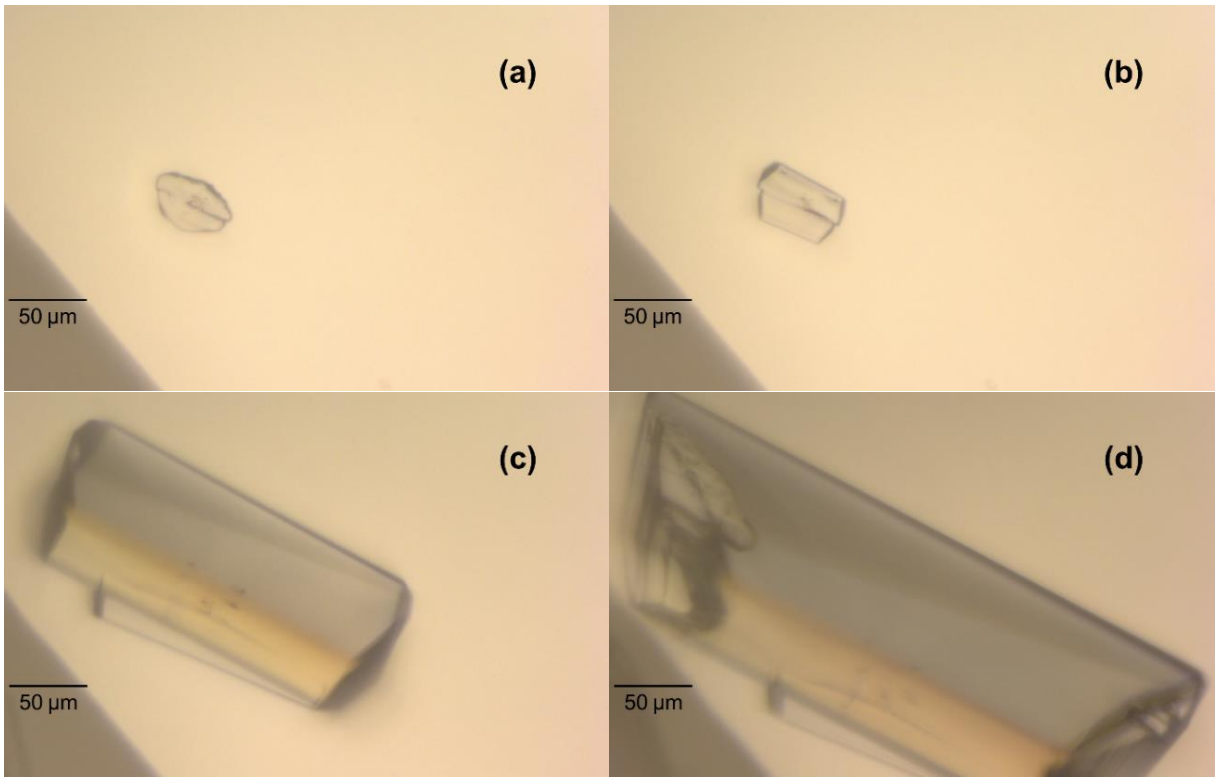

Figure II- 21: Observation of the growth of a particle of ss-S-Ibu-S-αMBA upon cooling from 40 °C to 0 °C at 1 K.min^{-1}. From (a) to (b), the crystal seems to undergo a 'healing' step. This phase appears to continue and to be followed by a growth step between (b) and (c). Finally, the growth continued from (c) to (d), and rough surfaces appeared at the extremities of the particle. These micrographs were taken by optical microscopy, within the Linkam THMS 600 chamber, at a magnification of 20.

The video from which the micrographs of Figure II- 21 are extracted can be seen thanks to the QR code of Figure II- 22. The URL can also be found in the caption of the figure.

Figure II- 22: QR code to see the video of the 'self-healing' and growth of a ss-S-Ibu-S-αMBA particle upon cooling from 40 °C to 0 °C at 1 K.min^{-1}. This video was recorded within the Linkam THMS 600 chamber, with a Leica Flexacam Camera C3 equipping an optical microscope at a magnification of 20. The video is also available through the following URL: https://drive.google.com/file/d/19b_gF5R-59n-v6AiUEf9lLg7EstQ0smL/view?usp=sharing.

This observed phase of ‘self-healing’ is probably favored by the rough and porous surface of the extremities of the particles, as shown in Figure II- 23.

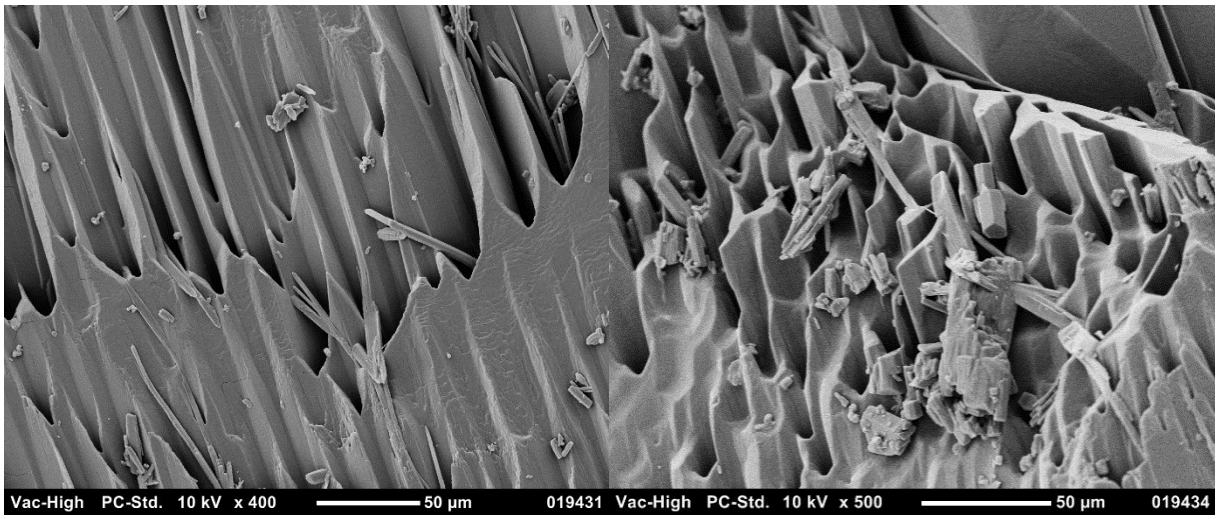

Figure II- 23: SEM photographs of the surface of the ends of a particle from the same experiment than that of Figure II- 21. The structure seems to be alveolar, like honeycombs.

In conclusion, the experiments performed to probate the proposed growth mechanism were unsuccessful. Spontaneous nucleation always occurs, by means of evaporation, or on the walls of the used sample holder, even at low supersaturation. Also, the crystals picked up to be observed moved during the observation time. Such difficulties were also reported by Polyzois *et al.* (2022)[92].

The set-up of further experiments with this aim should be carefully thought. Preventing spontaneous nucleation seems tricky, however, the fixing of the chosen crystal should be possible, with a pierced small chamber within the Linkam hot stage for example. The supersaturation level should be carefully controlled: first of all, to limit the spontaneous nucleation, and, also, to be sufficient to observe the complete growth phenomenon, maybe until the formation of fluid inclusions.

The observations of the experiments in this section are consistent with the presence of inclusions at the ends of the ss-*S*-Ibu-*S*-αMBA particles. Indeed, their fibrous nature promotes the roughness and porosity of the crystal surface, especially at the particle extremities, which favors the development of inclusions[95]. A recent study also detailed the concomitant presence of solid solution and fluid inclusions[96].

In view of trying to find the other causes of the formation of the fluid inclusions, further investigations were realized. Since these vacuoles are filled with the mother liquors, their presence can affect the product purity; thus, this study also aimed at finding a solution to avoid their formation.

II.5. Fluid inclusions study

The fluid inclusions of ss-*S*-Ibu-*S*-αMBA were detected during the batch mode work performed on the chiral resolution of rac-Ibu by *S*-αMBA. By applying the method of Pope and Peachey (see Chapter IV section IV.2.1), in order to improve the crystal morphology, part of the resolving amine was replaced by soda. The resulting crystals showed symmetrical biphasic fluid inclusions, as shown in Figure II- 24.

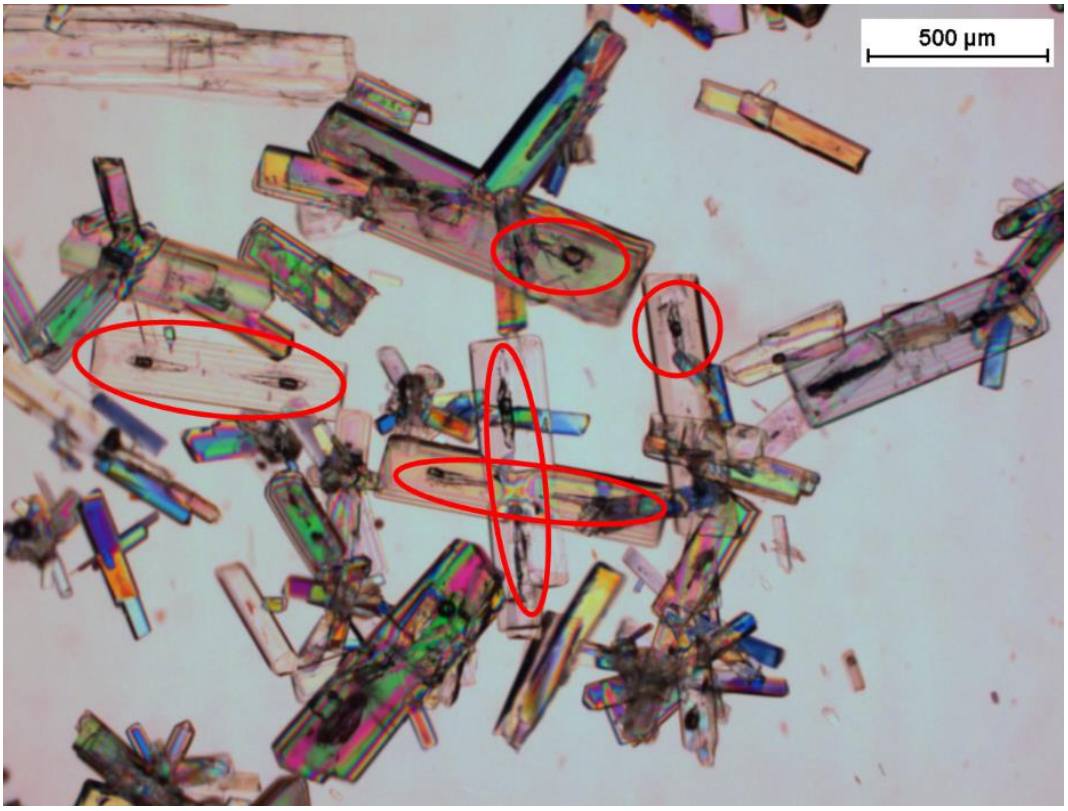

Figure II- 24: Micrograph of the product obtained in experiment B14 of Chapter IV section IV.2.1, taken by optical microscopy at a magnification of 2.5. Some fluid inclusions are encircled in red.

The thermal behavior of the fluid inclusions, as well as the influence of the process conditions were investigated. The results of this study are detailed in this section, after a brief introduction about the fluid inclusions in organic crystals. Part of the presented results were published in the journal *Crystals*[89].

II.5.1. Introduction to fluid inclusions in organic crystals

Inclusions are classified as macroscopic growth defects[97,98]. They are internal impurities, constituted of one or more phases. Theoretically, inclusions can potentially be formed in every crystalline compound. Since they are representative of the crystal environment during its growth, inclusions were intensively studied by mineralogists, and more especially by H. C. Sorby, known as the 'father of inclusions'[97,98].

As mentioned above, inclusions can be mono or polyphasic. The foreign phase(s) can be solid, liquid, or gaseous. In the case of fluid inclusions, the trapped impurity nature is liquid and/or gaseous.

Generally, the observation of reproducible fluid inclusions comes from a too high crystal growth rate as soon as the crystals exceed a threshold in size[99–103]. Nevertheless, other mechanisms have also been proposed[104–106]. In the end, three main types of formation can be distinguished[98]:

(1) Formation of *primary inclusions*, resulting from an imperfect closing of the growing crystal around a solid impurity on a surface.

(2) Development of *secondary inclusions*, formed along microfractures consolidated after the crystal growth.

(3) Formation of *'pseudo-secondary' inclusions*, also located along microfractures, but occurring during the growth step.

The shape of the formed cavities, or vacuoles, depends on the growth conditions, i.e., on the process conditions, such as the crystallization method, the stirring rate, the solvent nature, the medium atmosphere…[97]. This was demonstrated on RDX crystals for example[107–109]: by using different conditions of growth, they could either present a symmetrical pattern, or be completely irregular, with inclusion having a curved-tube shape known as 'necking'.

The crystals of the diastereomer *S*-Ibu-*S*-αMBA present two symmetrical vacuoles, located at both ends of the particle, as shown in Figure II- 24; such pattern was already reported[98]. This is in contrast with other cases for which fluid inclusions are repeated along a given crystallographic axis[102,110].

In the case of fluid inclusions within crystals from crystallization in solution, the formed vacuole will be mainly filled with the mother liquors. This can be dramatic in terms of product purity, especially in the situation of the crystallization of an API[97,98]. Other properties can be affected, like the biocompatibility, the structural purity, and the product stability (chemical nature and crystalline phase). Therefore, the understanding of the inclusion formation mechanism is important, in view to avoid it.

The studied fluid inclusions are filled with the saturated mother liquor and a bubble of gas (see Figure II- 24). To minimize the problem of fluid inclusions, the effect of the gas dissolved in the mother liquor should be investigated. CO_2 warrants special attention because its solubility is much greater than that of the other gases, and literature shows several examples of its importance in the formation of fluid inclusions[95,111].

To date, the mechanisms from which can result the presence of gas bubbles are not well-known. Nevertheless, the bubbles can belong to two different categories, described below. The thermal behavior of the bubbles depends on their kind. When they are part of the category of the shrinkage bubbles, there exists a specific temperature, called the homogenization temperature T_h. This temperature is that of the complete dissolution of the bubbles. Since gases have a retrograde solubility in solvent, upon heating, their solubility decreases. The temperature increase induces the rise of the pressure within the vacuole, which increases the solubility of gases. Therefore, the dissolution of gas bubbles is the results of antagonist and synergistic effects, which makes its prediction difficult[97].

In the end, the principal hypotheses, based on T_h, discern two types of bubbles[97,98]:

(1) *Shrinkage or retreat bubbles*, the most common type: it is generally the consequence of a lack of liquid within the inclusion cavity[97].

The gas bubble dissolves upon heating, when reaching the homogenization temperature, after a size reduction.

Upon cooling, the solubility (being presumed normal) decreases, and thus leads to crystallization on the inner wall of the cavity. The density of the crystal is generally greater than that of the mother liquor, therefore, because of a deficit in volume, the nucleation of a bubble of gas is induced. If it is usually a sudden nucleation[97], the nucleation of that bubble of gas may sometimes require quite a long period of time[112]. In case of fast cooling, several bubbles of gas could nucleate simultaneously. However, after a while, only the largest one usually survives because of the Laplace–Young equation: $\Delta P = \frac{2\gamma}{r}$. In this equation, ΔP is the difference of pressure between the interior and the exterior of the bubble of gas, γ is the surface tension and r is the radius of the gas bubble[113].

The nucleation of a retreat bubble can also occur after ageing at a constant temperature.

(2) *Persistent bubbles*: upon heating, the bubble of gas does not dissolve; no homogenization temperature is observed.

When a crystal is growing, there is a local heat release. This induces a local drop in solubility of gases dissolved in the solution (indeed, they all have a retrograde solubility). If the surface is rough, nucleation of micro or even nano bubbles of gas is facilitated[114]. When the cavity finally closes, these bubbles of gas are trapped.

A variant of that mechanism exists: when a crystal is growing and comes into contact with an already existing bubble of gas, by accident, this latest can be incorporated, with or without mother liquor around. The probability of such event decreases when the suspension is stirred.

A didactic graphical summary of the differences between shrinkage and persistent bubbles can be found in Figure 2-20 of the PhD thesis of Dr. E. Bobo[97].

The goal of the study of the inclusions encountered in crystals of ss-*S*-Ibu-*S*-αMBA is to understand the formation mechanism of those vacuoles, in order to find possible remedies for those drawbacks. The results are presented in the next section.

II.5.2. Results

The fluid inclusions of ss-*S*-Ibu-*S*-αMBA particles contains both liquid and gas. As explained in the introduction, the classification of the gas bubble can be assessed from its behavior upon temperature variation. This would permit to learn more about the formation of the inclusions. The experiments to study the thermal behavior of the gas bubble are detailed in the next section.

II.5.2.1. Thermal behavior

Homogenization temperature

In the first place, the investigation aimed at finding if a homogenization temperature is observable or not. Thereby, a particle of ss-*S*-Ibu-*S*-αMBA, containing two symmetrical fluid

inclusions (liquid + gas bubble), was inserted within the hot stage Linkam THMS 600 chamber. The sample was heated from 20 °C to 120 °C at 1K.min^{-1} and observed by optical microscopy. The full video can be seen thanks to the QR code of Figure II- 25. The URL can also be found in the caption of the figure.

Figure II- 25: QR code to see the video of the heating of a ss-S-Ibu-S-αMBA particle from 20 °C to 120 °C at 1 K.min^{-1}. This video was recorded within the Linkam THMS 600 chamber, with a Leica Flexacam Camera C3 equipping an optical microscope. The video is also available through the following URL: https://drive.google.com/file/d/1YAbA0cYW_I7YxrMpjy2H2UN0uIkyO0Dq/view?usp=sharing.

During the heating of the particle, each bubble moves in its own cavity, but they do not dissolve. At the end of the video, the particle dissolution brought about the opening of the two opposite vacuoles and the release of solvent. The crystal melts before any homogenization temperature can be observed. In addition, the size of the bubbles of gas appears too large to correspond to a simple retreat bubble. Therefore, it means that the bubbles of gas trapped in the fluid inclusions would more likely belong to the second category presented in the introduction: persistent bubbles. However, during another experiment, a microbubble of gas appeared after temperature cycling. Thus, the fluid inclusions of ss-*S*-Ibu-*S*-αMBA may exhibit a mix of the two kinds of bubbles: shrinkage bubbles and persistent ones, the latter being predominant.

Since the heating rate does not have a true impact on the observation of the homogenization temperature[97], no other value was tested.

Extracted photographs of the video available from the QR code of Figure II- 25 can be found in Figure II- 26. They show that the heating up to 120 °C turns the initial fibers aggregate in a particle exhibiting a less fibrous micro-structure, probably by means of diffusion. The interface between the two parts of the particle is also visible.

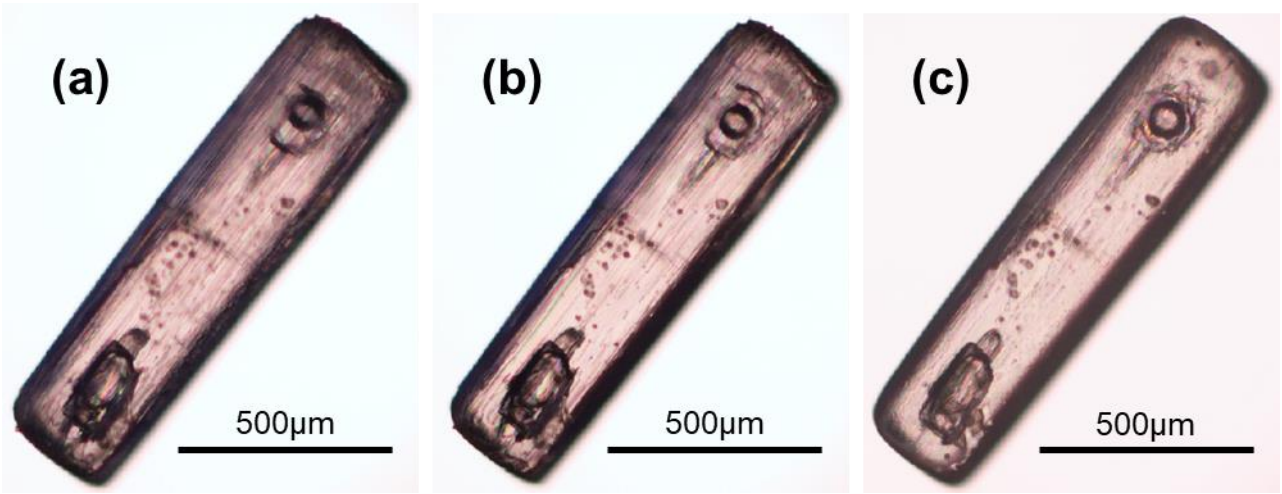

Figure II- 26: Particle of ss-S-Ibu-S-αMBA under heating (from 20 °C to 120 °C at 1 K.min^{-1}) at three different stages: (a) at T= 32 °C, (b) at T= 69 °C and (c) at T= 98 °C.

The thermal behavior of the fluid inclusions was also investigated with the application of temperature cycles, as detailed in the next section.

Temperature cycling effect

To study the effect of temperature cycling on ss-*S*-Ibu-*S*-αMBA, a particle was inserted within the hot stage Linkam THMS 600 chamber. The sample went through the temperature cycles described in Figure II- 27, and was observed by optical microscopy.

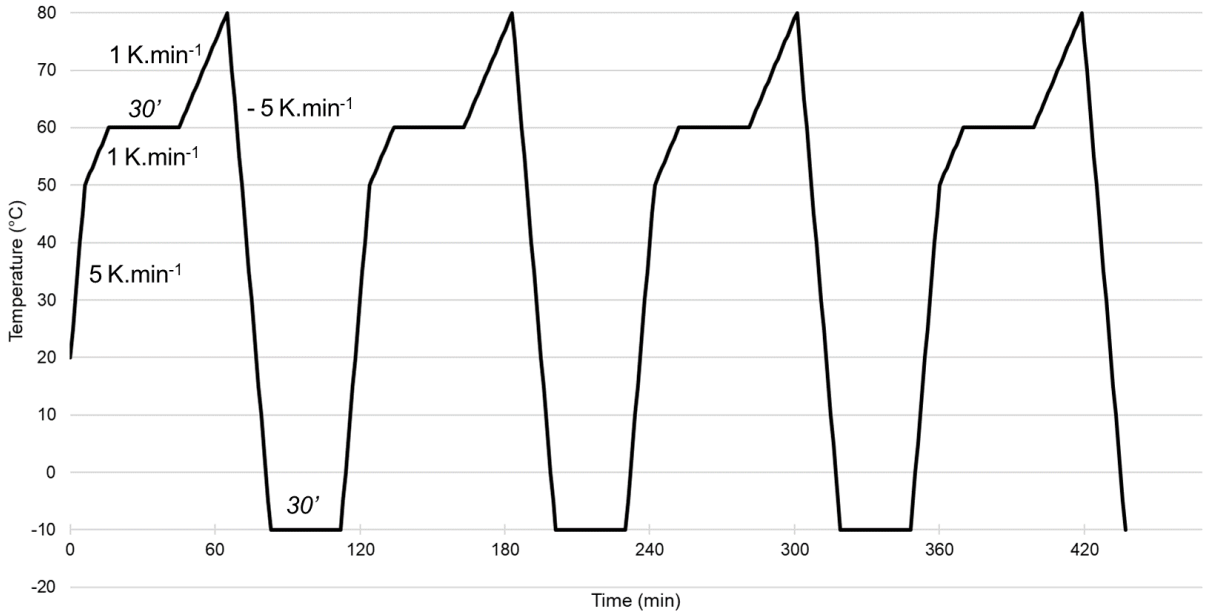

Figure II- 27: Temperature cycles undergone by the particle of ss-S-Ibu-S-αMBA.

The full video can be seen thanks to the QR code of Figure II- 28. The URL can also be found in the caption of the figure. Extracted photographs of the video available from the QR code of Figure II- 28 can be found in Figure II- 29.

Figure II- 28: QR code to see the video of the temperature cycling effects on a particle of ss-S-Ibu-S-αMBA (see Figure II- 27). This video was recorded within the Linkam THMS 600 chamber, with a Leica Flexacam Camera C3 equipping an optical microscope. The video is also available through the following URL: https://drive.google.com/file/d/1A40oR_ptYBk2FXje9F9KtvfQhRgxbjfk/view?usp=sharing.

Upon temperature cycling, the fluid inclusions undergo various cycles of dissolution and recrystallization. When the temperature increases, the liquid dissolves the walls of the cavity, which then seems widened. During the cooling step, the walls reform; the vacuole size decreases. The gas bubble size and shape vary a little bit, but no dissolution is observed, confirming the conclusions of the previous section.

Moreover, as the temperature cycles progress, the two fluid inclusions seem to migrate towards the particle extremities, as if they were evacuated. Such behavior was already reported[98], and was observed again during another experiment.

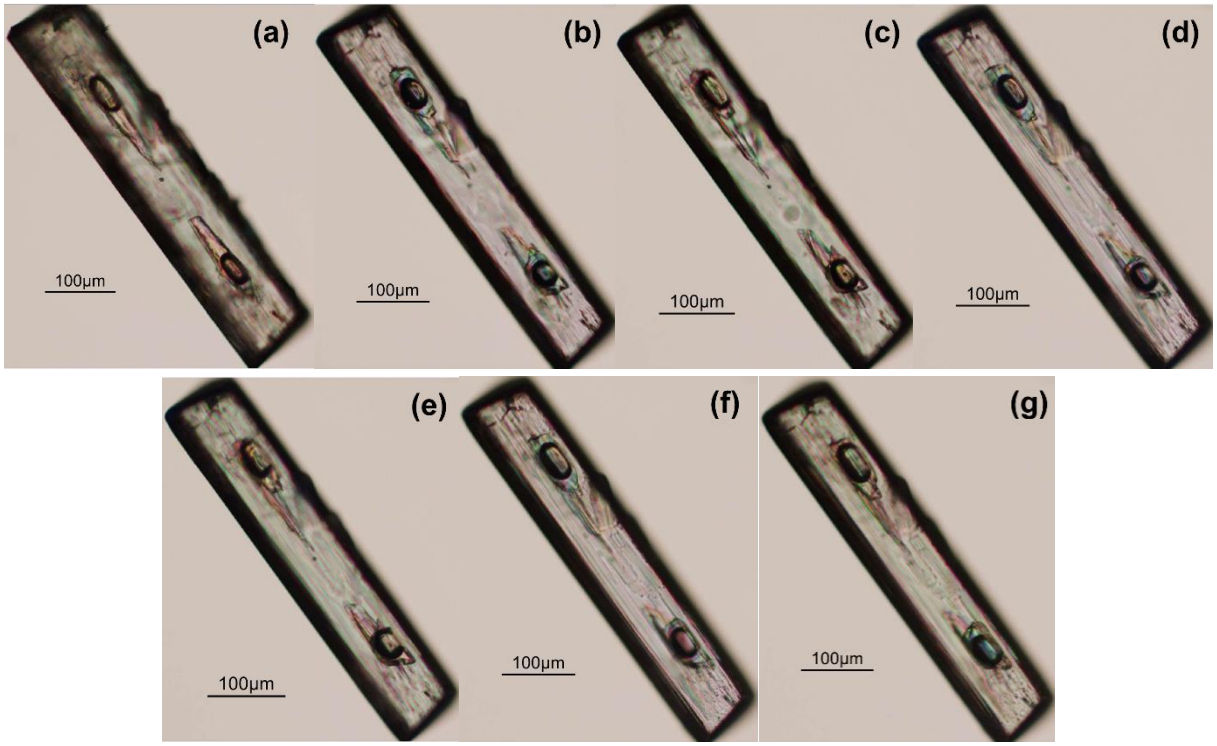

Figure II- 29: Photographs of a particle of ss-S-Ibu-S-αMBA undergoing the temperature cycles of Figure II- 27, extracted from the video available with the QR code of Figure II- 28. (a) t = 0 min, T = 20 °C; (b) t = 66 min, T = 80 °C; (c) t = 114 min, T = -10 °C; (d) t = 186 min, T = 80 °C; (e) t = 234 min, T = -10 °C; (f) t = 306 min, T = -10 °C; (g) t = 360 min, T = 80 °C.

Another classical effect of the application of temperature cycles is the modification of the vacuole shape into a 'negative crystal', in view of minimizing its surface energy[97,98]. Such transformation was not observed with the particles of ss-*S*-Ibu-*S*-αMBA. This may also be due to their fibrous nature since the compound crystallizes as aggregates of fibers. The self-assembly of the fibers is supposed to minimize the surface energy of the 'crystal'[92], therefore, the evolution towards negative crystal may not be necessary. Also, still because of their fibrous nature, the interior of the particles is not homogeneous, which may limit the vacuole transformation.

In addition to the thermal behavior, the influence of the conditions of growth on the formation of the fluid inclusions were also investigated. The study is described in the next section.

II.5.2.2. Influence of the growth conditions

In the first place, the nature of the solvent was investigated. It was reported that the solvent nature has an influence on the crystal aggregation[92], and since the fibrous nature of the ss-*S*-Ibu-*S*-αMBA was proved to promote the formation of fluid inclusions, the effect of this parameter on the inclusions may be non-negligible.

Figure II- 24 showed the platelet-shaped crystals obtained when part of the resolving amine of the chiral resolution of rac-Ibu is replaced by soda, added in water. In Figure II- 30a, the soda was added to the medium in technical ethanol. The principal effect is evident: the modification of the habit, from needle to platelet, is due to water and not to soda.

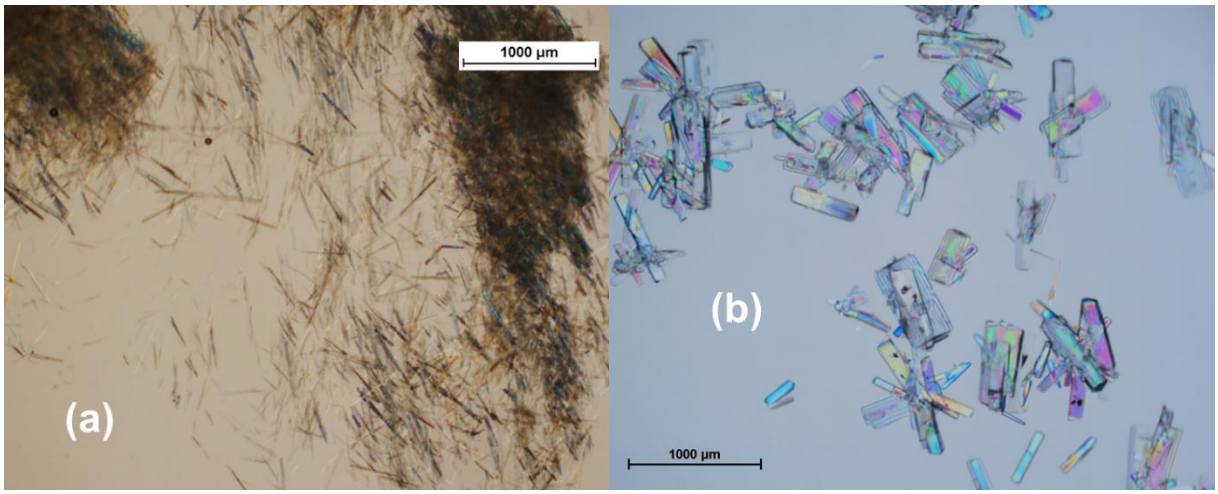

Figure II- 30: Micrographs of ss-S-Ibu-S-αMBA obtained (a) by adding the soda in technical ethanol (EtOH/H_2O 95/5 w/w) and (b) by adding water without soda, taken by optical microscopy.

In order to confirm that statement, water was added to the medium, without soda. The resulting crystals are shown in Figure II- 30b: they exhibit the desired platelet shape. In addition, the product showed fewer fluid inclusions.

The conclusions of the comparison between these different products were excellent regarding the objectives of the process optimization developed in batch mode: water is the habit modifier, and without soda, the particles exhibit less fluid inclusions.

Secondly, the purity of the solvent was investigated. Pure *S*-Ibu-*S*-αMBA was made in pure ethanol (99.8 %) and in technical ethanol (or azeotropic ethanol, i.e., EtOH/H_2O 95/5 w/w). The corresponding crystals are respectively exhibited in Figure II- 31 a-b and c-d.

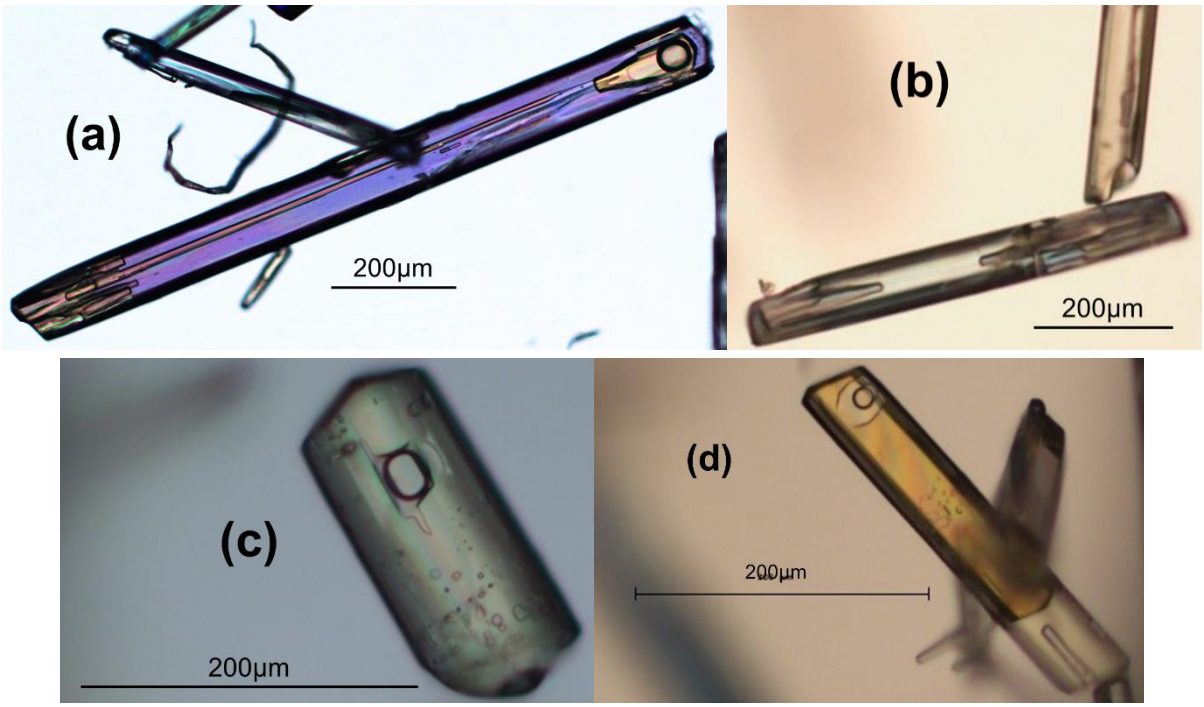

Figure II- 31: Micrographs of particles of pure S-Ibu-S-αMBA obtained by cooling from 40 °C to 20 °C (a-b) in pure ethanol (99.8 %) and (c-d) in azeotropic ethanol (EtOH/H_2O 95/5 w/w); taken by optical polarized light microscopy.

The solvent purity has a clear effect, as seen in Figure II- 31. In micrographs (a) and (b), the crystals of the pure diastereomer *S*-Ibu-*S*-αMBA obtained in pure ethanol are elongated, and present conical fluid inclusions. The vacuoles seem to occupy an important fraction of the particles. Photographs (c) and (d) display the crystals of the pure *SS* diastereomer obtained in azeotropic ethanol. Their fluid inclusions could be oblong or even rectangular with a large bubble of gas.

Also, the influence of the purity of the particles can be noted. Indeed, in comparison with Figure II- 24, showing particles of ss-*S*-Ibu-*S*-αMBA, the crystals of pure *S*-Ibu-*S*-αMBA presented in Figure II- 31 are thinner, and the fluid inclusion vacuoles are different.

The variety of the fluid inclusions that may be encountered can be illustrated in Figure II-32.

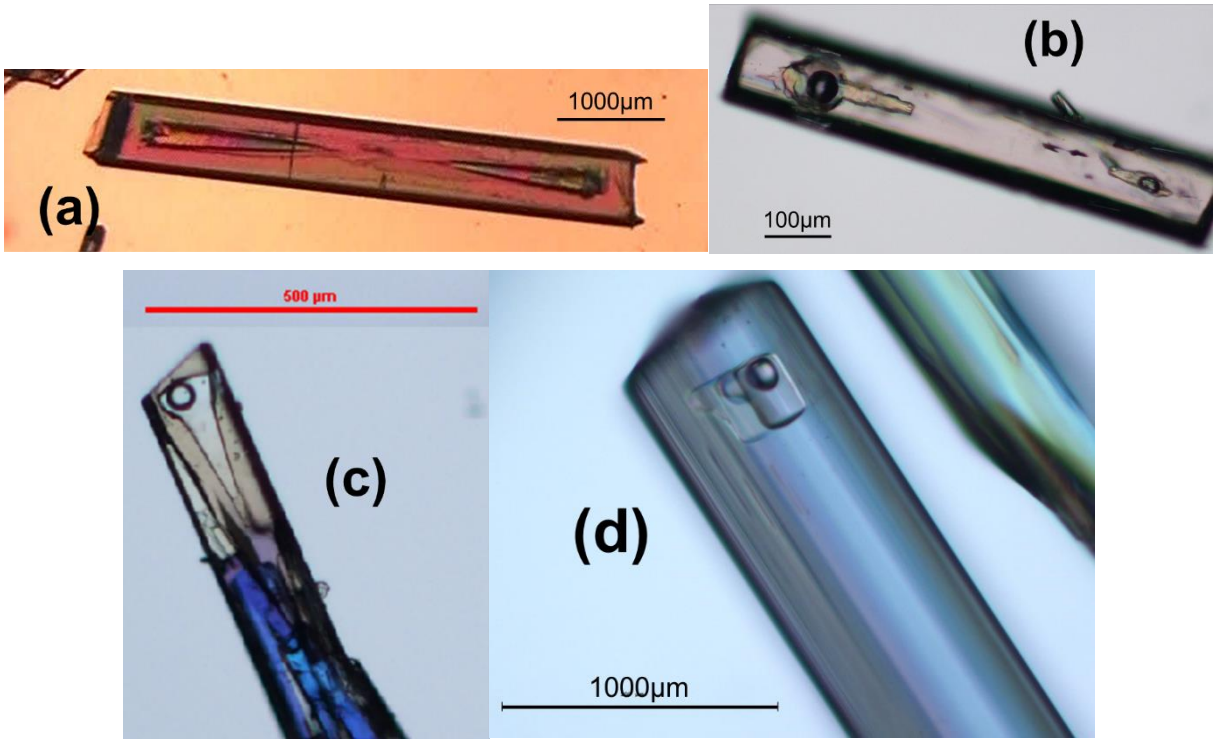

Figure II- 32: Photographs of different particles, exhibiting different shape of inclusion(s), taken by optical polarized light microscopy. (a) Crystal obtained with pure S-Ibu and S-αMBA in pure methanol. (b) Particle of ss-S-Ibu-S-αMBA obtained by replacing part of the resolving amine by soda, added in water, with a cooling rate of 0.5 K.min^{-1}. (c) Pure SS diastereomer obtained in pure ethanol, showing the angle disruption in the conical shape fluid inclusion. (d) Pure SS diastereomer obtained in pure ethanol, and its squared fluid inclusion.

When the pure diastereomer is crystallized in methanol, it exhibits two symmetrical fluid inclusions, that can look like an hourglass (a). No bubble of gas was observed.

In the vast majority of the cases, there is a single fluid inclusion at both ends of the particles. They are located close to the tips of the particles. They are also symmetrical in position and shape. The most probable cavity shape of particles obtained when replacing a part of the resolving amine by soda in water is a flattened elongated cone expanding towards the extremity of the particle and containing a large bubble of gas (see Figure II- 24). However, the vacuole sometimes shows a modified shape, as seen on the crystal in Figure II- 32b, with its two different fluid inclusions.

Occasionally, as displayed in Figure II- 32c, the projection of the conical shape of the cavity could have two (or more) angles. The angle disruption has been observed close to the tip of the particle. This testifies for different regimes during crystal growth.

The classical conical shape of the fluid inclusions is not always encountered, as shown in Figure II- 32d, with a squared vacuole.

The variety of the fluid inclusions appearance confirms the influence of the environment on the crystal and inclusion shape.

II.6. Discussion, conclusions, and perspectives

This first experimental chapter aimed at introducing the system on which the continuous mode will be tested: diastereomers *S*-Ibu-*S*-αMBA and *R*-Ibu-*S*-αMBA formed during the Pasteurian resolution of rac-Ibu with *S*-αMBA.

Firstly, in order to design a robust chiral resolution process, the solubility of rac-Ibu and of the desired diastereomer *S*-Ibu-*S*-αMBA was measured. The data of this latter were processed in different manners, in order to find the best solubility model for the different ratio ethanol/water studied. In the end, it appeared that the exploitation with Excel was the closest to the experimental data.

Also, the effect of chiral purity on solubility was confirmed: as chiral purity increases, solubility decreases.

Then, the phase diagram between the two diastereomers *S*-Ibu-*S*-αMBA and *R*-Ibu-*S*-αMBA was studied and updated compared with the one already reported in the literature[87,89]. A partial solid solution on the side of the less soluble salt, ss-*S*-Ibu-*S*-αMBA, has been evidenced by using chiral HPLC, DSC and XRPD. The monophasic domain width in composition has been assessed at circa 13 %w at room temperature and 17 %w at the temperature of the eutectic invariant. This limit of miscibility of ss-*S*-Ibu-*S*-αMBA restricts the diastereomeric excess reachable after a single resolution step. Therefore, the maximum diastereomeric purity achievable is restraint by heterogeneous equilibria.

The miscibility in the solid state of the undesired diastereomer in the structure of *S*-Ibu-*S*-αMBA induces the formation of fibrous crystals. Apart from an external shape suggesting single crystals, those particles are actually an ordered aggregation of parallel fibers, stacked along their common main axis ‘a’. They present variable degrees of microscopic order; indeed, several studies by SCXRD revealed an ill-defined order in the reciprocal lattice. Conversely, one of the picked up ‘twinned’ crystals served the structure resolution.

The surprising fibrous nature of ss-*S*-Ibu-*S*-αMBA particles has interrogated their qualification as ‘single crystals’. Indeed, they seems to exhibit an acicular mosaicity, where the degree of order may vary from one fiber to another. Therefore, the terms ‘fibrous crystals’, ‘polycrystalline aggregates’ or ‘fibers assembly’ would be more correct.

A growth mechanism was proposed, attempting to explain the aspect of the ss-*S*-Ibu-*S*-αMBA crystals. Unfortunately, no proper experimental set-up could be found to probate the mechanism, but it served the observation of a crystal ‘self-healing’ preceding the growth phenomenon. Further experiments should be performed to prove the expressed hypotheses.

The application of the Pope and Peachey procedure in batch mode (see Chapter IV) resulted in crystals exhibiting fluid inclusions at their extremities. The mechanism of formation of an inclusion results from the interplay between many factors. When the particle becomes large enough, the correct feeding of the center is more difficulty compared to the border. As soon as a small cuvette has been formed, the feeding of the center of the depression becomes even more difficult, sustaining and even amplifying the process. This results in a conical aspect of the cavity. When the environmental conditions change, the angle of the cone adapts. When the supersaturation drops, it is possible to close up the cavity. Such occurrence is not surprising regarding the fibrous nature of the particles, inducing a certain roughness of the crystal surface, which promotes the formation of inclusions[95].

Annealing of the fibrous crystals at different temperatures revealed that diffusion becomes sufficient only at a high temperature of ≈100 °C. In that case, the dissolution around the fluid inclusions led to the piercing of the two opposite cavities and thus the release of solvent. Prior to this event, no homogenization could be observed, suggesting that at least part of the gas trapped in the inclusion comes from a nucleation process of micro-bubbles on the very rough surfaces at the tips of the particles. These porous surfaces are prompt to adsorb the gas dissolved in the mother liquor. In conclusion, the bubbles of gas of the fluid inclusions of ss-*S*-Ibu-*S*-αMBA are probably persistent bubbles.

Since the nature of the gas can have an important influence on the fluid inclusions[97], the phase(s) trapped in the vacuoles should be characterized in further work. Confocal Raman spectroscopy seems particularly appropriate.

The fibrous nature of the diastereomer promotes the roughness and porosity of the crystal surface, which favors the formation of inclusions. Nevertheless, the environment of the particle during growth also impacts the development of fluid inclusions, as mentioned above. The nature of the solvent, as well as its purity can affect the crystal and the inclusion shape. This was demonstrated with the comparison between pure ethanol and azeotropic ethanol.

The purity of the product also has an influence. In addition to modifying the aspect of the crystals, the presence of the undesired diastereomer within the structure of *S*-Ibu-*S*-αMBA impacts the inclusion shape too.

Furthermore, it appeared that the nice crystal morphology of platelet was due to water and not to soda. Nonetheless, the presence of this latter seemed to increase the frequency of the fluid inclusions in the fibrous crystals.

The study of the fluid inclusions of the ss-*S*-Ibu-*S*-αMBA fibrous crystals can be refined in further work, by examining the impact of supersaturation, soda amount, gas bubbling or cooling rate could for example.

Thanks to the different experimental studies, two levers were identified to avoid the formation of fluid inclusions which are defects that can affect the product purity.

In the first place, water was proved to be the habit modifier, and the presence of soda to increase the number of fluid inclusions. Hence, the removal of soda in the process limits the formation of inclusions.

Secondly, the bubbles of gas observed in most of the fluid inclusions of ss-*S*-Ibu-*S*-αMBA are mainly persistent bubbles. Generally, the improvement of the medium mixing can be preventive.

To conclude, in order to avoid the formation of fluid inclusions in particles of ss-*S*-Ibu-*S*-αMBA, crystal growth should be performed in soda free solution at lower supersaturation, in a vigorously stirred and degassed mother liquor. This procedure was experimented and validated at laboratory scale.

Before starting the Couette-Taylor experiments presented in Chapter IV, the continuous set-up was examined and sometimes modified. Indeed, to ensure the good proceedings of the process feed, a prototype had to be designed. Also, some improvements were directly made on the CT device environment. The next chapter deals with the implementation and the evolution of the continuous set-up used in the continuous experiments presented in Chapter IV.

Chapter III. Continuous set-up

III.1. Couette-Taylor crystallizer

The Couette-Taylor (CT) reactor used in this work was manufactured by Laminar Co., Ltd. It is shown in Figure III- 1 and schematically represented in Figure III- 2.

The inner cylinder ($r_i = 19.5$ mm) can rotate while the outer ($r_o = 23.4$ mm) is at rest. The gap width d between the two cylinders is 3.9 mm. The CT crystallizer total capacity is 100 mL. To avoid any hydrostatic pressure effect, it is placed horizontally[56].

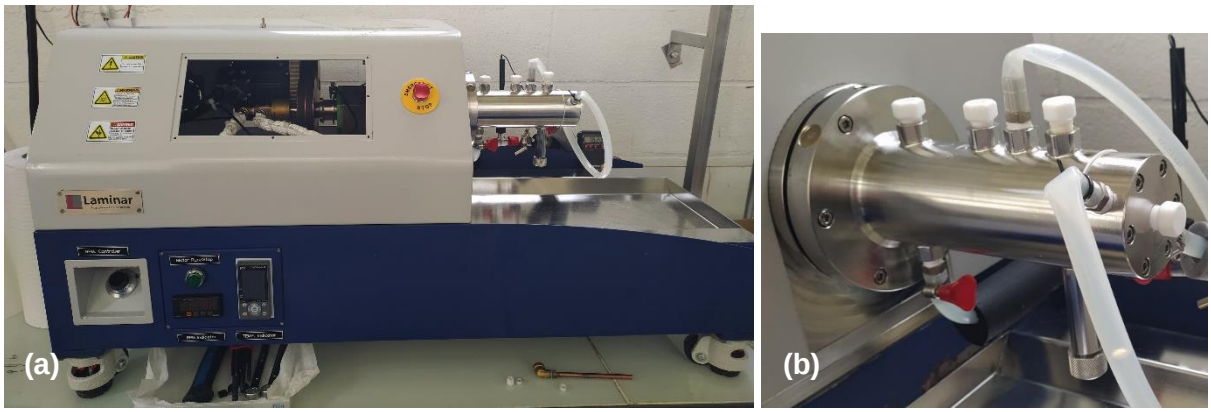

Figure III- 1: Photos of the Couette-Taylor reactor: (a) whole device, (b) closed reactor part.

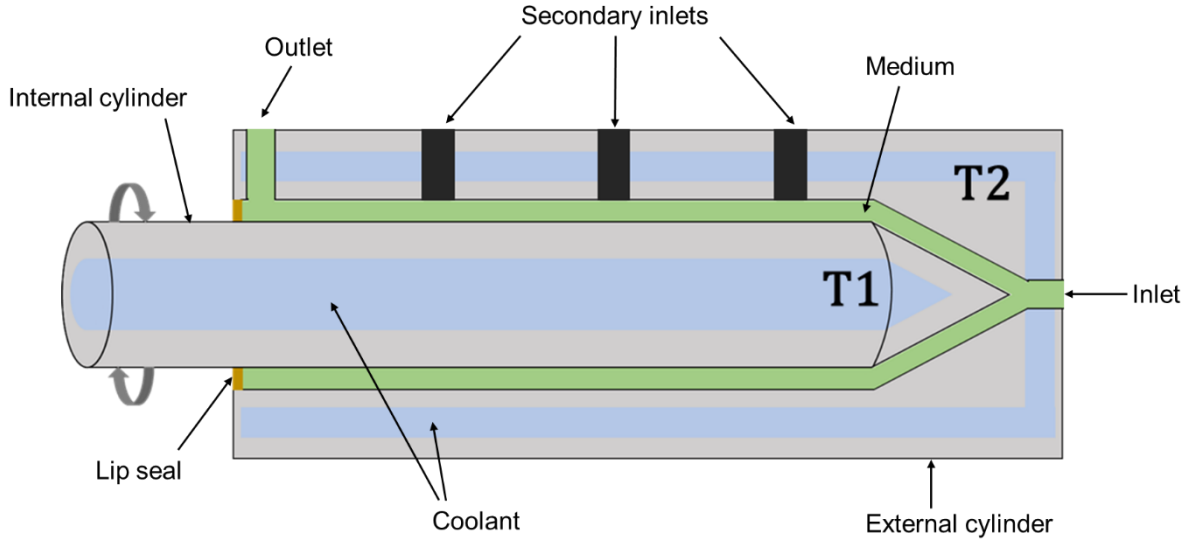

Figure III- 2: Schematic representation of the Couette-Taylor crystallizer used in this work.

As depicted in Figure III- 2, the two cylinders are independently thermoregulated. T1 is the set temperature of the thermostat of the internal cylinder, and T2 the set temperature of the thermostat of the outer cylinder. Thanks to this feature, the reactor can be used in the non-isothermal mode[62].

In the presented work, the CT reactor is used in continuous mode. To ensure a correct continuous feeding, the upstream part of the continuous set-up must be carefully investigated.

III.2. Feeding part design

A preliminary experiment aimed at testing the feeding of the CT reactor with a suspension. This trial was unsuccessful: the peristaltic pump was not able to transport the suspension. A solution was sought, but there was a constraint regarding the tubing diameter due to the reactor's inlet. Regarding this limitation, no viable solution could be considered.

In conclusion, the feeding has to be done with a solution.

III.2.1. Feeding constraints

First of all, if the CT reactor must be fed with a solution, this means that the crystallization will take place within the crystallizer.

The feeding solution(s) could be stored in a tank upstream the CT reactor. Nevertheless, continuous experiments can take several hours, and by keeping the studied system at the ambient temperature for a long time, crystallization can occur inside the feeding tank. To avoid the crystallization risk, the solution could be maintained at high temperature. However, because of the experiment duration, this can lead to chemical degradation. The solution to this threefold problem was then to separate the two reagents in two different tanks, thermoregulated at 30 °C.

Before entering the CT reactor and crystallize, the two solutions must be mixed and heated. To achieve these two needs, a specific glass piece was designed.

III.2.2. Mixing piece design

If various systems have been considered (chromatography capillaries or coils in a temperature-regulated bath, heating tape), the final decision regarding the design of the mixing piece was to create it with the glassblower of the university. Two different models have been designed and used for the presented work.

To avoid unwelcome crystallization within the mixing piece, the temperature at which the two initial solutions gather is important. To ensure the reach of a safe minimum temperature of 40 °C, calculations were made regarding the length of the pipes before the meeting zone.

III.2.2.1. Determination of the necessary minimum length of the inlet pipes[4,115]

Simplification hypotheses

The system can be simplified by assimilating it to a counter-current heat exchanger. The schematic representation of this simplification can be found in Figure III- 3, with the mass flow ($kg.h^{-1}$) of the hot part $\dot{m}_h$ and of the cold part $\dot{m}_c$, the temperature (K) of the hot fluid at the inlet $T_{h,i}$ and at the outlet $T_{h,o}$, and the temperature (K) of the cold fluid at the inlet $T_{c,i}$ and at the outlet $T_{c,o}$.

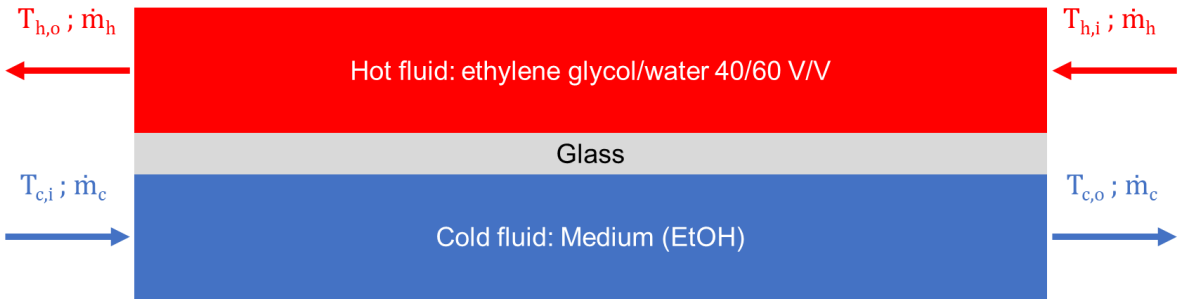

Figure III- 3: Simplified system: counter-current heat exchanger.

For calculation simplifications, the following hypotheses are formulated:

- the heat exchanger is assumed to be adiabatic, which means that there are no interactions with the outside of the system,
- the system is supposed to have reached steady state, i.e. there is no production or accumulation in the heat balance,
- the cold part, that is to say the medium, is reduced to the solvent,
- the axial conduction alongside the tubes is negligible,
- the fluid heat capacities Cp are constant,
- the global heat transfer coefficient H along the heat exchanger is constant.

The needed length of the pipes L_{pipe} (m) is directly linked to the exchange area S (m²) through the formula presented in Equation III- 1, with D_{pipe} and R_{pipe} respectively the pipe diameter (m) and radius (m).

$$S = \pi D_{pipe} L_{pipe} = 2\pi R_{pipe} L_{pipe}$$ *Equation III- 1*

To minimize the piece size, the selected tubes should be small. Among the available pipes of the glassblower, that with the smallest outer diameter is 0.01 m, with a wall thickness of 0.0015 m

The minimum exchange surface S needed to reach a safe minimum temperature of 40 °C is directly correlated with the heat flow necessary to heat up the entering fluids.

Calculation of the heat flow Φ

In a counter-current heat exchanger, the heat flow Φ in $J.s^{-1}$ is defined as in Equation III- 2, with H the global heat transfer coefficient in $W.m^{-2}.K^{-1}$, S the exchange area (m²) and $\Delta T_{lm-counter}$ the logarithmic mean temperature difference for counter-current flow[115] in K.

$$\Phi = HS\Delta T_{lm-counter} \quad with \quad \Delta T_{lm-counter} = \frac{(T_{h,i} - T_{h,o}) - (T_{c,o} - T_{c,i})}{ln\frac{(T_{h,i} - T_{h,o})}{(T_{c,o} - T_{c,i})}}$$

Equation III- 2

Equation III- 2 can be transformed in Equation III- 3 to take S out.

$$S = \frac{\Phi}{H\Delta T_{ml-contre}}$$ *Equation III- 3*

Firstly, the heat flow Φ must be determined, thanks to Equation III- 4, with $\dot{m}$ the mass flow in kg.h^{-1}, Cp the heat capacity in J.kg^{-1}.K^{-1} and ΔT the temperature difference between the inlet and the outlet.

$$\Phi = \dot{m} * Cp * \Delta T \qquad \textit{Equation III- 4}$$

The system is in steady state, thus the heat flow of the hot part equals that of the cold part. This is transcribed in Equation III- 5.

$$\Phi = \dot{m}_h * Cp_h * (T_{h,i} - T_{h,o}) = \dot{m}_c * Cp_c * (T_{c,o} - T_{c,i}) \qquad \textit{Equation III- 5}$$

With the known values in the cold part, the heat flow can be calculated thanks to Equation III- 5. Nevertheless, $T_{h,i}$ and $T_{h,o}$ are necessary to determine the logarithmic mean temperature difference in Equation III- 2. $T_{h,i}$ is imposed during the experiment, and $T_{h,o}$ can be taken out from Equation III- 5:

$$T_{h,o} = T_{h,i} - \frac{\dot{m}_c}{\dot{m}_h}\frac{Cp_c}{Cp_h}(T_{c,o} - T_{c,i}) \qquad \textit{Equation III- 6}$$

Now, the missing value to determine S with Equation III- 3 is the global heat transfer coefficient H.

Calculation of the global heat transfer coefficient H

In the system, the heat transfer occurs through convection in the fluid (see Figure III- 4 hot and cold parts) and through conduction in the glass wall.

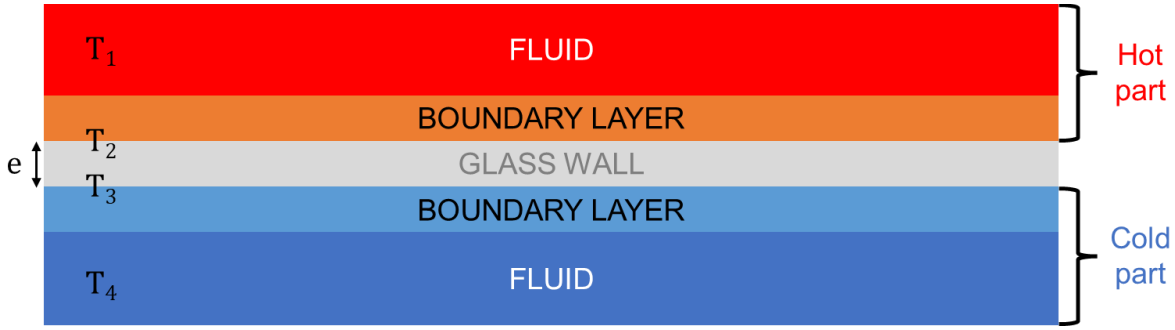

Figure III- 4: Schematic representation of the simplified system for the calculation of H.

In the hot part, the convective transfer is defined in Equation III- 7, with Φ_h the heat flow in the hot part (J.s^{-1}), h_h the convection coefficient in the hot part (W.m^{-2}.K^{-1}), S the exchange surface (m) and T_1 and T_2 respectively the temperatures of the hot fluid and at the wall (K). The sign '-' needs to be added because the heat flow is positive from the fluid core to the wall.

$$\Phi_h = -h_h S(T_2 - T_1) \qquad \textit{Equation III- 7}$$

Equation III- 7 can also be written as:

$$(T_1 - T_2) = \frac{\Phi_h}{h_h S} \qquad \textit{Equation III- 8}$$

The conductive transfer in the glass wall is defined in Equation III- 9, with Φ_w the heat flow in the glass wall (J.s^{-1}), λ_w the thermal conductivity of the glass wall (W.m^{-1}.K^{-1}), S the exchange surface (m), e the wall thickness (m) and T_2 and T_3 respectively the temperatures at the hot and cold walls (K). Equation III- 9 can also be written as in Equation III- 10.

$$\Phi_w = \frac{\lambda_w S}{e}(T_2 - T_3)$$ *Equation III- 9*

$$(T_2 - T_3) = \frac{\Phi_w e}{\lambda_w S}$$ *Equation III- 10*

In the cold part, the convective transfer is defined in Equation III- 11, with Φ_c the heat flow in the cold part (J.s^{-1}), h_c the convection coefficient in the cold part (W.m^{-2}.K^{-1}), S the exchange surface (m) and T_3 and T_4 respectively the temperatures at the wall and of the cold fluid (K). The heat flow is positive from the wall to the fluid core. Equation III- 11 can also be written as in Equation III- 12.

$$\Phi_c = h_c S(T3 - T4)$$ *Equation III- 11*

$$(T3 - T4) = \frac{\Phi_c}{h_c S}$$ *Equation III- 12*

The system has reached the steady state, i.e. there is no energy accumulation or production. Thus:

$$\Phi_h = \Phi_w = \Phi_c = \Phi$$ *Equation III- 13*

Then, Equation III- 8, Equation III- 10 and Equation III- 12 can be summed:

$$(T_1 - T_4) = \frac{\Phi}{h_h S} + \frac{\Phi e}{\lambda_w S} + \frac{\Phi}{h_c S}$$ *Equation III- 14*

There is a resistance to the heat transfer due to the glass wall and to the boundary layers on both sides (Figure III- 4). The total resistance R_t in W.K^{-1} is defined as the sum of the resistances generated by the boundary layers in the hot and cold parts R_h and R_c, and by that of the glass wall R_w:

$$R_t = R_h + R_w + R_c$$ *Equation III- 15*

R_t can also be defined as:

$$R_t = \frac{(T_1 - T_4)}{\Phi}$$ *Equation III- 16*

By injecting Equation III- 14 in Equation III- 16:

$$R_t = \frac{1}{h_h S} + \frac{e}{\lambda_w S} + \frac{1}{h_c S}$$ *Equation III- 17*

The global heat transfer coefficient H in W.m^{-2}.K^{-1} can written as:

$$H = \frac{1}{R_t S}$$ *Equation III- 18*

In the studied system, as the glass wall is that of a pipe: the surface between the hot part and the glass wall, and that between the glass wall and the cold part are different. Thus, the global heat transfer coefficient must be defined for the surface S_h (m) between the hot part and the glass wall, for that between the glass wall and the cold part S_c (m), and for the average surface S_a (m). The three expressions are depicted in Equation III- 19, Equation III- 20 and Equation III- 21.

$$H_h = \frac{1}{R_t S_h} = \frac{1}{\frac{1}{h_h} + \frac{e}{\lambda_w}\frac{S_h}{S_a} + \frac{1}{h_c}\frac{S_h}{S_c}}$$ *Equation III- 19*

$$H_c = \frac{1}{R_t S_c} = \frac{1}{\frac{1}{h_h}\frac{S_c}{S_h} + \frac{e}{\lambda_w}\frac{S_c}{S_a} + \frac{1}{h_c}}$$ *Equation III- 20*

$$H_a = \frac{1}{R_t S_a} = \frac{1}{\frac{1}{h_h}\frac{S_a}{S_h} + \frac{e}{\lambda_w} + \frac{1}{h_c}\frac{S_a}{S_c}}$$ *Equation III- 21*

In the above equations, the convection coefficients h_h and h_c can be determined thanks to the dimensionless Nusselt number Nu, as shown in Equation III- 22, with D_h the hydraulic diameter in m and λ_{fluid} the thermal conductivity of the fluid in $W.m^{-1}.K^{-1}$.

$$Nu = \frac{hD_h}{\lambda_{fluid}}$$ *Equation III- 22*

The Nusselt number is correlated to the Reynolds and Prandtl numbers Re and Pr, through an empirical relationship of the form of Equation III- 23. The coefficients α, β and γ vary according to the flow regime characteristics (Re, Pr) and to the system geometry[115,116].

$$Nu = \alpha Re^{\beta} Pr^{\gamma}$$ *Equation III- 23*

With the calculation of Nu, the convection coefficients h_h and h_c can be determined, serving the calculation of the global heat transfer coefficients H_h, H_c and H_a thanks to Equation III- 19, Equation III- 20 and Equation III- 21. With these results, the heat flow Φ can be estimated, then the exchange surface S, and finally the pipe length L_{pipe}.

III.2.2.2. First prototype

In the first place, the prototype model was inspired from the static mixers that can be found in the chemical and pharmaceutical industry. The idea was to design a double-jacketed Y-shaped piece, in order to be able to regulate its temperature.

The initial plan was to fulfill this piece with a structured metal packing or random packings such as Raschig rings. However, the design of a packing suitable for such small piece seemed technically impossible. The considered solution was then to use two frit glass sections in the main pipe to ensure mixing.

The schematic representation of this first mixing piece model is depicted in Figure III- 5. Two taps were added, in order to measure the temperature where the two solutions mix, and before the entrance into the CT crystallizer.

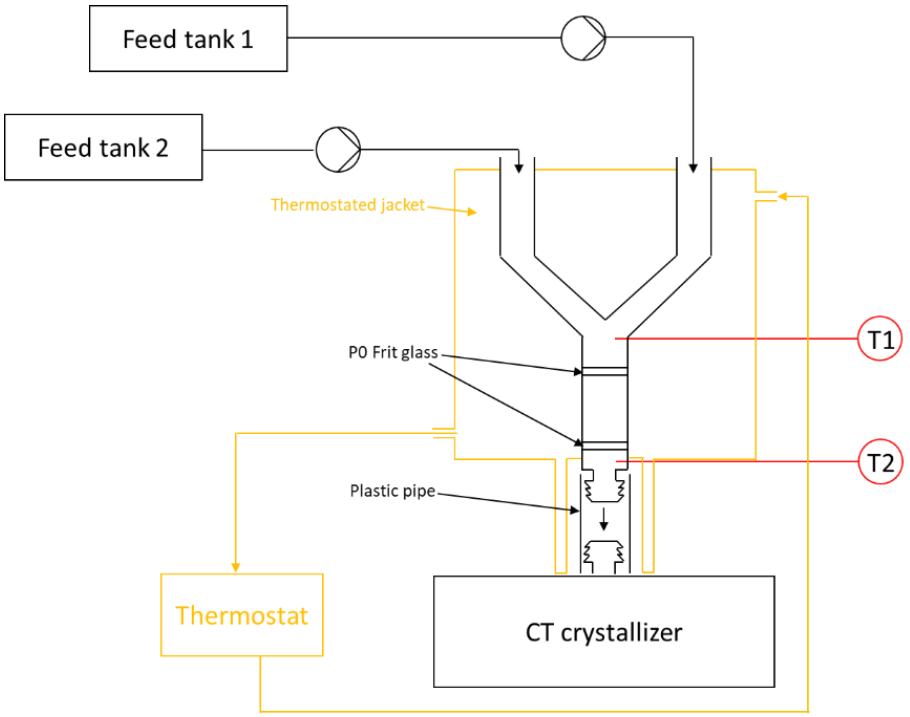

Figure III- 5: Schematic representation of the first model of the mixing piece.

III.2.2.2.1. Length of the inlet pipes

By using the reasoning of section III.2.2.1, the minimum pipe length necessary for the feeding solutions to reach 40 °C was calculated.

Firstly, the Reynolds numbers of the cold and hot parts were calculated; the results are detailed in Appendix B.

Then, the different calculations presented in section III.2.2.1 were done; the results are presented in Appendix C.

In the studied system, the flow regime in the cold part is laminar (see Appendix B, section B.1). As the fluid goes through a pipe[115,116]: $Nu = 4.364$.

Regarding the hot part, the flow regime being turbulent (see Appendix B, section B.2), the Nusselt number was calculated thanks to the correlation in agreement with the determined Prandtl number (see Appendix C section C.2.1).

Next, the convection coefficients h_h and h_c were determined (Appendix C section C.2.2), serving the calculation of the global heat transfer coefficients H_h, H_c and H_a (Appendix C section C.2.3). The heat flow Φ was then estimated, serving the determination of the exchange surface.

In the end, the calculations gave a minimum inlet pipe length of L_{pipe} = 13.5 cm.

Figure III- 6 shows the photos of the first prototype of the mixing piece. This first version was simplified for technical reasons: the jacket has not been extended around the outlet of the piece. The junction between the Y-shaped connection and the CT crystallizer was insulated to limit heat loss.

Figure III- 6: Photos of the first prototype of the temperature regulated Y-shaped connection.

III.2.2.2.2. First prototype tests

Temperature test

The Y-shaped connection was tested in the conditions of the very first process of chiral resolution supposed to be tested in the CT crystallizer. This crystallization step of this process occurs in methanol.

For a thermostat set temperature of 70 °C, the medium started to boil. The set temperature was then decreased to 60 °C. The temperatures measured at T1 and T2 (see Figure III- 5) were respectively comprised between 58.5 and 59.8 °C, and between 59.5 and 59.9 °C. It means that the actual heat transfer was better than that expected.

Mixing test

The mixing efficiency of the first prototype was tested with colored solutions. As shown in Figure III- 7, the colored solutions struggle to mix.

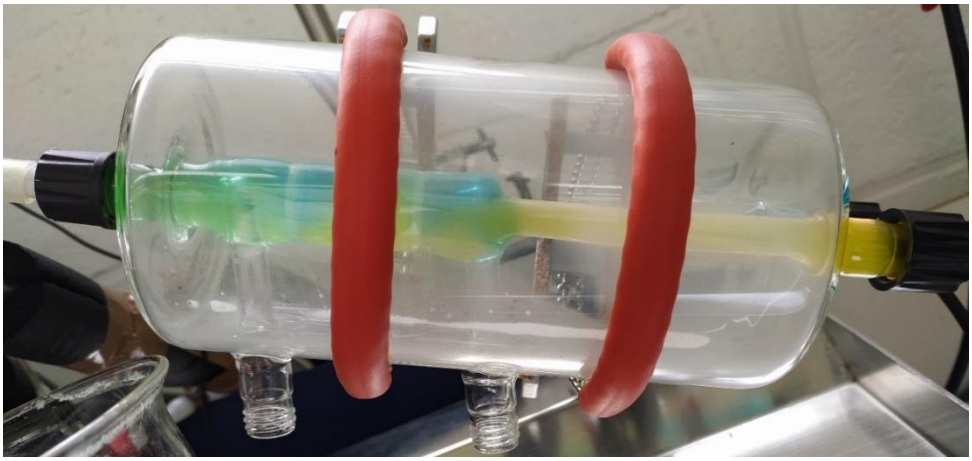

Figure III- 7: Test of the mixing efficiency of the Y-shaped connection with colored solutions

The poor mixing efficiency of the Y-shaped connection is due to the low linear velocities of the feed solutions, because of the long residence time in the CT crystallizer and of the tube diameter.

With these conditions, turbulence is not reachable. Mixing involves energy dissipation, and in the present case, the pressure drop is too low. The two frit glasses are not enough to intertwine the layers of fluid to ensure good mixing.

To increase the linear velocities, a reduction of the tube diameter could be considered, but this is not technically possible: smaller diameter glass tubes were not readily available. Also, the residence time being a parameter to study, long values must also be tested.

Solutions including baffled inserts were considered, but if they would have increased the macro-mixing, the meso- and micro-mixing would not have been efficient because of the low linear velocities.

To conclude, with the study constraints, turbulence can only be achieved with a mobile stirrer.

This first prototype was used for a preliminary series of continuous experiments (see Chapter IV section IV.1.2), while the design of a second mixing piece prototype was investigated.

III.2.2.3. Second prototype

As seen in the previous section, to reach turbulence, the mixing piece must not be designed as a static mixer but rather as a mixing chamber with a stirrer.

Other solutions were investigated, like a coil system with Corning System, the *f*Reactor™ from Interchim® or a batch jacketed oscillatory baffled reactor from NiTech® Solutions. Nevertheless, with the presence of a glass blower within the faculty, the glass design solution remained the simplest and most accessible one.

III.2.2.3.1. Design of the mixing chamber

In the first place, different designs were imagined and explored. Some of them are depicted in Figure III- 8.

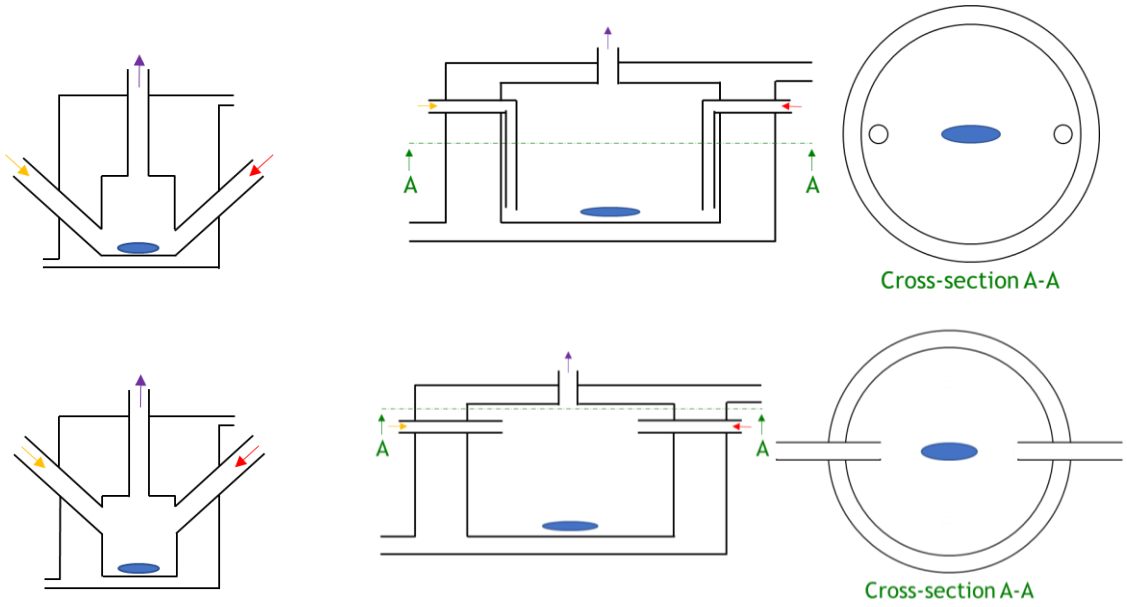

Figure III- 8: Four of the explored designs for the second prototype of the mixing piece.

To understate the dead volume before the entrance in the CT reactor, the volume of the mixing chamber should be minimized. The limitation to this minimization is the technical feasibility:

(1) the necessary space between the tip of the inlet tapping and its welding in the chamber's wall must be of minimum 10 mm,

(2) the space required between the two tips of the face-to-face inlets must be of minimum 15 mm,

(3) the free space around a welding must exceed 5 mm in order to warranty the welding quality.

Following the previous requisitions, the mixing chamber was done from a tube with an outer diameter of 40 mm with a wall thickness of 2.5 mm. As the thinnest tubes have an outer diameter of 10 mm, by considering the necessary free space of 5 mm around a welding, the chamber's height could not be below 20 mm. These dimensions give a dead volume of 19.2 mL, which is acceptable.

The mixing efficiency is ensured by a bar magnet and a magnetic stirrer. In addition, this dynamic mixing area serves the softening of the flowrate variability due to the peristaltic pump.

III.2.2.3.2. Design of the inlet pipes

For this second prototype, the minimum pipe length for the inlet solutions was also determined. When it was designed, the studied process was that of Chapter IV section IV.4. Thereby, the cold part was assimilated to the solvent mixture ethanol/water 76/24 w/w.

Calculations are detailed in appendix D, based on those of appendices B and C. It gives a minimum pipe length of L_{pipe} = 12 cm to ensure the heat up of the two feeding solutions from 30 °C to 40 °C before they gather.

Regarding the size of the outer tube (that of the jacket): if the two inlet pipes are facing each other on the same axis, this would give an inner diameter of minimum 120 + 120 + 15(requisition 2 of section III.2.2.3.1) = 255 mm. Such large tube was not available and there would be a technical issue considering the piece low height.

Increasing the height would have given a piece hard to handle. The solution was then to bend the inlet pipes. The dimensioned schematic representation of the second prototype of the mixing piece can be found in Figure III- 9. Also, to avoid diffusion from one inlet to the other, the two tapings were shifted (see Cross-section A-A of Figure III- 9).

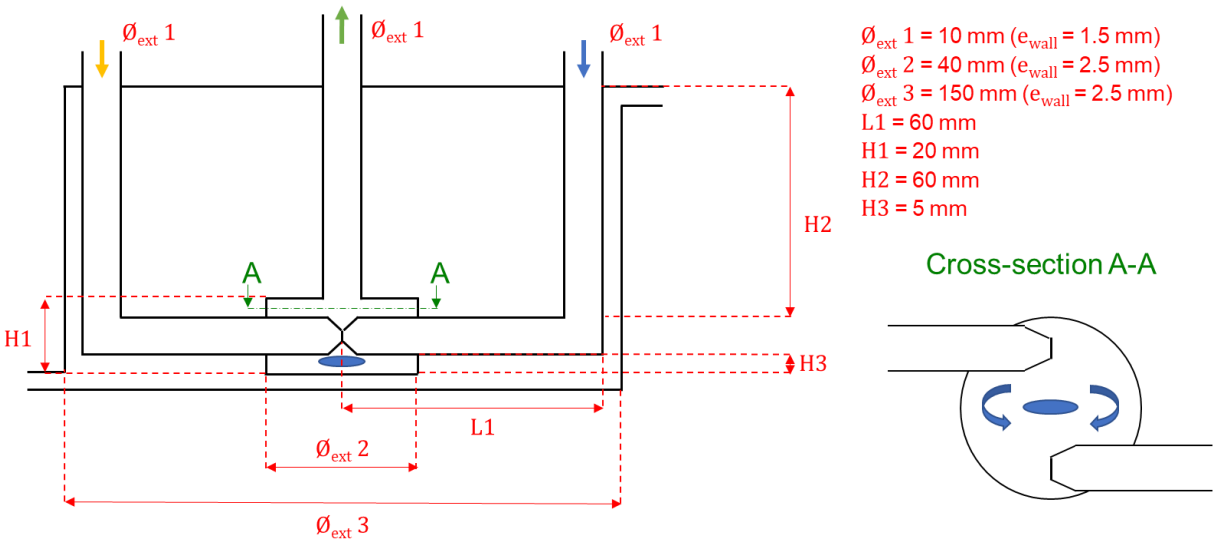

Figure III- 9: Dimensioned scheme of the second prototype of the temperature-regulated mixing piece.

The manufactured second prototype is displayed in Figure III- 10.

Figure III- 10: Manufactured second prototype of the mixing piece.

III.2.2.3.3. Second prototype tests

Temperature

The mixing chamber was tested with a mixture of ethanol/water 76/24 w/w. For a thermostat set temperature of 70 °C, the temperature measured within the mixing chamber was 65.5 °C. It means that the actual heat transfer was better than that expected.

Regarding that, as 65.5 °C is very close to the boiling temperature of ethanol, and to limit the coolant evaporation, the working set temperature was decreased to 60 °C.

Mixing

The mixing efficiency was tested with colored solutions. Figure III- 11 shows the result: the mixing is effective.

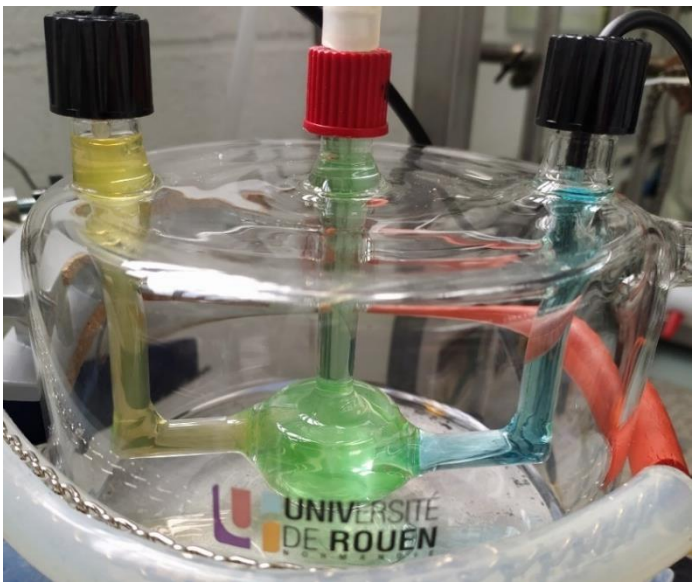

Figure III- 11: Mixing efficiency test of the second prototype

The design of the feeding part of the CT crystallizer was an important part of the reflection around the continuous set-up. In parallel of this design work, some issues were detected regarding the inner cylinder temperature regulation efficiency. This is described in the following section.

III.3. Investigations around the temperature regulation of the inner cylinder

The shaft of the CT crystallizer was changed at the beginning of the present work, because of coolant leaks noticed on the old one. To ensure the good assembly of the new one, tests were made regarding the temperature regulation efficiency within the CT crystallizer.

III.3.1. Temperature regulation efficiency of the inner cylinder

III.3.1.1. Preliminary evaluation of the temperature regulation efficiency

In the first place, the CT reactor was filled with water. The inner cylinder was thermoregulated at 20 °C; no temperature regulation was set for the outer cylinder.

After 1 h of rotation at 1500 rpm, the zone around the lip seal was overheated. This heat generation has spread over the shaft up to the conical part, despite the inner cylinder temperature regulation, as depicted in Figure III- 12a.

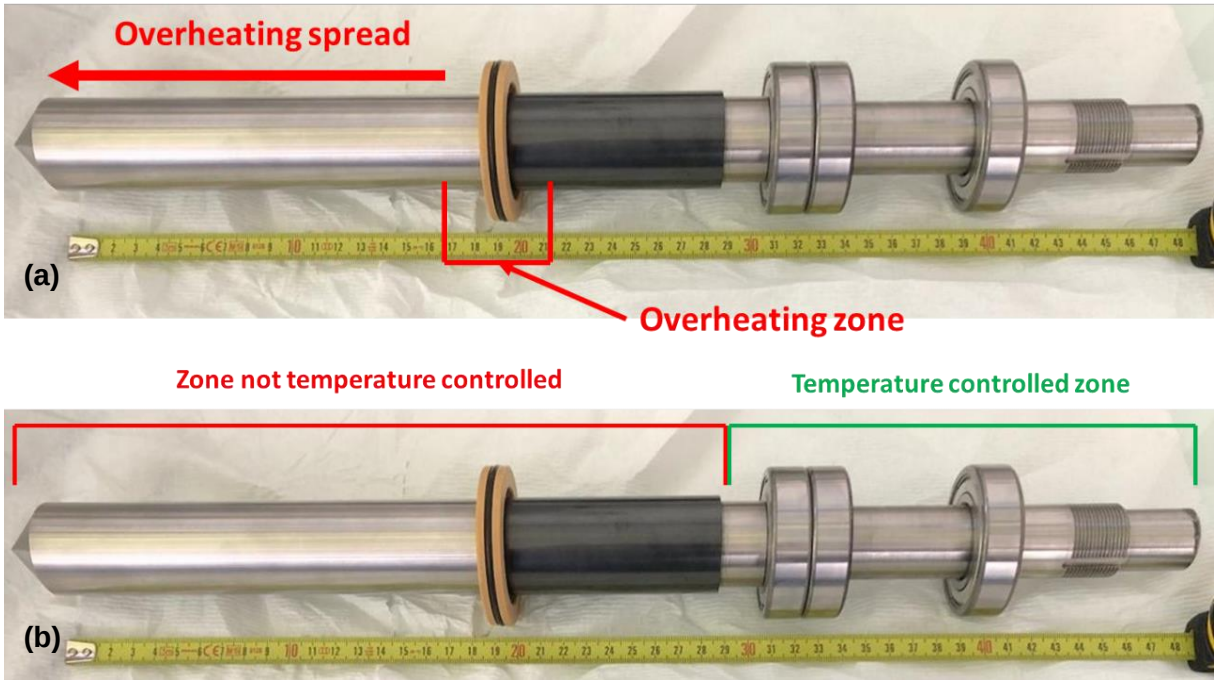

Figure III- 12: Disassembled inner cylinder. (a) view of the overheating zones and (b) view of the zones apparently not temperature-controlled (red), and temperature-controlled (green).

A second test was performed: the internal cylinder was left overnight with a temperature regulation of 10 °C. The following day, the 'red' part shown in Figure III- 12b (which includes the active part beyond the lip seal) was not temperature controlled. It was at room temperature while the « out-of-reactor » part (in green on Figure III- 12b) seemed to be correctly regulated. Same observations were made with a temperature regulation set at 60 °C.

A third test was made, with an increased coolant flow rate. The set temperature of the inner cylinder thermostat was put at 10 °C (T_j) and the coolant flow rate was at its maximum value. The external cylinder was assembled and regulated at 20 °C.

After 1 h of equilibration, with no rotation, the temperature was measured at four points (see Figure III- 13):

- T1 before the lip seal,
- T2 after the lip seal,
- T3 on the conical part,
- T4 on the coolant tube coming out of the shaft.

The CT crystallizer fulfilled with water was then rotated at 1500 rpm for 1 h. A second series of measurements was realized after this rotation time.

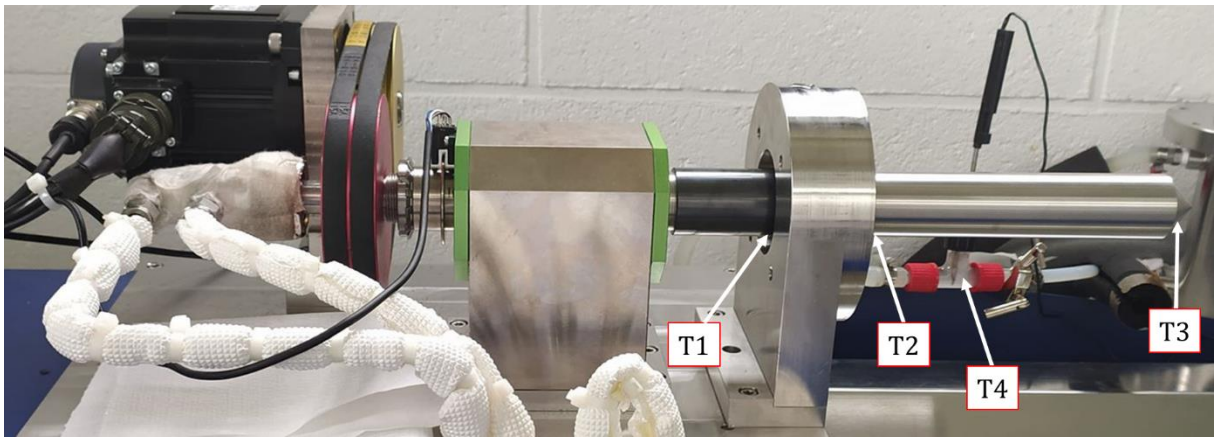

Figure III- 13: Location of the temperature measurements of the third test.

The results of this third test are presented in Table III- 1. The effect of the heat generated by the friction with the lip seal is clear (+7 °C for T2). There is also an evident temperature gradient along the reactor (+7 °C between T3 and T2 after 1 h of rotation).

Temperature point	Temperature after 1 h of equilibration (°C)	Temperature after 1 h of rotation at 1500 rpm (°C)
T_j	10.9	10.6
T1	24.8	**34.1**
T2	22.4	**29.7**
T3	22.4	**22.2**
T4	13.5-14.5	14.0-15.0

Table III- 1: Results of the temperature measurements of the third test.

These temperature variations can be problematic for the implementation of crystallization processes, as the medium will be heated up close to the outlet of the reactor.

If the most evident cause of the poor temperature regulation of the inner cylinder is the heat generated by the friction of the rotating shaft with the lip seal, the temperature regulation system must also be investigated. This is the topic of the next section. The heat generation due to the friction with the lip seal is covered in section III.3.2.

III.3.1.2. Length of the internal pipe of the rotary joint

To ensure the regulation of the temperature, the coolant can arrive inside the internal cylinder through a component called “rotary joint” or “rotary seal”, as shown on Figure III- 14.

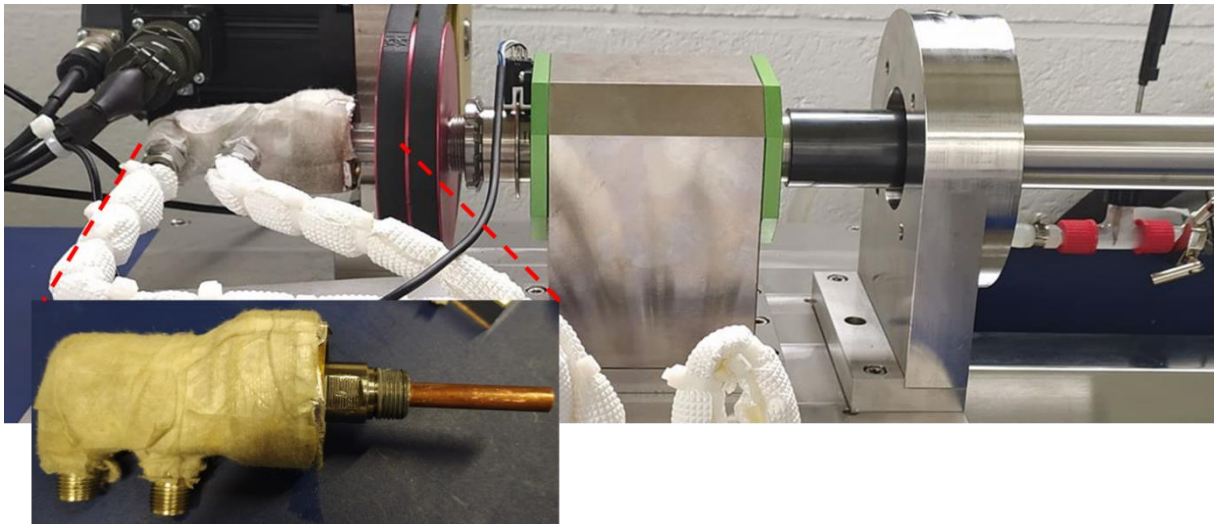

Figure III- 14: Location and photo of the “rotary joint” or “rotary seal”.

The coolant enters the inner cylinder through the internal pipe of the rotary joint, which measures 8 cm. As seen on Figure III- 12b, this means that the end of the pipe coincides with the first bearing level. Thus, for the last 40 cm of the shaft, the turnover of the coolant is poor. Consequently, for the active part of the shaft in the CT reactor (i.e. the last 20 cm beyond the lip seal) the temperature regulation cannot be optimum.

Proposed solution

To address this issue, the considered solution was to lengthen the internal pipe of the rotary seal, so that the coolant reaches the conical part of the internal cylinder. As shown in Figure III- 15 (b), the coolant can return outside the inlet pipe, taking along a few calories coming from the heat generated by the friction with the lip seal.

Nevertheless, this longer pipe can generate more vibration and noise. To limit this effect, a ‘guiding’ annular piece made in Teflon was inserted. Its schematic representation can be found in Figure III- 16.

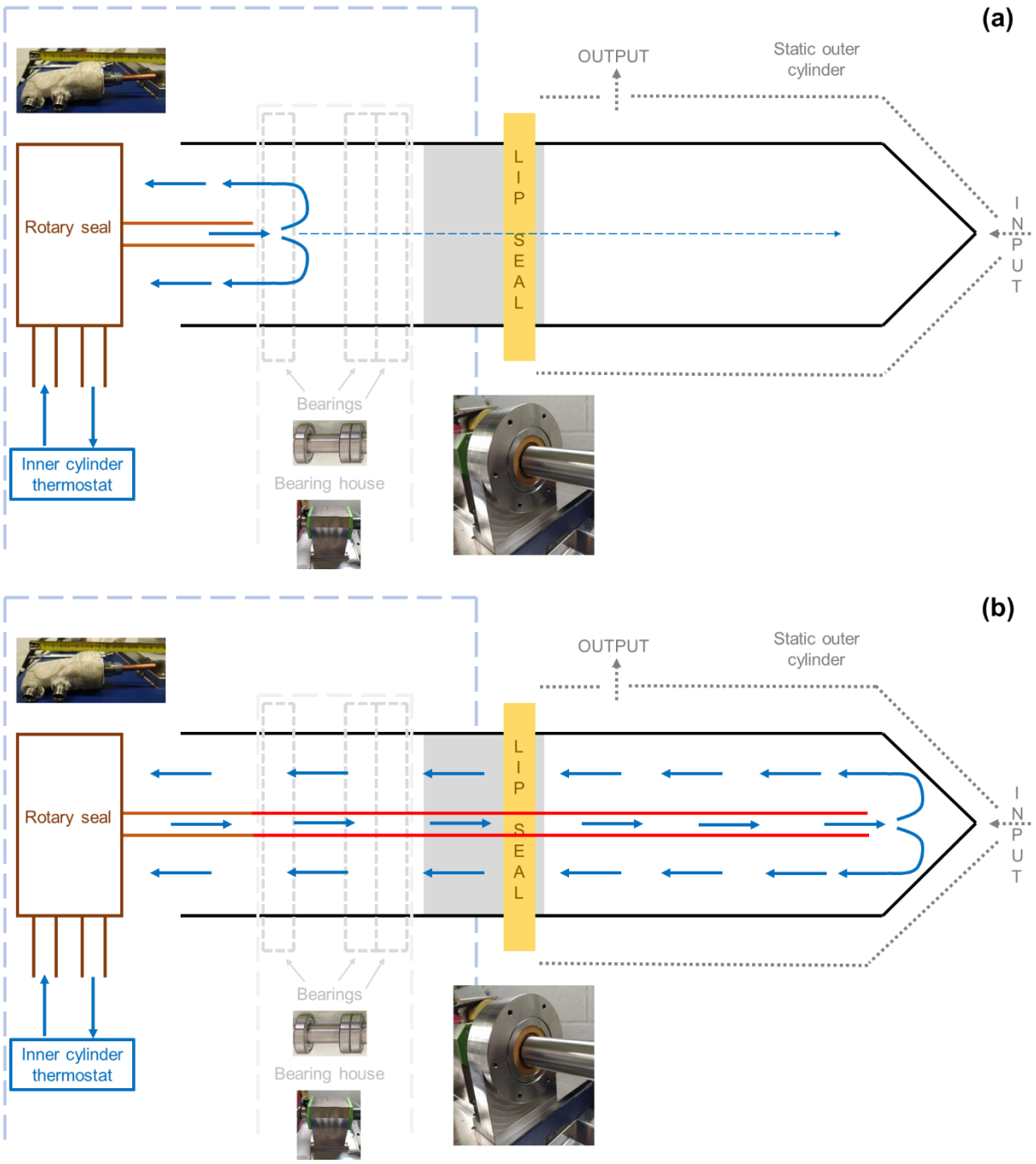

Figure III- 15: Schematic representation of the coolant circulation within the inner cylinder (a) with the initial pipe of the rotary joint and (b) with a longer pipe.

Figure III- 16: Schematic representation of the 'guiding' annular piece of the rotary joint pipe.

Temperature measurements after the replacement of the rotary seal pipe

Once the longer pipe of the rotary joint was installed, new temperature measurements were done, to check the effect of the modification.

Like the third test of section III.3.1.1, the set temperature of the inner cylinder thermostat was put at 10 °C and the coolant flow rate was at its maximum value. After 1 h of equilibration, without rotation, the temperature was measured at four points (see Figure III- 13). The compared results can be found in Table III- 2.

Temperature point	**Temperature after 1 h of equilibration with the old rotary joint pipe (°C)**	**Temperature after 1 h of equilibration with the new rotary joint pipe (°C)**
T_j	10.9	**10.3**
T1	24.8	**20.3**
T2	22.4	**20.8**
T3	22.4	**22.4**
T4	13.5-14.5	**18.3**

Table III- 2: Temperature measurements at four points before and after the lengthen of the rotary joint pipe.

The temperature regulation is improved, especially around the conical part. The coolant turnover is better, which increases the efficiency of the regulation.

Another aspect has been explored to enhance even more the temperature control: the type of tubes used to connect the thermostat and the internal cylinder.

III.3.1.3. Thermostat specific hoses

At the beginning, the inner cylinder and its thermostat were connected with insulated silicon hoses. However, regarding the poor efficiency of the temperature regulation, they were replaced by specific thermostat insulated pipes like the ones presented in Figure III- 17.

Figure III- 17: Specific thermostat insulated pipes.

After their installation, thanks to special adaptors, temperature measurements were performed again.

Also, as the hoses were no longer in silicon, the initial coolant – a mix of ethylene glycol and water 40/60 V/V – was replaced by silicon oil. This latter is supposed to be more adapted for temperature regulation with thermostats.

The procedure for the temperature measurements was the following:

- Equilibration of the temperature of the inner cylinder at 15 °C for 2 h
- Start of the temperature regulation of the external cylinder at 15 °C, then equilibration for 5 h,
- Rotation of the inner cylinder at 1500 rpm for 1 h,
- Temperature measurements at 4 points (see Figure III- 18).

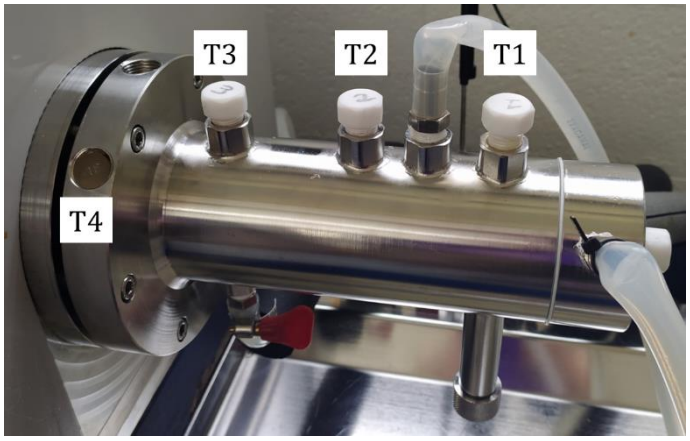

Figure III- 18: Location of the four points of temperature measurements to test the replacement of the hoses.

The results can be found on the graph of Figure III- 19. The impact of the hose replacement, combined with the coolant modification, is clear: the temperature regulation is more efficient with the specific thermostat insulated hoses and with silicon oil.

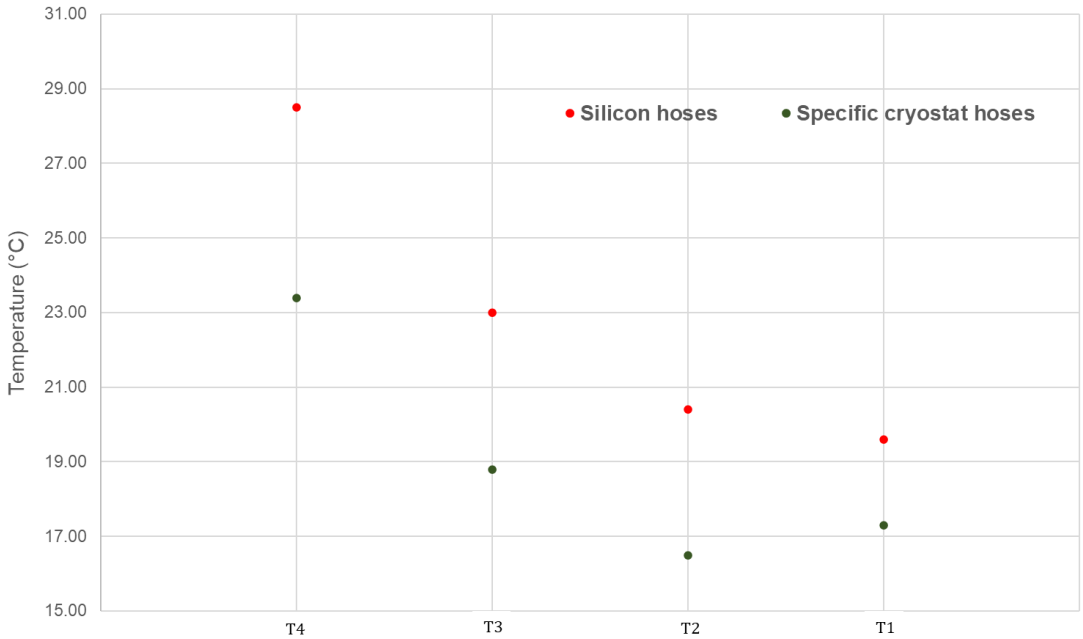

Figure III- 19: Graphical results of the temperature measurements to evaluate the temperature regulation efficiency of the inner cylinder according to the hoses used: in red, with silicon hoses; in dark green, with specific thermostat insulated hoses.

As mentioned in section III.3.1.1, the inner cylinder temperature regulation was also affected by the friction of the shaft with the lip seal when rotating. Investigations were made to address this problem; they are detailed in the next section.

III.3.2. Heat generated by the friction with the lip seal

Previous temperature measurements have evidenced a specific heat generation in the region of the lip seal. This phenomenon is due to the friction between the inner cylinder shaft and the lip seal (see Figure III- 20).

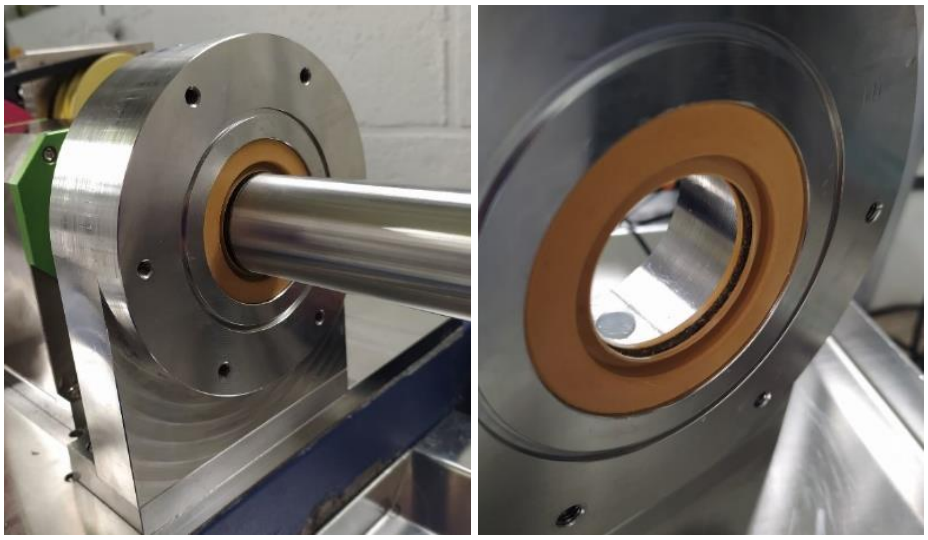

Figure III- 20: Photographs of the lip seal (orange piece) zone.

The lip seal being located near the outlet of the reactor (see Figure III- 2), the heat generated because of the friction could heat up the outgoing medium and dissolve part of the crystals. Such event should be avoided, to limit the effect on productivity and yield.

To address the issue, the replacement of the lip seal by a bearing ring was considered. As it would be one of the extremities of the reactor, this component must be hermetic and resistant to classic solvents such as ethanol, methanol, or acetone.

This inquiry was submitted, among others, to SKF, one of the biggest manufacturers of bearing rings. After some exchanges, their conclusions were that a bearing ring cannot provide the desired hermeticity, and that the current system seems to be the best solution. Nevertheless, they offered recommendations regarding the use of such seal, in order to minimize the friction with the internal cylinder shaft.

During the continuous experiments, the friction indeed occurred, but the increase of the medium temperature at the CT reactor's outlet appeared to be limited by the efficient outer cylinder temperature regulation.

III.4. Final continuous set-up

The final continuous set-up is presented in Figure III- 21 and Figure III- 22. The mixing chamber drawn is the second prototype, used for experiments of Chapter IV sections IV.4 and IV.6. Experiments of Chapter IV section IV.1.2 were performed with the first mixing piece prototype.

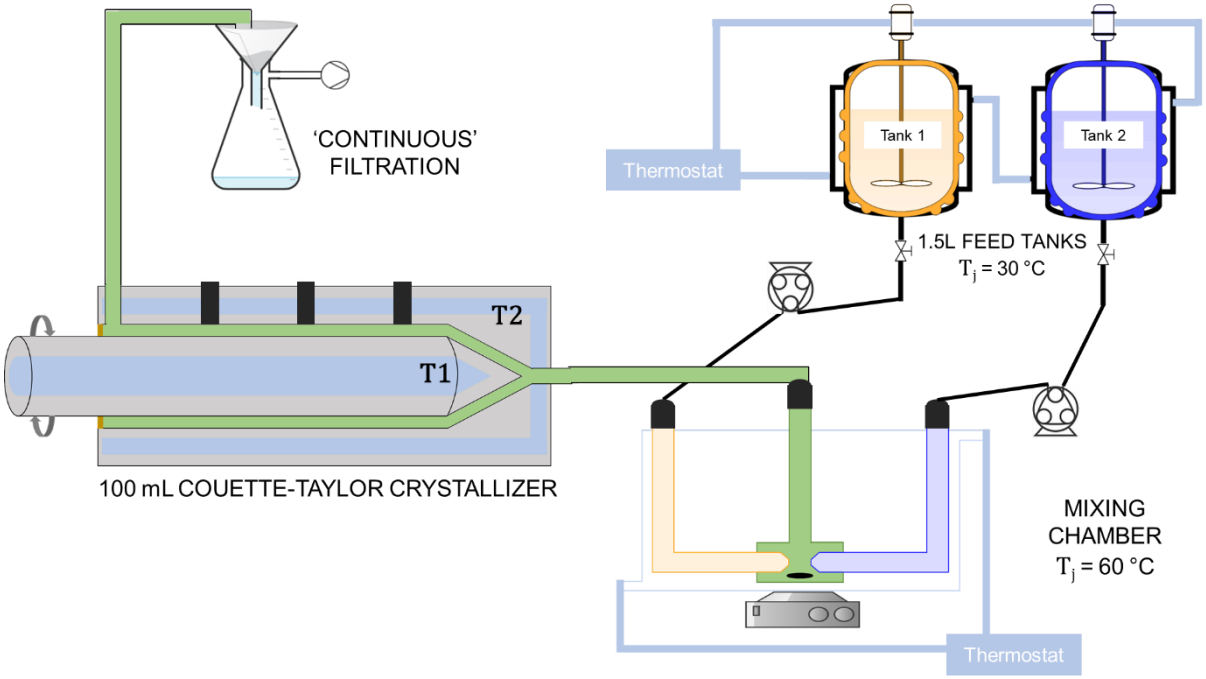

Figure III- 21: Schematic representation of the continuous set-up.

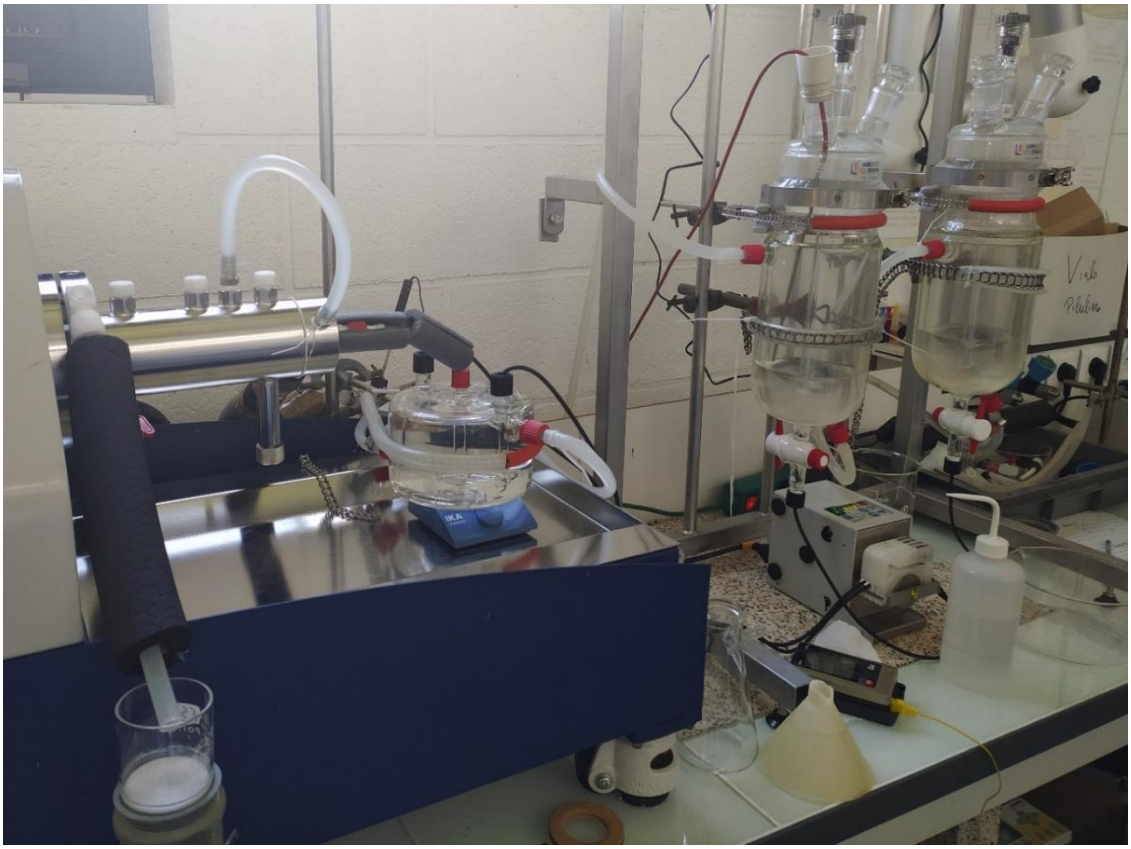

Figure III- 22: Photo of the final continuous set-up.

The feeding solutions were transported from the feed tanks to the CT crystallizer, by passing through the mixing piece, by using a peristaltic pump Ismatec Reglo Digital ISM833C.

Hereafter is the list of the thermostats used:

- CT inner cylinder: Lauda Proline RP890,
- CT outer cylinder: Lauda Proline RP845,
- Mixing chamber: Huber ministat cc2,
- Feeding tanks: Lauda Eco RE420.

The experiments presented in section IV.1.2 and in section IV.4 were performed with the thermostats fulfilled with a mix of ethylene glycol/water 40/60 V/V, except that of the mixing piece: to have a better vision of the inside of the mixing piece, the coolant filling up the Huber ministat cc2 was water.

Water has better heat transfer characteristics ($\lambda_{water,70\,°C} = 0.657\,W.m^{-1}.K^{-1}$), and anyway, as seen in the previous sections, the heat transfer within the mixing prototypes appeared to be better than expected.

For the experiments of section IV.6, as the inner cylinder thermostat hoses were changed, the coolant of the Lauda Proline RP890 was replaced by silicon oil.

The continuous set-up was efficient for the performed experiments, nevertheless, future improvements can be planned, to go towards a more industrial installation.

III.5. Future improvements to plan

To ensure a robust scale-up, the continuous set-up may be improved at various parts.

First of all, the mixing piece should be ‘updated’ towards a more industrial design. Contacts with potential providers were attempted, but the small scale and the low linear velocities were an obstacle.

In the same way, investigations can be carried out regarding the pumping part: peristaltic pumps are useful on a laboratory scale, because of their small size, but they need to be regularly calibrated to avoid drifts.

Regarding the heating part, the optimization touches the used hoses: the ideal set-up would only include specific tubes as the ones presented in Figure III- 17 rather than silicon tubes.

Finally, the main portion that could be improved is the filtration part. In the presented work, it consisted in using a sintered funnel with a vacuum pump. The funnel was changed according to the collection time. To perform a ‘real’ continuous filtration, different device can be explored, such as band filter (sort of filtering “caterpillar track”), continuous filtration carousel (CFC)[9,117] or rotating disk filtration[118].

Chapter IV. Continuous chiral resolution of racemic Ibuprofen

This fourth and final chapter presents the experimental work performed on the chiral resolution of rac-Ibu by *S*-αMBA in batch mode and in continuous mode. The batch work was conducted in parallel of the continuous experiments, to serve the process optimization and the generation of data to compare the two modes.

In the first place, preliminary experiments were performed, to get familiar with the chiral resolution process of rac-Ibu with *S*-αMBA.

It is noteworthy to mention that all temperatures refer to the set temperature of the thermostat.

IV.1. Preliminary experiments

IV.1.1. Batch mode

The set-up of the batch mode experiments is described in Appendix A section A.2.

IV.1.1.1. Chiral resolution process definition

Based on previous work done in the lab, a first process was tried for the chiral resolution of rac-Ibu with *S*-αMBA in ethanol, with the addition of the amine at ambient temperature. This first experiment was stopped during the addition since the product violently precipitated.

A second trial was done, with a heating step preceding the amine addition: no precipitation occurs. This process was retained:

1- Dissolution at 25 °C of 1 equivalent of rac-Ibu in 15.5 V[2] of technical ethanol (i.e. EtOH/H_2O 95/5 w/w, see section II.2.2), which gives a concentration in rac-Ibu of 7.5 %w,

2- Heating to 65 °C (maximum heating rate of the thermostat),

3- Addition of 1 equivalent of *S*-αMBA at 1.5 mL.min^{-1},

4- Hold at 65 °C for 30 min,

5- Cooling down to 20 °C with a rate of 0.5 °C.min^{-1},

6- Filtration of the product on a glass filter of porosity P3 and diameter 20, 40, 60 or 80 mm according to the scale,

7- Drying at 40 °C.

In addition to the definition of the batch process, the effect of temperature cycling on chiral purity was rapidly studied. Indeed, as the continuous CT crystallizer can be considered as a series of micro-stirred tanks, in case of temperature gradient between the two cylinders, the medium undergoes numerous temperature cycles all along the continuous reactor.

IV.1.1.2. Temperature cycling effect on chiral purity

In the first place, an experiment at small scale (0.5 g) was performed, with the process defined in the previous section. At the end of step 5, temperature cycles were implemented,

[2] The number of volumes of solvent is an industrial unit, based on the mass of the main reactant. For 2 g of reactant, 15.5 V of solvent equals 15.5x2 = 31 mL.

following the temperature scheme given in Figure IV- 1. The product was sampled at four different moments, as shown in Figure IV- 1.

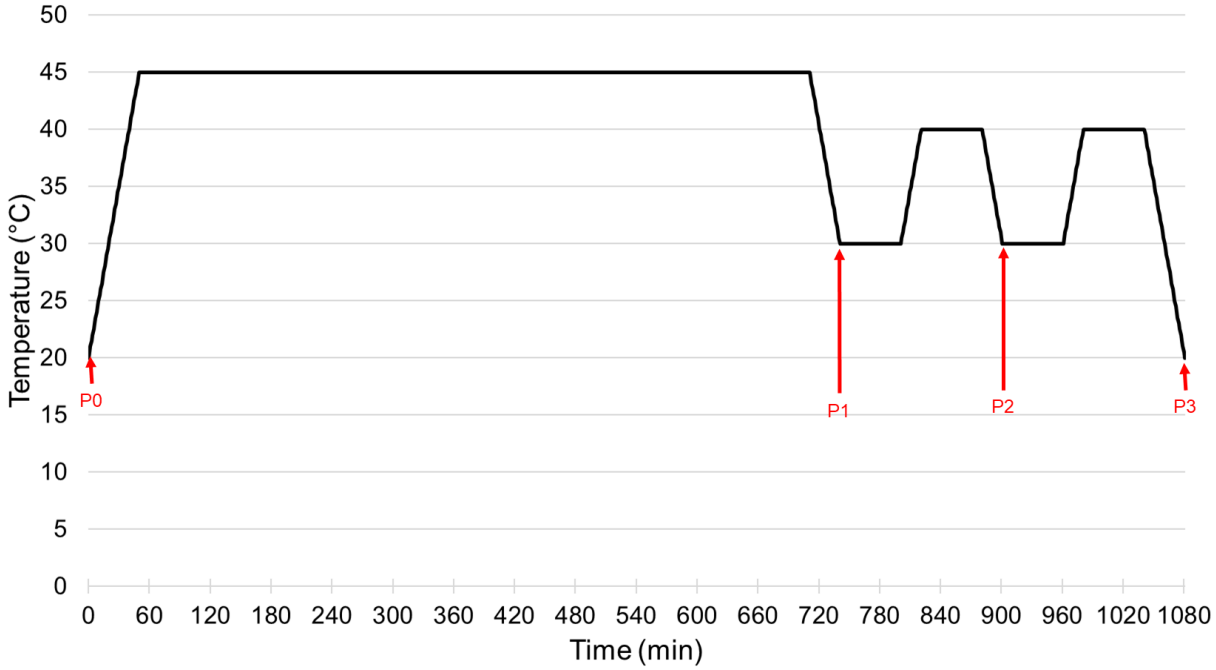

Figure IV- 1: First test of temperature cycling effect on chiral purity of S-Ibu-S-αMBA obtained by chiral resolution of rac-Ibu with S-αMBA (scale: 0.5 g). All rates were of 0.5 °C.min^{-1}. In the first cycle, the temperature of 45 °C was maintained for 11 h. The other hold times were of 1 h. Four samples were taken: P0, before the temperature cycling; P1 after the first temperature cycle; P2 after the second cycle; and P3 after the third and last temperature cycle.

The chiral purity of each sample was determined by chiral HPLC. The results are shown in Table IV- 1.

Sample	P0	P1	P2	P3
Diastereomeric excess (de)	0.67	0.77	0.77	0.76

Table IV- 1: Chiral purity of the four samples of the first test of temperature cycling (scale: 0.5 g).

It clearly appears that the first temperature cycle has an impact on chiral purity, since the diastereomeric excess (Equation II- 2) increased from 0.67 to 0.77. The other temperature cycles did not seem to have a strong effect on chiral purity.

However, to confirm this trend, two other experiments were performed, at a larger scale: 5 g scale for experiment B1 and 10 g scale for experiment B2, respectively with and without temperature cycling. The temperature cycles imposed is shown in Figure IV- 2.

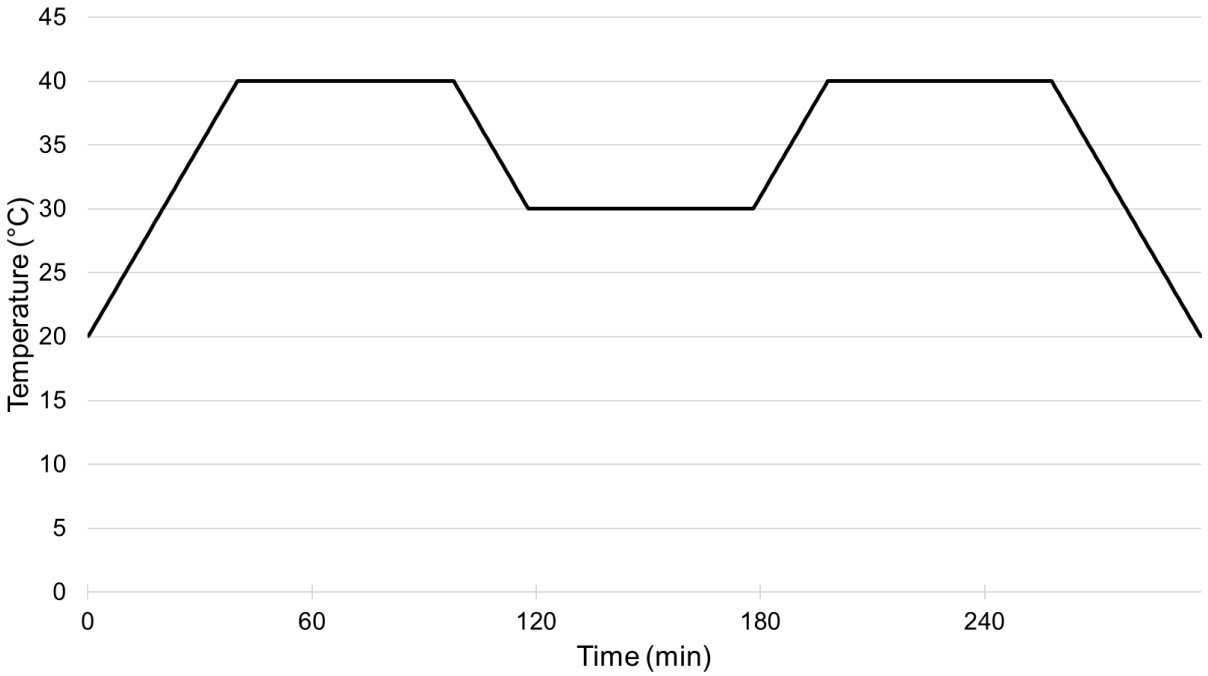

Figure IV- 2: Temperature cycle imposed to the experiment B1 (5 g scale). All rates were of 0.5 °C.min^{-1}, and all hold times of 1 h.

The results of the two trials B1 and B2 can be found in Table IV- 2. The expressions used to calculate the yield and the diastereomeric yield are:

$$Yield = \frac{m_{collected}}{m_{expected}} * 100$$ *Equation IV- 1*

$$Diastereomeric\ yield = \frac{de * m_{collected}}{m_{expected}} * 100$$ *Equation IV- 2*

Experiment	Temperature cycling	Scale (g)	Yield (%)	Diastereomeric excess (de)	Diastereomeric yield (%)
B1	Yes	5	39.1	0.66	26
B2	No	10	41.1	0.60	24.5

Table IV- 2: Results of the experiments B1 and B2 performed to test the effect of temperature cycling.

If the yield is pretty close in both experiments, the benefit of temperature cycling in experiment B1 regarding chiral purity is clear, as well as on the diastereomeric yield.

To conclude from the results of these three experiments, it appeared that a temperature gradient has a positive effect on the chiral purity of the product *S*-Ibu-*S*-αMBA. This is encouraging regarding the implementation of the chiral resolution of rac-Ibu with *S*-αMBA in the continuous CT device.

The results of the first CT experiments are presented hereafter.

IV.1.2. Continuous mode

The chiral resolution of rac-Ibu by *S*-αMBA was experimented in the continuous mode within a Couette-Taylor crystallizer. The unique flow motion of such continuous reactor has been tackled in Chapter I (section I.3.3). The continuous set up used in the presented work was extensively described in Chapter III.

This first series of continuous experiments was performed in technical ethanol (i.e., at azeotropic composition EtOH/H_2O 95/5 w/w) with a rotation speed of 1000 rpm and a residence time of 15 min.

Three experiments were run, with variation of the temperature difference between the two cylinders. Three temperature gradients ΔT were tested: 0 (Run 1), 10 °C (Run 2) and 20 °C (Run 3). The definition of ΔT can be found in Equation IV- 3 with $T1$ the set temperature of the thermostat of the inner cylinder and $T2$ the set temperature of the thermostat of the outer cylinder.

$$\Delta T = T1 - T2 \qquad \textit{Equation IV- 3}$$

Runs 1 and 2 lasted ten residence times and Run 3 nine (encrustation issue at the end of the nineth fraction). The product collected during one residence time correspond to 'one fraction'. Each fraction was collected, weighed, and analyzed by chiral HPLC.

Five indicators were calculated, to evaluate the experiment results:

- Global productivity (g.L^{-1}.min^{-1}): defined in Equation IV- 4, with $m_{collected}$ the mass of the solid recovered from V, the volume of suspension collected during $t_{collection}$, the duration of the fraction collection, i.e., the residence time, here.

$$Global\ productivity = \frac{m_{collected}}{V * t_{collection}} \qquad \textit{Equation IV- 4}$$

- Global yield (%): defined in Equation IV- 1, with $m_{expected}$ the maximum mass of solid that can be recovered from V during $t_{collection}$.
- Diastereomeric excess: defined in Equation II- 1, or Equation II- 2 for the direct calculation from chiral HPLC analysis. This value defines the effectiveness of the process in separating *S*-Ibu-*S*-αMBA and *R*-Ibu-*S*-αMBA.
- Diastereomeric productivity (g.L^{-1}.min^{-1}): defined in Equation IV- 5, with de the diastereomeric excess.

$$Diastereomeric\ productivity = \frac{de * m_{collected}}{V * t_{collection}} \qquad \textit{Equation IV- 5}$$

- Diastereomeric yield (%): defined in Equation IV- 2.

Global productivity and global yield refer to the whole collected product, which include *S*-Ibu-*S*-αMBA and *R*-Ibu-*S*-αMBA. Thus, the diastereomeric productivity and the diastereomeric yield had to be introduced, in order to define the real production in the desired diastereomer. The average results of each experiment are presented in Table IV- 3.

Run	ΔT (°C)	Global productivity ($g.L^{-1}.min^{-1}$)	Global yield (%)	Diastereomeric excess	Diastereomeric productivity ($g.L^{-1}.min^{-1}$)	Diastereomeric yield (%)
1	0	2.322	38.8	0.46	1.062	17.7
2	10	2.382	39.8	0.48	1.149	19.2
3	20	2.166	36.2	0.48	1.048	17.5

Table IV- 3: Averages of the ten fractions of runs 1 and 2, and of the nine fractions of run 3 for: the global productivity, the global yield, the diastereomeric excess, the diastereomeric productivity and the diastereomeric yield.

The yield obtained is almost as good as that obtained in batch mode in the previous section. This conclusion is not surprising: the trend of continuous processes to give lower yield than batch ones was already reported[8,33]. However, as the global productivity seems very good, an interesting solution could be to implement a recycling system of the mother liquors, in a lower domain of temperatures, which has already proven its efficiency regarding yield[15,35,38].

By contrast, the chiral purity is globally really lower than that obtained in batch mode. The reason might be linked to the filtration process which is not specifically adapted to the continuous mode (see Chapter III section III.5).

Actually, the filtration was complicated for the three experiments. Therefore, optical microscopy and SEM analyses were performed, to have an idea of the crystal size and shape. The micrographs are respectively shown in Figure IV- 3 and Figure IV- 4. The obtained crystals appeared to be needle-shaped, which can explain the problematic filtration.

The presence of the temperature gradient has apparently an influence on the crystal size: this is especially evident between Run 1 (ΔT=0 °C) and Run 2 (ΔT=10 °C) on Figure IV- 3 and Figure IV- 4: the size increases when there is a ΔT. It also seems to improve the results presented in Table IV- 3.

However, the temperature gradient of 20 °C is probably too high: productivity and yield decrease (Table IV- 3), and the crystal population seems more heterogeneous.

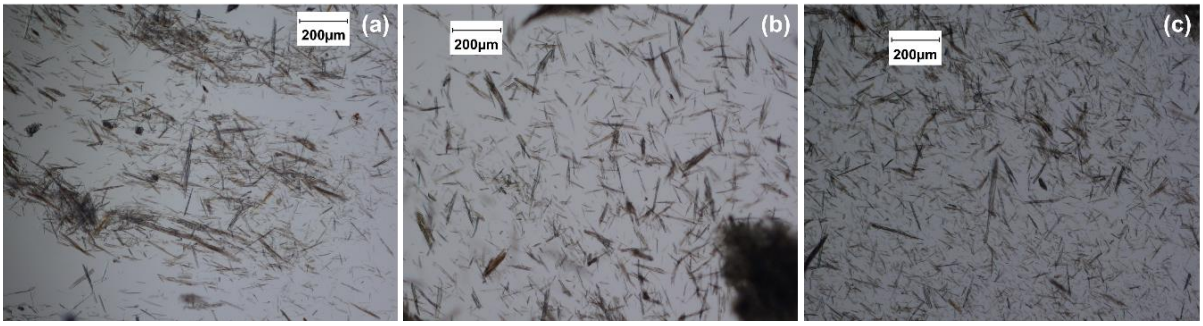

Figure IV- 3: Micrographs of the fraction 9 (i.e., collected after eight residence times, between 120 and 135 min) of (a) run 1, (b) run 2 and (c) run 3, taken by optical microscopy at a magnification of 5.

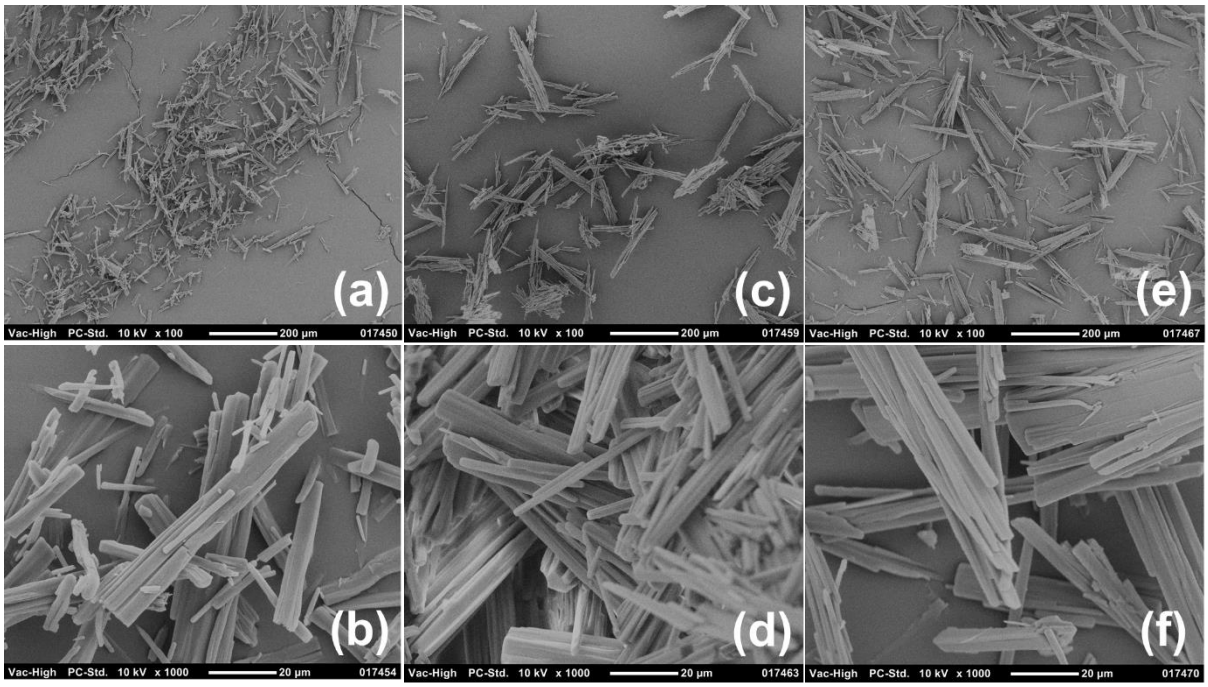

Figure IV- 4: Micrographs of the fifth fraction (i.e., collected after four residence times, between 60 and 75 min) of (a)-(b) run 1, (c)-(d) run 2 and (e)-(f) run 3, taken by SEM at a magnification of 100 for (a)-(c)-(e) and 1000 for (b)-(d)-(f).

Moreover, the product quality and quantity fluctuate along the experiment with $\Delta T = 20$ °C (Figure IV- 7), and the reactor clogged before the end of the test. Such high temperature difference possibly generates strong variations of the local supersaturation, which alters the efficiency of the process.

In the two other runs, the steady state functioning seems to be reached quickly (Figure IV- 5 and Figure IV- 6).

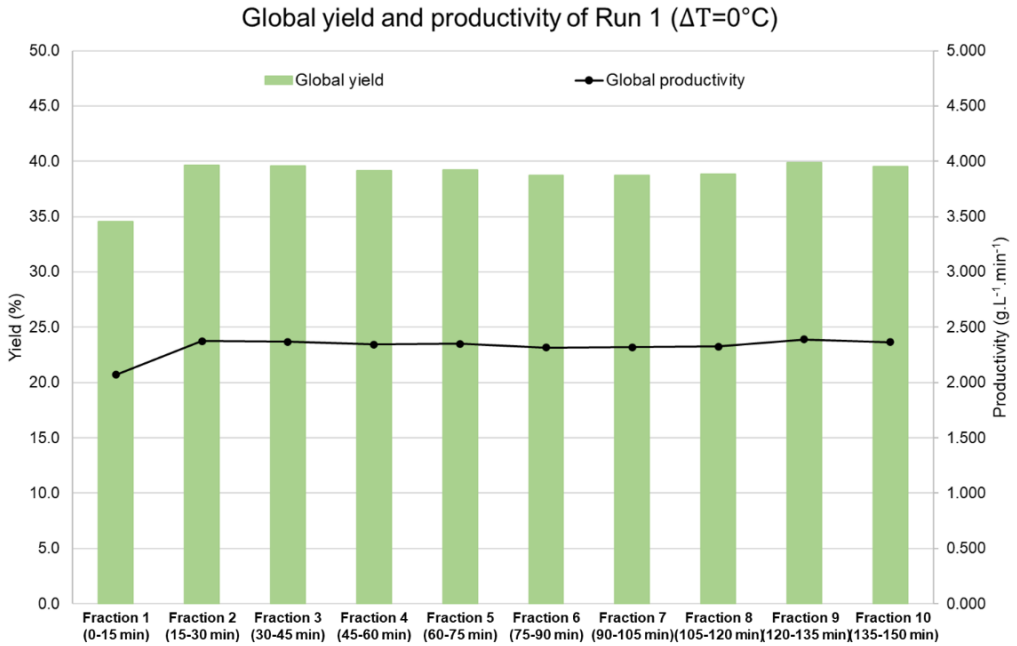

Figure IV- 5: Global yield and productivity of Run 1 for each collected fraction.

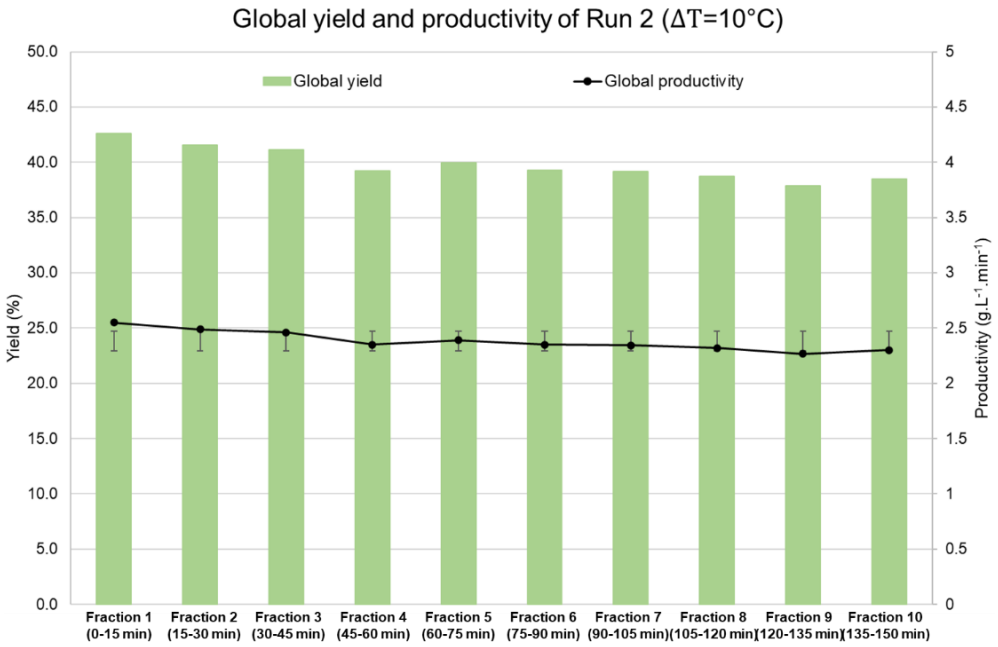

Figure IV- 6: Global yield and productivity of Run 2 for each collected fraction.

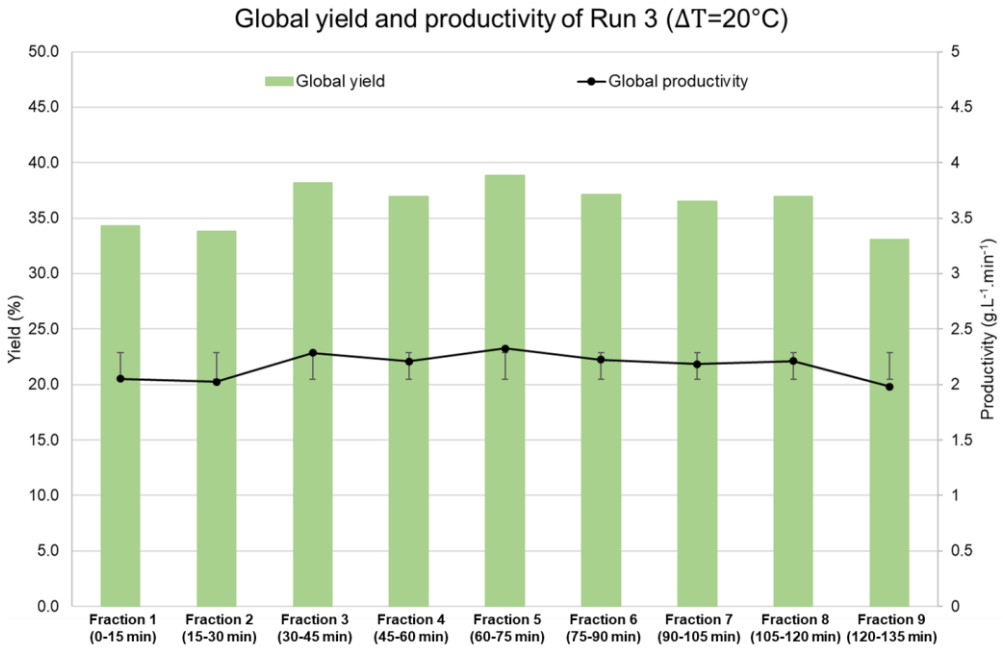

Figure IV- 7: Global yield and productivity of Run 3 for each collected fraction.

To conclude about this first series of continuous experiments, the continuous mode seems applicable to the chiral resolution by diastereomeric salt formation of rac-Ibu by *S*-αMBA. Also, the presence of a temperature gradient appeared to enhance the global and diastereomeric yield and productivity, and a little bit the chiral purity. The impact on the crystal size is clear too. Nevertheless, this positive effect can fade if the temperature difference between the two cylinders is too high.

During these first continuous process experiments, issues were encountered with respect to filtration. Indeed, the recovered crystals was needle-shaped and small, which is not suitable for an effective filtration process. The process was then returned to batch mode study, to be optimized regarding the shape and size of the obtained crystals.

IV.2. Process optimization for crystal shape in batch mode

Since the solubility of the diastereomer *S*-Ibu-*S*-αMBA is not so high in technical ethanol (see solubility measurements in Chapter II section II.2.2), the use of the Pope and Peachey procedure seemed interesting to try[27,28], in order to avoid the obtaining of small acicular crystals.

IV.2.1. Pope and Peachey method

To apply the Pope and Peachey method, the process described in section IV.1.1.1 was modified as followed:

1- Dissolution of 1 equivalent of rac-Ibu in 15.5 V of technical ethanol at 25 °C,
2- Heating to 65 °C (maximum heating rate of the thermostat),
3- Addition of $(1\text{-}x)$ equivalents of *S*-αMBA + x equivalents of NaOH 1 M at 1.5 mL.min^{-1},
4- Hold at 65 °C for 30 min,
5- Cooling down to 20 °C with a rate of 0.5 °C.min^{-1},
6- Filtration of the product on a glass filter of porosity P3 and diameter 20, 40, 60 or 80 mm according to the scale,
7- Drying at 40 °C.

The first trial (experiment B3) gave nice platelet-shaped crystals, larger than those obtained with the previous process (experiment B2 in section IV.1.1.2), as shown in Figure IV- 8.

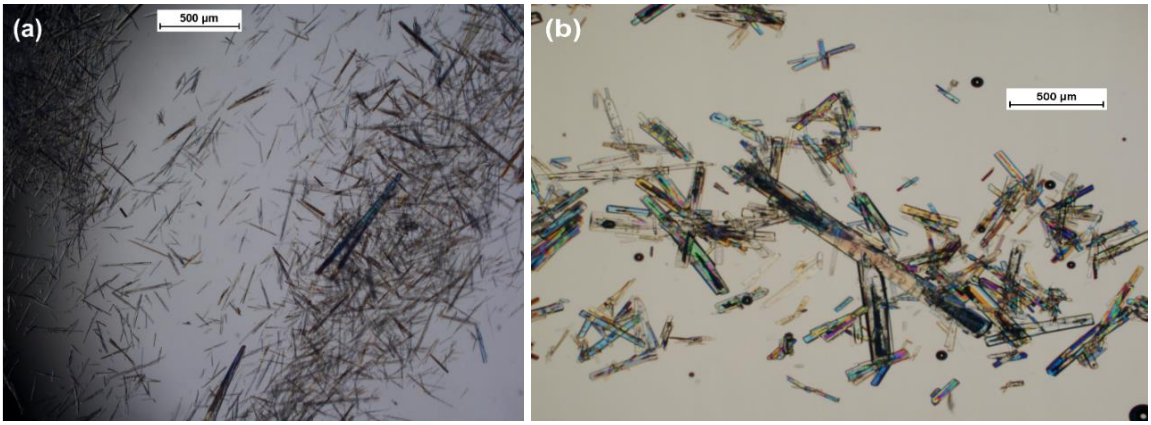

Figure IV- 8: Micrographs of the product obtained (a) from experiment B2 and (b) from experiment B3, taken by optical microscopy at a magnification of 2.5.

The results of this first experiment with Pope and Peachey method are presented in Table IV-4. The diastereomeric excess obtained is similar to that obtained in experiment B1, with temperature cycling (0.65 vs 0.66). However, the yield was lower than that obtained in experiments B1 and B2 (21.1 % vs 39.1 % and 41.1 %). To improve the yield, a study on the impact of the concentration was launched.

Experiment	Scale (g)	Technical EtOH volume (V)	NaOH equivalents	Washing	Yield (%)	Diastereomeric excess	Diastereomeric yield (%)
B3	12	15.5	0.4	No	21.1	0.65	13.8
B4	8	10	0.4	No	32.7	0.58	19.0
B5	25	5	0.4	No	35.3	0.64	22.6
B6a	20	7.5	0.4	No	-	0.49	-
B6b				Yes	-	0.61	-
B6c				Yes (x2)	-	0.61	-
B6d				Yes (x3)	30.3	0.61	18.3
B7	8	7.5	0.5	Yes	28.2	0.51	14.4
B8	20	7.5	0.45	Yes	32.2	0.57	18.3
B9	20	7.5	0.4	Yes	30.9	0.61	18.7
B10	8	7.5	0.4	Yes	29.8	0.60	17.9
B11	20	7.5	0.35	Yes	34.3	0.56	19.3
B12	8	7.5	0.35	Yes	31.9	0.54	17.3
B13	8	7.5	0.33	Yes	33.6	0.61	20.4
B14	8	7.5	0.3	Yes	34.5	0.68	23.4
B15	20	7.5	0.28	Yes	36.0	0.50	17.9
B16	20	7.5	0.25	Yes	39.3	0.58	22.7
B17	8	7.5	0.25	Yes	37.6	0.61	22.8
B18	20	7.5	0.2	Yes	40.3	0.44	17.8
B19	8	7.5	0.1	Yes	47.1	0.21	9.7

Table IV- 4: Results of the batch experiments led in section IV.2.1. Different parameters were modified along the study, in order to optimize the chiral resolution process. Experiments B3 to B5 were done during the dilution optimization (section IV.2.1.1). Experiment B6 was performed to study the influence of the filtration cake washing (section IV.2.1.2). Experiments B7 to B19 were set up to find the optimal number of equivalents of NaOH (section IV.2.1.3).

IV.2.1.1. Dilution optimization

To increase the yield of the process, the medium concentration was tested in experiments B3, B4 and B5, with respective numbers of volumes of technical ethanol of 15.5, 10 and 5 V. An attempt was also made with 2.5 V, but it resulted in a massive precipitation during the addition of the bases at high temperature. The yield, chiral purity and diastereomeric yield obtained are presented in Table IV- 4.

It clearly appears that, as expected, the yield increases with the medium concentration. Nevertheless, in experiment B5 (5 V), nucleation started at 53 °C, which seemed quite high in view of transferring the process to continuous mode. Indeed, to ensure that no crystallization will take place before the CT crystallizer inlet, a safe process considers a spontaneous crystallization below 40 °C (see Chapter III section III.2). Thus, a number of technical EtOH volumes of 7.5 seemed to be a good compromise.

The chiral purity obtained in experiment B4 was surprisingly low. It appeared to be an exceptional value. Diastereomeric excesses achieved in experiments B3 and B5 are similar to previous results of B1 and B2.

The yield and diastereomeric yield remain lower than those obtained in experiments B1 and B2. Nevertheless, this loss can be acceptable since the new crystal morphology and size are more suitable for an efficient filtration process.

XRPD analysis was performed on the products recovered from experiments B3, B4 and B5. The overlay can be found in Figure IV- 9, including a comparison with the references.

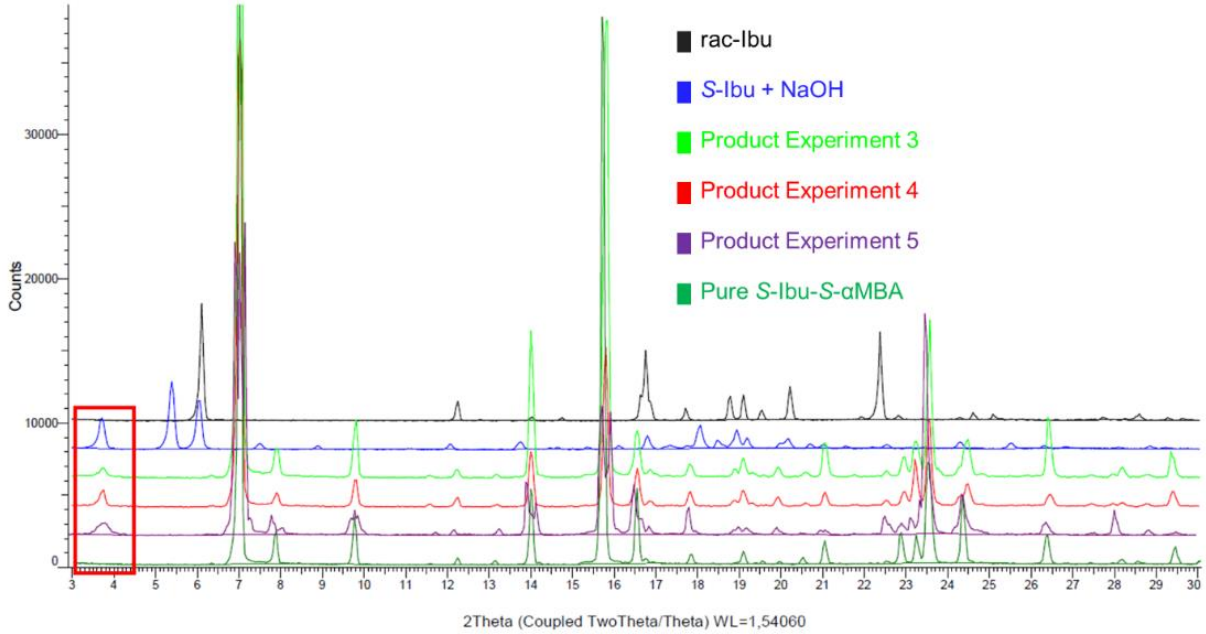

Figure IV- 9: XRPD overlay of the diffractograms of (from top to bottom): the racemic Ibuprofen (black), the product made by recrystallizing pure S-Ibu with NaOH (blue), the product of experiment B3 (light green), the product of experiment B4 (red), the product of experiment B5 (purple) and the pure S-Ibu-S-αMBA (dark green).

On the XRPD overlay, an impurity is clearly observable at 3.75 °2θ, including on the diffractogram of the product of the recrystallization of pure *S*-Ibu with soda (blue). In view of eliminating this impurity, a cake washing study was considered.

IV.2.1.2. Cake washing study

Experiment B6 was carried out to study the influence of washing the filtration cake on the impurity observed at 3.75 °2θ. As water seems to be a good antisolvent for the diastereomer, washings with 2 V of distilled water were tested.

The product of experiment B6 was sampled before any washing (B6a), after one washing (B6b), two washings (B6c) and three washings (B6d).

The results are presented in Table IV- 4, and the XRPD diffractograms of the four samples can be found in Figure IV- 10.

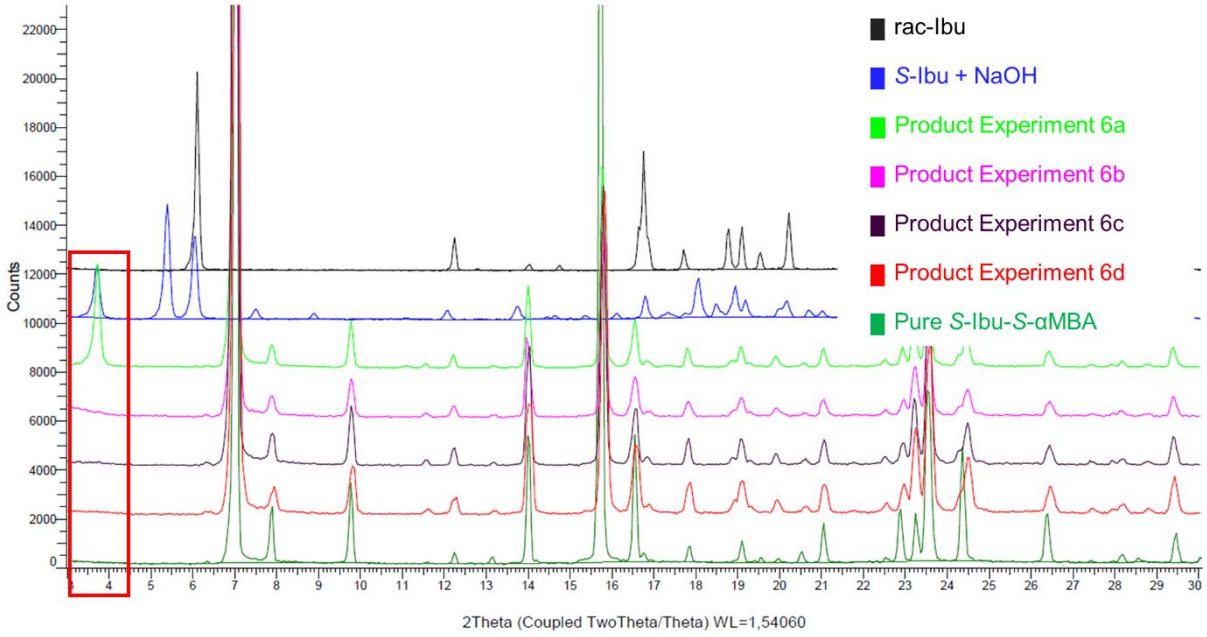

Figure IV- 10: XRPD overlay of the diffractograms of (from top to bottom): the racemic Ibuprofen (black), the product made by recrystallizing pure S-Ibu with NaOH (blue), the sample B6a, made before the washings on the product of experiment B6 (light green), the sample B6b, made after one washing with 2 V of water (pink), the sample B6c, made after two washings (dark purple), the sample B6d, made after three washings (red) and the pure S-Ibu-S-αMBA (dark green).

The effect of the washings on the impurity is evident: it is totally removed after the first washing with 2 V of water. Also, it seems that the chiral purity is enhanced thanks to the first washing (see Table IV- 4).

To conclude, if the implementation of a washing step can induce a small decrease of the yield, the benefits regarding the structural purity and the diastereomeric excess are clear. Therefore, one washing step was added to the chiral resolution process with the Pope and Peachey method.

The next step of the process optimization was focused on the number of equivalents of soda.

IV.2.1.3. NaOH number of equivalents

Different numbers of equivalents of NaOH were tested in experiments 7 to 19 (Table IV-4).

The first striking impact regards the yield: when the amount of soda increases, the yield decreases. However, below 0.25 eq., nucleation starts at a temperature higher than 40 °C, therefore, the process is not considered as transferrable to continuous mode (see Chapter III section III.2.2).

Regarding chiral purity, a maximum seems reached for 0.3 eq. To conclude, 0.3 eq. appeared to be the optimum amount of soda to maximize the yield with a good chiral purity.

Also, the repeatability of the process was tested with experiments B9, B10, B11, B12, B16 and B17. The results are consistent; thus, the process is repeatable.

The different parameters studied led to an optimized chiral resolution process, with the Pope and Peachey procedure. However, during this process optimization, some specific defects were detected in the crystals: fluid inclusions (Figure IV- 11).

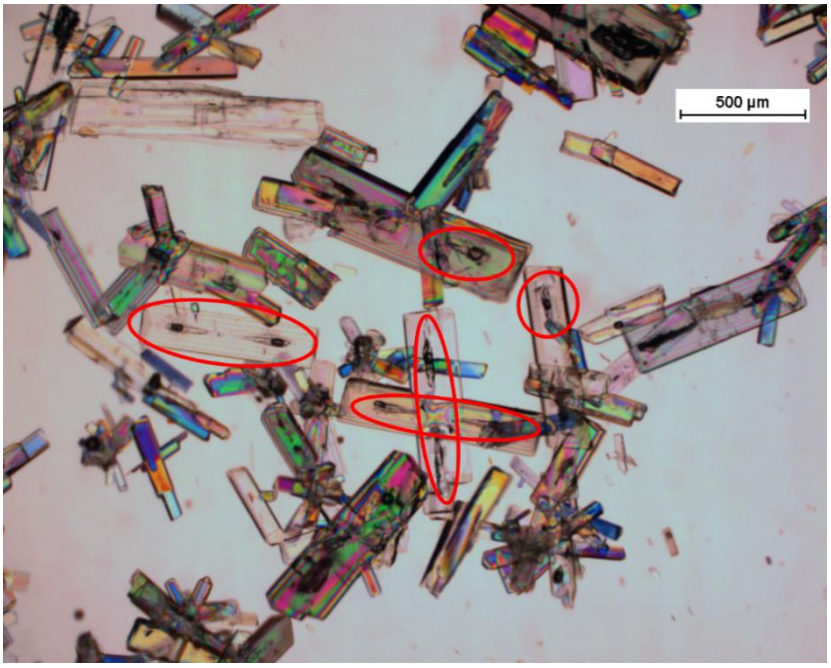

Figure IV- 11: Micrograph of the product obtained in experiment B14 taken by optical microscopy at a magnification of 2.5. Some fluid inclusions are encircled in red.

The study of these fluid inclusions was addressed in Chapter II. The inclusions encountered in crystals of *S*-Ibu-*S*-αMBA contain the process mother liquors, and also sometimes a bubble of gas. The presence of the mother liquors within the crystals can be dramatic regarding chiral purity. Nevertheless, it has been observed that without soda and with a vigorous stirring, fluid inclusions can be avoided. In addition, it appeared that the nice platelet morphology was not due to soda, but to water.

In view of the above conclusions, the chiral resolution process needed to be modified. Soda was no longer used, but it seemed necessary to add water to technical ethanol in order to obtain the nice platelet-shaped crystals. To optimize the process, the EtOH/H_2O ratio required an investigation.

IV.2.2. Optimization of the process with water and without soda

In the first place, the water mass fraction of the previous experiments was calculated, to have a first evaluation. Results can be found in Table IV- 5.

Experiment	Water mass fraction	Experiment	Water mass fraction
B3	0.13	B12	0.22
B4	0.19	B13	0.21
B5	0.33	B14	0.20
B6	0.25	B15	0.18
B7	0.29	B16	0.17
B8	0.26	B17	0.17
B9	0.24	B18	0.14
B10	0.24	B19	0.08
B11	0.22		

Table IV- 5: Calculation of the water mass fraction of experiments B3 to B19.

Regarding these results, the following water mass fractions were tested: 0.17, 0.21, 0.22, 0.24, 0.27, 0.28, 0.29, 0.33, 0.38. Experiments B20 to B31 were performed, including repetitions, to test the repeatability of the process, following this updated procedure:

1- Dissolution of 1 equivalent of rac-Ibu in 7.5 V of technical ethanol ((1-x) %w) at 25 °C,
2- Heating to 65 °C (maximum heating rate of the thermostat),
3- Addition of 1 equivalent of *S*-αMBA + x %w water at 1.5 mL.min^{-1},
4- Hold at 65 °C for 30 min,
5- Cooling down to 20 °C with a rate of 0.5 °C.min^{-1},
6- Filtration of the product on a glass filter of porosity P3 and diameter 20, 40, 60 or 80 mm according to the scale,
7- Cake washing with 2 V of distilled water,
8- Drying at 40 °C.

As expected, the obtained product exhibited a nice platelet habit, as shown in Figure IV- 12.

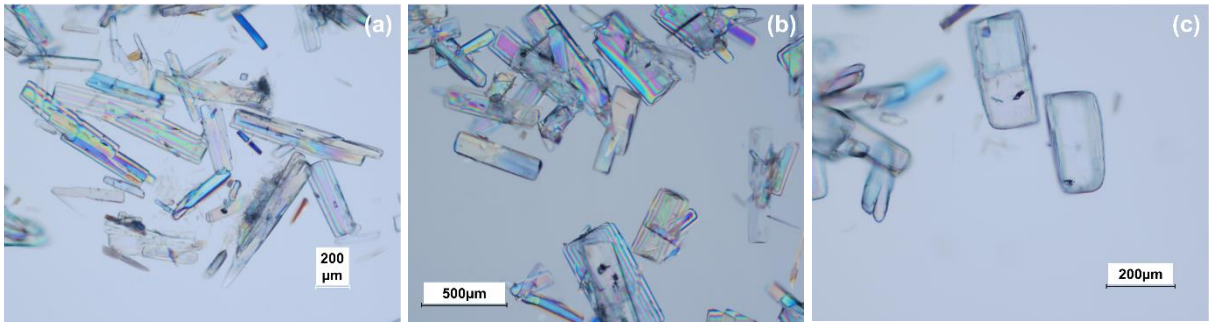

Figure IV- 12: Micrograph of the product obtained in experiment (a) B22, (b) B29 and (c) B31, taken by optical microscopy at a magnification of 5.

The results of experiments B20 to B31 are presented in Table IV- 6.

Experiment	Scale (g)	Water mass fraction	Yield (%)	Diastereomeric excess	Diastereomeric yield (%)
B20	1.5	0.17	43.4	0.65	28.0
B21	1.5	0.21	45.5	0.62	28.0
B22	20	0.22	48.8	0.52	25.3
B23	1.5	0.24	43.9	0.67	29.4
B24	1.5	0.24	42.9	0.70	29.9
B25	1.5	0.27	47.8	0.59	28.1
B26	1.5	0.27	42.9	0.67	28.6
B27	20	0.28	44.8	0.50	22.5
B28	20	0.29	58.5	0.35	20.6
B29	8	0.33	41.5	0.61	25.4
B30	8	0.33	52.6	0.46	24.1
B31	8	0.38	34.2	0.49	16.8

Table IV- 6: Results of experiments B20 to B31, studying the influence of the water mass fraction on the yield, diastereomeric excess and diastereomeric yield.

The yield and chiral purity were represented as a function of the water mass fraction in Figure IV- 13.

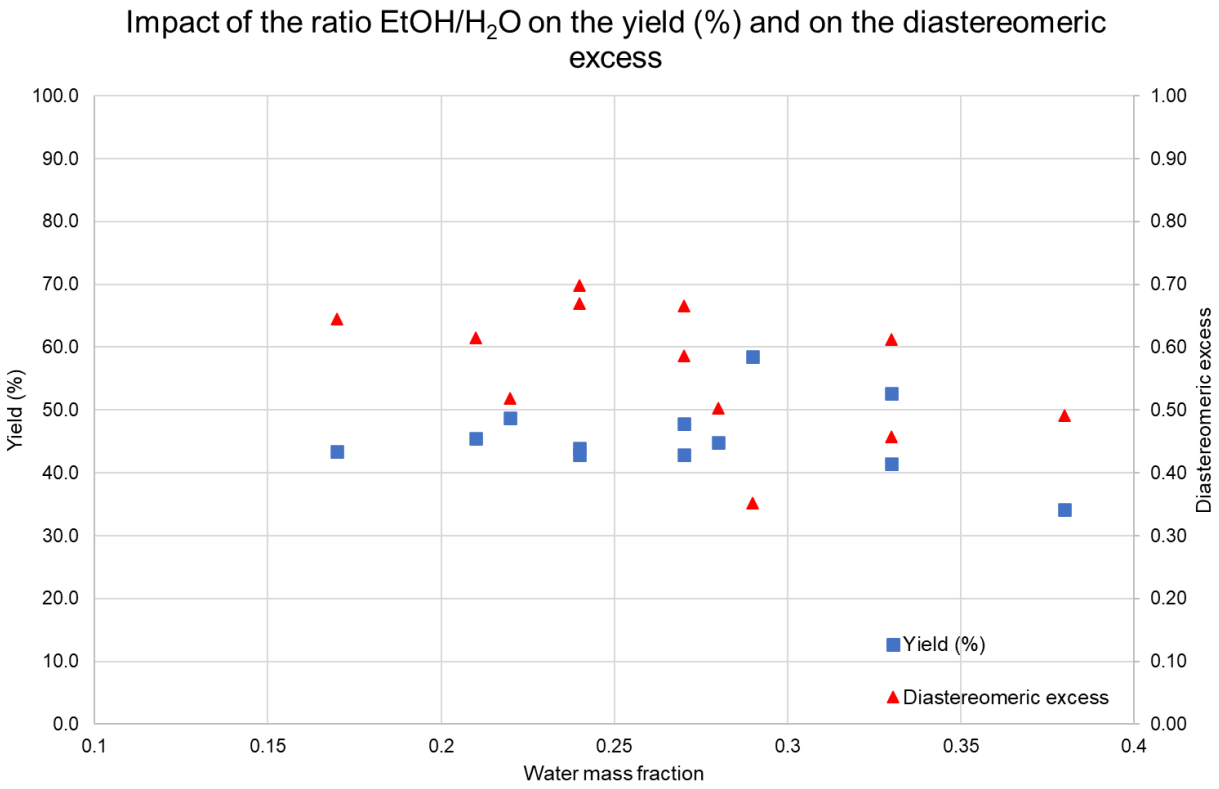

Figure IV- 13: Representation of the yield and diastereomeric excess obtained in the experiments B20 to B31 as a function of the water mass fraction.

The results are dispersed, and no trend can be drawn. The elimination of the fluid inclusions does not seem to significantly increase the chiral purity. Nevertheless, the best diastereomeric purity and yield are achieved with a water mass ratio of 0.24. Therefore, it is the solvent ratio that was implemented in the first screening of continuous chiral resolution of *S*-Ibu with *S*-αMBA (see section IV.4). As shown in Table II- 2, it corresponds to a mass fraction [technical EtOH]/H_2O of 80/20.

Since many parameters can impact a continuous process, this next series of continuous experiments, performed with a solvent ratio EtOH/H_2O of 76/24 w/w, was rationalized with a Design of Experiments (DoE) approach[84]. Such methodology serves to obtain a robust operating point, and levers for further process optimization. The next section describes the philosophy around the construction of the DoE, to study the continuous chiral resolution of rac-Ibu by diastereomeric salt formation with *S*-αMBA.

IV.3. Rationalization of the continuous study through a DoE approach

IV.3.1. Principle

The principle of a DoE is to study simultaneously the impact of different factors on (a) response(s). The selection of the factors to study must be carefully thought: they must be accurately controlled and independent one to each other. In the DoE approach, the correct definition of the study (factors, responses, studied range…) is essential[119].

The questions and the hypotheses are converted into a mathematical model. This can typically be shaped into a polynomial model, such as the following one, which considers three factors, X_1, X_2 and X_3, with two levels[119,120]:

$$Y = b_0 + b_1X_1 + b_2X_2 + b_3X_3 + b_{1.2}X_1X_2 + b_{1.3}X_1X_3 + b_{2.3}X_2X_3 + b_{1.1}X_1^2 + b_{2.2}X_2^2 + b_{3.3}X_3{}^2$$

Equation IV- 6

In Equation IV- 6, Y is the response and the 'b' values are the estimated coefficients: b_0 is the constant (or intercept), b_i represent the principal effect of the factor X_i, $b_{i.j}$ correspond to the interaction effect between X_i and X_j, and $b_{i,i}$ characterize the quadratic (or curvature) effect of X_i.

The first choice to make is the DoE family to implement, according to the study conditions previously defined: screening, quantitative study of factors, response surface methodology or mixture design.

Here, the screening design seems the most suitable one to begin with. Indeed, it is recommended to identify the active factors[120]. In such design, the model is stated as linear, and only the principal estimated coefficient b_i of Equation IV- 6 are considered.

Once the factors identified as the most impacting ones are selected, the levels of each factors should be selected, in agreement with the selected DoE design. The level choice is a critical step in the DoE construction: they must be sufficiently distinct and not too close to each other to obtain significantly different and informative results.

After the selection of the factors and their levels, the matrix of experiments can be constructed. In this matrix, each experiment represents a unique combination of the different levels of each factor. This step partially determines the robustness of the DoE.

Based on the built matrix of experiments, the experimental part can be performed. It is noteworthy to mention that to avoid the time effects, the experiments should be randomly performed[120]. The matrix of experiments can evolve during the study, according to the obtained results, for example, in case of the identification of a factor level as a process abortion cause.

The responses to study should be adapted to the study objectives. Their statistical analysis and interpretation serve the evaluation of each factor's model, and, in the case of the screening design, the identification of the most impacting factor(s).

IV.3.2. Application to the present work

In continuous crystallization, many process conditions can have an impact on the product characteristics (yield, chiral purity…). In the present continuous work, seven parameters have been identified as potential DoE factors. They deal with the features offered by the CT crystallizer (parameters 1, 2, 3 and 5), with the continuous mode (parameter 4) and with the crystallization process (parameters 6 and 7):

(1) Absolute temperature difference between the two cylinders $|\Delta T|$, with $|\Delta T| = |T1 - T2|$,

(2) Sign of ΔT, i.e., which cylinder is the cold part when the other is the hot one,

(3) Rotation speed Ω,

(4) Residence time t, i.e., flowrate,

(5) Reference temperature T_{ref}, i.e., target temperature within the CT crystallizer, with $T_{ref} = \frac{T1+T2}{2}$,

(6) Supersaturation β,

(7) Solvent mass ratio EtOH/H_2O.

Since the screening design seems the most suitable one, this is not in agreement with the study of the seven factors. The factors suspected as the most impacting ones should be selected, as well as their levels.

The DoE matrix of experiments can then be built with the 'Screening' tool of Azurad software (see Appendix A section A.10). By using an exchange algorithm, a D-optimal matrix of with minimal inflation factors on the model coefficient can be established.

In this continuous study, five responses have been considered to study the influence of the factors on the product features:

- Global productivity ($g.L^{-1}.min^{-1}$),
- Global yield (%),
- Diastereomeric excess,
- Diastereomeric productivity ($g.L^{-1}.min^{-1}$),
- Diastereomeric yield (%).

The expression of each studied response can be respectively found in Equation IV- 4, Equation IV- 1, Equation II- 1, Equation IV- 5 and Equation IV- 2.

The different responses can be processed within the 'Screening' tool of Azurad software, which can assess a 'weight' of impact for every investigated factor, and a first outline of their best level(s). Eventually, the screening study can lead to the definition of a first operating point, and of the optimization levers for further development.

It is noteworthy to mention that during the statistical analysis of a response, the results of certain experiment(s) can be estimated as aberrant *for this response processing*, typically through the analysis of the residues. The discarding of this deviant experiment for one response does not imply that it has to be discarded for the others, if this is not justified. Azurad software allows the user to deselect one experiment for a given response, without affecting the other responses.

The statistical analysis and interpretation plots from Azurad can be used to evaluate the reliability of each factor's model and to determine the most impacting parameter(s) and their preferential set-up regarding each response.

For the individual factor effect evaluation:

- Pareto plots and the total effect plot,
- p-values of t test on coefficient.

For the model reliability:

- correlation coefficient R^2 of the model: the closer it is to 1, the better is the adjustment of the model to the experimental observations.
- p-value of F test on regression: the lower it is, the more significant is the chosen model.
- p-value of F test on lack of fit: the higher the better; a low value for the lack of fit means that that chosen model cannot explain all the experimental observations.

In some cases, with screening design, the simplified model selected may not be significant while some coefficient effects are. Sometimes even, the effects of the factors do not appear to be statistically significant, but Pareto analysis shows that one factor is responsible for most of the variability observed. This can happen if important interaction effects exist.

After this brief introduction about the DoE rationalization of the study of the continuous chiral resolution of rac-Ibu with *S*-αMBA, the implementation, the results and the interpretation of the first screening performed in continuous mode are described in the next section.

IV.4. First screening in continuous mode

This series of continuous experiments was performed using the process developed in section IV.2.2, with a solvent ratio EtOH/H_2O of 76/24 w/w (i.e., [technical EtOH]/H_2O 80/20 w/w).

The two first experiments were realized with a solvent mixture amount of 7.5 V, but this dilution was too low, and the reactor clogged after less than 2 residence times t (10 min). It was then decided to divide by two the medium concentration. Therefore, to avoid any fouling, the medium was diluted in 15 V of EtOH/H_2O 76/24 w/w, which is equivalent to a diastereomer concentration within the CT crystallizer between 0.109 and 0.111 $g_{diastereomer}/g_{saturated\ solution}$ (according to the average temperature inside the reactor).

IV.4.1. Set-up of the Design of Experiments (DoE)

In the first place, the factors of this first screening must be chosen, among the seven presented in section IV.3.2. The parameters assessed to be the most impacting ones are those related to the CT crystallizer and to the continuous mode, i.e., parameters 1 to 5. Parameters 1 and 2 have been gathered as one factor, which finally gives a screening of four factors:

(1)(2) Temperature difference between the two cylinders ΔT, with $\Delta T = T1 - T2$,

(3) Rotation speed Ω,

(4) Residence time t, i.e., flowrate,

(5) Reference temperature T_{ref}, i.e., target temperature within the CT crystallizer, with $T_{ref} = \frac{T1+T2}{2}$.

Three levels were then chosen for each of the four factors.

IV.4.1.1. Choice of the factor levels

Temperature difference between the two cylinders ΔT (°C)

This factor gathers the parameters 1 (absolute temperature difference |ΔT|) and 2 (sign of ΔT) identified in section IV.3.2. It can be defined as the subtraction presented in Equation IV- 7, with T1 the set temperature of the thermostat of the inner cylinder and T2 the set temperature of the thermostat of the outer cylinder.

$$\Delta T = T1 - T2 \qquad \textit{Equation IV- 7}$$

Since the two cylinders are temperature-controlled independently, the temperature gradient direction can be inverted, in other words, each cylinder can be the hot one or the cold one. This is given by the sign of ΔT: sign '-' refers to the inner cylinder being the cold part and the outer cylinder being the hot one; sign '+'refers to the reverse situation. This aspect of the factor is important, as it has already been reported as impacting the product features[62].

Eventually the three chosen levels were: -10 °C; 0 °C; +10 °C.

The investigation of this 3-level factor will confirm the potential advantage of applying a temperature gradient within the CT crystallizer, as already suspected in the preliminary CT

experiments (section IV.1.2). If it is validated, it should also indicate the best gradient orientation.

Rotation speed Ω (rpm)

Before choosing the three levels of the rotation speed factor, the critical rotation speed must be determined.

As described in Chapter I (section I.3.3.3), it can be calculated from Equation I- 1, by substituting the Taylor number Ta by the critical Taylor number Ta^*_c, retrieved from Equation I- 2. The two equations are reminded hereafter:

$$Ta = \frac{\Omega_i^2 r_i d^3}{\nu^2} \qquad \textit{Equation I- 1}$$

$$Ta^*_c = Ta^*_c(Re_z = 0) + 26.5 Re_z{}^2 \qquad \textit{Equation I- 2}$$

In Equation I- 2, the critical Taylor number without an axial flow, $Ta^*_c(Re_z=0)$, can be found in the literature, according to the CT reactor geometry and to which cylinder can rotate. Re_z, the axial Reynolds number, can be calculated using Equation I- 3:

$$\mathrm{Re}_z = \frac{dV_m}{\upsilon} \qquad \textit{Equation I- 3}$$

The system geometry can be characterized by the ratio $\frac{d}{r_i}$, or by the radius ratio $\eta_r = \frac{r_i}{r_o}$, with r_i the inner cylinder radius and r_o that of the outer cylinder[45,56].

The parameter μ indicate the rotating cylinder(s): $\mu = \frac{\Omega_o}{\Omega_i}$, with Ω_o the rotation speed of the outer cylinder, and Ω_i that of the inner cylinder[45]. In the used CT crystallizer, the inner cylinder can rotate, while the outer is at rest, therefore: $\mu = 0$.

As indicated in Chapter III (section III.1), r_i = 19.5 mm and r_o = 23.4 mm, which gives η_r = 0.83. According to the work of Donnelly and Schwarz (1965)[53], these characteristics give a critical Taylor number of 1902. This number is the critical Taylor number without an axial flow, $Ta^*_c(Re_z=0)$; the correction given by Equation I- 2 must be applied.

Re_z (Equation I- 3) can be calculated with the following data: d = 4 mm and ν = 2.55 mm².s^{-1}. The mean axial linear velocity Vm (m.s^{-1}) depends on the studied residence time. Three residence times are investigated (see next section), 5, 15 and 30 min. The corresponding linear velocities are: 1.67x10^{-7}, 5.56x10^{-8} and 2.78 x10^{-8} m^3.s^{-1}, which respectively gives $Ta^*_c(Re_z=0)$ = 1928, 1905 and 1903. It appears that the correction proposed by Maron and Cohen (1991) is negligible, even for short residence times.

Afterwards, the critical rotation speed and the rotation speed range of each CT flow regime (presented in Chapter I, section I.3.3.4) were calculated. According to the residence time (5, 15 or 30 min) the boundaries of the rotation speed ranges differ from 1 to 5 units; the values displayed in Table IV- 7 are those for a residence time of 15 min.

Ta/Ta^*_c	Flow regime	Rotation speed range (rpm)
Ta/Ta^*_c <1	Laminar Couette flow	Ω < 31
1< Ta/Ta^*_c <9	Laminar periodic Taylor vortex flow	31 < Ω < 94
9< Ta/Ta^*_c <176.89	Singly periodic wavy vortex flow ↳ **To study with 200 rpm**	94 < Ω < 416
176.89< Ta/Ta^*_c <324	Doubly periodic wavy vortex flow ↳ **To study with 500 rpm**	416 < Ω < 563
324< Ta/Ta^*_c <1089	Weakly turbulent wavy vortex flow ↳ **To study with 1000 rpm**	563 < Ω < 1032
1089< Ta/Ta^*_c <25600	Turbulent vortex flow	1032 < Ω < 5003
25600< Ta/Ta^*_c	Turbulent aperiodic flow	5003 < Ω

Table IV- 7: Taylor number and rotation speed ranges of each flow regime encountered in the used CT crystallizer for a residence time of 15 min. Among the mentioned flow regimes, three will be studied: the singly periodic wavy vortex flow (Ω = 200 rpm), the doubly periodic wavy vortex flow (Ω = 500 rpm) and the weakly turbulent wavy vortex flow (Ω = 1000 rpm).

Finally, three flow regimes were chosen to be studied with rotation speeds of: 200 rpm, 500 rpm and 1000 rpm. These values are the three levels of the factor rotation speed.

Residence time t (min)

To select relevant values for the levels of the factor residence time, the literature was investigated. It seems that residence time in CT crystallizers typically ranges between 1 min to 60 min[57]. Considering the technical feasibility aspects, it has been chosen to study: 5 min, 15 min and 30 min.

Reference temperature T_{ref}, or target temperature within the CT crystallizer (°C)

In the continuous set-up, extensively described in Chapter III, the CT reactor's temperatures are monitored directly by the thermostats of the two cylinders. Though, the average temperature inside the continuous crystallizer impacts the results, but it cannot be monitored directly, which is a problem to set it as a DoE factor (see section IV.3.1). Consequently, to study different temperatures of crystallization, a reference temperature T_{ref} has to be introduced, related to the set temperature of each cylinder's thermostat. Its expression is given in Equation IV- 8, with $T1$ the set temperature of the inner cylinder thermostat and $T2$ the set temperature of the outer cylinder thermostat:

$$T_{ref} = \frac{T1 + T2}{2} \qquad \textit{Equation IV- 8}$$

In this manner, as $T1$ and $T2$ can be precisely monitored, T_{ref} can be used as the factor related to the average temperature wanted within the CT crystallizer. Thereby, T_{ref} and ΔT are two independent factors, imposing the set temperatures of each cylinder's thermostat $T1$ and $T2$.

The processes used in batch mode all included a cooling step to 20 °C. In this first screening, it has been decided to experiment the same value, one higher value and one lower

value. Thus, the effect of the increase and of the decrease of the final temperature could be studied. Finally, the selected values of T_{ref} were: 15, 20 and 25 °C.

The summary of the investigated factors and levels can be found in Table IV- 8.

X	Name of the factor	Level	Value of the level
X1	Temperature difference ΔT (°C)	0	-10
		1	0
		2	+10
X2	Rotation speed Ω (rpm)	0	200
		1	500
		2	1000
X3	Residence time t (min)	0	5
		1	15
		2	30
X4	Temperature inside the CT crystallizer T_{ref} (°C)	0	15
		1	20
		2	25

Table IV- 8: Factors and levels of the first screening on the continuous chiral resolution by diastereomeric salt formation of rac-Ibu with S-αMBA.

After the selection of the three levels of the four factors of this first screening, the corresponding matrix of experiments needs to be constructed.

IV.4.1.2. Construction of the matrix of experiments

The DoE matrix of experiments was built with the 'Screening' tool of Azurad software. By using an exchange algorithm, a D-optimal matrix of 10 experiments was chosen with minimal inflation factors on the model coefficient (experiments 1 to 10 in Table IV- 9).

The analysis of these ten first experiments led to the implementation of 4 more experiments (including 2 repetitions). The full matrix of experiments and its corresponding experimentation plan can be found in Table IV- 9.

Experiment	Repetition	Matrix of experiments				Experimentation plan			
		X1	*X2*	*X3*	*X4*	*ΔT (°C)*	*Ω (rpm)*	*t (min)*	T_{ref} *(°C)*
1	2	2	0	0	0	10	200	5	15
2	1	0	2	2	0	-10	1000	30	15
3	1	0	1	0	1	-10	500	5	20
4	1	1	1	1	0	0	500	15	15
5	2	2	2	1	1	10	1000	15	20
6	1	1	0	2	1	0	200	30	20
7	1	0	0	1	2	-10	200	15	25
8	1	1	2	0	2	0	1000	5	25
9	1	2	1	2	2	10	500	30	25
10	1	2	2	2	2	10	1000	30	25
11	2	0	2	1	2	-10	1000	15	25
12	2	1	2	0	0	0	1000	5	15
13	1	0	2	0	0	-10	1000	5	15
14	1	2	2	0	0	10	1000	5	15

Table IV- 9: First screening matrix of experiments and its corresponding experimentation plan, constructed with the 'Screening' tool of the software Azurad. Experiments 1 to 10 are part of the initial DoE construction. Experiments 11 to 14 were performed after the analysis of experiments 1 to 10.

To complete the design of this first screening, the last step was the finalization of the experimental procedure, regarding the number of residence times that should last the experiments, and the fraction collection.

IV.4.1.3. Experimental procedure finalization

Since the steady state seems to be reached quickly within the CT crystallizer (see section IV.1.2), the experiments were decided to last 10 residence times; also, the analysis of each fraction (product recovered in 1 residence time) does not seem necessary.

If each one of the ten fractions was collected and weighed, only fractions 3 (2 to 3 residence times), 5 (4 to 5 residence times) and 8 (7 to 8 residence times) were analyzed, by chiral HPLC and XRPD.

The results of the first screening on the continuous chiral resolution by diastereomeric salt formation of rac-Ibu with *S*-αMBA are presented and discussed in the next section.

IV.4.2. Results of the first screening and discussion

Surprisingly, the yield distribution of the 10 collected fractions was not as constant as expected. This will be discussed in section IV.4.3. However, since the yield distribution patterns on repeated trials are very similar, this did not appear to be due to experimental error in the

execution of samplings or analyses. Therefore, it was decided to analyze the average of the results of fractions 3, 5 and 8 for each response.

The results of each experiments are displayed in Table IV- 10: the average of the 'global' responses was calculated with all the fractions, while that of the 'diastereomeric' results was determined with the fractions analyzed by chiral HPLC, i.e., fractions 3, 5 and 8.

As mentioned before, XRPD analysis was also performed on fractions 3, 5 and 8. All the analyzed samples exhibited the correct solid phase. As an example, Figure IV- 14 shows the diffractograms of fractions 3, 5 and 8 of experiment 2, compared with rac-Ibu, pure *S*-Ibu-*S*-αMBA and with the calculated diffractogram (obtained from the published data at 173 K of Lemmerer[83]).

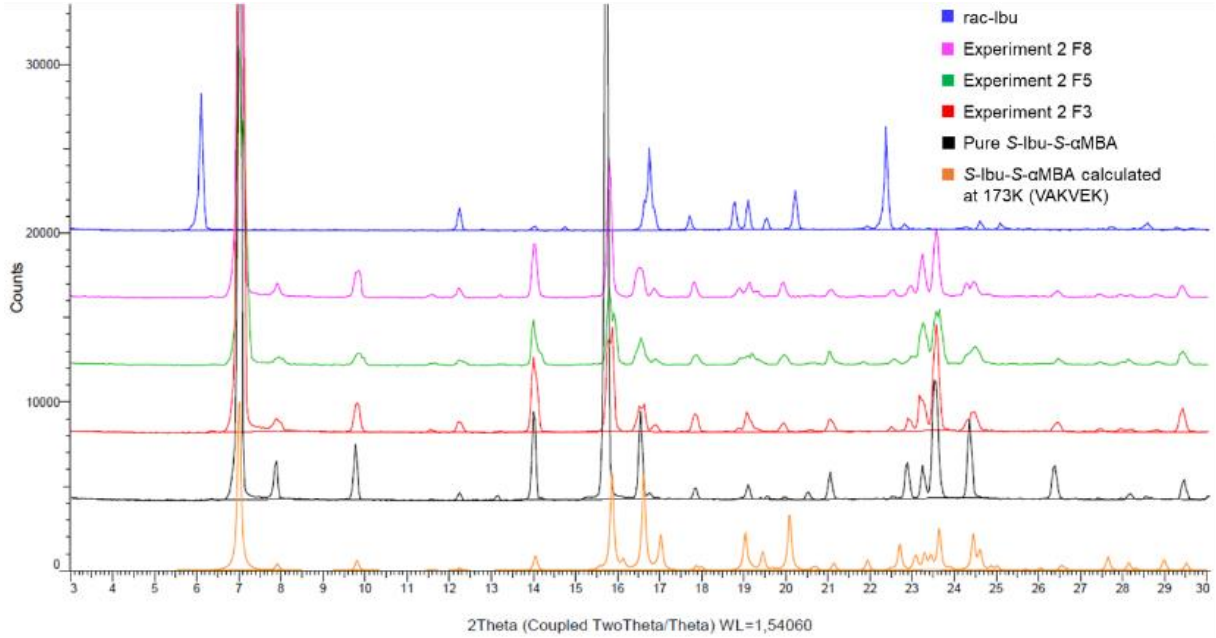

Figure IV- 14: XRPD overlay of fractions 3, 5 and 8 of experiment 2, compared with rac-Ibu, pure S-Ibu-S-αMBA and with the calculated diffractogram obtained from the published structure VAKVEK[83].

The products obtained from chiral resolution exhibit small peak shifts compared with the pure material collected at room temperature. They are due to the presence of a partial solid solution enriched in *S*-Ibu-*S*-αMBA (see section II.3.1).

The results of the five studied responses were processed within the software Azurad, to provide a statistical analysis and interpretation for each one, as described in section IV.3.2. The detailed report about every response can be found in Appendix E section E.1.

Globally, the productivities are significantly enhanced by the use of continuous mode rather than batch mode. No significant increase of the diastereomeric purity was observed, but the temperature gradient of the CT crystallizer, combined with its highly efficient mixing, gives high diastereomeric excess in a very repeatable manner. Unfortunately, but unsurprisingly[8,33], the calculated yields appeared to be lower in continuous mode; an efficient solution may be the implementation of a recycling system[15,35,38].

Based on this statistical analysis of the model selected for every response, first assumptions can be expressed about the four studied factors, ΔT, Ω, t and T_{ref}. However, regarding the unexpected yield distribution observed, these hypotheses should be carefully considered.

Experiment	Global productivity ($g.L^{-1}.min^{-1}$)	Global yield (%)	Diastereomeric excess	Diastereomeric productivity ($g.L^{-1}.min^{-1}$)	Diastereomeric yield (%)
1 R1	1.317	14.7	0.53	1.139	6.3
1 R2	1.103	12.1	0.54	0.997	5.5
2	0.085	5.8	0.69	0.093	3.1
3	1.623	15.9	0.62	1.986	10.9
4	0.626	18.8	0.58	0.736	12.2
5 R1	0.135	4.3	0.70	0.151	2.5
5 R2	0.232	7.2	0.68	0.284	4.7
6	0.151	11.1	0.67	0.217	7.1
7	0.246	6.3	0.70	0.414	6.8
8	1.432	13.9	0.67	1.753	9.6
9	0.006	0.4	0.58	0.006	0.2
10	0.017	1.0	0.64	0.015	0.5
11 R1	0.106	3.5	0.71	0.105	1.7
11 R2	0.773	11.8	0.71	0.539	8.9
12 R1	2.217	22.1	0.58	2.311	12.8
12 R2	3.976	19.6	0.57	1.992	11.0
13	2.688	26.4	0.58	2.883	15.9
14	3.185	15.7	0.59	1.657	9.2

Table IV- 10: Average responses for every experiment of the first screening. For 'global' results, the average has been calculated with all the fractions; for 'diastereomeric' results, the average has been calculated with the fractions analyzed by chiral HPLC, i.e., fractions 3, 5 and 8. In the column "Experiment", 'R' stands for repetition.

IV.4.2.1. Temperature difference ΔT

The temperature difference between the two cylinders is one the two factors that have an impact, even small, on every studied response. It mainly impacts global and diastereomeric yields, and diastereomeric excess.

The use of the CT crystallizer in isothermal mode ($\Delta T = 0$ °C) seems to enhance productivity and yield. It can be explained because the increase of the temperature difference leads to a nucleation occurrence at higher supersaturation[74]. This means that crystallization needs a higher driving force to start. When there is no temperature difference, the nucleation starts 'earlier' and can then results in a higher production of crystals.

However, the non-isothermal mode has a clear influence on diastereomeric excess. Best diastereomeric excesses were obtained when the inner cylinder was the cold part, ($\Delta T = -10$ °C; with the outer hot cylinder). This non-isothermal mode also seems to have a positive effect on productivity and yield. The reverse mode (hot internal cylinder and cold external cylinder) did not lead to any response improvement. The difference of results according to the non-isothermal mode was also reported by Wu *et al.* (2015)[62]. It is linked to the driving forces of dissolution and recrystallization exerted respectively in the heating part boundary layer and in the cooling part boundary layer. The temperature regulation of each cylinder may not be equally efficient, which can explain why one non-isothermal mode appears to be better than the other.

For further studies, the non-isothermal mode implying the inner cylinder as the cold part and the outer as the hot part should be preferred, regarding its positive impact on diastereomeric excess, productivity, and yield. Also, the range of studied ΔT should be extended.

The second factor which has an influence on the five studied responses is the residence time.

IV.4.2.2. Residence time t

If this parameter impacts every response, its influence is notably strong on productivity and yield. The best results were obtained at t = 5 min. More generally, when the residence time decreases, the productivity and the yield increase. With short residence times, the cooling is faster, which increases the nucleation rate, thus the yield and the productivity. However, the side effect is a broader PSD, i.e., a less homogeneous powder.

Nevertheless, this factor should be carefully handled regarding the chiral purity. Indeed, 5 min of residence time resulted in low diastereomeric excesses. A compromise may be found by using 10 min for example. Anyway, the value 30 min should be eliminated in the future work.

IV.4.2.3. Rotation speed Ω

The rotation speed seems to have an important influence on diastereomeric excess, and also a small impact on global productivity. In both cases, the level 1000 rpm gives the best results.

The positive effect of the rotation speed increase can be explained by an enhancement of heat and mass transfer rates[51,57,60]. On the one hand, the enhanced mass transfer leads to productivity improvement. On the other hand, the diastereomeric excess is strongly impacted by the presence of a temperature gradient; since the heat transfer rate can be improved by increasing the rotation speed, the efficiency of the temperature difference is also improved[62], leading to a higher chiral purity.

Rotation speed did not appear to have a real influence on the other responses.

Regarding the previous remarks, the rotation speed level of 1000 rpm seems to be the most suitable one for the studied process.

IV.4.2.4. Reference temperature T_{ref} (target temperature within the CT crystallizer)

The last factor tested in this first screening is the target temperature within the CT reactor, i.e., the reference temperature T_{ref}. Its impact globally seems to be small, but it still exists for global productivity, global yield and diastereomeric excess.

Regarding global productivity and global yield, the decrease of T_{ref} leads to an increase of both responses. This trend was expected, as the decrease of temperature leads to an increase in supersaturation, hence in the mass of product that can crystallize.

For the diastereomeric excess, the effect is less intuitive. Up to 20 °C, the diminution of T_{ref} improves the chiral purity, but the lowest level 15 °C resulted in poor diastereomeric excesses.

The effect of T_{ref} is not easy to evluate, no levels can reasonably be eliminated at this stage. The study of this factor through a surface response design should be more conclusive.

This first screening led to some assumptions about the four studied factors. However, as mentioned before, the yield distribution of the ten collected fractions appeared to be highly inconstant in a very surprising, and *repeatable*, manner. This behavior was not expected at all, since the preliminary CT experiments showed fast reach of the steady state functioning in the CT crystallizer (see section IV.1.2). This unusual comportment is discussed in the next section.

IV.4.3. Unusual yield behavior

The unusual behavior of the yield distribution observed while performing the first screening led to many questions. Surprisingly the patterns on repeated trials are very similar, thus, the cause does not appear to be due to experimental error in the execution of samplings or analyses. The reflection about this issue gave rise to three different hypotheses.

IV.4.3.1. First hypothesis: slower reach of the steady state

As mentioned before, the first CT experiment results predicted a fast reach of the steady state functioning in the CT device. However, the yield distribution of the experiments of the first screening appeared to be highly but repeatably irregular. This is shown in Figure IV- 15: from fraction 1 F1 to fraction 10 F10, the strange yield pattern is repeatable from one experiment to another, in the same process conditions. Regarding that, three experiments have been

performed during 20 residence times instead of 10, to see if this peculiarity was due to fouling or if it was a matter of steady state. Those are experiments 11 R2, 12 R2 and 14 (Table IV- 9).

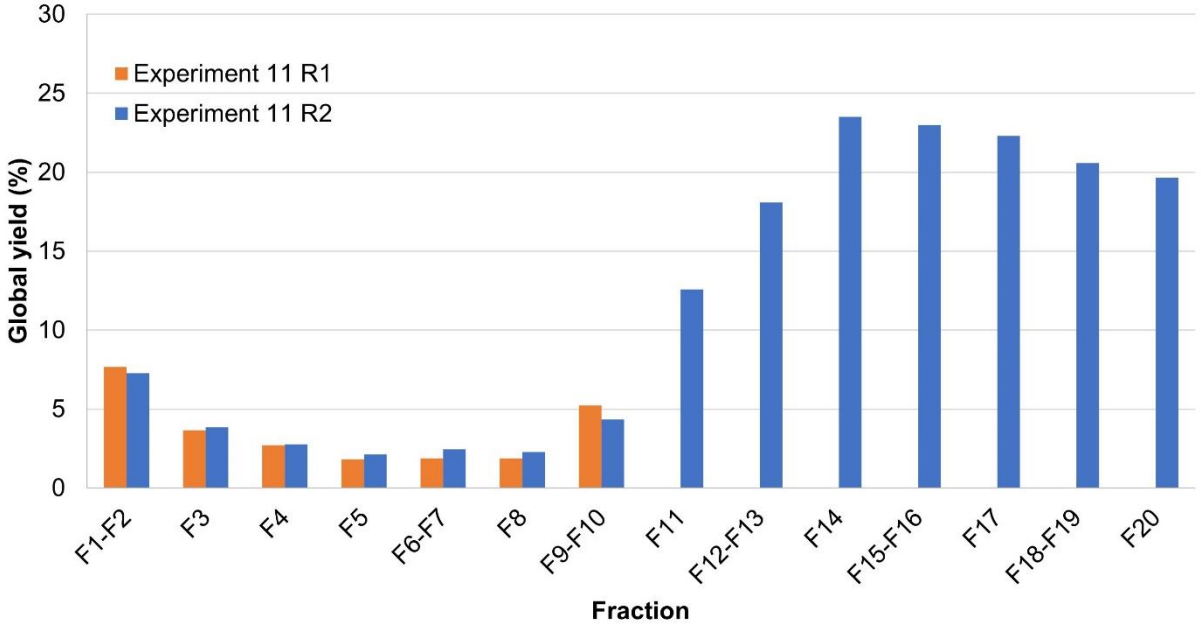

Figure IV- 15: Global yield histogram for experiments 11 R1 (orange) and 11 R2 (blue). Experiment 11 R1 lasted 10 residence times and experiment 11 R2 lasted 20 residence times.

The results of the 20-residence time experiments led to the hypothesis that in the process conditions of the first screening, steady state is not reached as soon as in the CT preliminary experiments. It seems to be achieved after 14-15 residence times (Figure IV- 15).

Also, it seems that yield and productivity are enhanced when the steady state is reached. Chiral purity remains stable all along the experiments.

Regarding that, the interpretation of the DoE has been checked. It appeared that the trends identified for every studied factor remain identical.

In conclusion, further experiments should last longer, considering that steady state seems not to be achieved before 12-13 residence times.

However, the need of such a high number of residence times to reach the steady state is surprising. Hence, another hypothesis was explored: the repeatable shape of the yield distribution might look like a part of a periodic oscillation (Figure IV- 15). The work realized to investigate this second assumption is detailed in the next section.

IV.4.3.2. Second hypothesis: oscillatory behavior

This second hypothesis originates from the work of Natalukha and Buyevich, when they work on unsteady processes of continuous crystallization in the 90s[121–123]. Such behavior was mainly observed in cases of strong dependence of the nucleation rate upon supersaturation: small disturbances can then induce instabilities. These instabilities can become regular oscillations of the driving force, and of important process parameters. Eventually, the set-up of auto-oscillating regimes of crystallization can be observed. In this last case, Buyevich proposed the following mechanism[121]:

(1) Nucleation and growth of the formed nuclei,

(2) Decrease of the supersaturation level,

(3) Decrease of the nucleation rate and, consequently, reduction of the inner release of matter,

(4) After a while, total transient number of crystals diminishes,

(5) Decrease of the total surface area of crystals available for mass transfer,

(6) Increase of the local supersaturation (locally),

(7) Return to step 1.

This auto-oscillating regime can significantly alter important operational characteristics of crystallization device, without any modification in the external conditions[121]. Nevertheless, the modulation of the frequency and amplitude of the oscillations is possible, typically with a recycling system[122,123].

Such oscillatory behavior was already observed in MSMPR[121], but never in PFC-type continuous crystallizer. The verification seemed then mandatory.

Experiment 12 (Table IV- 9) was performed again, aiming at an experiment duration of 50 residence times, in order to: (i) verify if the nature of the yield distribution is oscillatory and (ii) if it is, find its frequency and amplitude. This experiment was named O(scillation)1.

Figure IV- 16 shows the comparison between the yield distribution of experiments 12 R1 (orange), 12 R2 (blue) and O1 (grey). The three experiments exhibit the same distribution pattern on the shared fractions. However, experiment O1 was stopped after 32 residence times, because of a blockage. This was identified as a consequence of the high supersaturation ratio β of 3.3 and/or the fast residence time of 5 min.

Thereby two other experiments were set-up: O2 at a lower supersaturation level (3.1) and O3 at a longer residence time (10 min). The global yield distribution of these two experiments can respectively be found in Figure IV- 17 and Figure IV- 18.

Experiment O2 (Figure IV- 17) was stopped after 45 fractions because of a blockage. This clogging issue was fixed by heating up the CT reactor to 40 °C and flushing it with technical ethanol for 5 min. The set temperature of the system was then put back to 15 °C, and after 20 min (with the circulation of ethanol), the feeding reactors were reconnected to the crystallizer and 8 other fractions were collected (in red in Figure IV- 17).

No specific oscillatory behavior was found, but the tested cleaning procedure seemed interesting. Also, the dilution of the medium has impacted the yield: it has decreased it. Almost no product was collected during a certain number of fractions: this was attributed to encrustation of the reactor.

Experiment O3 (Figure IV- 18) exhibits a striking erratic yield distribution, but no oscillation, or blockage was observed. The yield seems similar, nay better, when decreasing the residence time.

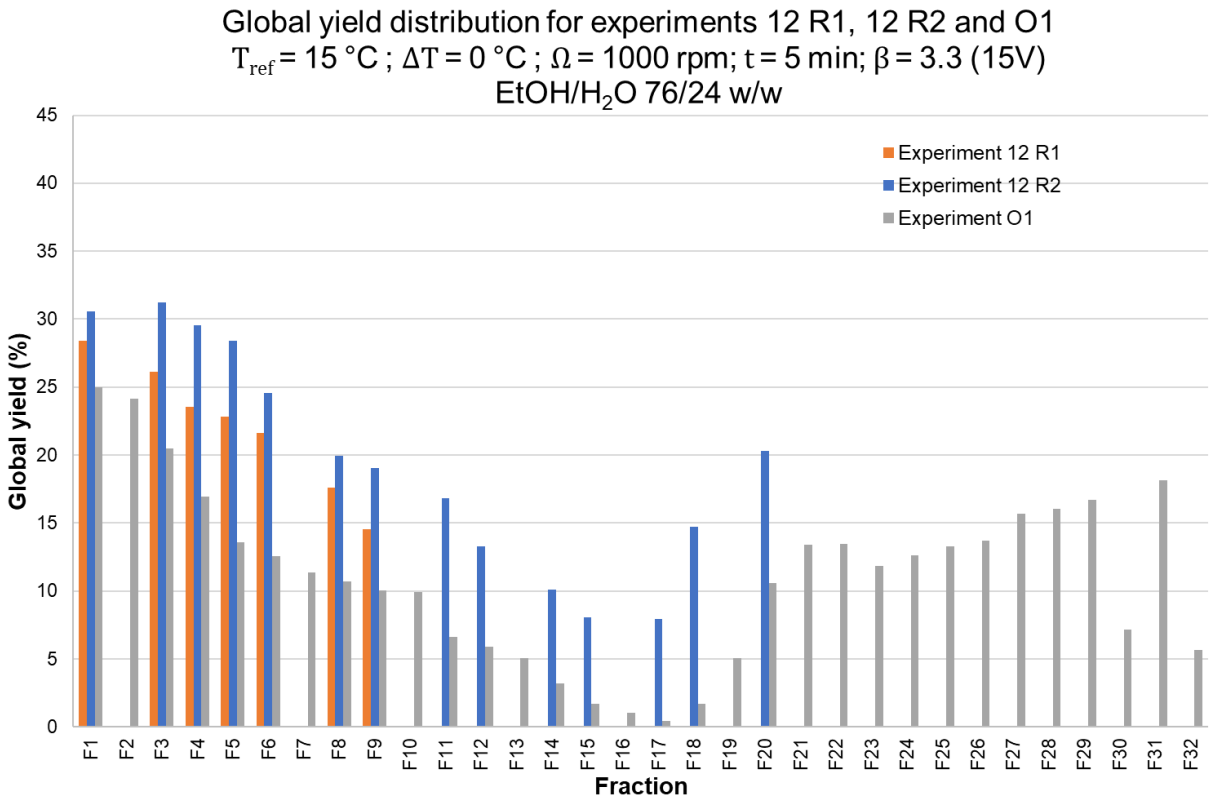

Figure IV- 16: Global yield distribution for experiments 12 R1 (orange), 12 R2 (blue) and O1 (grey). Experiment 12 R1 lasted 10 residence times, experiment 12 R2 lasted 20 residence times and experiment O1 lasted 32 residence times.

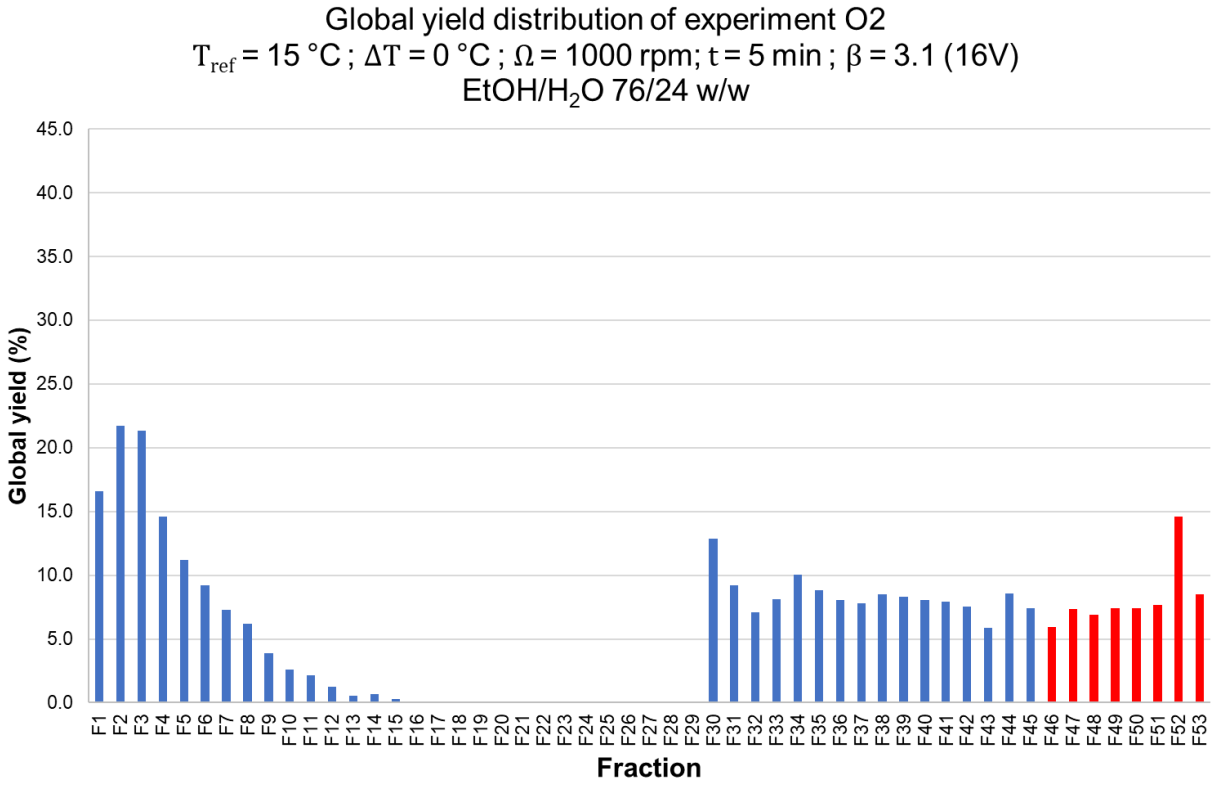

Figure IV- 17: Global yield distribution of experiment O2. The conditions are that of experiment O1, but with a lower supersaturation level β of 3.1. Blockage occurred after fraction 45. It was eliminated by heating up the CT reactor to 40 °C and flushing it with technical ethanol. Fractions 46 to 53 (red) were collected after the return of the crystallizer to the reference temperature of 15 °C.

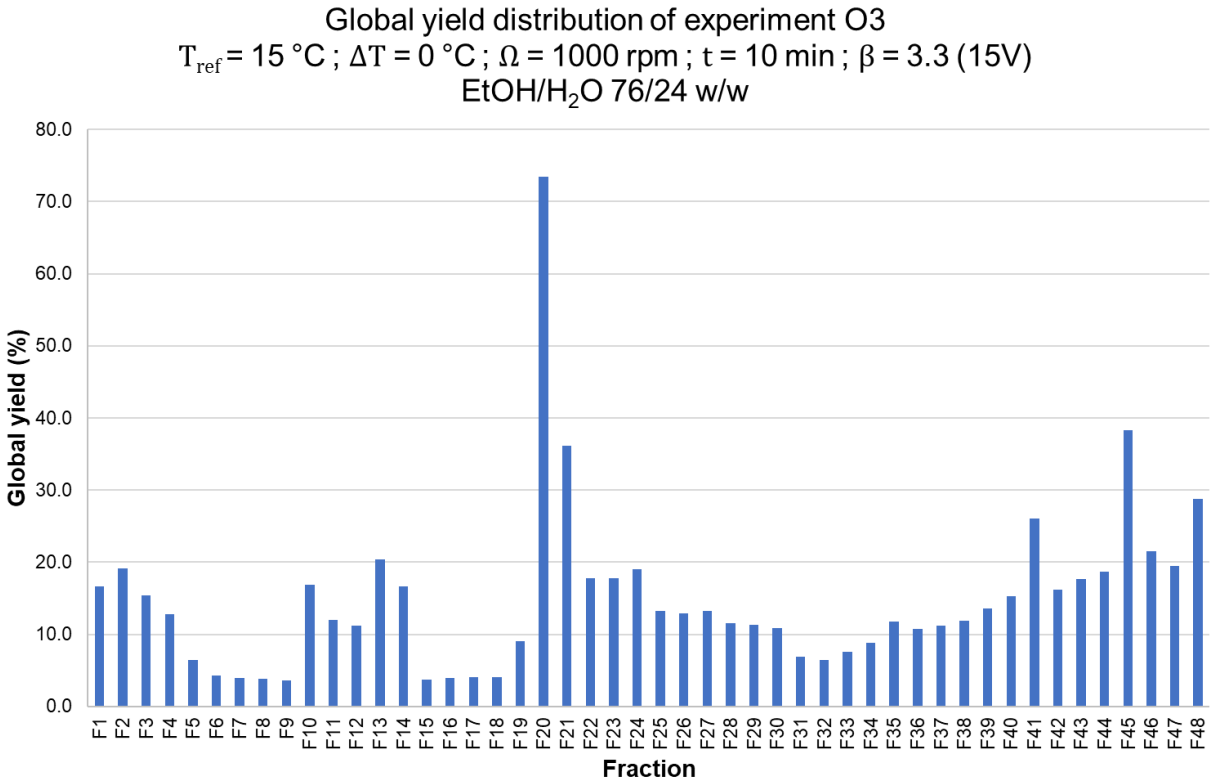

Figure IV- 18: Global yield distribution of experiment O3. The conditions are that of experiment O1, but with a slower residence time t of 10 min.

Some samples of experiment O3 were analyzed by optical microscopy; the micrographs are shown in Figure IV- 19. After the massive product release during fraction 20, some very big 'abraded' crystals are observed.

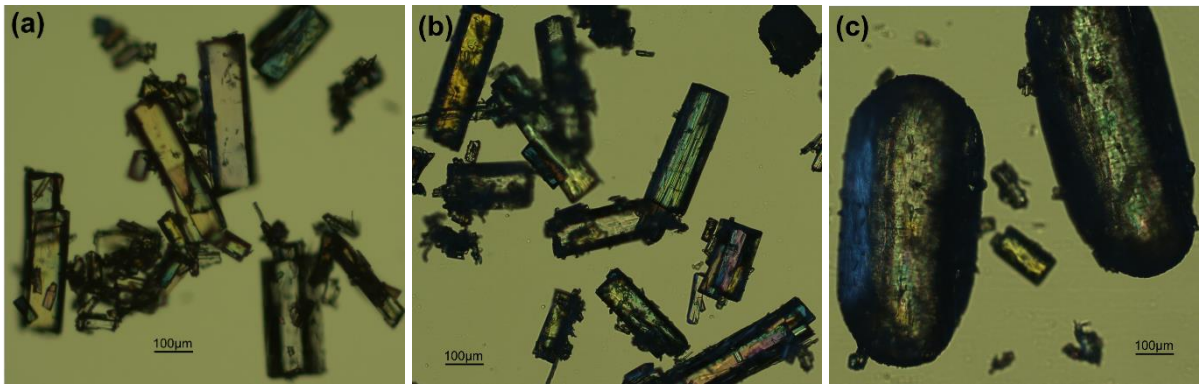

Figure IV- 19: Micrographs of the product obtained in experiment O3 (a) F1-F4: fibrous platelets, (b) F15-F19: thinner fibrous platelets and (c) F20-F48: small platelets and very big 'abraded' oblong particles, taken by optical microscopy at a magnification of 5.

Experiments O1, O2 and O3 did not show any oscillatory behavior. Nevertheless, the encrustation trend seems clear, especially in the case of experiment O2, with the yield decrease observed between fractions 3 to 29. The product collection could then start again.

According to the product of experiment O3 analyzed by optical microscopy, it seems that some crystals are stuck within the CT crystallizer, probably because of encrustation. They mature, but are abraded, probably by the crystals of the crust(s) (Figure IV- 19c). After some time, they are massively released. The hypothesis is that during 'a while', the crust resists, but a breach

might be created by force of pressure exerted by the arriving particles and the large crystals. This may lead to a detachment of part of the crust, and to a new pathway for the crystals along the CT crystallizer.

In conclusion, no oscillatory behavior was observed so far, but the tendency of the system to block in the used process conditions is clear; it is probably due to encrustation. The dilution of the medium (experiment O2) or the decrease of the residence time (experiment O3) do not seem to prevent this trend.

The last hypothesis about the yield distribution difference in regularity between the preliminary CT experiments and the first screening experiments concerns the solvent ratio.

IV.4.3.3. Third hypothesis: solvent ratio

In the preliminary CT experiments, the process was realized in technical ethanol (i.e., azeotropic ethanol, containing 5 %w of water). Because of filtration issues, the process was modified (see batch study in section IV.2.2), leading to the use of the solvent mixture EtOH/H_2O 76/24 w/w. This mixture was that used in the first screening continuous experiments. Thereby, the unusual yield distribution may be due to wettability issues, because of the modification of the solvent ratio.

To verify this assumption, experiment O4 was performed. It has the same conditions than O3 (see previous section), but the solvent used is technical ethanol (i.e., EtOH/H_2O 95/5 w/w). Its yield distribution is presented in Figure IV- 20: the yield distribution seems quite stable, unlike that of experiment O3.

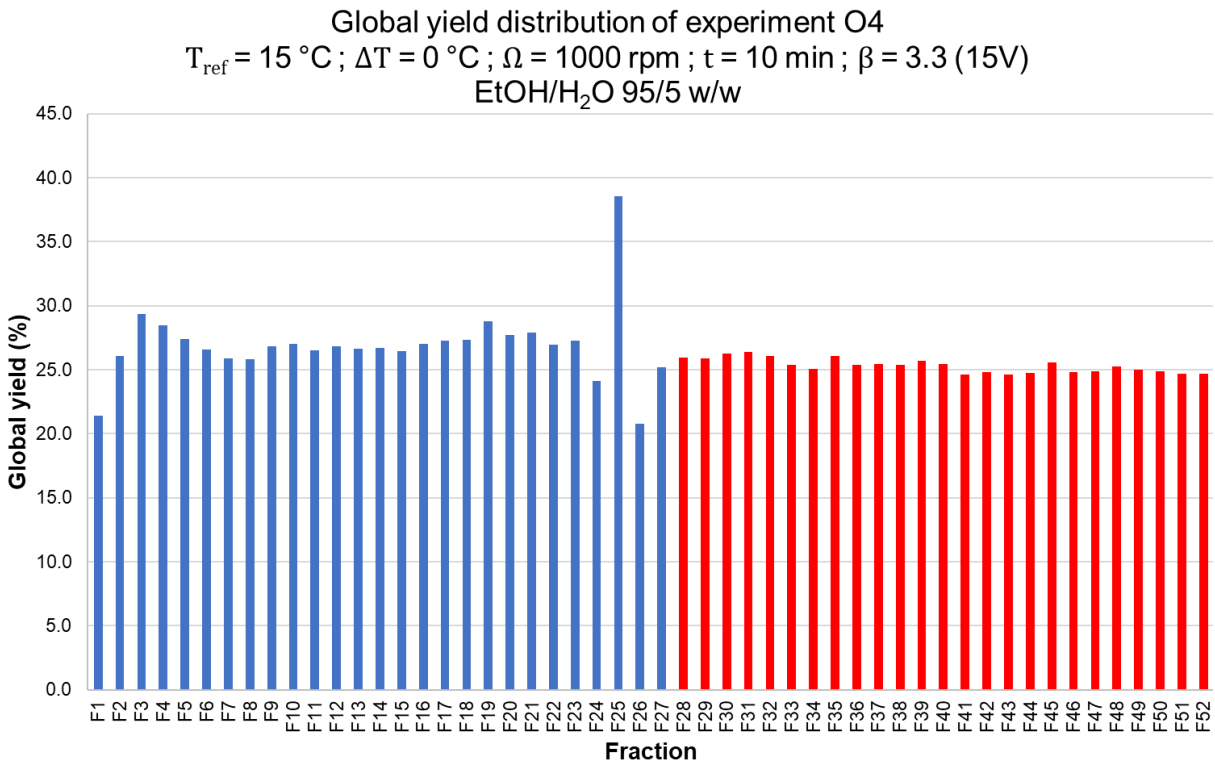

Figure IV- 20: Global yield distribution of experiment O4. The conditions are that of experiment O3, but with a solvent ratio EtOH/H_2O of 95/5 w/w instead of 76/24 w/w. Blockage occurred after fraction 27. It was eliminated by heating up the CT reactor to 40 °C and flushing it with technical ethanol. Fractions 28 to 52 (red) were collected after the return of the crystallizer to the reference temperature of 15 °C.

A clogging issue occurred during experiment O4, after 27 residence times. It was fixed by heating up the CT reactor to 40 °C and flushing it with technical ethanol for 15 min. The set temperature of the system was then put back to 15 °C, and after 45 min (with the circulation of ethanol), the feeding reactors were reconnected to the crystallizer and 25 other fractions were collected (in red in Figure IV- 20). The yield distribution after the cleaning procedure seemed even more stable than before.

Two experiments were run to see if this last observation was concluding: one implementing the cleaning procedure before the start of the experiment, and one applying it after 1 h of experiment. It was not conclusive. Nevertheless, the cleaning procedure appeared to be efficient in case of blockage.

To conclude, the erratic yield behavior observed during the screening experiments seems to be due to wettability issues, because of an amount of water too important. Thus, it was decided to modify the solvent ratio of the chiral resolution process from EtOH/H_2O 76/24 to 95/5 w/w (i.e., technical ethanol), since this solvent ratio appeared to be better to ensure a more constant yield. Even if the obtained crystal shape in azeotropic ethanol is not the best one for the filtration process (see section IV.1.2), the priority was given to the yield distribution.

Before implementing this new process in continuous experiments, another series of batch experiments was conducted, in technical ethanol. This new sequence was also the opportunity to standardize the batch procedure, to ensure a correct comparison with continuous mode, especially regarding the productivity.

IV.5. Batch standardized experiments in technical ethanol

According to the previous conclusions, a new process procedure was established:

1- Dissolution at 25 °C during 15 min of 1 equivalent of rac-Ibu in the wanted volume of technical ethanol (corresponding to the studied supersaturation ratio[3] at 20 °C, i.e., the final temperature),
2- Heating to 65 °C with a rate of 5 °C.min^{-1},
3- 20 min after the start of step 2, addition of 1 equivalent of *S*-αMBA at 1.5 mL.min^{-1},
4- 5 min after the start of step 3, cooling down to 20 °C with the studied cooling rate,
5- Filtration of the product on a glass filter of porosity P3 and diameter 20, 40, 60 or 80 mm according to the scale,
6- Cake washing with 2 V of distilled water,
7- Drying at 40 °C.

To maximize the collected information with a minimum number of experiments, this batch study was rationalized through a small screening design.

At the beginning, the goal was to test three factors with two levels, as shown and explained in Table IV- 11. However, the studied supersaturation levels appeared to be to too low to induce crystallization at 20 °C (in batch mode).

Factor	Level	Reason
Scale (g)	4	Test the influence of the scale on the process results in batch mode
	6	
Supersaturation ratio β	2.2	Use the same supersaturation ratios that those of the second screening (see section IV.6.1)
	2.5	
Cooling rate (°C.min^{-1})	0.3	Evaluate the influence of the cooling rate velocity
	0.6	

Table IV- 11: Factors and levels chosen in the first place for the DoE in batch mode

In the end, the study of this factor in batch mode was abandoned. It was replaced by the use of a fixed supersaturation ratio of 2.8, which can indeed induce a spontaneous crystallization at 20 °C.

The matrix of experiments built with the two left factors and its results can be found in Table IV- 12. To compare the results with those of the continuous mode, the same responses were studied.

[3] The calculations were made with the expression of β presented in section I.1.2 and with the solubility equation given by Excel regression for EtOH/H2O 95/5 w/w in Figure II- 4: $C^* = 0.0033T^2 - 0.0687T + 3.867$ (with C* in %w and T in °C).

Exp.	Experimentation plan		Global productivity ($g.L^{-1}.min^{-1}$)	Global yield (%)	Diast. excess	Diast. productivity ($g.L^{-1}.min^{-1}$)	Diast. yield (%)
	Scale (g)	*Cooling rate (°C.min^{-1})*					
B32	6	0.6	0.109	33.2	0.58	0.063	19.2
B33	4	0.6	0.123	38.8	0.47	0.058	18.2
B34	6	0.3	0.099	37.3	0.63	0.062	23.6
B35	4	0.3	0.101	38.5	0.61	0.062	23.7

Table IV- 12: Matrix of experiments and results of the screening in batch mode.

Likewise screening of the continuous mode, the results were processed through the software Azurad. The analysis did not go as far as that of continuous mode DoE, for which the statistical evaluation with the software is described in section 0 .

Also, the models were estimated as poorly reliable because of the number of performed experiments. Therefore, only trends can be assessed. In addition, it is noteworthy to mention that the importance of some factors can be hidden or enhanced because of interactions between them.

The influence scores given in Figure IV- 21 to Figure IV- 25 are extrapolated from the Pareto plots (coefficients) provided by Azurad. The (a) figures gives the relative influence of each factor, and the effect of their levels can be found in (b).

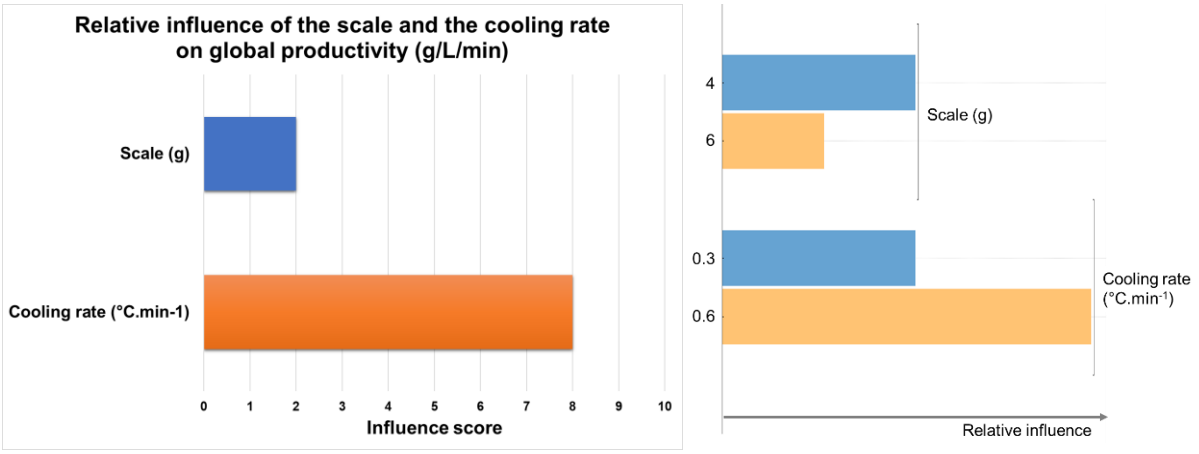

(a) **(b)**

Figure IV- 21: Results from Azurad for global productivity: (a) Relative influence of the scale and the cooling rate on the global productivity. (b) Total effect plot taken from Azurad for every factor, the bars give the relative effect of each level to improve global productivity.

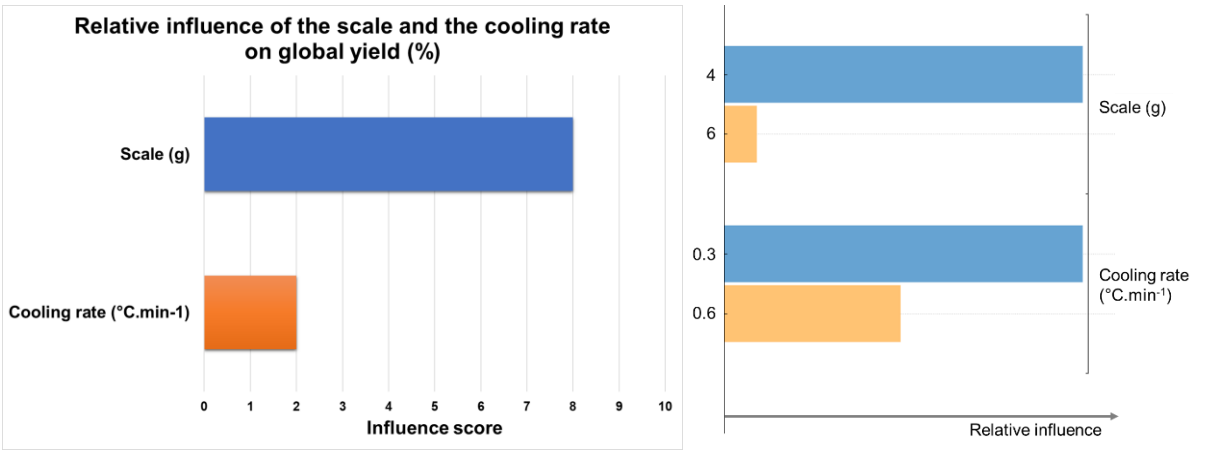

(a) **(b)**

Figure IV- 22: Results from Azurad for global yield: (a) Relative influence of the scale and the cooling rate on the global yield. (b) Total effect plot taken from Azurad; for every factor, the bars give the relative effect of each level to improve global yield.

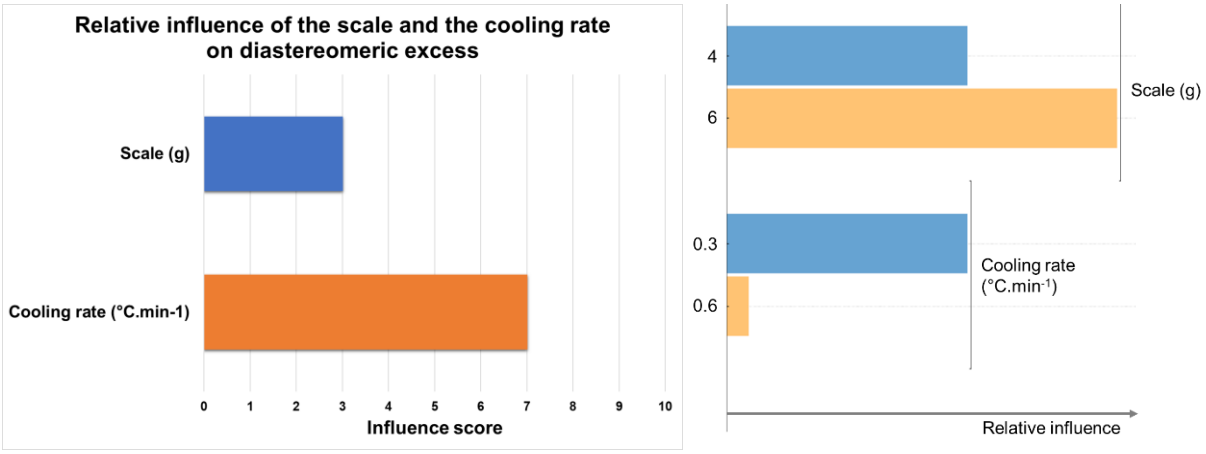

(a) **(b)**

Figure IV- 23: Results from Azurad for diastereomeric excess: (a) Relative influence of the scale and the cooling rate on the diastereomeric excess. (b) Total effect plot taken from Azurad; for every factor, the bars give the relative effect of each level to improve diastereomeric excess.

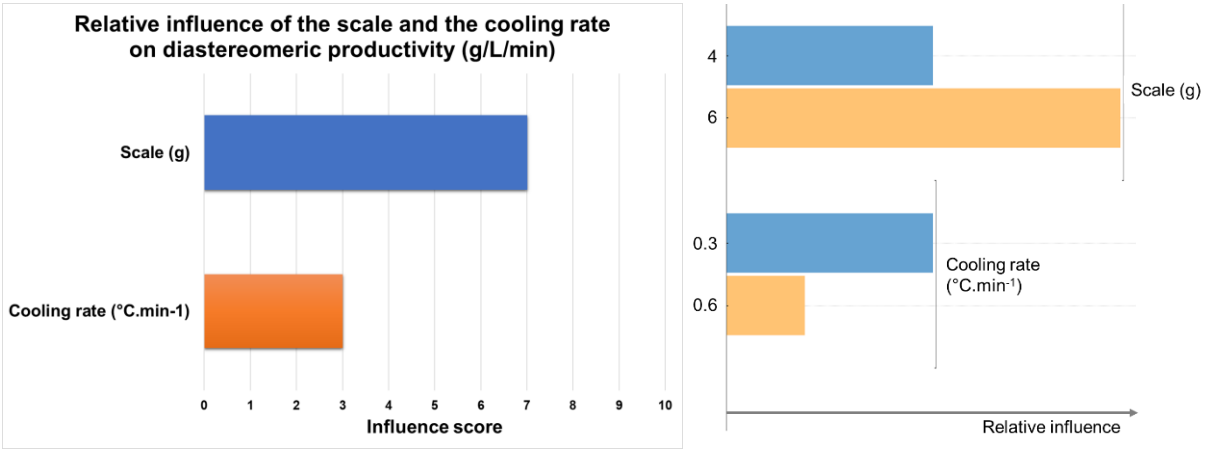

(a) **(b)**

Figure IV- 24: Results from Azurad for diastereomeric productivity: (a) Relative influence of the scale and the cooling rate on the diastereomeric productivity. (b) Total effect plot taken from Azurad; for every factor, the bars give the relative effect of each level to improve diastereomeric productivity.

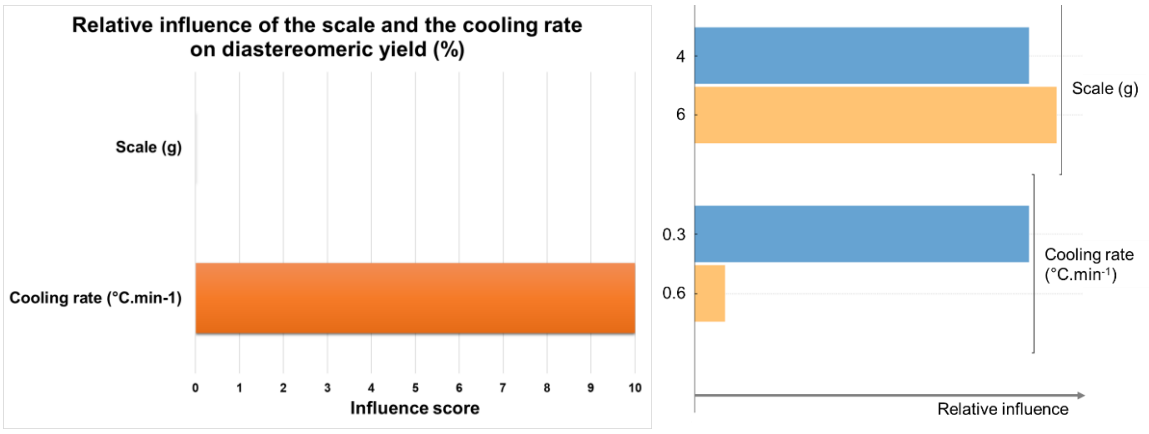

Figure IV- 25: Results from Azurad for diastereomeric yield: (a) Relative influence of the scale and the cooling rate on the diastereomeric yield. (b) Total effect plot taken from Azurad; for every factor, the bars give the relative effect of each level to improve diastereomeric yield.

The scale seems to mainly impacts the global yield and diastereomeric productivity, but also the global productivity and the diastereomeric excess.

For the global responses, the smaller the scale the better. Such result can be explained by the difference of the reactor's size: in larger reactors, the heat and mass transfers are generally less effective, and less homogeneous in the bulk. Therefore, the crystallization kinetics can be hindered, resulting in a lower amount of recovered product.

Regarding diastereomeric excess and productivity, it seems that the results are improved by a higher scale. However, this assumption may most likely be biased by the very low diastereomeric excess recovered in experiment B33 (Table IV- 12).

The cooling rate seems to have a strong influence on the global productivity and the diastereomeric excess and yield. Even if it is weaker, it also impacts the global yield and the diastereomeric productivity. It is noteworthy to mention that such effects could be modified if a seeding procedure was added to the process.

As expected, a fast-cooling rate improves the global productivity, since it reduces the experiment duration. However, this level is not the best one for diastereomeric productivity, which results are more similar to those of diastereomeric excess.

The decrease of the cooling rate globally seems to improve all the other responses. This can be expected for global yield, as a gentler cooling rate is better for crystal nucleation and growth. Also, when the cooling rate is reduced, the system has more time to reach the thermodynamic state, thus, in this case, to crystallize the less soluble salt, which is the desired one. Therefore, this is probably the reason why the decrease of the cooling rate enhances the diastereomeric responses.

This standardized batch study permitted the generation of data in batch mode, to compare with the results of the further work in continuous mode. Nevertheless, the supersaturation ratio β had to be increased, in order to induce crystallization at the wanted temperature of 20 °C. This must be kept in mind when comparing the results of the two modes.

Also, it was the opportunity to study the influence of the scale of the experiment and of the cooling rate. An interesting conclusion is that a faster cooling rate improves the global productivity: in the continuous experiments, the cooling is quite fast, since the hot medium enters the cold CT reactor. Therefore, such trend suggests that the productivity in the continuous crystallizer can be greater than in batch mode, which was indeed already observed.

IV.6. Second screening in continuous mode

For the continuation of the work within the CT crystallizer, a new screening design was set-up. In this second DoE in continuous mode, regarding the conclusions made after the first one (see section IV.4.3), the chiral resolution of rac-Ibu with *S*-αMBA was performed in technical ethanol (i.e., EtOH/H_2O 95/5 w/w ca. the azeotropic composition).

IV.6.1. Set-up of the new DoE

Among the four parameters studied in the first screening in continuous mode, three were kept for this second one. Since the solvent mixture changed, it seemed important to confirm the assumptions previously made on temperature difference ΔT, rotation speed Ω and residence time t. The reference temperature T_{ref} would need to be studied through a surface response design, hence, it was not incorporated as a DoE factor in this second screening, and was fixed at 20 °C. The new introduced factor is the supersaturation ratio β, in order to investigate the impact of the medium dilution on the process results.

The choice of the four factors' levels is detailed in the next section.

IV.6.1.1. Choice of the second screening factors' levels

Temperature gradient ΔT (°C)

This factor contains the temperature gradient sign, i.e., which cylinder is the cold part when the other is the hot one, and its absolute value.

In the first screening, only two absolute values were tested: 0 and 10 °C. This could only indicate the impact of the presence of a temperature gradient. Here, another one was added: 5 °C. In this way, the effect of the temperature difference between the two cylinders can be refined.

In the conclusions about the four studied factors in the first DoE, the non-isothermal mode implying the inner cylinder as the cold part and the outer as the hot part (sign '-') gave the best results of diastereomeric excess, productivity, and yield. Nevertheless, since a new absolute gradient value was added, it seemed important to keep the temperature difference sign in this second screening design, since the effect of the temperature gradient might be non-linear.

Therefore, five levels were chosen for this first factor: -10, -5, 0, 5 and 10 °C.

Rotation speed Ω (rpm)

In the first DoE, three levels were selected to study the rotation speed impact: 200, 500 and 1000 rpm. The importance of the rotation speed on the investigated responses seemed limited, and the level 1000 rpm appeared to be the best one. However, the effect of rotation speed was not linear for every response, more specifically for the diastereomeric excess, which was significantly impacted by rotation speed. This is why two levels were studied in this second DoE: 500 and 1000 rpm. The level 200 rpm was eliminated as it did not lead to a proper suspension of the medium.

Residence time t (min)

The residence time showed a strong influence on the different investigated responses. If a short residence time led to the best results in terms of yield and productivity, this was the opposite for the diastereomeric excess. The levels were then reprocessed: the 30 min value was eliminated and replaced by a value comprised between 5 and 15 min (the two other levels of the first DoE), looking for a compromise between yield, productivity, and chiral purity. Therefore, the three levels investigated in the second screening were: 5, 10 and 15 min.

Supersaturation ratio β

This factor was introduced to study the impact of the medium concentration on the process results. To establish an interesting range of values to study, the reflection was based on the supersaturation ratios β of the previous CT experiments: they were comprised between 2.8 and 3.3. In the first place, two levels were chosen: 2.5 and 3.1.

However, the first experiment with $\beta = 3.1$ was stopped after 11 residence time because of blockage. This was expected after observing that the suspension going out of the CT in this case was very dense.

The experiments with $\beta = 2.5$ were conducted correctly without fouling. This level was conserved, but the second was changed to 2.0. Nevertheless, with this value, the amount of product recovered was really low, sometimes too low to perform the necessary analyses. It was then replaced by a higher supersaturation level.

In the end, the two studied levels were 2.2 and 2.5.

The summary of the investigated factors and levels can be found in Table IV- 13.

X	Name of the factor	Level	Value of the level
X1	Temperature difference ΔT (°C)	0	-10
		1	-5
		2	0
		3	+5
		4	+10
X2	Rotation speed Ω (rpm)	0	500
		1	1000
X3	Residence time t (min)	0	5
		1	10
		2	15
X4	Supersaturation ratio β	0	2.2
		1	2.5

Table IV- 13: Factors and levels of the second screening on the continuous chiral resolution by diastereomeric salt formation of rac-Ibu with S-αMBA.

After the selection of the levels of the four factors of this second screening in continuous mode, the corresponding matrix of experiments needed to be constructed. Each experiment represents a unique combination of the different levels of each factor. This is described in the next section.

IV.6.1.2. Construction of the matrix of experiments

The DoE matrix of experiments was built with the 'Screening' tool of Azurad software. By using an exchange algorithm, a D-optimal matrix of 12 experiments was chosen with minimal inflation factors on the model coefficient (experiments 1 to 12 in Table IV- 14).

Experiment	Matrix of experiments				Experimentation plan			
	X1	*X2*	*X3*	*X4*	*ΔT (°C)*	*Ω (rpm)*	*t (min)*	*β*
1	4	1	0	1	10	1000	5	2.5
2	0	0	0	0	-10	500	5	2.2
3	4	1	2	0	10	1000	15	2.2
4	2	0	2	1	0	500	15	2.5
5	1	1	2	0	-5	1000	15	2.2
6	0	1	1	1	-10	1000	10	2.5
7	3	0	0	0	5	500	5	2.2
8	2	1	0	1	0	1000	5	2.5
9	4	0	1	0	10	500	10	2.2
10	1	0	1	1	-5	500	10	2.5
11	3	1	2	1	5	1000	15	2.5
12	2	1	1	0	0	1000	10	2.2
13	0	1	0	1	-10	1000	5	2.5
14 (3)	4	1	2	0	10	1000	15	2.2
15	4	0	0	0	10	500	5	2.2
16 (8)	2	1	0	1	0	1000	5	2.5
17	2	1	1	1	0	1000	10	2.5

Table IV- 14: Second screening matrix of experiments and its corresponding experimentation plan, constructed with the 'Screening' tool of the software Azurad. Experiments 1 to 12 are part of the initial DoE construction. Experiments 13 to 17 were performed during the tests of the in-line modification of a parameter directly at the end of an initial run (see Table IV- 15). Experiment 3 and 14 and 8 and 16 are considered as repetitions.

In addition to these 12 experiments selected with Azurad software, other tests were performed. It consisted in an in-line modification of one DoE parameter. Five tests were realized; they are summarized in Table IV- 15. At the end of the concerned runs (column "Initial experiments"), the chosen parameter was changed. Once the modification was effective, the second part of the run started. Meanwhile, the continuous flow was maintained.

The discussion and conclusions about the effect of the realized modifications are detailed in section IV.6.3.

Also, these tests permitted the addition of 5 more experiments to the matrix of experiments (experiments 13 to 17 in Table IV- 14), including two repetitions of the initial matrix (experiments 3 and 14, and 8 and 16). The full matrix of experiments and its corresponding experimentation plan can be found in Table IV- 14.

Initial experiment	Initial parameter	Modified experiment	Modified parameter
1	ΔT = +10 °C	13	ΔT = -10 °C
(Run not exploited)	T_{ref} = 15 °C	14	T_{ref} = 20 °C
7	ΔT = +5 °C	15	ΔT = +10 °C
(Run not exploited)	Ω = 200 rpm	16	Ω = 1000 rpm
8	t = 5 min	17	t = 10 min

Table IV- 15: Summary of the parameters modified at the end of the concerned runs.

To complete the design of this second DoE in continuous mode, the last step was the selection of the number of fractions to collect and analyze, and of the responses to analyze, in order to discriminate the different process conditions. This is discussed in the next section.

IV.6.1.3. Fraction collection and choice of the DoE responses

To choose the number of residence times that should last the experiments, the following assumption was made, regarding the previous experiments' observations: around 12 residence times should serve the reach of the steady state. To draw the yield distribution and to perform the necessary analyses, an appropriate number of fractions must be collected. Therefore, the 12 preliminary fractions can be followed by 15 residence times, supposedly at the steady state. Experiments 1 to 12 were then performed during 27 residence times.

Regarding the experiments performed to test the in-line modification of a parameter, i.e., experiments 13 to 17, they lasted 15 residence times.

Each fraction was collected, and the ones analyzed by chiral HPLC and XRPD are presented in Table IV- 16.

Experiment set	Analyzed fraction	Corresponding number of residence times	Experiment set	Analyzed fraction	Corresponding number of residence times
Experiments 1 to 12	2	1 to 2	Experiments 13 to 17	1 (28)	0 to 1 (27 to 28)
	5	4 to 5		2 (29)	1 to 2 (28 to 29)
	8	7 to 8		4 (31)	3 to 4 (30 to 31)
	15	14 to 15		5 (32)	4 to 5 (31 to 32)
	18	17 to 18		7 (34)	6 to 7 (33 to 34)
	22	21 to 22		8 (35)	7 to 8 (34 to 35)
	26	25 to 26		11 (38)	10 to 11 (37 to 38)
				13 (40)	12 to 13 (39 to 40)
				15 (42)	14 to 15 (41 to 42)

Table IV- 16: Analyzed fractions and its corresponding number of residence times for the two experiment sets.

The chosen responses for this second screening are the same than those of the first one (see section IV.3.2).

In addition, considering the number of fractions collected and analyzed, it was decided to calculate the standard deviation of each response for every experiment. The results of this calculation were also processed into Azurad software, in order to determine the degree of responsibility of each factor for the potential variability of the response.

The standard deviation serves the evaluation of the mean deviations of each value x_i from the average $\bar{x}$. It was calculated in the unit of the response thanks to Equation IV- 9, and then expressed in percentage with respect to the average response.

$$Std.dev. = \sqrt{\frac{\sum_{i=1}^{n}(x_i - \bar{x})^2}{n-1}}$$ *Equation IV- 9*

The results of the second screening on the continuous chiral resolution by diastereomeric salt formation of rac-Ibu with *S*-αMBA in technical ethanol were processed within the 'Screening' tool of Azurad software. They are presented and discussed in the next section.

IV.6.2. Results of the second screening and discussion

As in the first screening, the yield distribution of the experiments was not as constant as expected. It seemed less erratic using EtOH/H2O 95/5 w/w than 76/24 w/w, but the expected constancy of the preliminary CT experiments was not encountered. This was assessed to be a consequence of encrustation. The section IV.6.4 presents the discussion about this issue, and the appropriate solutions.

Consequently, like for the first screening, it was decided to consider the average of the results for each response. The results are presented in Table IV- 17. It appeared that the standard deviations for global productivity and global yield are correlated. It is the same for diastereomeric productivity and diastereomeric yield. Therefore, only one result is presented for both couples of responses.

XRPD analysis was performed on the fractions identified in Table IV- 16. All the analyzed samples exhibited the correct solid phase. As in the first screening (see Figure IV- 14), the products obtained from chiral resolution exhibit small peak shifts compared with the pure material collected at room temperature. They are due to the presence of a partial solid solution enriched in *S*-Ibu-*S*-αMBA.

Experiment	Global productivity ($g.L^{-1}.min^{-1}$)	Global yield (%)	Std. dev. global productivity and yield (%)	Diastereomeric excess	Std dev. diast. excess (%)	Diastereomeric productivity ($g.L^{-1}.min^{-1}$)	Diastereomeric yield (%)	Std dev. diast. productivity and yield (%)
1	2.461	14.6	38	0.62	3	1.632	9.7	39
2	1.253	8.5	50	0.68	1	0.846	5.7	58
3	0.242	4.9	93	0.67	3	0.185	3.8	88
4	0.666	11.9	50	0.68	1	0.456	8.1	56
5	0.177	3.6	145	0.70	3	0.135	2.8	153
6	0.978	11.6	37	0.67	2	0.728	8.6	38
7	1.959	13.3	36	0.65	1	1.270	8.6	40
8	1.704	10.1	66	0.64	2	1.124	6.7	73
9	0.677	9.2	42	0.65	2	0.499	6.8	35
10	0.832	9.9	45	0.68	2	0.528	6.3	45
11	0.322	5.7	77	0.67	3	0.247	4.4	73
12	0.377	5.1	112	0.65	4	0.286	3.9	118
13	0.086	0.5	68	0.67	-	0.114	0.7	-
14 (3)	0.257	5.2	84	0.68	2	0.184	3.7	72
15	1.051	7.1	49	0.67	2	0.670	4.5	59
16 (8)	3.321	19.7	45	0.69	1	2.732	16.2	42
17	0.445	2.6	64	0.68	1	0.247	1.5	79

Table IV- 17: Average responses for every experiment of the second screening. For 'global' results, the average has been calculated with all the fractions; for 'diastereomeric' results, the average has been calculated with the fractions analyzed by chiral HPLC (see Table IV- 16). Experiment 3 and 14 and 8 and 16 are considered as repetitions. N.B.: Std. dev. = standard deviation; diast. = diastereomeric.

The results of the eight studied responses were processed within the software Azurad, to provide a statistical analysis and interpretation for each one, as described in section IV.3.2. A detailed report about every response can be found in Appendix E section E.2. Globally, the responses' models are not as significant as those in the first screening design. Nevertheless, some trends can be drawn.

Like in the first screening, the continuous mode seems to significantly improve the productivities, in comparison with the batch mode. This characteristic may be interesting to counterbalance the low yield obtained, in association with a recycling system.

Diastereomeric excess appeared to be improved by 18 % on average by transferring the process from batch to continuous mode. Moreover, the access to high chiral purity seems to be quite repeatable. In addition, an interesting observation was made: the diastereomeric excess tends to rise as the experiment progresses ($0.01 \leq \Delta de \leq 0.04$). This is probably due to the back diffusion that can be induced by the opposite direction of rotation of the neighboring vortices (illustrated in Figure I- 7). Since the wanted diastereomer seems to dominate the other in the process conditions, such characteristic is truly beneficial for the process results.

Thereby, based on this statistical analysis and interpretation of the model chosen for every response, first trends can be drawn for the four studied factors, ΔT, Ω, t and β. However, since encrustation seems to be there again, these assumptions should be wisely deemed.

IV.6.2.1. Temperature difference ΔT

Unlike the observations made in the first screening in EtOH/H_2O 76/24 w/w, the temperature gradient between the two cylinders has shown a weaker impact in this second screening performed in azeotropic ethanol.

ΔT seems to mainly impact the diastereomeric excess. The effect is identical to that already observed in the first screening: the use of the CT crystallizer in non-isothermal mode, with the inner cylinder as the cold part and the outer cylinder as the hot one (sign '-'), gives the best results of chiral purity. By contrast, the reverse non-isothermal mode should be avoided, regarding diastereomeric excess.

This latter is not true concerning the global and diastereomeric yields. Indeed, if the impact of the temperature difference is not linear (probable consequence of potential interactions with other parameters), it seems that a positive gradient leads to a yield increase. However, the predominance of $\Delta T = 0$ °C as a yield enhancer, detected in the first DoE, is not observed in the second screening design. Also, unlike the first screening, where this factor appeared to be really impacting, the global and diastereomeric yields are only a little influenced by the temperature gradient.

Contrary to the observations in the first screening, the impact of the temperature gradient on global and diastereomeric productivities is negligible. Therefore, the apparent positive effect of the use of the CT reactor in isothermal mode ($\Delta T = 0$ °C), like in the first DoE, should be moderated.

The temperature difference between the two cylinders also plays a role in the variability of the different analyzed responses. It is especially the case for productivity and yield (diastereomeric and global). A trend seems to be drawn: the use of the non-isothermal mode

'+' seems to reduce the standard deviation of the global results. An hypothesis can be assessed to explain this result: a positive gradient corresponds to the inner cylinder being the hot one; as the rotation of this cylinder generates heat because of the friction with the lip seal (see section III.3.2), the conjunction of these two effects probably leads to more stability than the situation when the inner cylinder is the cold part. However, the level $\Delta T = -10$ °C do not follow this tendency. It may be due to a threshold effect, or to interaction(s) with other factors.

The standard deviation of the diastereomeric excess is also affected by ΔT. Nevertheless, its impact appeared to be highly non-linear: no trend can be assessed as such. This can be due to the chosen regression model, which did not fit well the experimental results for this response. It might also be a consequence of interaction(s) with other factors.

Considering the previous assumptions, the adjustment of the temperature gradient between the two cylinders must be carefully examined, according to the desired effect. Indeed, the use of a 'negative' ΔT promotes the chiral purity, but it can be problematic for yield and dramatic in terms of variability of the collected mass of product (productivity and yield). The extension of the study of this parameter through a surface response design should be more conclusive.

Also, it could be interesting to separate the gradient direction and its absolute value in two distinct factors, as planned initially, in order to evaluate their impact separately.

IV.6.2.2. Residence time t

Like in the first screening, the residence time has an influence on every studied response.

Its impact is predominant on the global and diastereomeric productivities. The preponderance of $t = 5$ min as a productivity enhancer is evident, as in the first DoE. For short residence times, the cooling is faster, which increases the nucleation rate. The side effect is the recovery of a crystal population with a broad PSD, i.e., a less homogeneous powder.

The same assumptions can be made for global and diastereomeric yields, even if the residence time is a little bit less impacting on these responses. The lower the residence time the higher the productivity and the yield.

The residence time has also an important effect on the diastereomeric excess. Nevertheless, its effect is the opposite of that on productivities and yields: a longer stay in the efficient mixing CT reactor seems to have a positive impact on chiral purity. This confirms the observation during the first screening, but the impact of residence time on diastereomeric was not estimated as high.

The effect of t on the variability of the studied responses appeared to be non-linear. Nonetheless, as this impact was identified as limited nay negligible, the analysis does not need to go further. The poor influence of the residence time on the standard deviation of the different investigated responses is surprising: a fast t could be expected to slow the stability reach of the system, and lead to variability of the process results.

The conclusions of the second screening regarding the effect of the residence time are similar to that exposed in the first screening. This parameter must be carefully adjusted to ensure a sufficient productivity/yield with a good chiral purity.

IV.6.2.3. Rotation speed Ω

In this second screening design, unlike in the first one, the rotation speed has a very limited effect on the five main responses. However, its influence is more significant on the variability of these responses.

The impact of Ω is negligible on global and diastereomeric productivities, and for diastereomeric excess.

It seems that the level 500 rpm should be preferred to 1000 rpm to increase the diastereomeric and global yields, but this assumption should be modulated regarding the small influence exerted by Ω.

The standard deviation of the chiral purity is mainly impacted by the rotation speed. The effects of the two studied levels are clear: the lowest level seems to limit the standard deviations. If the mixing effects are probably less efficient when decreasing the rotation speed, they also might be less intense, thus more stable. Therefore, the diastereomeric excess is less subject to variability. However, it is noteworthy to mention that the mean deviations to the average chiral purity are very low (see Table IV- 17), hence, this conclusion should be moderated.

Even if the influence of the rotation speed is less important on the variability of the productivities and yields, the same observations about the rotation speed levels were made.

In the first screening, the level 1000 rpm gave the best process results. The striking differences observed in this second screening are probably due to the change of solvent mixture: the reduction of the water amount affected the viscosity of the medium and the morphology of the crystals, as explained in section IV.2. The effect of the rotation speed in this different medium has changed.

IV.6.2.4. Supersaturation ratio β

The supersaturation ratio was the new factor introduced in this second screening.

The degree of supersaturation is the principal parameter conditioning the results of yields among the studied factors. When β increases, the diastereomeric and global yields are improved. Such observation was expected since the amount of product that can potentially be recovered is increased when the supersaturation is higher.

The same effect can be observed for diastereomeric and global productivities, but it should be modulated as the influence of the residence time on these responses is poor.

The supersaturation ratio β also appeared to have an influence on the variability of the productivities and yields. Surprisingly, the increase of β appears to improve the regularity of the results. Such observation was not anticipated: as the medium is more concentrated at higher supersaturation, the system is expected to be less stable.

The impact of the supersaturation ratio on the chiral purity and its standard deviation seems negligible.

A last conclusion can be assessed, about the comparison between the batch and continuous mode. As explained in section 0, in batch mode, the supersaturation ratio must at least equal 2.8 for nucleation to be induced at 20 °C. In CT experiments, lower degrees of

supersaturation permit the occurrence of nucleation at 20 °C. This is probably due to the excellent heat and mass transfer rates of the CT crystallizer.

The results of the second screening in continuous mode, performed in technical ethanol, permitted to express various assumptions about the four studied factors. Some of them were expected, and similar to the conclusions of the first screening design, but unexpected observations were also made. Also, the responses' models of this second DoE are not as significant as in the first one, which led to less clear trends. Regarding that, the suspicion of interactions between factors is high.

The experimental plan realized did not permit the design of a complete interaction study, but primary interpretations can be made with the proper graphical representation. This is described in the next section.

IV.6.2.5. Suspected interactions

When interactions between parameters are suspected, a first verification can be realized, by using the appropriate graphical representation, as in Figure IV- 26.

In this figure, it is clear that no effect of the supersaturation ratio level can be stated without mentioning the level of the rotation speed. Therefore, the two factors cannot be interpreted separately. It means that an interaction effect exists between Ω and β for global productivity.

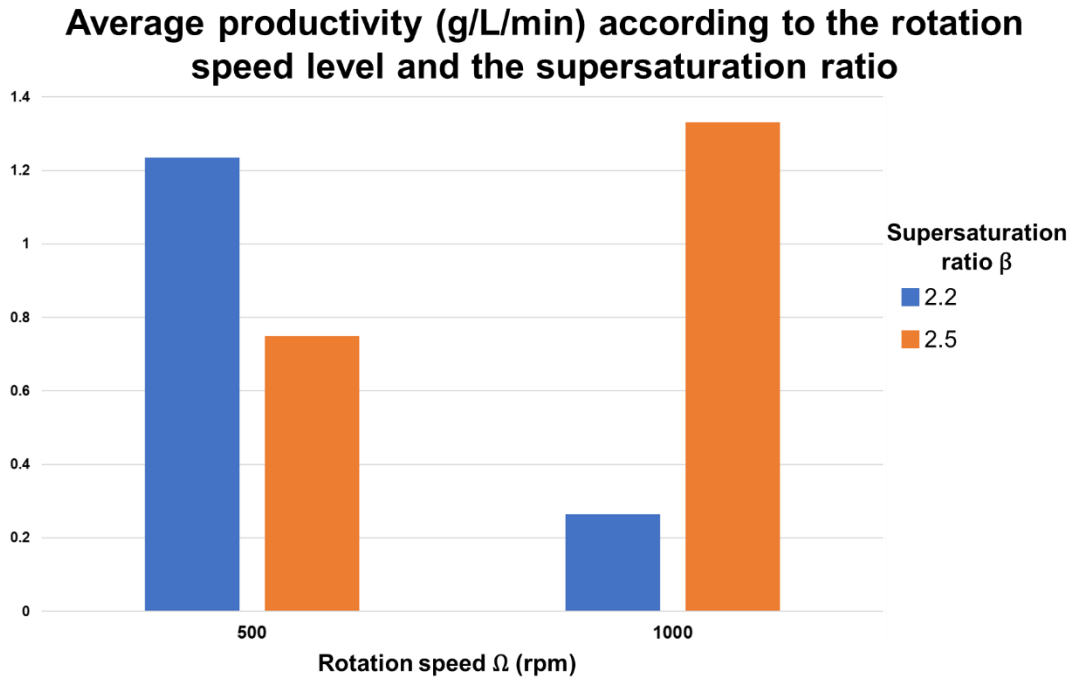

Figure IV- 26: Representation of the average global productivity ($g.L^{-1}.min^{-1}$) as a function of two factors: rotation speed Ω (rpm) and supersaturation ratio β.

Such graphical representation was made for every couple of studied parameters and for each response. The majority of the couples shows a potential interaction. Therefore, a complete interaction study could be interesting to implement.

However, such DoE design requires a large number of experiments: for example, with the factors and levels selected for the second screening, a minimum of thirty experiments is

necessary to process an interaction study with Azurad software. To take the maximum advantage of each experiment, experiments already performed should be 'reused', and if a surface response design is also set-up, the implementation of common experiments should be maximized.

In parallel of the second screening study on the continuous chiral resolution of rac-Ibu with *S*-αMBA, tests of in-line modification of one parameter were performed (see section IV.6.1.2). The results of these five experiments are discussed in the next section.

IV.6.3. Effect of the modification of one process conditions during the continuous run

To test the reactivity of the CT crystallizer to in-line parameter change, and to see the effects on the collected product, five modifications were tested:

- inversion of the sign of ΔT, i.e., the hot inner cylinder became the cold part, and the reverse for the outer cylinder,
- increase of the medium average temperature by increasing T_{ref},
- increase of the temperature gradient ΔT within the continuous crystallizer,
- increase of the rotation speed Ω,
- increase of the residence time t.

Table IV- 15 summarized the applied changes. The desired parameter was adjusted at the end of the 27 residence times of the initial experiment. Once the modification was effective, the second part of the run started.

Initial experiment	Initial parameter	Modified experiment	Modified parameter
1	ΔT = +10 °C	13	ΔT = -10 °C
(Run not exploited)	T_{ref} = 15 °C	14	T_{ref} = 20 °C
7	ΔT = +5 °C	15	ΔT = +10 °C
(Run not exploited)	Ω = 200 rpm	16	Ω = 1000 rpm
8	t = 5 min	17	t = 10 min

Table IV- 15: Summary of the parameters modified at the end of the concerned runs.

The results of the initial and modified experiments are presented in Table IV- 18.

Modification of the sign of ΔT

Between experiment 1 and experiment 13, the cold and hot cylinders were inverted: the inner hot cylinder became the cold one, and the outer cold cylinder became the hot part.

As shown in Table IV- 18, the overall results are worse after the parameter adjustment, except for the diastereomeric excess. This confirms the trend identified in the second screening design.

However, such modification is probably excessive for the system since clogging occurred after only four residence times. It may be tested again with a lower temperature gradient, but the actual ratio benefits/risks of such modification seems low.

Modified parameter	Experiment	Global prod.($g.L^{-1}.min^{-1}$)	Global yield (%)	Std. dev. global prod. and yield (%)	Diast. excess	Std dev. diast. excess (%)	Diast. prod. ($g.L^{-1}.min^{-1}$)	Diast. yield (%)	Std dev. diast. prod. and yield (%)
ΔT = +10 °C	**1**	2.461	14.6	38	0.62	3	1.632	9.7	39
ΔT = -10 °C	**13**	0.086	0.5	68	0.67	-	0.114	0.7	-
T_{ref} = 15 °C	**-**	0.889	18.1	13	0.66	2	0.562	11.4	18
T_{ref} = 20 °C	**14**	0.257	5.2	84	0.68	2	0.184	3.7	72
ΔT = +5 °C	**7**	1.959	13.3	36	0.65	1	1.270	8.6	40
ΔT = +10 °C	**15**	1.051	7.1	49	0.67	2	0.670	4.5	59
Ω = 200 rpm	**-**	2.046	12.2	44	0.64	2	1.260	7.5	56
Ω = 1000 rpm	**16**	3.321	19.7	45	0.69	1	2.732	16.2	42
t = 5 min	**8**	1.704	10.1	66	0.64	2	1.124	6.7	73
t = 10 min	**17**	0.445	2.6	64	0.68	1	0.247	1.5	79

Table IV- 18: Average responses for every initial and modified experiment of the tests presented in Table IV- 15. Some modifications led to premature end of experiments, because of clogging issue: experiment 13 was aborted after 4 residence times t, experiment 15 after 8t and experiment 17 after 4t. For 'global' results, the average has been calculated with all the fractions; for 'diastereomeric' results, the average has been calculated with the fractions analyzed by chiral HPLC (see Table IV- 16). N.B.: Std. dev.=standard deviation; diast. = diastereomeric; prod. = productivity.

Increase of T_{ref}

Experiment 14 was performed with $T_{ref} = 20$ °C, following another experiment (not presented in this work) with $T_{ref} = 15$ °C.

As expected, the productivities and yields decreased: the solubility is higher because of the temperature increase. The variability of these responses is also worse, it can be due to a certain time in stabilizing the new temperature.

Chiral purity seems to be improved, but this effect is suspected to be linked with the already mentioned increase of diastereomeric purity as the experiment progresses, because of back diffusion.

Increase of the temperature gradient ΔT

At the end of experiment 7, the temperature difference between the two cylinders was increased from 5 °C to 10 °C, starting experiment 15.

As shown in Table IV- 18, the overall results are worse after the parameter modification, except for the diastereomeric excess. This latter is supposed to be linked with the chiral purity enhancement as the experiment progresses.

The decrease of the productivities and yields can be due to an enhanced dissolution phenomenon as the temperature of the hot inner cylinder was increased. It may also be a consequence of encrustation on the colder outer cylinder. Blockage indeed occurred: after eight residence times the experiment stopped.

Increase of the rotation speed Ω

Experiment 16 was performed with $\Omega = 1000$ rpm, following another experiment (not presented in this work) with $\Omega = 200$ rpm.

The improvement of the results shown in Table IV- 18 is evident. This observation may be a proof of the existence of interactions between factors. Indeed, in the analysis of the second screening, the rotation speed globally appeared to have a small influence on the studied responses, whereas the benefit of this parameter adjustment is clear in Table IV- 18.

Nevertheless, it is noteworthy to remind that the 200-rpm level was not studied in the second screening, whereas it was in the first one. Yet, in the first screening, the rotation speed influence seemed higher. Therefore, there might be a threshold effect: above a certain sufficient rotation speed (apparently comprised between 200 and 500 rpm), its impact is negligible.

Increase of the residence time t

At the end of experiment 8, the flowrate was adjusted to change the residence time from 5 min to 10 min, starting experiment 17.

The consequences are comparable with those of the inversion of the sign of ΔT: the overall results are worse after the modification of the flowrate, except for the diastereomeric excess. This confirms the trend identified in the second screening design, that an increase of the residence time increases the chiral purity.

Nonetheless, as the inversion of the sign of ΔT, this parameter change seems excessive for the system since blockage occurred after only four residence times, even if the new residence

time was slower than the initial one. Such modification should be carried out very finely and little by little or avoided.

Conclusions

The in-line adjustment of a process parameter must be carefully carried out. Some modifications have to be thought meticulously, when realized on the temperature gradient ΔT or on the residence time t for example. The balance benefits-risks must be thoroughly evaluated. The tuning of T_{ref} or of Ω seems easier and more bearable for the running system.

This short study aimed at introducing the subject of parameter modification of running continuous experiments in the CT crystallizer. It would be interesting to extend this investigation as the in-line adjustment of a process parameter can be a useful tool to cure quickly and efficiently a potential issue, without stopping the continuous production.

Apart the possible decreases of the results (yield, productivity, chiral purity…) due to some specific process conditions, the main problem encountered in continuous processes is the encrustation. This is suspected to be the principal cause of the yield distribution variations met in the presented continuous work. If its effect seemed less important in the second screening, with technical ethanol, it was still present.

The next section deals with this common issue of the continuous processes, and presents solutions that should be considered for a safe and confident use of the CT reactor as a continuous crystallizer.

IV.6.4. Encrustation issue and proposed solutions

As mentioned in section I.3.2.1, when presenting the challenges of continuous crystallization, the principal risk encountered in such process is fouling and blockage[8,33,35,38,40,42–44], causing major operational and economic issues. Because of its larger surface-area-to-volume, such problem more often occurs in PFC-based systems than in MSMPRs[43].

The reasons of the induction of encrustation can be numerous, and this subject has attracted a lot of attention in the past years, going hand in hand with the growing interest in continuous processes. Among the most common causes, there is the control of nucleation. Indeed, the control of secondary and heterogeneous nucleations is often hardly manageable[3,4,43]. The origin of the crust can also be due to adsorption of the crystals onto a solid surface, or because of local solvent evaporation[43].

In the present case, two main sources were identified. In the first place, the unique CT flow motion can generate small zones where the supersaturation is high, especially when there is a temperature gradient between the two cylinders. Such variations of supersaturation can induce the local deposition of crystals[43]. Secondly, the mixing effects in the entrance zone of the CT crystallizer are probably less efficient because of its conical shape. Areas where the flow velocity is reduced are more prone to encrustation[4,43].

The consequences of the reactor's encrustation are blockage, thermal resistance and, in the end, alteration of the product quality and yield[42–44]. Moreover, in the case of CT crystallizer, the thickness of the crust reduces the gap width between the two cylinders. This parameter is

a key value in the design of a continuous process for CT reactor, and its modification can strongly affect the results. Therefore, the need for efficient solutions to prevent the formation of encrustation seems critical to work safely with a CT crystallizer.

The solutions reported in the literature can be divided in three main categories: equipment-based strategies, preventive actions included in the developed process and analytical control strategies.

The anti-fouling strategy can be thought very early, during the design of the continuous crystallizer. Firstly, the presence of dead zones must be avoided as much as possible. Then, solutions of mechanical cleaning (baffles, scrapers…) or ultrasonic vibration systems can be incorporated to the reactor[42,43], but their impact on the process results must be evaluated. Finally, the inner surfaces have to be checked; the possible use of a coating can be interesting, but it is generally expensive[42,43,124].

The development of the continuous process can also be the opportunity to implement solutions to prevent encrustation. The easiest one to set up is the reduction of the supersaturation ratio. However, this will only delay the encrustation formation, and the mass of collected product will decrease[43,124]. Secondly, the addition of chemical antifoulants or additives has already proven its efficiency. Nonetheless, the impact on the crystallization process must be examined, as well as the eventual restrictions regarding safety, health and environment[42,43,124]. Lastly, a promising solution is the preventive implementation of periodic temperature cycling, carefully designed in order to maintain the continuous operation and ensure the constancy of the product features[8,42–44]. An additional unconventional solution can be cited: if it appears that the crust is at the steady state, and that its thickness is maintained over time, then it may be possible to work with it[43]. However, this added layer must be considered in the process design (temperature regulation, higher wall thickness…).

The last kind of antifouling solutions relies on the analytics. Indeed, Acevedo *et al.* (2019) described in a review the development of an Automated Direct Nucleation Control (ADNC), used in a cooling crystallization process in MSMPR[43]. This system is based on the measurement of the number of chords by FBRM; if the determined number is different of the target, the control system will automatically modifier the temperature of the process. One of the drawbacks of this strategy is the crystal quality, that can be affected by the temperature variations. Another similar example was reported, using cameras instead of FBRM. The principal disadvantage of this analytical technique is that the crust needs to be thick enough to be detected[43].

In the present work, the use of a chemical additive was tested. Since the encrustation was suspected to be due to wettability issues, at the end of the first screening (see section IV.4.3), a wetting agent, Tween 20, was selected. An experiment called M1 was set-up, in the same conditions than O1 (see section IV.4.3.2), with an addition of 10 %w (related to the total mass of solution) of Tween 20. The resulting global yield distribution is shown in Figure IV- 27. The experiment lasted longer, but a blockage was finally encountered, and the same erratic behavior was observed. The amount of Tween 20 could be increased, but at some point, the product crystals may be affected. To date, this potential solution was not taken further.

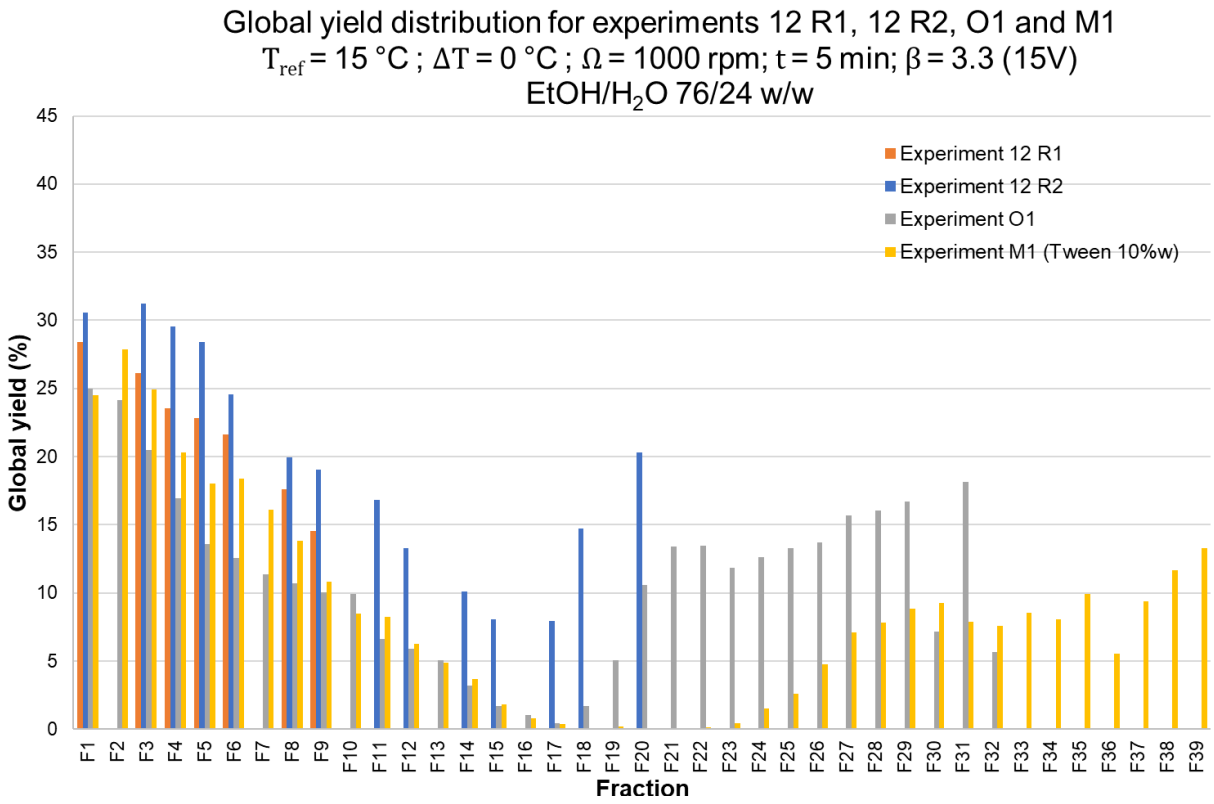

Figure IV- 27: Global yield distribution for experiments 12 R1 (orange), 12 R2 (blue), O1 (grey) and M1 (yellow). Experiment 12 R1 lasted 10 residence times, experiment 12 R2 lasted 20 residence times, experiment O1 lasted 32 residence times and experiment M1 lasted 39 residence times.

Among the antifouling solutions presented above, one seems particularly attractive: the preventive implementation of temperature cycling. Indeed, the use of the temperature increase coupled with pure solvent circulation has already proven its efficiency on blockage (see section IV.4.3). The injection of pure solvent as an effective cleaning procedure was also reported in the literature[42].

In addition, the cleaning liquors could be recycled, to recover the wanted product deposed in the crust. In an ideal set-up, the recycling stream could join that of the filtration liquors.

A simulated solution, based on the preventive temperature cycling and called Simulated Moving Plug Flow Crystallizer (SM-PFC), was presented by Majumder during the congress ECCG7[124]. It consists in a system of four independent PFC segments, that can be connected to work together. The principle is to work with three of them, while the (potentially) encrusted fourth one is cleaned. Therefore, the run would be uninterrupted by the encrustation resolution.

This last simulated design is very interesting, and the idea of applying it to a set-up constituted of CT crystallizers came up. Several CT reactors could be used in parallel on a hypothetical production line. After a defined period (circa 10 residence times), one crystallizer would be disconnected from the others, to undergo a preventive cleaning procedure, i.e., temperature cycle(s) with pure solvent circulation. Afterwards, it would be reconnected to the global system, and the following one would be separated to be cleaned. A minimum of three CT crystallizers seems necessary to maintain the production level, but a number of four would be ideal.

Ideally, the cleaned liquors and the filtration liquors would be recycled. In addition to the yield maximization, this would also limit the CSD impact of temperature cycling[44,124].

Also, the implementation of a longitudinal temperature gradient within the CT crystallizer would ease and probably improve the results of a cooling crystallization process. Indeed, by gradually decreasing the temperature along the reactor, the crystallization would be smoother and easier to control.

To conclude, the best solution to avoid encrustation seems to be the use of temperature cycling. The ideal continuous set-up would include four parallel CT crystallizers, connected but independent. The preventive cleaning procedure (temperature cycling with pure solvent flush) would be periodically applied to each CT reactor, and the cleaned liquors as well as the filtration liquors would be recycled. Finally, each CT crystallizer would have the possibility of performing axial and longitudinal temperature gradient.

The development of such system would imply many considerations to carefully limit the process kinetics variations and to ensure a constant product yield, productivity, and quality. A parallel simulation work could be interesting to potentially help in the orientation of the experimental investigations.

The conclusions about the whole current chapter are presented in the next section.

IV.7. Conclusions and perspectives

Chapter IV presented the work performed on the process of chiral resolution of rac-Ibu by diastereomeric salt formation with *S*-αMBA, in batch and in continuous modes.

Preliminary batch experiments served the development of the first process, in technical ethanol (ethanol at azeotropic composition with 5 %w of H_2O), which was then performed within the CT crystallizer. The first continuous experiments resulted in needle-shaped crystals, unsuitable for filtration process.

To address the filtration troubles encountered in the preliminary CT runs, another batch optimization study was realized, using the Pope and Peachey method with the replacement of a part of *S*-αMBA by soda. The effect on the crystal morphology was clear, since the initial needle-shaped particles became nice platelets crystals.

Also, during these investigations, fluid inclusions were observed in the crystals of *S*-Ibu-*S*-αMBA; their deeper analysis was presented in Chapter II section II.5. In the end, it appeared that contrary to the initial thought, the habit modifier was the water, in which soda was added to the medium, and not soda itself. This latter also appeared to promote the formation of fluid inclusions. Therefore, a new process in a mixture EtOH/H_2O 76/24 w/w and without soda was developed.

This implementation of this new process in the continuous mode was rationalized through a Design of Experiments (DoE) approach. After the definition of the studied factors (ΔT, t, Ω and T_{ref}) and of the analyzed responses (global and diastereomeric productivities and yields, and chiral purity), the first screening was performed. If the statistical analysis provided by the software Azurad were good, the presented conclusions about the influence of each investigated factor were questioned because of encrustation issues.

After some tests, this problem was attributed to wettability in the used solvent mixture.

Since the wettability issues were not observed in the first continuous experiments, performed in azeotropic ethanol, the chiral resolution process was again developed in this solvent (EtOH/H_2O 95/5 w/w mixture). The last results were obtained from standardized batch experiments, in order to be as comparable as possible with the continuous runs.

A second screening design was set up, in technical ethanol, with three of the four factors studied in the first DoE: ΔT, t, Ω. T_{ref} was replaced by the supersaturation level β. This second screening was also the opportunity to study the effect of in-line modification of one process parameter. Some primary conclusions are promising, and the extension of such study could be interesting. Indeed, the in-line change of a parameter can be a useful tool to cure quickly and efficiently a potential issue, without stopping the continuous production.

The main studied responses in the second screening were the same as in the first one. If some conclusions of the first screening were confirmed in the second one, surprising differences were also noted. In both screening, the factor's levels that seem to increase yield and productivity decrease the chiral purity. The reverse is also true. Thereby, the level of the concerned factors, ΔT and t, should be carefully selected.

In addition, in the second screening, the standard deviation of the responses was calculated and integrated to the DoE. This permitted the separated evaluation of the influence

of the studied factors on the variability of each response. Indeed, the factors can have a certain influence on a response, but its impact may be different on the response standard deviation.

For example: the rotation speed Ω seemed to have a negligible influence on the global productivity, but it appeared to have a significant impact on the standard deviation of the global productivity (see Appendix E sections E.2.1 and E.2.3). Therefore, the studied responses and their standard deviation are not always impacted by the investigated factors in the same way.

Sometimes even, as seen in the example, the parameters that have an influence on the response's variability do not have any on the responses themselves. This feature can be very nice, as it means that the modification of a parameter can improve the statistical variability of a response during a given experiment, without affecting the response average value. In a case like the example above, if the average value of the production's global productivity is correct, but fluctuations are observed, the adjustment of the rotation speed could be interesting. Such parameter tuning would reduce the global productivity variability over time, without affecting its average value.

The results of the second screening, as well as the differences observed between the two DoEs suggest the existence of interactions between the studied factors. The number of experiments performed did not permit a proper interaction study. Further investigations in this direction should be done. Moreover, as some factors were identified as interesting to be studied with a surface response, it would be smart to extend the DoE by building a matrix of experiments that could suit both interaction study and surface response. The already realized experiments should be included. In this way, every experiment can be exploited to the maximum.

In further work, another aspect of the crystal features should be added: crystal size and morphology. The effects of the use of the CT crystallizer on these two characteristics would be really interesting to study. Such analyses can be time-consuming, therefore, the installation of in-line probes, such as Blaze Metrics, FBRM or PVM could be an elegant solution.

Nevertheless, the conclusions stated before are questionable since the continuous system appeared to be prone to encrustation. The reflection about this issue, widely discussed in the last section, gave rise to the proposition of an ideal system to perform continuous production in CT crystallizer(s). This would consist in a set-up of four independent CT crystallizers, parallelly connected. Each reactor would be periodically disconnected from the system, to undergo a preventive antifouling cleaning procedure, including temperature cycling and pure solvent circulation. A recycling stream could be implemented to recover the filtration and cleaning liquors. Finally, to better control the crystallization process, each CT crystallizer would have the possibility of performing axial and longitudinal temperature gradient.

General conclusion and some perspectives

The main objective of the present work was to implement the chiral resolution of racemic Ibuprofen (rac-Ibu) by diastereomeric salt formation with *S*-αMethylBenzylAmine (*S*-αMBA) in a continuous crystallizer called Couette-Taylor crystallizer. Because of its unique flow motion, the CT reactors can provide excellent mass and heat transfer rates. Previous results obtained on deracemization processes were promising regarding the implementation of chiral resolution by crystallization processes in CT crystallizers, especially in the cases of compounds produced at large scale, like Ibuprofen.

Firstly, the system to resolve was investigated, which led to the revision of the phase diagram between the two diastereomers *S*-Ibu-*S*-αMBA and *R*-Ibu-*S*-αMBA: a partial solid solution on the side of the less soluble salt was evidenced.

The crystals belonging to the partial solid solution domain exhibit a surprising fibrous aspect. This latter was studied, arousing a discussion around the qualification as single crystals of these fibers' aggregates. A growth mechanism was proposed, but further experiments are necessary to probate it.

Also, in certain process conditions, the particles of *S*-Ibu-*S*-αMBA present biphasic fluid inclusions. They appeared to be constituted of the mother liquors and of (a) persistent bubble(s). The investigations performed around the formation of the fluid inclusions served the formulation of a procedure to prevent it.

Before starting the Couette-Taylor experiments, the continuous set-up was carefully examined. To respect the identified feeding constraints, a prototype mixing and heating the two feeding solutions was designed, in two different versions, since the first one appeared to be inefficient regarding mixing.

Some improvements were also directly made on the Couette-Taylor environment.

Finally, the chiral resolution process of rac-Ibu with *S*-αMBA was studied in batch and in continuous mode. The continuous investigations were rationalized through two different designs of experiments (DoE), in order to determine the impact of five of the seven parameters identified as potential DoE factors: ΔT, t, Ω, T_{ref} and β.

Unsurprisingly, the yield of continuous experiments is about 2 times lower in comparison with batch mode. Nevertheless, it is largely counterbalanced by productivity, therefore, this drawback can be limited by the implementation of a recycling system of the mother liquors in a lower domain of temperatures. Indeed, in the suitable process conditions, the continuous mode outstandingly improves the productivity by a minimum of 1.5 times, and up to 30 times. Also, diastereomeric purity appeared to be enhanced by 18 % on average. By transferring the process from batch to continuous mode the access to high diastereomeric excesses seems ensured, in a repeatable manner.

If some trends could be determined about the influence of the studied parameters, the continuous process development was unfortunately disturbed by a classical continuous mode drawback: encrustation. This issue is bothersome since the thickness of the crust affects the gap width between the two cylinders. The further work should give the priority to encrustation prevention.

The encrustation issue and potential solutions were extensively discussed at the end of the last chapter. An ideal CT set-up was concepted, consisting in the association of four

independent CT device, connected in parallel, with the possibility of disconnecting one without affecting the others. The disconnected reactor would undergo a preventive antifouling cleaning procedure, including temperature cycling and pure solvent circulation. To prevent the encrustation risk, each CT crystallizer would be periodically disconnected to the system. A cleaning procedure of 30 min (5 min at 40 °C then 25 min to go back to the initial temperature) with a flush of solvent should be sufficient. Considering it, the productivity would still be exceptionally enhanced up to 25 times, in comparison with batch mode.

Also, in view of improving the yield, a recycling stream could be implemented to recover the filtration and cleaning liquors. Finally, to better control the crystallization process, each CT crystallizer would have the possibility of performing axial and longitudinal temperature gradient.

While the prevention of encrustation is of paramount importance, another aspect of continuous installation must also be considered: filtration. The set-up of continuous filtration seems mandatory to implement a proper continuous process. In addition, this would give a technical access to shorter residence times, which are generally suitable in plug flow systems[10]. Continuous filtration device were already reported in the literature, and even commercialized, like continuous filtration carousel (CFC).

Other set-up improvements should be studied, like the 'update' of the mixing prototype towards a more industrial design, the pumping part, and the hoses connecting the thermostats to the different parts.

Also, the incapacity to 'see' what can occur within the CT crystallizer can strongly delay the detection and resolution of potential issue during the continuous experiments. In view of that, the installation of in-line probes such as Blaze Metrics, FBRM, PVM or fiber optic camera could be really interesting. In the case of encrustation, such tools would give the possibility to localize the zone where the crystals deposition starts, which can help the design of the most suitable solution. The use of glass-made CT reactors can also be considered.

In a general manner, the implementation of a process in the continuous mode requires some optimization investigations. This mode implies the set-up of long experiments, which should be carefully prepared, to limit the occurrence of failed runs. Therefore, the related studies can be time-consuming. However, this can largely be counterbalanced by the benefits of the switch to the continuous production mode.

The use of a DoE approach to rationalize a continuous study seems adapted, regarding the number of parameters that can impact the process results. Nevertheless, this methodology is maybe more suitable to experiments that can be rapidly set-up and performed. Thereby, the ratio benefits / time consumption of its implementation for long continuous experiments should be carefully examined.

References

(1) Coquerel, G. The 'Structural Purity' of Molecular Solids—An Elusive Concept? *Chem. Eng. Process* **2006**, *45* (10), 857–862. https://doi.org/10.1016/j.cep.2005.10.011.
(2) Lifshitz, R. What Is a Crystal? *Zeitschrift für Kristallographie* **2007**, *222* (6), 313–317. https://doi.org/10.1524/zkri.2007.222.6.313.
(3) Biscans, B. Cristallisation en solution - Procédés et types d'appareils. *T. I.* **2013**, *TIP598WEB* (J2788 V2). https://doi.org/10.51257/a-v2-j2788.
(4) Klein, J.-P.; Boistelle, R.; Dugua, J. Cristallisation industrielle - Aspects pratiques. *T. I.* **1994**, No. J2788 V1.
(5) Puel, F.; Veesler, S.; Mangin, D. Cristallisation - Aspects théoriques. *T. I.* **2005**, *TIP452WEB* (J2710 V2). https://doi.org/10.51257/a-v2-j2710.
(6) Coquerel, G. Crystallization of Molecular Systems from Solution: Phase Diagrams, Supersaturation and Other Basic Concepts. *Chem. Soc. Rev.* **2014**, *43* (7), 2286–2300. https://doi.org/10.1039/C3CS60359H.
(7) Couvrat, N.; Sanselme, M.; Poupard, M.; Bensakoun, C.; Drouin, S. H.; Schneider, J.-M.; Coquerel, G. Solid-State Overview of R-Baclofen: Relative Stability of Forms A, B and C and Characterization of a New Heterosolvate. *J. Pharm. Sci.* **2021**, *110* (10), 3457–3463. https://doi.org/10.1016/j.xphs.2021.06.018.
(8) Zhang, D.; Xu, S.; Du, S.; Wang, J.; Gong, J. Progress of Pharmaceutical Continuous Crystallization. *Engineering* **2017**, *3* (3), 354–364. https://doi.org/10.1016/J.ENG.2017.03.023.
(9) Liu, Y. C.; Domokos, A.; Coleman, S.; Firth, P.; Nagy, Z. K. Development of Continuous Filtration in a Novel Continuous Filtration Carousel Integrated with Continuous Crystallization. *Org. Process Res. Dev.* **2019**, *23* (12), 2655–2665. https://doi.org/10.1021/acs.oprd.9b00342.
(10) Rougeot, C.; Hein, J. E. Application of Continuous Preferential Crystallization to Efficiently Access Enantiopure Chemicals. *Org. Process Res. Dev.* **2015**, *19* (12), 1809–1819. https://doi.org/10.1021/acs.oprd.5b00141.
(11) Wang, Y.; Chen, A. Crystallization-Based Separation of Enantiomers. In *Stereoselective Synthesis of Drugs and Natural Products*; Andrushko, V., Andrushko, N., Eds.; John Wiley & Sons, Inc.: Hoboken, NJ, USA, 2013; pp 1663–1682. https://doi.org/10.1002/9781118596784.ssd056.
(12) Kirkiacharian, S. Chiralité et médicaments. *T. I.* **2005**, *TIP598WEB* (P3340 V1). https://doi.org/10.51257/a-v1-p3340.
(13) Srisanga, S.; ter Horst, J. H. Racemic Compound, Conglomerate, or Solid Solution: Phase Diagram Screening of Chiral Compounds. *Cryst. Growth Des.* **2010**, *10* (4), 1808–1812. https://doi.org/10.1021/cg901483v.
(14) Eriksson, T.; Björkman, S.; Höglund, P. Clinical Pharmacology of Thalidomide. *Eur. J. Clin. Pharmacol.* **2001**, *57* (5), 365–376. https://doi.org/10.1007/s002280100320.
(15) Lorenz, H.; Temmel, E.; Seidel-Morgenstern, A. CHAPTER 12 Continuous Enantioselective Crystallization of Chiral Compounds. In *The Handbook of Continuous Crystallization*; The Royal Society of Chemistry, 2020; pp 422–468. https://doi.org/10.1039/9781788013581-00422.
(16) Ciriani, M.; Oliveira, R.; Afonso, C. A. M. Semi-Continuous and Continuous Processes for Enantiomeric Separation. *Green Chem.* **2022**, *24* (11), 4328–4362. https://doi.org/10.1039/D1GC03668H.
(17) Siedlecka, R. Recent Developments in Optical Resolution. *Tetrahedron* **2013**, *69* (31), 6331–6363. https://doi.org/10.1016/j.tet.2013.05.035.
(18) Coquerel, G. Chiral Discrimination in the Solid State: Applications to Resolution and Deracemization. In *Advances in Organic Crystal Chemistry: Comprehensive Reviews 2015*; Tamura, R., Miyata, M., Eds.; Springer Japan: Tokyo, 2015; pp 393–420. https://doi.org/10.1007/978-4-431-55555-1_20.
(19) Fogassy, E.; Nógrádi, M.; Kozma, D.; Egri, G.; Pálovics, E.; Kiss, V. Optical Resolution Methods. *Org. Biomol. Chem.* **2006**, *4* (16), 3011–3030. https://doi.org/10.1039/b603058k.
(20) Faigl, F.; Fogassy, E.; Nógrádi, M.; Pálovics, E.; Schindler, J. Strategies in Optical Resolution: A Practical Guide. *Tetrahedron: Asymmetry* **2008**, *19* (5), 519–536. https://doi.org/10.1016/j.tetasy.2008.02.004.
(21) Coquerel, G. Preferential Crystallization. In *Novel Optical Resolution Technologies*; Sakai, K., Hirayama, N., Tamura, R., Eds.; Topics in Current Chemistry; Springer-Verlag Berlin Heidelberg: Berlin, Heidelberg, 2006; Vol. 269, pp 1–51. https://doi.org/10.1007/128_2006_077.
(22) Coquerel, G.; Hoquante, M. Spontaneous and Controlled Macroscopic Chiral Symmetry Breaking by Means of Crystallization. *Symmetry* **2020**, *12* (11), 1796. https://doi.org/10.3390/sym12111796.
(23) Oketani, R.; Hoquante, M.; Brandel, C.; Cardinael, P.; Coquerel, G. Resolution of an Atropisomeric Naphthamide by Second-Order Asymmetric Transformation: A Highly Productive Technique. *Org. Process Res. Dev.* **2019**, *23* (6), 1197–1203. https://doi.org/10.1021/acs.oprd.9b00133.
(24) Pasteur, L. Transformation Des Acides Tartriques En Acide. Découverte de l'acide Tartrique Inactif. Nouvelle Méthode de Séparation de l'acide Racémique En Acides Tartriques Droit et Gauche. *CR Acad. Sci.* **1853**, *37*.
(25) Viedma, C.; Coquerel, G.; Cintas, P. 22 - Crystallization of Chiral Molecules. In *Handbook of Crystal Growth (Second Edition)*; Nishinaga, T., Ed.; Elsevier: Boston, 2015; pp 951–1002. https://doi.org/10.1016/B978-0-444-56369-9.00022-8.
(26) Sakai, K.; Sakurai, R.; Hirayama, N. Molecular Mechanisms of Dielectrically Controlled Resolution (DCR). In *Novel Optical Resolution Technologies*; Sakai, K., Hirayama, N., Tamura, R., Eds.; Topics in Current Chemistry; Springer: Berlin, Heidelberg, 2007; pp 233–271. https://doi.org/10.1007/128_071.
(27) Wilen, S. H.; Davidson, R.; Spector, R.; Steffanou, H. Application of the Procedure of Pope and Peachey to the Resolution of Alcohols. *J. Chem. Soc. D* **1969**, No. 11, 603–604. https://doi.org/10.1039/c29690000603.

(28) Pope, W. J.; Peachey, S. J. The Application of Powerful Optically Active Acids to the Resolution of Externally Compensated Basic Substances. Resolution of Tetrahydroquinaldine. *J. Chem. Soc., Trans.* **1899**, *75*, 1066–1093. https://doi.org/10.1039/CT8997501066.
(29) Marckwald, W. Ueber Ein Bequemes Verfahren Zur Gewinnung Der Linksweinsäure. *Berichte der deutschen chemischen Gesellschaft* **1896**, *29* (1), 42–43. https://doi.org/10.1002/cber.18960290106.
(30) Hughes, D. L. Applications of Flow Chemistry in Drug Development: Highlights of Recent Patent Literature. *Org. Process Res. Dev.* **2018**, *22* (1), 13–20. https://doi.org/10.1021/acs.oprd.7b00363.
(31) Hughes, D. L. Applications of Flow Chemistry in the Pharmaceutical Industry—Highlights of the Recent Patent Literature. *Org. Process Res. Dev.* **2020**, *24* (10), 1850–1860. https://doi.org/10.1021/acs.oprd.0c00156.
(32) Badman, C.; Cooney, C. L.; Florence, A.; Konstantinov, K.; Krumme, M.; Mascia, S.; Nasr, M.; Trout, B. L. Why We Need Continuous Pharmaceutical Manufacturing and How to Make It Happen. *J. Pharm. Sci.* **2019**, *108* (11), 3521–3523. https://doi.org/10.1016/j.xphs.2019.07.016.
(33) Wood, B.; Girard, K. P.; Polster, C. S.; Croker, D. M. Progress to Date in the Design and Operation of Continuous Crystallization Processes for Pharmaceutical Applications. *Org. Process Res. Dev.* **2019**, *23* (2), 122–144. https://doi.org/10.1021/acs.oprd.8b00319.
(34) Cole, K. P.; Johnson, M. D. Continuous Flow Technology vs. the Batch-by-Batch Approach to Produce Pharmaceutical Compounds. *Expert Rev. Clin. Pharmacol.* **2018**, *11* (1), 5–13. https://doi.org/10.1080/17512433.2018.1413936.
(35) Wang, T.; Lu, H.; Wang, J.; Xiao, Y.; Zhou, Y.; Bao, Y.; Hao, H. Recent Progress of Continuous Crystallization. *J. Ind. Eng. Chem.* **2017**, *54* (25), 14–29. https://doi.org/10.1016/j.jiec.2017.06.009.
(36) Su, Q.; Nagy, Z. K.; Rielly, C. D. Pharmaceutical Crystallisation Processes from Batch to Continuous Operation Using MSMPR Stages: Modelling, Design, and Control. *Chem. Eng. Process.* **2015**, *89*, 41–53. https://doi.org/10.1016/j.cep.2015.01.001.
(37) Tężyk, M.; Milanowski, B.; Ernst, A.; Lulek, J. Recent Progress in Continuous and Semi-Continuous Processing of Solid Oral Dosage Forms: A Review. *Drug Dev. Ind. Pharm.* **2016**, *42* (8), 1195–1214. https://doi.org/10.3109/03639045.2015.1122607.
(38) Ma, Y.; Wu, S.; Macaringue, E. G. J.; Zhang, T.; Gong, J.; Wang, J. Recent Progress in Continuous Crystallization of Pharmaceutical Products: Precise Preparation and Control. *Org. Process Res. Dev.* **2020**, *24* (10), 1785–1801. https://doi.org/10.1021/acs.oprd.9b00362.
(39) Rogers, L.; Jensen, K. F. Continuous Manufacturing – the Green Chemistry Promise? *Green Chem.* **2019**, *21* (13), 3481–3498. https://doi.org/10.1039/C9GC00773C.
(40) Rivera, N. R.; Kassim, B.; Grigorov, P.; Wang, H.; Armenante, M.; Bu, X.; Lekhal, A.; Variankaval, N. Investigation of a Flow Step Clogging Incident: A Precautionary Note on the Use of THF in Commercial-Scale Continuous Process. *Org. Process Res. Dev.* **2019**, *23* (11), 2556–2561. https://doi.org/10.1021/acs.oprd.9b00366.
(41) Baumann, M.; Moody, T. S.; Smyth, M.; Wharry, S. A Perspective on Continuous Flow Chemistry in the Pharmaceutical Industry. *Org. Process Res. Dev.* **2020**, *24* (10), 1802–1810. https://doi.org/10.1021/acs.oprd.9b00524.
(42) Majumder, A.; Nagy, Z. K. Dynamic Modeling of Encrust Formation and Mitigation Strategy in a Continuous Plug Flow Crystallizer. *Cryst. Growth Des.* **2015**, *15* (3), 1129–1140. https://doi.org/10.1021/cg501431c.
(43) Acevedo, D.; Yang, X.; Liu, Y. C.; O'Connor, T. F.; Koswara, A.; Nagy, Z. K.; Madurawe, R.; Cruz, C. N. Encrustation in Continuous Pharmaceutical Crystallization Processes—A Review. *Org. Process Res. Dev.* **2019**, *23* (6), 1134–1142. https://doi.org/10.1021/acs.oprd.9b00072.
(44) Koswara, A.; Nagy, Z. K. Anti-Fouling Control of Plug-Flow Crystallization via Heating and Cooling Cycle. *IFAC-PapersOnLine* **2015**, *48* (8), 193–198. https://doi.org/10.1016/j.ifacol.2015.08.180.
(45) Chandrasekhar, S. Chapter VII The Stability of Couette Flow. In *Hydrodynamic and Hydromagnetic Stability*; Chandrasekhar, S., Ed.; Clarendon Press: Oxford University Press: Oxford, 1961; pp 272–342.
(46) Donnelly, R. J.; Fultz, D. Experiments on the Stability of Viscous Flow between Rotating Cylinders II. Visual Observations. *Proc. R. Soc. Lond. A* **1960**, *258* (1292), 101–123. https://doi.org/10.1098/rspa.1960.0177.
(47) Couette, M. Distinction de deux régimes dans le mouvement des fluides. *J. Phys. Theor. Appl.* **1890**, *9* (1), 414–424. https://doi.org/10.1051/jphystap:018900090041401.
(48) Charru, F. 4.4 Instabilité centrifuge de Couette-Taylor. In *Instabilités hydrodynamiques*; EDP Sciences: Paris, France, 2007.
(49) Taylor, G. I. Stability of a Viscous Liquid Contained between Two Rotating Cylinders. *Phil. Trans. R. Soc. A Philos. Trans. R. Soc. A-Math. Phys. Eng. Sci.* **1923**, *223* (605–615), 289–343. https://doi.org/10.1098/rsta.1923.0008.
(50) Kim, W.-S. Application of Taylor Vortex to Crystallization. *J. Chem. Eng. Japan* **2014**, *47* (2), 115–123. https://doi.org/10.1252/jcej.13we143.
(51) Nguyen, A.-T.; Yu, T.; Kim, W.-S. Couette-Taylor Crystallizer: Effective Control of Crystal Size Distribution and Recovery of l-Lysine in Cooling Crystallization. *J. Cryst. Growth* **2017**, *469* (1), 65–77. https://doi.org/10.1016/j.jcrysgro.2016.10.020.
(52) Sparrow, E. M.; Munro, W. D.; Jonsson, V. K. Instability of the Flow between Rotating Cylinders: The Wide-Gap Problem. *J. Fluid Mech.* **1964**, *20* (1), 35–46. https://doi.org/10.1017/S0022112064001008.
(53) Donnelly, R. J.; Schwarz, K. W. Experiments on the Stability of Viscous Flow between Rotating Cylinders - VI. Finite-Amplitude Experiments. *Proc. R. Soc. Lond. A* **1965**, *283* (1395), 531–556. https://doi.org/10.1098/rspa.1965.0044.

(54) Kataoka, K. CHAPTER 9. TAYLOR VORTICES AND INSTABILITIES IN CIRCULAR COUETTE FLOWS. In *Encyclopedia Of Fluid Mechanics Vol-1*; Cheremisinoff, N. P., Ed.; Houston, 1986; Vol. 1, pp 237–274.

(55) Maron, D. M.; Cohen, S. Hydrodynamics and Heat/Mass Transfer near Rotating Surfaces. In *Advances in Heat Transfer*; Hartnett, J. P., Irvine, T. F., Cho, Y. I., Eds.; Elsevier, 1991; Vol. 21, pp 141–183. https://doi.org/10.1016/S0065-2717(08)70335-6.

(56) Kang, S. H.; Lee, S. G.; Jung, W. M.; Kim, M. C.; Kim, W.-S.; Choi, C. K.; Feigelson, R. S. Effect of Taylor Vortices on Calcium Carbonate Crystallization by Gas–Liquid Reaction. *J. Cryst. Growth* **2003**, *254* (1–2), 196–205. https://doi.org/10.1016/S0022-0248(03)01152-7.

(57) Nguyen, A.-T.; Kim, J.-M.; Chang, S.-M.; Kim, W.-S. Taylor Vortex Effect on Phase Transformation of Guanosine 5-Monophosphate in Drowning-Out Crystallization. *Ind. Eng. Chem. Res.* **2010**, *49* (10), 4865–4872. https://doi.org/10.1021/ie901932t.

(58) Thai, D. K.; Mayra, Q.-P.; Kim, W.-S. Agglomeration of Ni-Rich Hydroxide Crystals in Taylor Vortex Flow. *Powder Technol.* **2015**, *274*, 5–13. https://doi.org/10.1016/j.powtec.2015.01.008.

(59) Nguyen, A.-T.; Joo, Y. L.; Kim, W.-S. Multiple Feeding Strategy for Phase Transformation of GMP in Continuous Couette–Taylor Crystallizer. *Cryst. Growth Des.* **2012**, *12* (6), 2780–2788. https://doi.org/10.1021/cg201361e.

(60) Park, S.-A.; Lee, S.; Kim, W.-S. Polymorphic Crystallization of Sulfamerazine in Taylor Vortex Flow: Polymorphic Nucleation and Phase Transformation. *Cryst. Growth Des.* **2015**, *15* (8), 3617–3627. https://doi.org/10.1021/acs.cgd.5b00002.

(61) Kim, W.-S.; Yu, T.; Whu, Z. Method for Conductiong Deracemization Using Taylor Flow and a Device Therefor. 10,106,408, October 23, 2018.

(62) Wu, Z.; Seok, S.; Kim, D. H.; Kim, W.-S. Control of Crystal Size Distribution Using Non-Isothermal Taylor Vortex Flow. *Cryst. Growth Des.* **2015**, *15* (12), 5675–5684. https://doi.org/10.1021/acs.cgd.5b00431.

(63) Marc, L.; Guillemer, S.; Schneider, J.-M.; Coquerel, G. Continuous Chiral Resolution of Racemic Ibuprofen by Diastereomeric Salt Formation in a Couette-Taylor Crystallizer. *Chem. Eng. Res. Des.* **2022**, *178*, 95–110. https://doi.org/10.1016/j.cherd.2021.12.016.

(64) Chandrasekhar, S. The Stability of Viscous Flow between Rotating Cylinders. *Mathematika* **1954**, *1* (1), 5–13. https://doi.org/10.1112/S0025579300000474.

(65) Chandrasekhar, S. The Stability of Viscous Flow between Rotating Cylinders. *Proc. R. Soc. Lond. A* **1958**, *246* (1246), 301–311. https://doi.org/doi.org/10.1098/rspa.1958.0139.

(66) Donnelly, R. J. Experiments on the Stability of Viscous Flow between Rotating Cylinders I. Torque Measurements. *Proc. R. Soc. Lond. A* **1958**, *246* (1246), 312–325. https://doi.org/10.1098/rspa.1958.0140.

(67) Chandrasekhar, S.; Elbert, D. D. The Stability of Viscous Flow between Rotating Cylinders. II. *Proc. R. Soc. Lond. A* **1962**, *268* (1333), 145–152. https://doi.org/10.1098/rspa.1962.0131.

(68) Donnelly, R. J. Experiments on the Stability of Viscous Flow between Rotating Cylinders III. Enhancement of Stability by Modulation. *Proc. R. Soc. Lond. A* **1964**, *281* (1384), 130–139. https://doi.org/10.1098/rspa.1964.0173.

(69) Walowit, J.; Tsao, S.; DiPrima, R. C. Stability of Flow Between Arbitrarily Spaced Concentric Cylindrical Surfaces Including the Effect of a Radial Temperature Gradient. *J. Appl. Mech.* **1964**, *31* (4), 585–593. https://doi.org/10.1115/1.3629718.

(70) Donnelly, R. J.; Tanner, D. J. Experiments on the Stability of Viscous Flow between Rotating Cylinders. - V. The Theory of the Ion Technique. *Proc. R. Soc. Lond. A* **1965**, *283* (1395), 520–530. https://doi.org/10.1098/rspa.1965.0043.

(71) Donnelly, R. J. Experiments on the Stability of Viscous Flow between Rotating Cylinders - IV. The Ion Technique. *Proc. R. Soc. Lond. A* **1965**, *283* (1395), 509–519. https://doi.org/10.1098/rspa.1965.0042.

(72) Ali, M. A. The Stability of Couette Ow with an Inner Cylinder Rotating and Moving with a Constant Axial Velocity. *Fluid Dyn. Res.* **2000**, *27*, 109–115.

(73) Adebayo, D.; Al-Ameri, J.; Tyukin, I.; Rona, A. Linear Stability Analysis of the Flow between Rotating Cylinders of Wide Gap. *Eur. J. Mech. B Fluids* **2018**, *72*, 567–575. https://doi.org/10.1016/j.euromechflu.2018.07.002.

(74) Wu, Z.; Kim, D. H.; Kim, W.-S. Batch Cooling Crystallization in Non-Isothermal Taylor Vortex Flow: Effective Method for Controlling Crystal Size Distribution. *Cryst. Growth Des.* **2017**, *17* (1), 28–36. https://doi.org/10.1021/acs.cgd.6b00821.

(75) Park, S.; Kim, W.-S. Influence of Fluid Motions on Polymorphic Crystallization of L-Histidine: Taylor Vortex Flow and Turbulent Eddy Flow. *Cryst. Growth Des.* **2018**, *18* (2), 710–722. https://doi.org/10.1021/acs.cgd.7b01067.

(76) Schindler, M. Deracémisation Du Chlorate de Sodium Avec et sans l'influence Du Dithionate de Sodium. PhD thesis, Université de Rouen Normandie, Rouen, 2020.

(77) Hermans, T. M.; Bishop, K. J. M.; Stewart, P. S.; Davis, S. H.; Grzybowski, B. A. Vortex Flows Impart Chirality-Specific Lift Forces. *Nat. Commun.* **2015**, *6* (1), 5640. https://doi.org/10.1038/ncomms6640.

(78) Hermans, T. M.; Sato, A.; Marichez, V. Method for Chiral Resolution and Device Therefor. 10,597,339, March 24, 2020.

(79) Marichez, V.; Tassoni, A.; Cameron, R. P.; Barnett, S. M.; Eichhorn, R.; Genet, C.; Hermans, T. M. Mechanical Chiral Resolution. *Soft Matter* **2019**, *15* (23), 4593–4608. https://doi.org/10.1039/C9SM00778D.

(80) Evans, A. M. Comparative Pharmacology of S(+)-Ibuprofen and (RS)-Ibuprofen. *Clin. Rheumatol.* **2001**, *20* (1), 9–14. https://doi.org/10.1007/BF03342662.

(81) Bhattacharya, A.; Murphy, D. Temperature Selective Diastereo-Recognition (TSD): Enantiomeric Ibuprofen via Environmentally Benign Selective Crystallization. *Org. Process Res. Dev.* **2003**, *7* (5), 717–722. https://doi.org/10.1021/op030203i.
(82) Carvalho, P. O.; Cass, Q. B.; Calafatti, S. A.; Contesini, F. J.; Bizaco, R. Review- Alternatives for the Separation of Drug Enantiomers: Ibuprofen as a Model Compound. *Braz. J. Chem. Eng.* **2006**, *23* (3), 291–300. https://doi.org/10.1590/S0104-66322006000300003.
(83) Lemmerer, A.; Bourne, S. A.; Caira, M. R.; Cotton, J.; Hendricks, U.; Peinke, L. C.; Trollope, L. Incorporating Active Pharmaceutical Ingredients into a Molecular Salt Using a Chiral Counterion. *CrystEngComm* **2010**, *12* (11), 3634. https://doi.org/10.1039/c0ce00043d.
(84) Sánchez, A.; Valero, F.; Lafuente, J.; Solà, C. Highly Enantioselective Esterification of Racemic Ibuprofen in a Packed Bed Reactor Using Immobilised Rhizomucor Miehei Lipase. *Enzyme Microb. Technol.* **2000**, *27* (1–2), 157–166. https://doi.org/10.1016/S0141-0229(00)00207-6.
(85) Long, W. S.; Kamaruddin, A.; Bhatia, S. Chiral Resolution of Racemic Ibuprofen Ester in an Enzymatic Membrane Reactor. *J. Membr. Sci.* **2005**, *247* (1–2), 185–200. https://doi.org/10.1016/j.memsci.2004.09.019.
(86) Simon, M.; Wood, B.; Ferguson, S.; Glennon, B.; Jones, R. C. Diastereomeric Salt Crystallization of Chiral Molecules via Sequential Coupled-Batch Operation. *AIChE J.* **2019**, *65* (2), 604–616. https://doi.org/10.1002/aic.16466.
(87) Ebbers, E. J.; Plum, B. J. M.; Ariaans, G. J. A.; Kaptein, B.; Broxterman, Q. B.; Bruggink, A.; Zwanenburg, B. New Resolving Bases for Ibuprofen and Mandelic Acid: Qualification by Binary Phase Diagrams. *Tetrahedron: Asymmetry* **1997**, *8* (24), 4047–4057. https://doi.org/10.1016/S0957-4166(97)00557-0.
(88) Nessim, R. I. Applicability of the Schroeder-van Laar Relation to Multi-Mixtures of Liquid Crystals of the Phenyl Benzoate Type. *Thermochimica Acta* **2000**, *343* (1), 1–6. https://doi.org/10.1016/S0040-6031(99)00309-3.
(89) Marc, L.; Lopes, C.; Schneider, J.-M.; Sanselme, M.; Coquerel, G. Impact of a Partial Solid Solution and Water Molecules on the Formation of Fibrous Crystals and Fluid Inclusions. *Crystals* **2021**, *11* (10), 1188. https://doi.org/10.3390/cryst11101188.
(90) Molnár, P.; Bombicz, P.; Varga, C.; Bereczki, L.; Székely, E.; Pokol, G.; Fogassy, E.; Simándi, B. Influence of Benzylamine on the Resolution of Ibuprofen with (+)-(R)-Phenylethylamine via Supercritical Fluid Extraction. *Chirality* **2009**, *21* (6), 628–636. https://doi.org/10.1002/chir.20655.
(91) Kaemmerer, H.; Lorenz, H.; Black, S. N.; Seidel-Morgenstern, A. Study of System Thermodynamics and the Feasibility of Chiral Resolution of the Polymorphic System of Malic Acid Enantiomers and Its Partial Solid Solutions. *Cryst. Growth Des.* **2009**, *9* (4), 1851–1862. https://doi.org/10.1021/cg8010508.
(92) Polyzois, H.; Guo, R.; Srirambhatla, V. K.; Warzecha, M.; Prasad, E.; Turner, A.; Halbert, G. W.; Keating, P.; Price, S. L.; Florence, A. J. Crystal Structure and Twisted Aggregates of Oxcarbazepine Form III. *Cryst. Growth Des.* **2022**, *22* (7), 4146–4156.
(93) Donnay, J. D. H.; Harker, D. A New Law of Crystal Morphology Extending the Law of Bravais. *Am. Mineral.* **1937**, *22* (5), 446–467.
(94) Taratin, N. V.; Lorenz, H.; Kotelnikova, E. N.; Glikin, A. E.; Galland, A.; Dupray, V.; Coquerel, G.; Seidel-Morgenstern, A. Mixed Crystals in Chiral Organic Systems: A Case Study on (*R*)- and (*S*)-Ethanolammonium 3-Chloromandelate. *Crystal Growth & Design* **2012**, *12* (12), 5882–5888. https://doi.org/10.1021/cg3003405.
(95) Zhou, J.; Hao, L.; Hao, H.; Ji, X.; Li, J.; Zhou, L. Formation Mechanism of Liquid Inclusions in Dicumyl Peroxide Crystals. *CrystEngComm* **2021**, *23* (23), 4214–4228. https://doi.org/10.1039/D1CE00437A.
(96) Wang, Y.; Li, H.; Raikes, M.; Linehan, B.; Robson, J.; Nordstrom, F. L. Formation of Macrotubular Crystals of Salicylic Acid through Ripening of Solid Solution Crystals Containing Impurity Gradients. *Cryst. Growth Des.* **2021**, *21* (7), 4100–4110. https://doi.org/10.1021/acs.cgd.1c00399.
(97) Bobo, E. Contribution on the Formation and the Behaviors of Fluid Inclusions in Crystals. PhD thesis, Université de Rouen Normandie, Rouen, 2016.
(98) Waldschmidt, A. Mécanisme de formation d'inclusions fluides lors de la croissance cristalline de molécules organiques: L'effet inattendu des gaz comme inhibiteurs de croissance. PhD thesis, Université de Rouen Normandie, Rouen, 2011.
(99) Mullin, J. W. *Crystallization*, 3rd Edition.; Butterworth-Heinemann: Oxford, 1993.
(100) Zhang, G. G. Z.; Grant, D. J. W. Formation of Liquid Inclusions in Adipic Acid Crystals during Recrystallization from Aqueous Solutions. *Cryst. Growth Des.* **2005**, *5* (1), 319–324. https://doi.org/10.1021/cg049868h.
(101) Brandel, C.; Gbabode, G.; Cartigny, Y.; Martin, C.; Gouhier, G.; Petit, S.; Coquerel, G. Crystal Growth, Structure, and Polymorphic Behavior of an Ionic Liquid: Phthalate Derivative of *N* -Butyl, *N* -Methylimidazolium Hexafluorophosphate. *Chem. Mater.* **2014**, *26* (14), 4151–4162. https://doi.org/10.1021/cm501220x.
(102) Bobo, E.; Petit, S.; Coquerel, G. Growth Rate Dispersion at the Single-Crystal Level. *Chem. Eng. Technol.* **2015**, *38* (6), 1011–1016. https://doi.org/10.1002/ceat.201400766.
(103) Yan, S.; Xie, C.; Zhang, X.; Zhou, L.; Hou, B.; Huang, J.; Zhou, L.; Yin, Q. Influence of Crystal Growth Conditions on Formation of Macroscopic Inclusions inside Thiourea Crystals. *ChemistrySelect* **2018**, *3* (8), 2293–2297. https://doi.org/10.1002/slct.201702679.
(104) Saito, N.; Yokota, M.; Sato, A.; Kubota, N. Growth Enhancement and Liquid-Inclusion Formation by Contacts on NaCl Crystal. *AIChE J.* **1999**, *45* (5), 1153–1156.
(105) Saito, N.; Yokota, M.; Fujiwara, T.; Kubota, N. Liquid Inclusions in Crystals Produced in Suspension Crystallization. *Chem. Eng. J.* **2000**, *79* (1), 53–59. https://doi.org/10.1016/S1385-8947(00)00143-1.

(106) Waldschmidt, A.; Dupray, V.; Berton, B.; Couvrat, N.; Petit, S.; Coquerel, G. Incidence of Crystal Growth Conditions on the Formation of Macroscopic Liquid Inclusions in Ciclopirox Crystals. *J. Cryst. Growth* **2012**, *342* (1), 72–79. https://doi.org/10.1016/j.jcrysgro.2011.02.047.
(107) Cooper, J.; Borne, L.; Coquerel, G. Antisolvent Addition: An Effective Method of Controlled Fluid Inclusion Formation in RDX Crystals. *Cryst. Growth Des.* **2020**, *20* (11), 7120–7128. https://doi.org/10.1021/acs.cgd.0c00604.
(108) Kim, J.-W.; Kim, J.-K.; Kim, H.-S.; Koo, K.-K. Application of Internal Seeding and Temperature Cycling for Reduction of Liquid Inclusion in the Crystallization of RDX. *Org. Process Res. Dev.* **2011**, *15* (3), 602–609. https://doi.org/10.1021/op100334y.
(109) Kim, J.-W.; Kim, J.-K.; Kim, H.-S.; Koo, K.-K. Characterization of Liquid Inclusion of RDX Crystals with a Cooling Crystallization. *Cryst. Growth Des.* **2009**, *9* (6), 2700–2706. https://doi.org/10.1021/cg801343b.
(110) Wang, Y.; Zhang, N.; Hou, B.; Yin, Q.; Gong, J.; Tang, W. Effect of Crystal Growth Kinetics on the Formation of Liquid Inclusions in Tetramethylpyrazine Crystals. *CrystEngComm* **2020**, *22* (11), 1991–2001. https://doi.org/10.1039/C9CE01965K.
(111) Waldschmidt, A.; Couvrat, N.; Berton, B.; Dupray, V.; Morin, S.; Petit, S.; Coquerel, G. Impact of Gas Composition in the Mother Liquor on the Formation of Macroscopic Inclusions and Crystal Growth Rates. Case Study with Ciclopirox Crystals. *Cryst. Growth Des.* **2011**, *11* (6), 2463–2470. https://doi.org/10.1021/cg200245m.
(112) Waldschmidt, A.; Rietveld, I.; Couvrat, N.; Dupray, V.; Sanselme, M.; Berton, B.; Nicolai, B.; Mahé, N.; Petit, S.; Céolin, R.; Coquerel, G. About Aged Heterogeneous Liquid Inclusions Inside Organic Crystals in Relation to Crystal Formation, Structure, and Morphology. *Cryst. Growth Des.* **2011**, *11* (6), 2580–2587. https://doi.org/10.1021/cg200331n.
(113) Bobo, E.; Lefez, B.; Caumon, M.-C.; Petit, S.; Coquerel, G. Evidence of Two Types of Fluid Inclusions in Single Crystals. *CrystEngComm* **2016**, *18* (28), 5287–5295. https://doi.org/10.1039/C6CE00956E.
(114) Jones, S. F.; Evans, G. M.; Galvin, K. P. Bubble Nucleation from Gas Cavities — a Review. *Adv. Colloid Interface Sci.* **1999**, *80* (1), 27–50. https://doi.org/10.1016/S0001-8686(98)00074-8.
(115) Rivallin, M. Ecole Nationale Supérieure de Chimie de Montpellier (National Graduate School of Chemistry of Montpellier) 3rd Year Course of Chemical Engineering: “Transferts de Chaleur et de Matière” (Transfer of Heat and Matter), 2014.
(116) *Fundamentals of Heat and Mass Transfer*, 6th ed.; Incropera, F. P., Dewitt, D. P., Bergman, T. L., Lavine, A. L., Eds.; John Wiley: Hoboken, NJ, 2007.
(117) Acevedo, D.; Peña, R.; Yang, Y.; Barton, A.; Firth, P.; Nagy, Z. K. Evaluation of Mixed Suspension Mixed Product Removal Crystallization Processes Coupled with a Continuous Filtration System. *Chem. Eng. Process.* **2016**, *108*, 212–219. https://doi.org/10.1016/j.cep.2016.08.006.
(118) Ochirkhuyag, B.; Mori, T.; Katsuoka, T.; Satone, H.; Tsubaki, J.; Choi, H.; Sugimoto, T. Development of a High-Performance Cake-Less Continuous Filtration System. *Chem. Eng. Sci.* **2008**, *63* (21), 5274–5282. https://doi.org/10.1016/j.ces.2008.07.009.
(119) Guillemer, S. Internal Training Session “Plans d’expériences - Niveau 1” (Design of Experiments - Level 1), 2022.
(120) Lewis, G. A.; Mathieu, D.; Phan-Tan-Luu, R. *Pharmaceutical Experimental Design*; CRC Press, 1998.
(121) Buyevich, Yu. A.; Mansurov, V. V.; Natalukha, I. A. Instability and Unsteady Processes of the Bulk Continuous Crystallization—I. Linear Stability Analysis. *Chem. Eng. Sci.* **1991**, *46* (10), 2573–2578. https://doi.org/10.1016/0009-2509(91)80050-9.
(122) Buyevich, Yu. A.; Mansurov, V. V.; Natalukha, I. A. Instability and Unsteady Processes of the Bulk Continuous Crystallization—II. Non-Linear Periodic Regimes. *Chem. Eng. Sci.* **1991**, *46* (10), 2579–2588. https://doi.org/10.1016/0009-2509(91)80051-Y.
(123) Natalukha, I. A. Unstable Regimes of Continuous Crystallization in a Cascade of Well-Mixed Vessels. *Chem. Eng. Sci.* **1996**, *51* (8), 1181–1185. https://doi.org/10.1016/0009-2509(95)00297-9.
(124) Majumder, A. ECCG7 Conference “A Novel Plug Flow Crystallizer Configuration for Tackling Encrustation Problem,” 2022.
(125) SMART for WNT/2000 V5. 622, Smart Software Reference Manual; Bruker Advanced X Ray Solutions, Inc.: Madison, WI, 2001.
(126) SAINT+ V6. 02; Saint Software Reference Manual; Bruker Advanced X Ray Solutions, Inc.: Madison, WI, 1999.
(127) Farrugia, L. J. WinGX Suite for Small-Molecule Single-Crystal Crystallography. *J. Appl. Cryst.* **1999**, *32* (4), 837–838. https://doi.org/10.1107/S0021889899006020.
(128) *Biovia Material Studio 2019 (19.1.0.2353), Copyright © 2018 Dassault Systèmes, all right reserved*. http://accelrys.com/products/collaborative-science/biovia-materials-studio (accessed 2021-08-31).

Appendices

A. Experimental part

A.1. Materials

Rac-Ibu has been supplied by Pharmadev; anhydrous sodium hydroxide, *S*-αMBA and HPLC trifluoroacetic acid by Acros Organics; HPLC n-heptane and HPLC ethanol by Fisher; technical ethanol, technical ethylene glycol, silicon oil 50 cS and HPLC propan-2-ol by VWR.

A.2. Batch mode experimental set-up

The small-scale batch experiments (below 5 g) were performed in glass vials with magnetic stirrers. The temperature was controlled with double jackets connected to a thermostat.

The experiments at higher scale were performed in stirred, double-jacketed wall reactors of 150 or 250 mL, in which the temperature was regulated by a programmable thermostat Lauda Eco Silver RE415.

A.3. Solubility measurements

A.3.1. Visual estimation at the ambient temperature

Small amounts of solvent or solvent mixture (typically 100 µL) are added to a known mass of solute. Two additions should be separated by a little lapse of time, and the medium must be stirred. The first estimation of the solubility at the ambient temperature is comprised between the last add before the total dissolution and that just after.

Such method serves an evaluation of the range of concentrations to study within the Crystal 16, or a better preparation of solubility measurements by the gravimetric method. It could be compared with the estimation of the melting point of a compound on a Köfler bench before performing DSC analysis.

A.3.2. Crystal 16 (Technobis Crystallization Systems)

The principle of this technique is to estimate the temperature at which the solute completely dissolves, in a vial with a given concentration, by turbidimetry.

Vials are prepared with a known concentration and go through three temperature cycles. The system can estimate the turbidity of the medium by measuring the degree of transmission of a laser beam. Therefore, the solubility temperature (also called clear point) and the cloud point (i.e., the temperature at which nucleate the first crystals) at the studied concentration can be evaluated.

The used Crystal 16 is the second version of the device, controlled by the associated software v1.14.0. The data were exploited thanks to the associated software Crystal Clear v1.0 (Avantium).

The studied concentrations and the temperature program are indicated in the body of the manuscript.

The remaining solid of every vial was analyzed by XRPD to check that the phase did not change, which was not the case.

A.3.3. Gravimetric method

In the first place, a suspension of the solute in the solvent(s) is prepared at the given temperature. The suspension must be stirred during at least 2 h, to let time to the system to reach the thermodynamic equilibrium. Generally, an equilibration time of ca. 12 h is preferred. Then, the stirring is stopped, and after 30 min to 1 h of decantation, part of the supernatant is sampled and weighed. Next, the sample is dried. When the whole liquid is evaporated, the remaining solid is weighed.

The solubility C* can then be calculated in $g_{solute}/g_{saturated\ solution}$ with Equation A- 1.

$$C^* = \frac{m_{remaining\ solid}}{m_{sampled\ supernatant}} \qquad \textit{Equation A- 1}$$

The collected solid should be analyzed by X-Ray Powder Diffraction (XRPD), to check that the phase did not change in the studied solvent(s). In the presented work, all the solids recovered from solubility measurements exhibit the same phase than the initial product.

The solvent ratios and temperatures at which solubility was measured are indicated in the main body of the manuscript.

A.4. Chiral High Performance Liquid Chromatography (HPLC)

The chiral HPLC analyses were performed on a Thermoscientific system with Ultimate 3000 modules (Pump, Autosampler, RS variable wavelength detector) with a chiral column Daicel Chiralcel OD-H 5 µm 250−4.6 mm and the following conditions:

- Mobile phase: n-heptane/propan-2-ol/trifluoroacetic acid 100/1/0.1
- Flow rate: 1 $mL.min^{-1}$
- Wavelength: 225 nm
- Volume injected: 5 µL
- Oven temperature: 25 °C

Samples were dissolved in the mobile phase at a concentration of 1 $mg.mL^{-1}$.

Mobile phase and samples were sonicated for 10 min.

The software used to process the data is Thermo Scientific Dionex Chromeleon 6.8 Chromatography Data System.

A.5. X-Ray Powder Diffraction (XRPD)

XRPD measurements were carried out at ambient temperature on a Bruker D8 Discover apparatus, using the Cu Kα radiation (1.54 Å).

Classical measurements: The samples were scanned from 3 to 30° 2θ angles, with a 0.04° step (0.5 s duration). The detector slit was set at 0.6 mm.

Revised phase diagram measurements (section II.3): The samples were scanned from 3 to 30° 2θ angles, with a 0.02° step (2 s duration). The detector slit was set at 0.2 mm. The analyses were done using quartz as internal standard.

The software used to process the data is Bruker DIFFRAC.EVA V4.1.

A.6. Differential Scanning Calorimetry (DSC)

DSC measurements were performed on a Netzsch DSC 214 Polyma apparatus equipped with an intra-cooler and purged by nitrogen. The device is controlled with the software Netzsch Proteus Measurements v7.1.0.

Samples were weighed in 25 µL aluminum pans.

The software used to exploit the results is Netzsch Proteus Thermal Analysis v7.1.0.

The temperature programs used in the performed DSC analyses are described in the main body of the manuscript.

A.7. Single-Crystal X-Ray Diffraction (SCXRD)

The crystal structures were determined from single-crystal diffraction on a Bruker SMART diffractometer equipped with an APEX detector (with Mo Kα1 radiation: λ = 0.71073 Å).

The cell parameters and the orientation matrix of the crystal were preliminarily determined using SMART Software v5.622[125].

Data integration and global cell refinement were performed with SAINT Software v6.02[126]. The structures were solved by direct methods (SHEL- XS). Anisotropic displacement parameters were refined for all non-hydrogen atoms using SHEL-XL available with the WinGX package[127].

A.8. Scanning Electron Microscopy (SEM)

SEM photographs were taken with an SEM JEOL JCM 5000 NeoScope Secondary Electron imaging (high resolution and large depth of field; magnification from x10 up to x40000; high vacuum mode engaged; accelerating voltages of 10 kV).

Samples were prepared as follows: the powder samples were stuck on analyzing plots using conductive adhesives and then received a gold coating in order to reduce the charge accumulations during the observation using a NeoCoater MP-19020NCTR.

A.9. Optical Microcopy

Photographs and videos were taken with a Nikon Eclipse LV100 optical microscope, equipped with a Nikon Digital sight DS-Ri1 camera, or with a Nikon SMZ-10A binocular optical microscope equipped with a Sony Power HAD camera.

Both microscopes possess a pair of cross polarizers.

The software used to exploit the results is Nikon NIS Elements D V3.1.

To perform temperature-regulated microscopy, a hot/cold stage chamber Linkam THMS 600 was used (temperature range from -196 to +600 °C). Heating and cooling are controlled

with a Peltier system associated to the circulation of liquid nitrogen that can provide sub-ambient temperatures down to -196 °C.

The device is controlled with the software Linksys 32 v2.4.3.

The temperature programs used within the Linkam chamber are described in the main body of the manuscript.

A.10. Software

Material studio (Biovia): lattice parameters were obtained with Biovia Material Studio 2019 (19.1.0.2353)[128].

Dynochem (Scale-up System): Dynochem v6 works as an Excel add-in.

In this work, solubility modelling was realized thanks to two Excel files, developed by Scale-up System, called 'utilities': "Early phase solvent selection and solubility prediction" and "Solubility regression".

The characteristics of the solvents and solvent mixtures were determined thanks to the utility "DIPPR solvents".

Azurad (AZURAD SAS, France): DoE set-up, processing and analysis were realized with Azurad Basic version 1.3.4.

B. Reynolds number determination within the mixing piece

The dimensionless Reynolds number Re can be calculated as in Equation B- 1, with ρ the fluid density in kg.m^{-3}, U_m the fluid velocity in m.s^{-1}, D_h the hydraulic diameter in m and η the fluid dynamic viscosity in Pa.s.

$$Re = \frac{\rho U_m D_h}{\eta}$$ *Equation B- 1*

The fluid velocity U_m can be determined thanks to Equation B- 2, with Q_v the volume flow rate in m^3.s^{-1} and $S_{section}$ the pipe section in m². It is noteworthy to say that the volume flow rate Q_v to consider in the calculation of U_m should be the half of that within the CT reactor, as the medium is divided in two feeding tanks (see section III.2.1).

$$U_m = \frac{Q_v}{S_{section}}$$ *Equation B- 2*

$S_{section}$ can be calculated thanks to Equation B- 3.

$$S = \frac{\pi {D_h}^2}{4}$$ *Equation B- 3*

B.1. In the cold part (medium)

In the cold part of the mixing piece, the design aims at fulfilling the pipe of fluid. Thus, the hydraulic diameter D_h present in Equation B- 1 and Equation B- 3 can be assimilated to the pipe inner diameter.

The pipe where the medium circulates has an inner diameter of 0.007 m and an outer diameter of 0.01 m. The CT reactor has a total volume of 100 mL = 0.0001 m^3.

In adequation with the hypotheses of section III.2.2.1, the cold part medium is reduced to the solvent. The first process supposed to be tested in the CT crystallizer was done in methanol. Its density and dynamic viscosity were retrieved at 30 °C from the database of Dynochem software: $\rho_{MeOH,30\,°C} = 785\,kg.m^{-3}$ and $\eta_{MeOH,30\,°C} = 0.000504\,Pa.s$.

When this first design of the mixing piece was thought, the residence time t planned to be used was 15 min.

Regarding the considered values above, the results of Equation B- 1, Equation B- 2 and Equation B- 3 for the cold part are displayed in Table B- 1.

$S_{section}$ (x10^{-5} m²)	Q_v CT (x10^{-7} m^3.s^{-1})	Q_v 1 pipe mixing piece (x10^{-7} m^3.s^{-1})	U_m (x10^{-3} m. s^{-1})	Re	Flow regime
3.85	1.11	0.556	1.44	**16**	**LAMINAR**

Table B- 1: Result of the Reynolds number calculation for the cold part.

B.2. In the hot part (coolant)

The hydraulic diameter of the outer hot part is the annular section between 0.05 m (outer diameter) and 0.01 m (outer diameter of the inner pipe). This gives: $D_h = 0.05 - 0.01 = 0.04\,m$.

The coolant used for the CT experiments is a mix of ethylene glycol and water 40/60 V/V, heated up at 70 °C. The fluid mixture density and dynamic viscosity were retrieved at 70 °C from the "DIPPR solvents" utility of Dynochem: $\rho_{mixture,70\,°C} = 1018\,kg.m^{-3}$ and $\eta_{mixture,70\,°C} = 0.000663\,Pa.s$.

The volume flow rate of the thermostat used (Huber ministat cc2) given by the builder is 22 L.min^{-1}.

Regarding the considered values above, the results of Equation B- 1, Equation B- 2 and Equation B- 3 for the hot part are displayed in Table B- 2.

$S_{section}$ (x10^{-5} m²)	Q_v (x10^{-7} m^3.s^{-1})	U_m (x10^{-3} m. s^{-1})	Re	Flow regime
126	3667	292	**17925**	**TURBULENT**

Table B- 2: Result of the Reynolds number calculation for the hot part.

C. First prototype of the mixing piece: calculation of the minimum inlet pipe length

C.1. Calculation of the heat flow Φ and of the outlet temperature of the hot part $T_{h,o}$

The heat flow can be calculated in the cold part thanks to Equation III- 5: $\Phi = \dot{m}_c * Cp_c * (T_{c,o} - T_{c,i})$. The data and result are presented in Table C- 1.

$\dot{m}_c$ (x10^{-5} kg.s^{-1})	$Cp_c = Cp_{MeOH,\ 30\,°C}$ (J.kg^{-1}.K^{-1}) -retrieved from Dynochem database-	$T_{c,i}$ (°C)	$T_{c,o}$ (°C)	Φ (J.s^{-1})
4.36	2561	30	40	**1.12**

Table C- 1: Calculation of the heat flow on the cold part

The outlet temperature of the hot part $T_{h,o}$ can be determined thanks to Equation III- 6: $T_{h,o} = T_{h,i} - \frac{\dot{m}_c}{\dot{m}_h}\frac{Cp_c}{Cp_h}(T_{c,o} - T_{c,i})$. The data and result are presented in Table C- 2.

$T_{h,i}$ (°C)	$\dot{m}_h$ (x10^{-5} kg.s^{-1})	$Cp_h = Cp_{mixture,\ 70\,°C}$ (J.kg^{-1}.K^{-1}) -retrieved from the Dynochem "DIPPR solvents" utility-	$T_{h,o}$ (°C)
70	37336	3523	69.9992

Table C- 2: Calculation of the outlet temperature of the hot part

To check the obtained results, the calculation of Φ can be made with the data of the hot part: it also gives 1.12 J.s^{-1}. The obtained results are consistent.

With these last results, the logarithmic mean temperature difference for counter-current flow can be calculated (see Equation III- 2): it gives 34.8 K.

C.2. Calculation of the minimum pipe length for the first mixing piece prototype

C.2.1. Determination of the Nusselt number

The Nusselt number of the cold part is 4.36, as the flow regime is laminar[115,116].

Nevertheless, this number must be determined in the hot part, since the flow regime is turbulent. To find the suitable correlation to determine Nu, the Prandtl number must be estimated in the first place. Pr can be calculated with Equation C- 1.

$$Pr = \frac{Cp * \eta}{\lambda_{fluid}} \qquad \textit{Equation C- 1}$$

The coolant mixture heat capacity, dynamic viscosity and thermal conductivity were retrieved at 70 °C from the "DIPPR solvents" utility of Dynochem: $Cp_{mixture,70\,°C} = 3523\,kg.m^{-3}$, $\eta_{mixture,70\,°C} = 0.000663\,Pa.s$ and $\lambda_{mixture,70\,°C} = 0.486\,W.m^{-1}K^{-1}$. This gives: $Pr = 4.81$.

The Prandtl number being comprised between 1 and 20, the following correlation can be used[115]:

$$Nu = 0.0155 * Re^{0.83} Pr^{0.5}$$ *Equation C- 2*

Equation C- 2 gives $Nu = 115$.

The Nusselt number calculation serves the determination of the convection coefficients h_h and h_c.

C.2.2. Calculation of the convection coefficients h_h and h_c

The convection coefficient h can be taken out of Equation III- 22, as in Equation C- 3.

$$h = \frac{Nu * \lambda_{fluid}}{D_h}$$ *Equation C- 3*

The thermal conductivity methanol was retrieved from the database of Dynochem software: $\lambda_{MeOH,30\,°C} = 0.199\,W.m^{-1}.K^{-1}$.

The determination of the convection coefficients gives: $h_c = 124\,W.m^{-2}.K^{-1}$ and $h_h = 1400\,W.m^{-2}.K^{-1}$. Knowing that the glass wall thickness is $e = 0.0015\,m$ and that the glass thermal conductivity is $\lambda_w = 2\,W.m^{-1}.K^{-1}$ (given by the glass tubes provider), the global heat transfer coefficients H_c, H_h and H_a can now be calculated.

C.2.3. Calculation of the global heat transfer coefficients H_c, H_h and H_a and determination of the minimum pipe length

The length of the pipe can be calculated thanks to Equation III- 1, by determining first the exchange area S.

The exchange area S takes part in the formulae of the global heat transfer coefficients H_c, H_h and H_a (Equation III- 19, Equation III- 20 and Equation III- 21). H_c, H_h and H_a are independent from the exchange area values, as these coefficients are expressed per square meter (m^{-2}). They can be calculated with an arbitrary value of S. S_h, S_c and S_a can then be determined with Equation III- 3.

In parallel, different values of L_{pipe} can be tested to calculate S with Equation III- 1. The length L_{pipe} which gives the value of S closest to the values of S_h, S_c and S_a, calculated from Equation III- 3, is the needed one.

The results are identical for the cold part, the hot part and the average exchange surface area. A part of the values tested for the hot part are presented in Table C- 3.

L_{pipe} (m)	$S_{h,1}$ (x10^{-4} m²) Equation III- 1	H_h (W.m^{-2}.K^{-1}) Equation III- 19	$S_{h,2}$ (x10^{-4} m²) Equation III- 3
0.0125	3.93	76.1	4.22
0.0135	**4.24**		
0.0150	4.71		

Table C- 3: Results (hot part) of the investigation of the minimum length needed for the inlet pipe.

In the considered system, to heat up the cold methanol from 30 °C to 40 °C with a mixture of ethylene glycol/water 40/60 V/V at 70 °C, for pipes with an inner diameter of 0.0070 m, the minimum length should be 13.5 cm.

D. Second prototype of the mixing piece: calculation of the minimum inlet pipe length

The calculations follow those of appendices B and C.

The raw data that have changed and the results for a residence time of 15 min are presented in Table D- 1.

Reynolds number Re in the cold part (EtOH/H_2O 76/24 w/w)			
$\rho_{EtOH/H2O\ 76/24,\ 30\ °C,\ Dynochem}$ **(kg.m^{-3})**	824	$\eta_{EtOH/H2O\ 76/24,\ 30\ °C,\ Dynochem}$ **(x10^{-4} Pa.s)**	9.37
Re		**9 (Laminar)**	
Reynolds number Re in the hot part: identical to section B.2 of appendix B			
Re		**17925 (Turbulent)**	
Calculation of the heat flow Φ			
$\dot{m}_c$ **(x10^{-5} kg.s^{-1})**	4.58	$Cp_c = Cp_{EtOH/H2O\ 76/24,\ 30\ °C,\ Dynochem}$ **(J.kg^{-1}.K^{-1})**	2889
Φ (J.s^{-1})		**1.32**	
Calculation of the outlet temperature of the hot part $T_{h,o}$			
$T_{h,o}$ (°C)		**69.9990**	
Calculation of the convection coefficient of the cold part h_c			
$\lambda_{EtOH/H2O\ 76/24,\ 30\ °C,\ Dynochem}$ **(W.m^{-1}.K^{-1})**	0.274	**h_c (W.m^{-2}.K^{-1})**	**171**
Determination of the minimum pipe length L_{pipe}			
L_{pipe} (m)	**$S_{h,1}$ (x10^{-4} m²) Equation III- 1**	**H_h (W.m^{-2}.K^{-1})**	**$S_{h,2}$ (x10^{-4} m²) Equation III- 3**
0.0100	3.14	100.4	3.79
0.0120	**3.77**		
0.0125	3.93		

Table D- 1: New raw data and results of the calculation of the minimum length of the inlet pipes of the second mixing piece prototype.

In the considered system, to heat up the cold solvent mixture of ethanol/water 76/24 w/w from 30 °C to 40 °C with a mixture of ethylene glycol/water 40/60 V/V at 70 °C, the minimum pipe length should be 12 cm.

E. Screenings in continuous mode: statistical analysis of the response's results

The statistical analysis and interpretation of the responses' results in the screening designs were realized with the help of the software Azurad, in agreement with the explanations of section IV.3.2.

E.1. First screening

The next sections provide an analysis of the impact of the four factors studied in the first screening, ΔT, Ω, t and T_{ref}, on each studied response. The influence scores given in Figure E- 1 to Figure E- 5 are extrapolated from the Pareto plots (coefficients) provided by Azurad. It is noteworthy to remind that the importance of some factors can be hidden or enhanced because of interactions between them.

E.1.1. Global productivity

The regression model given by Azurad is significant with a p-value of 1.6 % and a correlation coefficient R^2 of 0.81. The lack of fit is not significant with a p-value of 40 %. Therefore, for global productivity, the experimental results and the screening model fit quite well.

It is evident from Figure E- 1a that the main impacting factor is the residence time t. Rotation speed Ω has a small influence on global productivity. The temperature difference ΔT and the reference temperature T_{ref} have a poor impact.

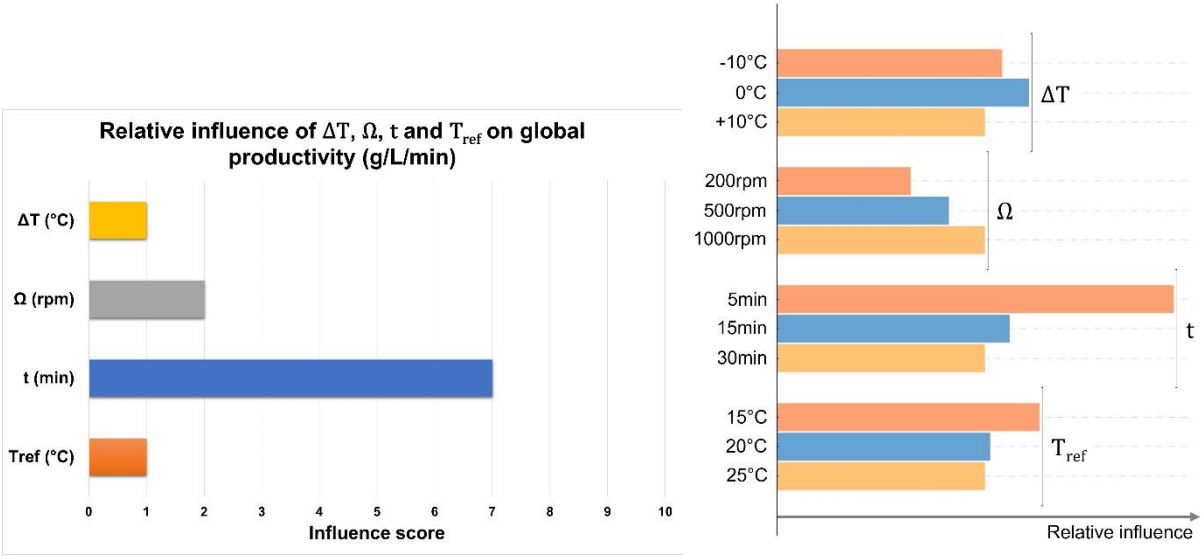

(a) **(b)**

Figure E- 1: Results from Azurad for global productivity: (a) Relative influence of the temperature difference ΔT, the rotation speed Ω, the residence time t and the reference temperature T_{ref} on the global productivity. (b) Total effect plot taken from Azurad; for every factor, the bars give the relative effect of each level to improve global productivity.

The impact of each factor level on the increase of the global productivity can be found in Figure E- 1b. The interpretation should be moderated regarding the influence of each factor discussed in the previous paragraph.

The predominance of t = 5 min as global productivity enhancer seems clear. The lower the residence time the higher the global productivity. At shorter residence times, the cooling is faster, which increases the nucleation rate. The side effect is the recovery of a crystal population with a broad PSD, i.e., a less homogeneous powder.

Regarding the rotation speed, it appears that the global productivity increases with the rpm. This result is consistent with an enhanced mass transfer for high rotation speed[51,57,60].

The use of the isothermal mode (ΔT = 0 °C) seems to improve global productivity, as well as the lower value of T_{ref}, 15 °C. However, these factors have a limited effect on the global productivity, thus, the assumptions about their influence should be moderated.

To conclude, the apparent best parameters to improve global productivity are: ΔT = 0 °C, Ω = 1000 rpm, t = 5 min and T_{ref} = 15 °C. It has been performed in repeated experiments 12 R1 and 12 R2, which indeed resulted in excellent global productivities (see results in Table IV-10).

Furthermore, the theoretical maximum global productivity per fraction was calculated thanks to Equation E- 1, with $m_{solvent,1\ fraction}$ the mass (g) of solvent that goes through the CT reactor during one residence time t (min), C_i the initial concentration in diastereomer (g.L^{-1}) – assuming that all the reactants are consumed – and C* the solubility (g.L^{-1}).

$$Global\ productivity_{max,theoretical} = \frac{m_{solvent,1\ fraction} * (C_i - C^*)}{t}$$

Equation E- 1

Table E- 1 shows the comparison between the maximum theoretical global productivity and the real global productivity calculated for each experiment. If the trends seem confirmed, sometimes, the actual global productivity is higher than that predicted. This is probably due to encrustation, which can induce a strong bias: when, after some time, a massive amount of product can be released, the productivity is artificially increased.

Experiment	Maximum theoretical global productivity ($g.L^{-1}.min^{-1}$)	Global productivity ($g.L^{-1}.min^{-1}$)
1 R1	1.146	1.317
1 R2	1.146	1.103
2	0.191	0.085
3	1.101	1.623
4	0.382	0.626
5 R1	0.367	0.135
5 R2	0.367	0.232
6	0.184	0.151
7	0.369	0.246
8	1.108	1.432
9	0.185	0.006
10	0.185	0.017
11 R1	0.369	0.106
11 R2	0.369	0.773
12 R1	1.146	2.217
12 R2	1.146	3.976
13	1.146	2.688
14	1.146	3.185

Table E- 1: Comparison between the maximum theoretical global productivity and the real global productivity calculated for each experiment.

In batch mode, the global productivity of the experiments presented in the section IV.2.2 was estimated between 0.080 $g.L^{-1}.min^{-1}$ to 0.242 $g.L^{-1}.min^{-1}$. It means that the continuous mode brings an outstanding increase of at least 16 times. This is far above the examples of transfer from batch mode to continuous mode found in the literature[15,50,86].

E.1.2. Global yield

During the processing of the global yield results, it appeared that the results of experiment 13 were aberrant. As a complementary experiment, it was possible to remove it from the experimental matrix (for this response study) without degrading the quality criteria.

The regression model (discarding experiment 13) is very significant with a p-value of 0.20 % and a R^2 of 0.91. The lack of fit is not significant with a p-value of 78 %. Thus, the experimental results and the screening model for global yield fit quite well.

As shown in Figure E- 2a, the two main impacting factors on the global yield are the temperature gradient ΔT and the residence time t. The reference temperature T_{ref} has also a little influence. The rotation speed Ω does not seem to have any impact on the global yield.

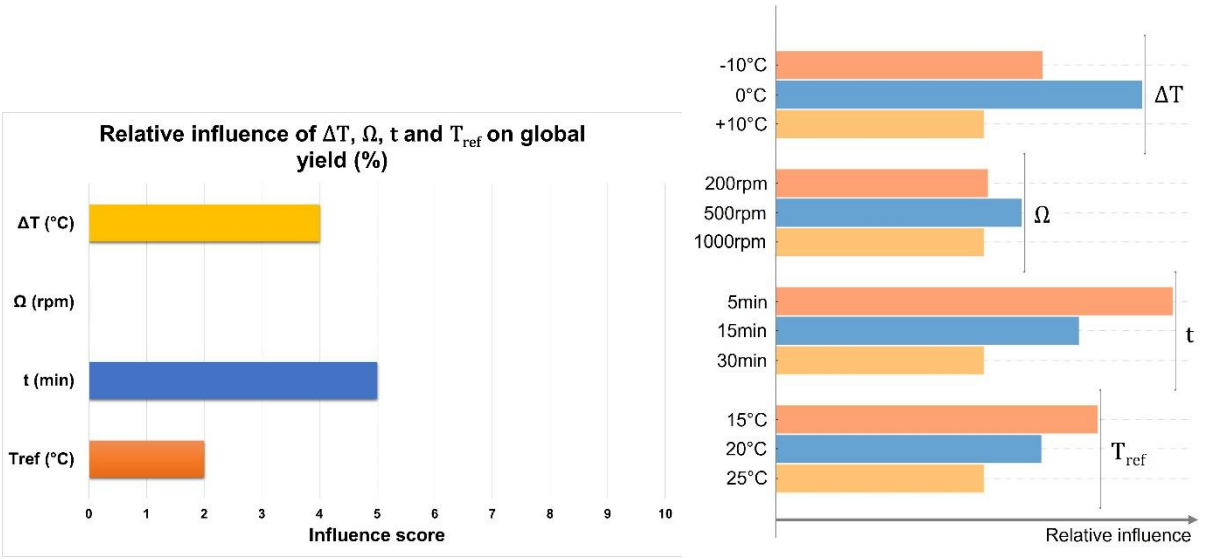

(a) **(b)**

Figure E- 2: Results from Azurad for global yield: (a) Relative influence of the temperature difference ΔT, the rotation speed Ω, the residence time t and the reference temperature T_{ref} on the global yield. (b) Total effect plot taken from Azurad; for every factor, the bars give the relative effect of each level to improve global yield.

The impact of each factor level on the increase of global yield can be found in Figure E- 2b. The interpretation should be modulated regarding the influence of each factor discussed before.

When looking at the most impacting factor, residence time, it appears that as it decreases, the global yield increases. As explained for global productivity, the cooling rate is higher for short residence times, which increases the nucleation rate.

The second most influential factor is the temperature difference ΔT. The use of the isothermal mode ($\Delta T = 0$ °C) seems to be the best option to improve the global yield. Wu *et al.* (2017) have shown that when the temperature gradient is increased, the nucleation occurs at higher supersaturation[74]. This means that crystallization needs a higher driving force to start. When there is no temperature difference, the nucleation starts 'earlier' and can then results in a higher production of crystals. It can explain why the isothermal mode leads to higher yields. Moreover, among the two non-isothermal modes, the one with the cold internal cylinder and the hot external cylinder ($\Delta T = -10$ °C) gives better results. This difference of results according to the non-isothermal mode has already been reported[62]. It is related to the driving forces of dissolution and recrystallization exerted respectively near the heating part boundary layer and the cooling part boundary layer. The temperature regulation of each cylinder may not be equally efficient, which can explain why one non-isothermal mode seems better than the other.

The decrease of T_{ref} seems to have a positive effect on the global yield, which can be expected as supersaturation increases when T_{ref} diminishes.

Finally, it seems that the best level for rotation speed is 500 rpm, but as shown in Figure E- 2a, this factor has a limited effect on the global yield.

In conclusion, the apparent best set of parameters to improve global yield is: $\Delta T = 0$ °C, t = 5 min and $T_{ref} = 15$ °C. This set of parameters has been repeated twice: in experiments 12 R1 and 12 R2, which indeed gave excellent global yields (see Table IV- 10).

The theoretical maximum global yield per fraction was calculated thanks to Equation E- 2, with $m_{solvent,1\ fraction}$ the mass (g) of solvent that goes through the CT reactor during one residence time t, C_i the initial concentration in diastereomer ($g.L^{-1}$) – assuming that all the reactants are consumed –, C* the solubility ($g.L^{-1}$), and $m_{expected}$ the mass (g) of diastereomer expected to be recovered during one residence time t.

$$Global\ yield_{max,theoretical} = \frac{m_{solvent,1\ fraction} * (C_i - C^*)}{m_{expected}}$$

Equation E- 2

Table E- 2 shows the comparison between the maximum theoretical global yield and the real global yield calculated for each experiment. The actual observed global yield is really lower than the maximum calculated yield, for each experiment.

Experiment	Maximum theoretical global yield (%)	Global yield (%)
1 R1	63.3	14.7
1 R2	63.3	12.1
2	63.3	5.8
3	60.6	15.9
4	63.3	18.8
5 R1	60.6	4.3
5 R2	60.6	7.2
6	60.6	11.1
7	60.6	6.3
8	60.6	13.9
9	60.6	0.4
10	60.6	1.0
11 R1	60.6	3.5
11 R2	60.6	11.8
12 R1	63.3	22.1
12 R2	63.3	19.6
13	63.3	26.4
14	63.3	15.7

Table E- 2: Comparison between the maximum theoretical global yield and the real global yield calculated for each experiment.

In batch mode, the global yield of experiments with the equivalent amount of water ranges from 42.9 % to 48.8 % (see Table IV- 6). Even the best results obtained in continuous mode

are about 2 times lower. To make sure that the maximum amount of product has been recovered, the mother liquors have been kept at room temperature for 2 days. It did not lead to any precipitation, which means that close to the highest yield was achieved for the starting concentration.

These results are not surprising as it has already been reported that continuous processes trend to give lower yield than batch ones[8,33]. However, as the global productivity is very good, the implementation of a recycling system of the mother liquors in a lower domain of temperatures could be an interesting solution. Such set-up has already proven its efficiency regarding yield[15,35,38].

After the analysis of the global responses, the next result to be analyzed is the diastereomeric excess, which characterizes the ability of the process conditions to separate the two diastereomers.

E.1.3. Diastereomeric excess

The regression model given by Azurad is very significant with a p-value near to 0 % and a R^2 of 0.92. The pure error between repeated experiments is very low but the lack of fit is significant, with a p-value of 1.4 %. It means that a small part of the observed experimental variability is not explained by the chosen model. This could be due to interaction effects between parameters.

As shown in Figure E- 3a, the temperature difference ΔT and the rotation speed Ω are the two most impacting factors on diastereomeric excess. The reference temperature T_{ref} has also some influence. Finally, the residence time t apparently has a poor impact on the diastereomeric excess.

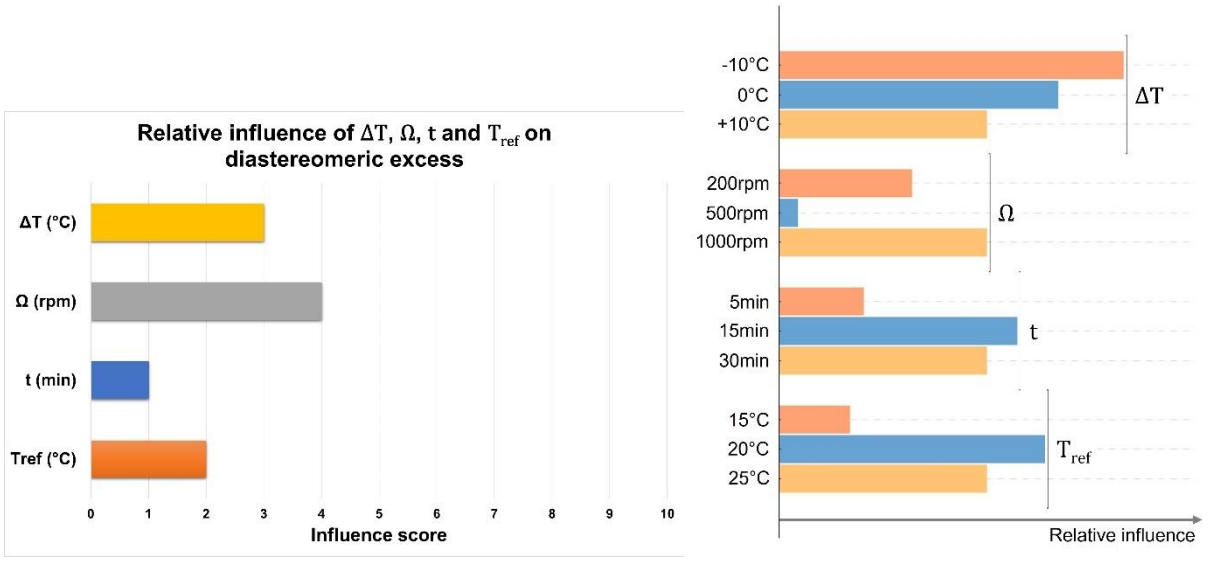

(a) **(b)**

Figure E- 3: Results from Azurad for the diastereomeric excess: (a) Relative influence of the temperature difference ΔT, the rotation speed Ω, the residence time t and the reference temperature T_{ref} on the diastereomeric excess. (b) Total effect plot taken from Azurad; for every factor, the bars give the relative effect of each level to improve the diastereomeric excess.

The impact of each factor level on the increase of the diastereomeric excess can be found in Figure E- 3b. The interpretation should be moderated regarding the influence of each factor discussed before.

The most influential parameter is the rotation speed, but its effect seems highly non-linear. This may be explained by potential interactions with other factors. The best rotation speed level to improve the diastereomeric excess is 1000 rpm.

The second most impacting factor is the temperature difference ΔT: it clearly appears that the use of the CT crystallizer in non-isothermal mode, with the inner cylinder as the cold part and the outer cylinder as the hot one, gives the best results of chiral purity. The presence of a temperature gradient was expected to improve chiral purity, as it has already proved its efficiency in deracemization processes[61,76]. In the opposite, the reverse non-isothermal mode should be avoided. Such difference between the two non-isothermal modes has already been reported[62].

Then, the decrease of T_{ref} gives a better diastereomeric excess, but shows a sort of limit at 20 °C. The same phenomenon is observed for the factor residence time, with the level 15 min. Again, this behavior may be clarified by studying the interactions between the different factors.

Eventually, the apparent best parameter set to improve chiral purity is: ΔT = -10 °C, Ω = 1000 rpm, t = 15 min and T_{ref} = 20 °C. Such experiment has not been performed, but the experiments 11 R1 and 11 R2 are quite close (T_{ref} = 25 °C) and resulted in the best diastereomeric excess (see Table IV- 10).

The chiral purity varies from 0.52 to 0.70 in the batch experiments with the equivalent amount of water (see Table IV- 6). The temperature gradient of the CT crystallizer, combined with its highly efficient mixing, gives better diastereomeric excess on average, in a very repeatable manner (see repeated experiments in Table IV- 10).

It is important to remind that the system Ibu-*S*-αMBA exhibits a partial solid solution enriched in *S*-Ibu-*S*-αMBA (see section II.3.2). The limit of miscibility of this solid solution at 20 °C is 13 % of *R*-Ibu-*S*-αMBA; therefore, achieving a diastereomeric excess higher than 0.74 in a single operation may be tricky.

To estimate the productivity and the yield in the wanted diastereomer, the 'diastereomeric' responses were introduced. The effects of the four studied factors on them are detailed in the two next sections.

E.1.4. Diastereomeric productivity

Like for the global yield, according to the analysis of the residues, experiment 13 appears to be aberrant in the processing of the diastereomeric productivity results. As previously said, this complementary experiment can be removed from the experimental matrix, without degrading the quality criteria.

The regression model (discarding experiment 13) is very significant with a p-value of 0.01 % and a R^2 of 0.96. The lack of fit is not significant with a p-value of 30 %. For diastereomeric productivity, the experimental results and the screening model fit quite well.

As global productivity, the diastereomeric productivity is mainly impacted by the residence time t (Figure E- 4a). The temperature difference ΔT also has an influence, but it is small. The rotation speed Ω and the reference temperature T_{ref} do not seem to have any impact.

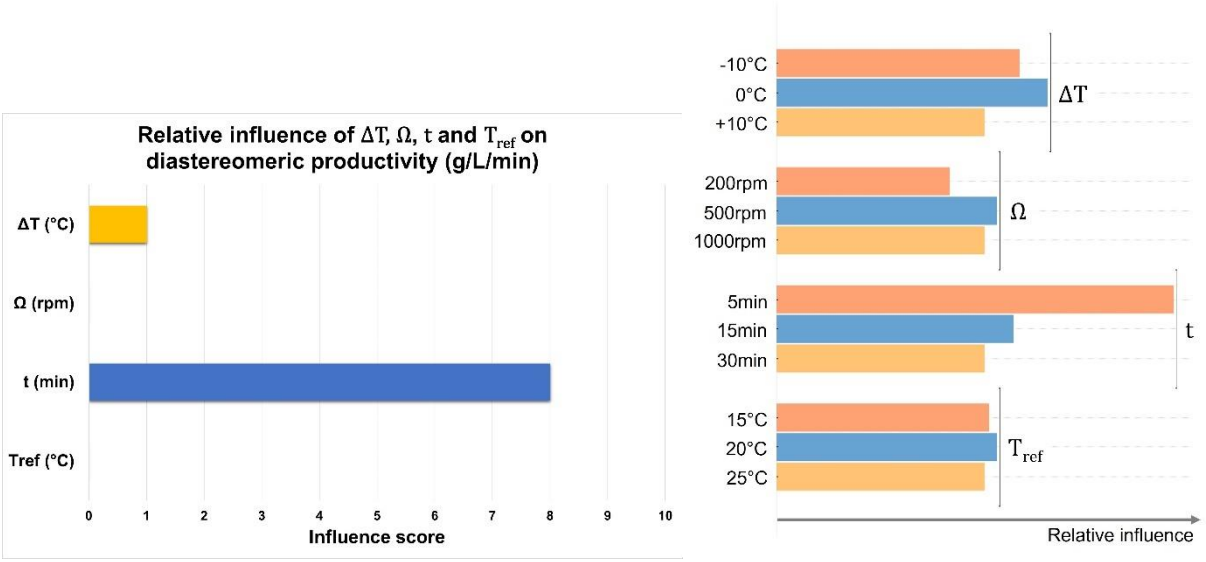

(a) **(b)**

Figure E- 4: Results from Azurad for the diastereomeric productivity: (a) Relative influence of the temperature difference ΔT, the rotation speed Ω, the residence time t and the reference temperature T_{ref} on the diastereomeric productivity. (b) Total effect plot taken from Azurad; for every factor, the bars give the relative effect of each level to improve the diastereomeric productivity.

The impact of each factor level on the increase of the diastereomeric productivity can be found in Figure E- 4b. The interpretation should be modulated regarding the influence of each factor discussed in the previous paragraph.

Like for global productivity, the predominance of t = 5 min as diastereomeric productivity enhancer seems clear. As explained before, the cooling rate is higher for short residence times, which increases the nucleation rate. The lower the residence time the higher the productivity.

The second factor with influence is the temperature difference ΔT. The use of the isothermal mode (ΔT = 0 °C) seems to be the best option to improve the diastereomeric productivity. Indeed, when the temperature gradient is increased, nucleation occurs at higher supersaturation[74], which can affect productivity. Also, among the two non-isothermal modes, the one with the cold inner cylinder (ΔT = -10 °C; with the outer hot cylinder) gives better results. This difference of results according to the non-isothermal mode has already been reported[62]. The influence of ΔT on diastereomeric productivity is more similar to its impact on global productivity than on diastereomeric excess.

The levels of the factors Ω and Tref are not easy to evaluate, but as explained above, they do not seem to impact the diastereomeric productivity.

To conclude, the use of ΔT = 0 °C and t = 5 min are recommended to improve diastereomeric productivity. The use of this parameter set in experiments 8, 12 R1 and 12 R2, gave excellent diastereomeric productivities (see Table IV- 10).

Also, it appeared that the influence of ΔT, Ω, t and T_{ref} on diastereomeric productivity is closer to that on global productivity than on diastereomeric excess.

In batch mode, the diastereomeric productivity of the experiments presented in the section IV.2 was estimated between 0.056 $g.L^{-1}.min^{-1}$ to 0.121 $g.L^{-1}.min^{-1}$. The use of continuous mode can apparently improve it by, at least, 8 times.

E.1.5. Diastereomeric yield

According to the analysis of the residues, experiments 11R1 and 13 appear to be aberrant in the processing of the diastereomeric yield results. These complementary experiments can be removed from the experimental matrix, without degrading the quality criteria.

The regression model (discarding experiments 11R1 and 13) is significant with a p-value of 0.56 % and a correlation coefficient R^2 of 0.91. The lack of fit is not significant with a p-value of 19 %. For diastereomeric yield, the experimental results and the screening model fit quite well.

Only two factors seem to have an influence on the diastereomeric yield: the temperature difference ΔT and the residence time t (Figure E- 5a). The rotation speed Ω and the reference temperature T_{ref} do not seem to have any impact.

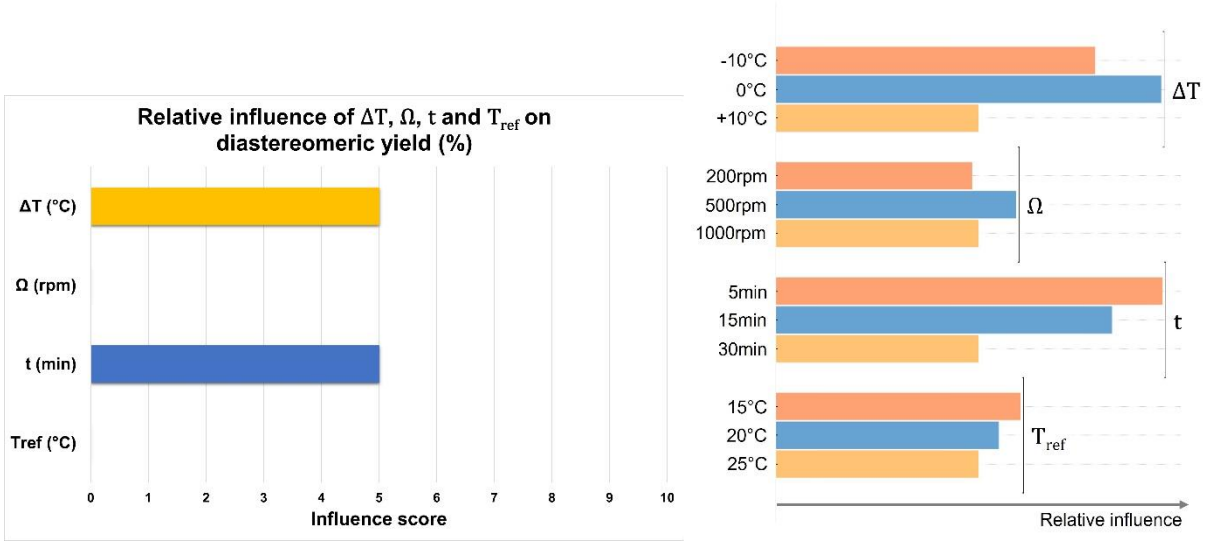

(a) **(b)**

Figure E- 5: Results from Azurad for the diastereomeric yield: (a) Relative influence of the temperature difference ΔT, the rotation speed Ω, the residence time t and the reference temperature T_{ref} on the diastereomeric yield. (b) Total effect plot taken from Azurad; for every factor, the bars give the relative effect of each level to improve the diastereomeric yield.

The impact of each factor level on the increase of the diastereomeric yield can be found in Figure E- 5b. The interpretation should be moderated regarding the influence of each factor discussed before.

Regarding the factor ΔT, the use of the isothermal mode (ΔT = 0 °C) seems to be the best option to improve the diastereomeric yield. Like for productivities and global yield, it can be explained because nucleation occurs at a higher supersaturation when the temperature gradient is increased[74]. Also, among the two non-isothermal modes, the one with the cold

inner cylinder (ΔT = -10 °C; with the hot outer cylinder) gives better results. Wu *et al.* (2015) already reported such difference[62].

Concerning the residence time t, as it decreases, the diastereomeric yield increases. This effect is the same as for productivities and global yield.

Some trends could be found for Ω and T_{ref}, but their influence on diastereomeric yield is apparently non-existent in the explored domain (Figure E- 5a).

In conclusion, ΔT = 0 °C and t = 5 min seems to be the best levels of the most important factors to improve diastereomeric yield. This parameter set has been used in experiments 8, 12 R1 and 12 R2, which indeed resulted in good diastereomeric yields (see Table IV- 10).

In a general way, the influence of ΔT, Ω, t and T_{ref} on diastereomeric yield is closer to that on global yield than on diastereomeric excess.

Batch mode diastereomeric yields, of experiments with the equivalent amount of water, range from 25.3 % to 29.9 %. Like for the results of global yield, the best results obtained in continuous mode are about 2 times lower. Again, this outcome is not surprising, and the use of a recycling system of the mother liquors at a lower temperature could be an efficient solution.

E.2. Second screening

The next sections provide an analysis of the impact of the four factors studied in the second screening design, ΔT, Ω, t and β, on each studied response. The influence scores given in Figure E- 6 to Figure E- 13 are extrapolated from the Pareto plots (coefficients) provided by Azurad. It is noteworthy to remind that the importance of some factors can be hidden or enhanced because of interactions between them.

E.2.1. Global productivity

During the processing of the global productivity results, it appeared that the results of experiments 13 and 16 were aberrant. As complementary experiments, it was possible to remove them from the experimental matrix (for this response study) without degrading the quality criteria.

The regression model (discarding experiments 13 and 16) given by Azurad is significant with a p-value of 0.0 % and a correlation coefficient R^2 of 0.86. The lack of fit is significant with a p-value of 1.8 %. %. It means that a small part of the observed experimental variability is not explained by the chosen model. This could be due to interaction effects between parameters.

It is evident from Figure E- 6a that the main impacting factor is the residence time t. The supersaturation ratio β and the temperature difference ΔT have a small influence on global productivity but that of the rotation speed Ω is negligible. These results are similar to those of the first screening: the influence of the residence time presses that of the other factors for global productivity.

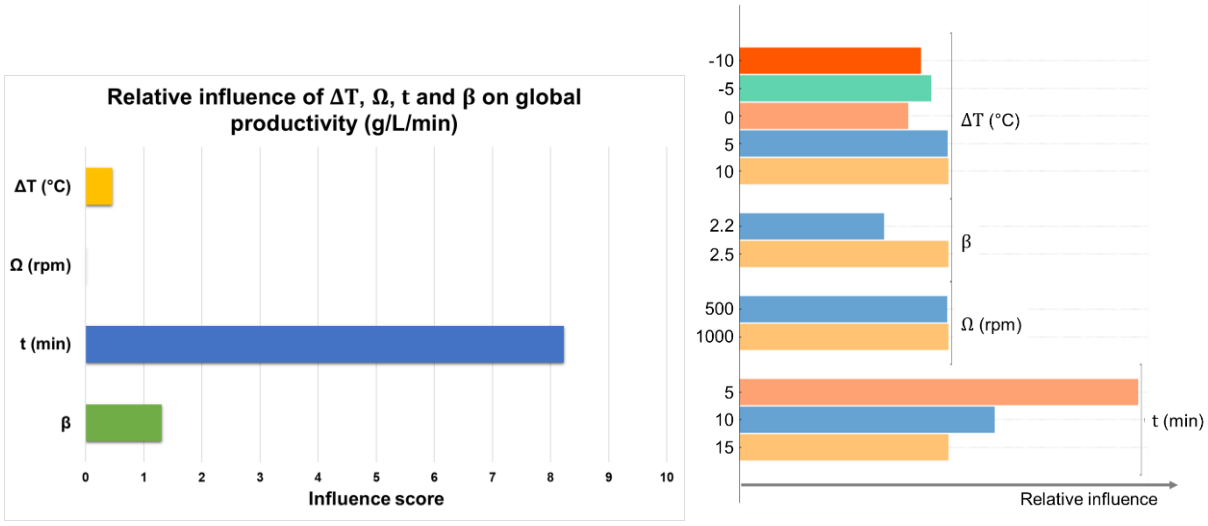

(a) **(b)**

Figure E- 6: Results from Azurad for global productivity: (a) Relative influence of the temperature difference ΔT, the rotation speed Ω, the residence time t and the supersaturation ratio β on the global productivity. (b) Total effect plot taken from Azurad; for every factor, the bars give the relative effect of each level to improve global productivity.

The impact of each factor level on the increase of the global productivity can be found in Figure E- 6b. The interpretation should be moderated regarding the influence of each factor discussed in the previous paragraph.

As in the first DoE, the predominance of t = 5 min as global productivity enhancer seems clear. The lower the residence time the higher the global productivity. For short residence times, the cooling is faster, which increases the nucleation rate.

Regarding the supersaturation ratio, when increasing it, the global productivity is improved. This can be expected since a higher supersaturation level means that there is more product that can crystallize.

Like in the first screening, the use of the isothermal mode ($\Delta T = 0$ °C) seems to improve global productivity. However, regarding the impact of this factor, this assumption should be moderated.

The levels of the factors Ω can hardly be discriminated, but as explained above, it does not seem to impact the global productivity.

To conclude, the apparent best parameters to improve global productivity are t = 5 min and $\beta = 2.5$. It has been performed in experiments 1, 8, 13 and 16. If the results of experiments 13 and 16 were estimated as aberrant, in terms of global productivity, experiments 1 and 8 indeed resulted in excellent global productivities (see results in Table IV- 17).

Moreover, like in the first screening, the theoretical maximum global productivity per fraction was calculated thanks to Equation E- 1. Table E- 3 shows the comparison between the maximum theoretical global productivity and the real global productivity calculated for each experiment.

If the trends seem confirmed, the actual global productivity is sometimes higher than that predicted. This is probably due to encrustation, which can induce a strong bias: after some time, part of the crust can separate, and a massive amount of product can be released.

Also, the aberrance of the results of experiments 13 and 16 seems clear with this comparison.

Experiment	Maximum theoretical global productivity ($g.L^{-1}.min^{-1}$)	Global productivity ($g.L^{-1}.min^{-1}$)
1	0.907	2.461
2	0.733	1.253
3	0.244	0.242
4	0.302	0.666
5	0.244	0.177
6	0.454	0.978
7	0.733	1.959
8	0.907	1.704
9	0.367	0.677
10	0.454	0.832
11	0.302	0.322
12	0.367	0.377
13	0.907	0.086
14	0.244	0.257
15	0.733	1.051
16	0.907	3.321
17	0.907	0.445

Table E- 3: Comparison between the maximum theoretical global productivity and the real global productivity calculated for each experiment.

In batch mode, the global productivity of the experiments presented in the section 0 was estimated between 0.099 $g.L^{-1}.min^{-1}$ to 0.123 $g.L^{-1}.min^{-1}$. It means that the continuous mode brings an exceptional increase of minimum 1.5 times, and up to 25 times. This is far above the examples of transfer from batch mode to continuous mode found in the literature[15,50,86]. In addition, batch mode experiments were performed with a higher supersaturation ratio β of 2.8 (to provoke nucleation, see section 0), which is a productivity enhancer. Therefore, for similar conditions, the improvement brought by the implementation of the continuous mode is probably even better.

E.2.2. Global yield

According to the analysis of the residues in the statistical analysis of Azurad, it appeared that the results of experiments 13, 16 and 17 were aberrant. As complementary experiments, it was possible to remove them from the experimental matrix without degrading the quality criteria.

The regression model (discarding experiments 13, 16 and 17) is significant with a p-value of 0.0 % and a correlation coefficient R^2 of 0.71. The lack of fit is significant with a p-value of

4.7 %. %. It means that a small part of the observed experimental variability is not explained by the chosen model. This may be due to interaction effects between parameters.

As shown in Figure E- 7a, the two main impacting factors on the global yield are the supersaturation level β and the residence time t. Unlike the first screening, the temperature gradient ΔT has a poor impact, like rotation speed Ω.

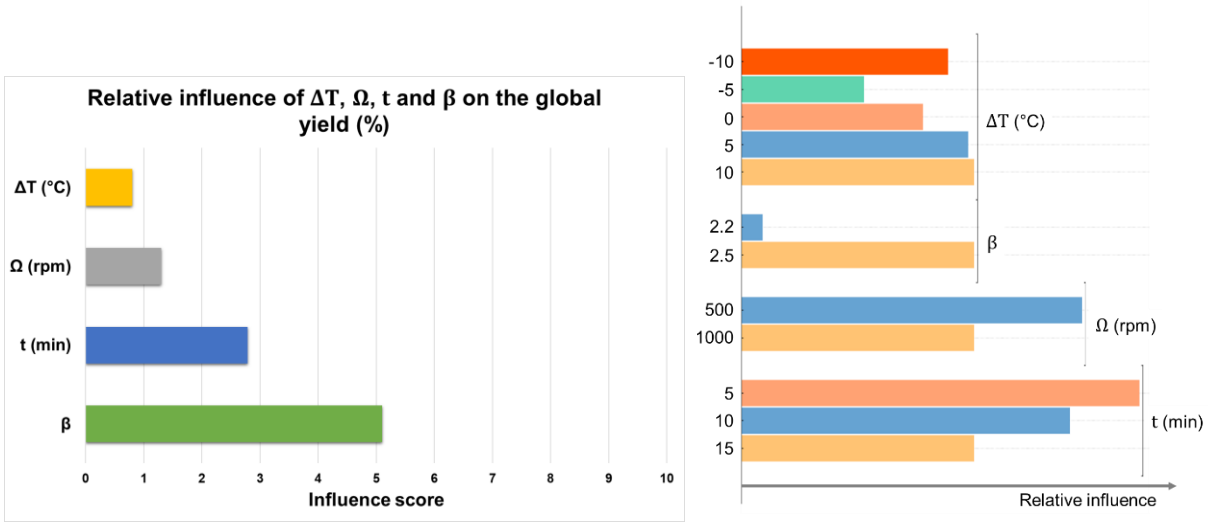

(a) **(b)**

Figure E- 7: Results from Azurad for global yield: (a) Relative influence of the temperature difference ΔT, the rotation speed Ω, the residence time t and the supersaturation ratio β on the global yield. (b) Total effect plot taken from Azurad; for every factor, the bars give the relative effect of each level to improve global yield.

The impact of each factor level on the increase of global yield can be found in Figure E- 7b. The interpretation should be modulated regarding the influence of each factor discussed before.

When looking at the most impacting factor, the supersaturation ratio, the improvement of the global yield is clear when β increases. Like for global productivity, this result was expected, since the amount of product that can crystallize is increased when the supersaturation is higher.

The second most influential factor is residence time t: it appears that as it decreases, the global yield increases, like in the first DoE. As explained in the previous section, the cooling rate is higher at shorter residence times, which increases the nucleation rate.

Finally, it seems that the best level for rotation speed is 500 rpm and that a temperature gradient ΔT = 10 °C enhances the global yield. However, as shown in Figure E- 7a, these factors have a limited effect on the global yield, thus, the assumptions about their influence should be moderated.

In conclusion, the apparent best set of parameters to improve global yield is similar to that determined for global productivity: t = 5 min and β = 2.5. This set of parameters has been used in experiments 1, 8, 13 and 16. The results of experiments 13 and 16 were estimated as aberrant, in terms of global yield, but experiments 1 and 8 indeed resulted in good global yields (see results in Table IV- 17). The predominance of the level β = 2.5 in the experiments with the best global yields is clear, the impact of the residence time is indeed lower.

In addition, the theoretical maximum global yield per fraction was calculated thanks to Equation E- 2. Table E- 4 shows the comparison between the maximum theoretical global yield and the real global yield calculated for each experiment. The actual observed global yield is really lower than the maximum calculated one, for each experiment.

Experiment	Maximum theoretical global yield (%)	Global yield (%)
1	53.9	14.6
2	49.6	8.5
3	49.6	4.9
4	53.9	11.9
5	49.6	3.6
6	53.9	11.6
7	49.6	13.3
8	53.9	10.1
9	49.6	9.2
10	53.9	9.9
11	53.9	5.7
12	49.6	5.1
13	53.9	0.5
14	49.6	5.2
15	49.6	7.1
16	53.9	19.7
17	53.9	2.6

Table E- 4: Comparison between the maximum theoretical global yield and the real global yield calculated for each experiment.

In batch mode, the global yield of experiments of section 0 ranges from 33.2 % to 38.8 % (see Table IV- 12). Even the best results obtained in continuous mode are about 2 times lower, as in the first screening. As already mentioned, these results are not surprising as it has already been reported that continuous processes trend to give lower yield than batch ones[8,33].

Thereby, the conclusion regarding global yield in this second screening is identical to that of the first screening: since the global productivity is very good, the implementation of a recycling system of the mother liquors in a lower domain of temperatures could be an interesting solution. Such set-up has already proven its efficiency regarding yield[15,35,38].

In the second screening, the number of collected fractions permitted the statistical analysis of the variability of the studied responses' results, by calculating the standard deviation of each response. It appeared that the results for global productivity and global yield are identical. The next section describes the analysis made with Azurad to estimate the impact of the four investigated factors on the variability of global productivity and global yield.

E.2.3. Standard deviation of the global responses

The regression model of the standard deviation of the global responses is very significant with a p-value of 0.30 % and a R^2 of 0.90. The lack of fit is not significant with a p-value of 44 %. Thus, the experimental results and the screening model fit very well.

Figure E- 8a shows the relative impact of the four studied factors on the variability of the global productivity and yield. The influence is equally divided between the temperature difference ΔT, the rotation speed Ω and the supersaturation ratio β. The residence time has also a small responsibility in the irregularities of the global productivity and yield, but it seems limited compared with the three other factors.

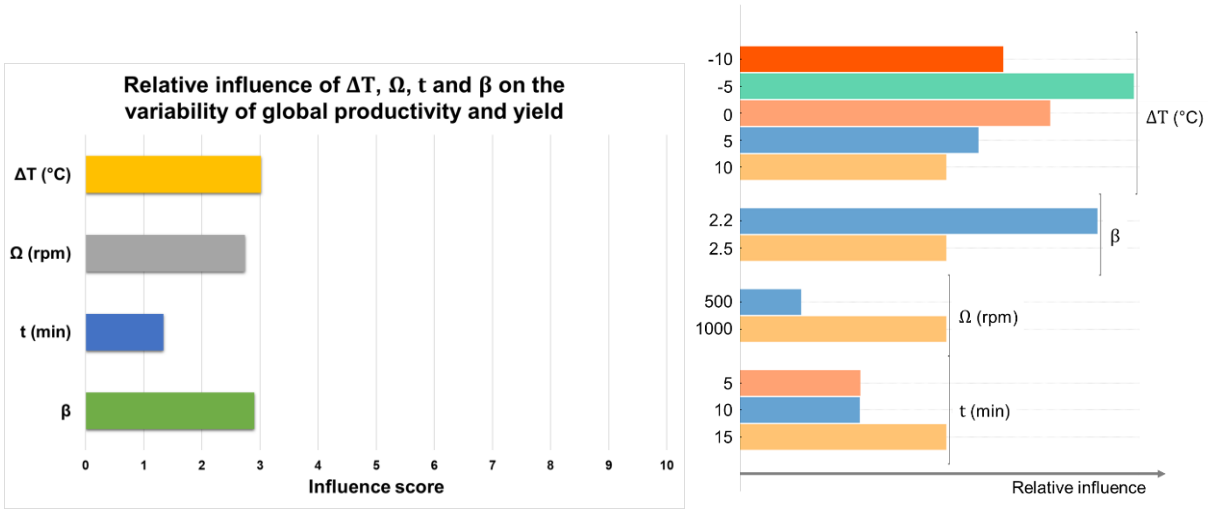

(a) **(b)**

Figure E- 8: Results from Azurad for the standard deviation of the global responses: (a) Relative influence of the temperature difference ΔT, the rotation speed Ω, the residence time t and the supersaturation ratio β on the variability of the global responses. (b) Total effect plot taken from Azurad; for every factor, the bars give the relative effect of each level on the variability of the global responses.

The impact of each factor level on the variability of the global responses can be found in Figure E- 8b. The interpretation should be moderated regarding the influence of each factor discussed in the previous paragraph.

The effect of the temperature gradient ΔT on the standard deviation of the global responses does not appear to be linear. This factor is probably affected by interaction(s) with other parameters. However, a trend seems to be drawn: the use of the non-isothermal mode '+' seems to reduce the variation of the global results from one fraction to another. An hypothesis can be assessed to explain this result: a positive gradient corresponds to the inner cylinder being the hot one; as the rotation of this cylinder generates heat because of the friction with the lip seal (see section III.3.2), the conjunction of these two effects probably leads to more stability than the situation when the inner cylinder is the cold part.

Regarding the rotation speed, the lowest level seems to limit the standard deviations. The mixing effects might be less intense, thus maybe more stable.

The increase of the supersaturation ratio β apparently improves the regularity of the results. This result is surprising, as the medium is more concentrated at higher supersaturation, the system is expected to be less stable.

A threshold effect can be observed for the residence time t. Nevertheless, its impact being limited, in comparison with the other factors, the analysis does not need to go further.

To conclude, the best set of parameters to ensure a certain constancy of the global productivity and yield seems to be: $\Delta T = +10\ °C$, $\Omega = 500$ rpm and $\beta = 2.5$. This combination was used in experiment 4 in which indeed the standard deviation of the global responses is low, but not the minimal one. Even if the model statistically seemed significant, a part of the experimental observations is probably not well-explained and would deserve more experiments to refine the conclusions.

E.2.4. Diastereomeric excess

During the processing of the diastereomeric excess results, it appeared that the results of experiments 15, 16 and 17 were aberrant. As complementary experiments, it was possible to remove them from the experimental matrix without degrading the quality criteria.

The regression model (discarding experiments 15, 16 and 17) given by Azurad is very significant with a p-value of 0.37 % and a R^2 of 0.92. The lack of fit is not significant, with a p-value of 67 %. Therefore, the experimental results and the screening model fit quite well.

As shown in Figure E- 9a, the residence time t and the temperature difference ΔT are the two most impacting factors on diastereomeric excess. This strong effect of the residence time is surprising, as this factor only had a poor impact on the chiral purity in the first screening. Also, the rotation speed Ω appears to have a very limited influence on diastereomeric excess in this second screening, unlike the observations of the first screening design. Finally, the newly studied factor, the supersaturation ratio β has a negligible impact on chiral purity.

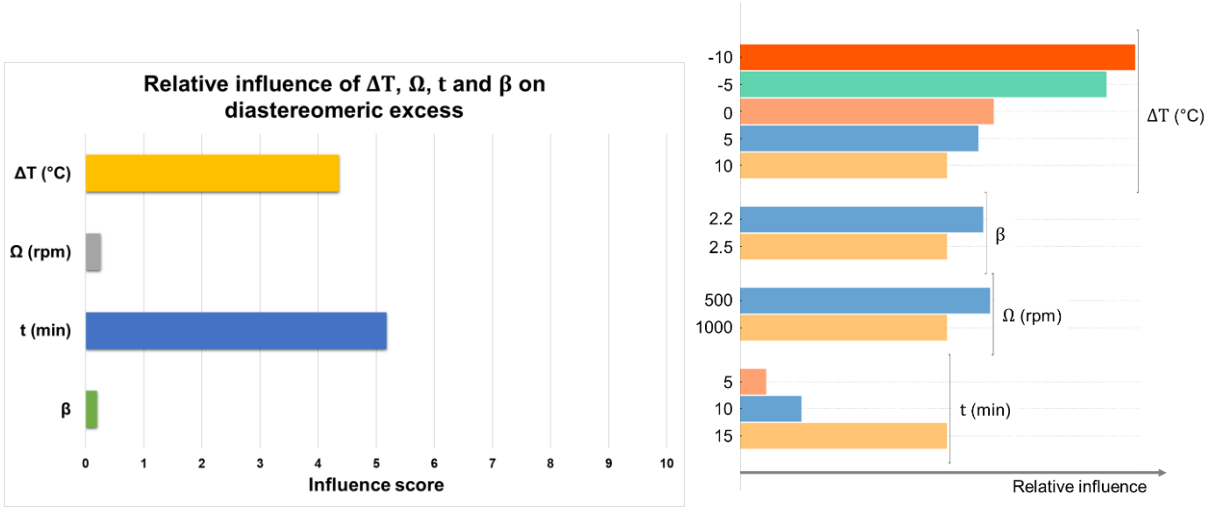

(a) **(b)**

Figure E- 9: Results from Azurad for the diastereomeric excess: (a) Relative influence of the temperature difference ΔT, the rotation speed Ω, the residence time t and the supersaturation ratio β on the diastereomeric excess. (b) Total effect plot taken from Azurad; for every factor, the bars give the relative effect of each level to improve the diastereomeric excess.

The impact of each factor level on the increase of the diastereomeric excess can be found in Figure E- 9b. The interpretation should be moderated regarding the influence of each factor discussed before.

The most influential parameter is the residence time t: its increase enhances the diastereomeric excess of the collected product. A longer stay in the efficient mixing CT reactor seems to have a positive impact on chiral purity. This trend is similar to that in the first screening, even if the impact of the factor strongly differs.

The second most impacting factor is the temperature difference ΔT: it clearly appears that the use of the CT crystallizer in non-isothermal mode, with the inner cylinder as the cold part and the outer cylinder as the hot one, gives the best results of chiral purity, as in the first screening. The presence of a temperature gradient was expected to improve chiral purity, as it has already proved its efficiency in deracemization processes[61,76]. In the opposite, the reverse non-isothermal mode should be avoided. Such difference between the two non-isothermal modes has already been reported[62].

Due to their apparent limited influence on the diastereomeric excess, no level of the rotation speed Ω and supersaturation ratio β should be favored.

Eventually, the apparent best parameter set to improve chiral purity is: $\Delta T = -10$ °C and $t = 15$ min. Such combination was not tested, but experiment 5, which resulted in the highest diastereomeric excess, was performed with $\Delta T = -5$ °C and $t = 15$ min.

The chiral purity varies from 0.47 to 0.63 in the batch experiments of section 0. The implementation of the chiral resolution of rac-Ibu with *S*-αMBA in the continuous mode ensures the access to high diastereomeric excesses, in a repeatable manner. In addition, the chiral purity can be improved by 18 % on average by transferring the process from batch to continuous mode.

Moreover, an interesting observation was made: the diastereomeric excess tends to increase as the experiment progresses ($0.01 \leq \Delta de \leq 0.04$). This may be due to the back diffusion that can be induced by the opposite direction of rotation of the neighboring vortices (illustrated in Figure I- 7). As long as the wanted diastereomer is majority, such characteristic is truly beneficial for the process results.

Like for the global responses, the standard deviation of the diastereomeric excess was calculated for each experiment. This result serves the evaluation of the impact of the four investigated factors on the variability of the chiral purity with Azurad.

E.2.5. Standard deviation of the diastereomeric excess

Experiment 13 was aborted after 4 residence times, and the small amount of collected product permitted the chiral HPLC analysis of only one fraction. Therefore, no standard deviation could be calculated for this experiment. Also, it appeared that the results of experiments 14, 16 and 17 were aberrant. As complementary experiments, it was possible to remove them from the experimental matrix (for this response study) without degrading the quality criteria.

The regression model (discarding experiments 13, 14, 16 and 17) of the standard deviation of the diastereomeric excess is poorly significant with a p-value of 15 % and a R^2 of 0.86. Because

of the number of discarded experiments, no lack of fit can be determined. The selected model does not fit well with the experimental results, this can be due to interactions between the studied factors. However, some trends can be observed.

Figure E- 10a shows the relative impact of the four studied factors on the variability of the diastereomeric excess. It seems that most of the irregularity of the chiral purity is due to the rotation speed Ω. This trend was unexpected, since the rotation speed has a very small influence on the diastereomeric excess results. Part of the variability can be attributed to the temperature difference ΔT, but the residence time t and the supersaturation ratio β only have a limited impact.

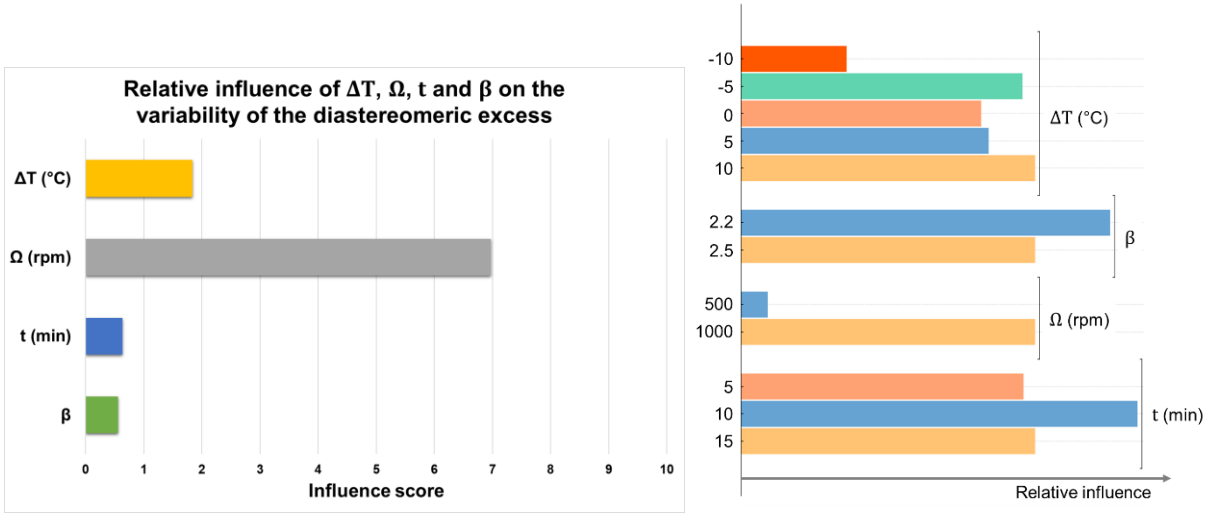

(a) **(b)**

Figure E- 10: Results from Azurad for the standard deviation of the diastereomeric excess: (a) Relative influence of the temperature difference ΔT, the rotation speed Ω, the residence time t and the supersaturation ratio β on the variability of the diastereomeric excess. (b) Total effect plot taken from Azurad; for every factor, the bars give the relative effect of each level on the variability of the diastereomeric excess.

The impact of each factor level on the variability of the chiral purity can be found in Figure E- 10b. The interpretation should be moderated regarding the influence of each factor discussed in the previous paragraph.

The difference of impact of the two levels of rotation speed is clear: the lowest level, 500 rpm seems to limit the standard deviations. The same observation was made when analyzing the standard deviation of the global responses. The mixing effects are probably less efficient when decreasing the rotation speed, but they also might be less intense, thus more stable.

The effect of the temperature gradient ΔT on the standard deviation of the diastereomeric excess is not linear. No trend can be assessed as such. Also, as mentioned before, the chosen regression model is poorly significant. This factor is probably subject to interaction(s).

Since their impact seems very limited, no level should be preferred for the residence time t and the supersaturation ratio β.

The determination of a good set of parameters to limit the variability of the chiral purity is hardly assessable. If the regression model can give a primary outline of the trends, its significance is too poor to conclude. Nevertheless, this conclusion can be modulated regarding

the values of standard deviation determined for the diastereomeric excess of each experiment (see Table IV- 17): if a variability exists, the mean deviations to the average chiral purity are very low.

E.2.6. Diastereomeric productivity

Like for global productivity, according to the analysis of the residues in the Azurad statistical analysis, experiments 13 and 16 appear to be aberrant. As previously said, these complementary experiments can be removed from the experimental matrix, without degrading the quality criteria.

The regression model (discarding experiments 13 and 16) is very significant with a p-value of 0.0 % and a R^2 of 0.83. The lack of fit is significant with a p-value of 0.17 %. It means that a small part of the observed experimental variability is not explained by the chosen model. This could be due to interaction effects between parameters.

The relative influence of each studied factor on diastereomeric productivity (Figure E- 11a) is almost identical to that on global productivity. The impact of residence time t is predominant. The supersaturation ratio has a small influence on global productivity and that of the temperature difference ΔT and the rotation speed Ω is negligible. These results are comparable to those of the first screening: the residence time influence presses that of the other factors for global and diastereomeric productivities.

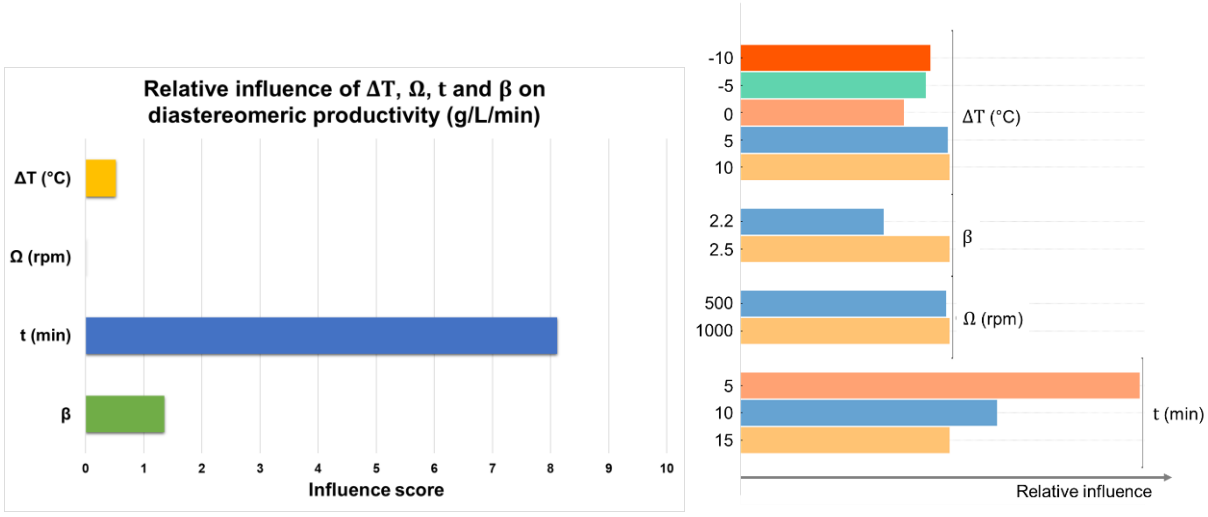

(a) **(b)**

Figure E- 11: Results from Azurad for the diastereomeric productivity: (a) Relative influence of the t temperature difference ΔT, the rotation speed Ω, the residence time t and the supersaturation ratio β on the diastereomeric productivity. (b) Total effect plot taken from Azurad; for every factor, the bars give the relative effect of each level to improve the diastereomeric productivity.

The impact of each factor level on the increase of the diastereomeric productivity can be found in Figure E- 11b. The interpretation should be modulated regarding the influence of each factor discussed in the previous paragraph.

Like for global productivity, the predominance of $t = 5$ min as a diastereomeric productivity enhancer seems clear. The lower the residence time the higher the diastereomeric productivity.

The increase of the supersaturation ratio β improves the diastereomeric productivity. This can be expected since the amount of product that can potentially crystallize is higher when the supersaturation is increased.

As in the first screening, the use of the isothermal mode (ΔT = 0 °C) seems to improve global productivity. However, regarding the impact of this factor, this assumption should be moderated.

The levels of the factors Ω are hardly discriminable, but as explained above, it does not seem to impact the diastereomeric productivity.

To conclude, the use of t = 5 min and β = 2.5 seems to be the most important to improve diastereomeric productivity. This parameter set was used in experiments 1, 8, 13 and 16. The results of experiments 13 and 16 were estimated as aberrant, in terms of diastereomeric productivity, but experiments 1 and 8 indeed resulted in high diastereomeric productivities (see results in Table IV- 17). Thus, the influence of ΔT, Ω, t and β on diastereomeric productivity is closer to that on global productivity than that on diastereomeric excess.

In batch mode, the diastereomeric productivity of the experiments presented in the section 0 was estimated between 0.058 $g.L^{-1}.min^{-1}$ to 0.63 $g.L^{-1}.min^{-1}$. The use of continuous mode can improve it by, at least, 2 times, and up to 30 times. The outstanding enhancement of the diastereomeric productivity is even probably underestimated, since the batch mode experiments were performed with a higher supersaturation ratio of 2.8 (to provoke nucleation, see section 0).

E.2.7. Diastereomeric yield

During the processing of the diastereomeric yield results, it appeared that the results of experiments 13, 16 and 17 were aberrant, like for global yield. As complementary experiments, it was possible to remove them from the experimental matrix without degrading the quality criteria.

The regression model (discarding experiments 13, 16 and 17) given by Azurad is significant with a p-value of 0.0 % and a correlation coefficient R^2 of 0.67. The lack of fit is significant with a p-value of 2.3 %. %. It means that a small part of the observed experimental variability is not explained by the chosen model. This could be due to interaction effects between parameters.

As shown in Figure E- 12a, like for global yield, the two factors with the most influence on the diastereomeric yield are the supersaturation level β and the residence time t. Unlike the first screening, the temperature gradient ΔT has a poor impact on the diastereomeric yield, like rotation speed Ω.

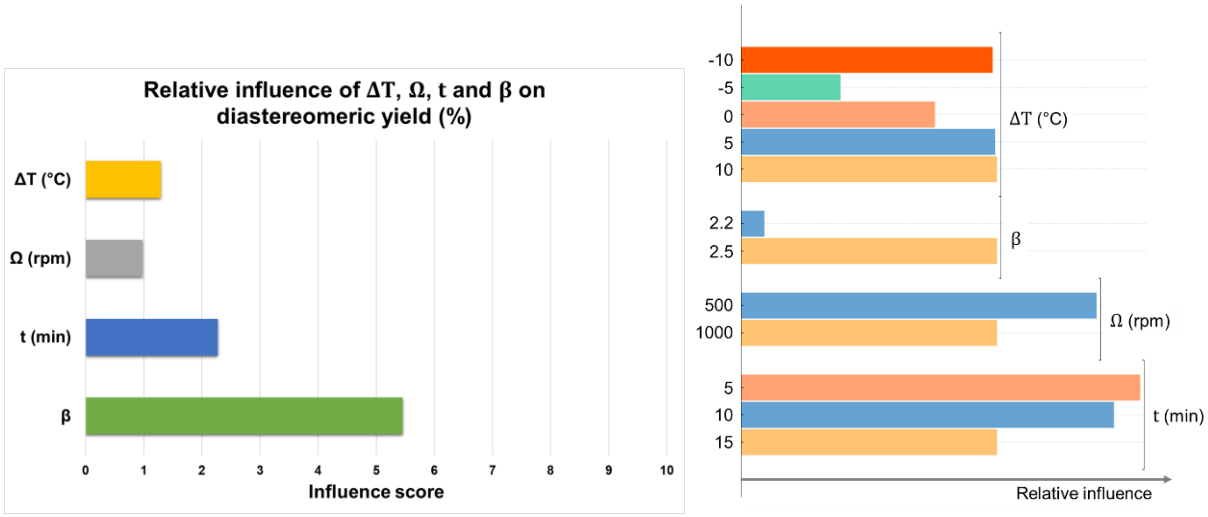

(a) **(b)**

Figure E- 12: Results from Azurad for the diastereomeric yield: (a) Relative influence of the temperature difference ΔT, the rotation speed Ω, the residence time t and the supersaturation ratio β on the diastereomeric yield. (b) Total effect plot taken from Azurad; for every factor, the bars give the relative effect of each level to improve the diastereomeric yield.

The impact of each factor level on the increase of the diastereomeric yield can be found in Figure E- 12b. The interpretation should be moderated regarding the influence of each factor discussed before.

Likewise global yield, the predominance of $\beta = 2.5$ as a diastereomeric yield enhancer seems clear. This result was expected since the amount of product that can potentially crystallize is increased when the supersaturation is higher.

Concerning the residence time t, it seems that as it decreases, the diastereomeric yield increases. This effect is the same as for productivities and global yield and was already observed in the first screening. The lower the residence time the higher the productivity and the yield.

The temperature difference ΔT levels' influence does not seem linear; therefore, it is not possible to state a trend for this factor. However, as shown in Figure E- 12a, its effect on diastereomeric yield is limited.

Finally, it seems that the best level for rotation speed is 500 rpm, but this indication should be modulated as the impact of the rotation speed on diastereomeric yield is poor.

In conclusion, the use of $\beta = 2.5$ and $t = 5$ min seems to be the most important to improve the diastereomeric yield. This set of parameters has been used in experiments 1, 8, 13 and 16. If the results of experiments 13 and 16 were estimated as aberrant, in terms of diastereomeric yield, experiments 1 and 8 indeed resulted in good diastereomeric yields (see results in Table IV- 17). The predominance of the level $\beta = 2.5$ in the experiments with the best global and diastereomeric yields is clear; the impact of the residence time seems less important.

Diastereomeric yields of batch experiments presented in section 0 range from 18.2 % to 23.7 %. Like for the results of global yield, the best results obtained in continuous mode are

about 2 times lower. Again, this outcome is not surprising, and the use of a recycling system of the mother liquors at a lower temperature could be an efficient solution.

Like for the global productivity and yield, the variability of the diastereomeric productivity and yield was determined by calculating the standard deviation of each response. It appeared that the results for diastereomeric productivity and diastereomeric yield are identical. The next section describes the analysis made with Azurad to estimate the impact of the four investigated factors on the variability of diastereomeric productivity and yield.

E.2.8. Standard deviation of the diastereomeric productivity and yield

Experiment 13 was aborted after 4 residence times, and the small amount of collected product permitted the chiral HPLC analysis of only one fraction. Therefore, no standard deviation could be calculated for this experiment. Also, it appeared that the results of experiment 16 were aberrant. As complementary experiments, it was possible to remove them from the experimental matrix without degrading the quality criteria.

The regression model (discarding experiments 13 and 16) of the standard deviation of the diastereomeric productivity and yield is very significant with a p-value of 0.80 % and a R^2 of 0.92. The lack of fit is not significant with a p-value of 53 %. Thus, the experimental results and the screening model fit very well.

Figure E- 13a shows the relative impact of the four studied factors on the variability of the diastereomeric productivity and yield. It seems that most of the irregularity of these responses is due to the temperature difference ΔT. Part of the variability can be attributed to the supersaturation ratio β and the rotation speed Ω. The residence time t has also a small responsibility in the irregularities of the global productivity and yield, but it seems limited compared with the three other factors

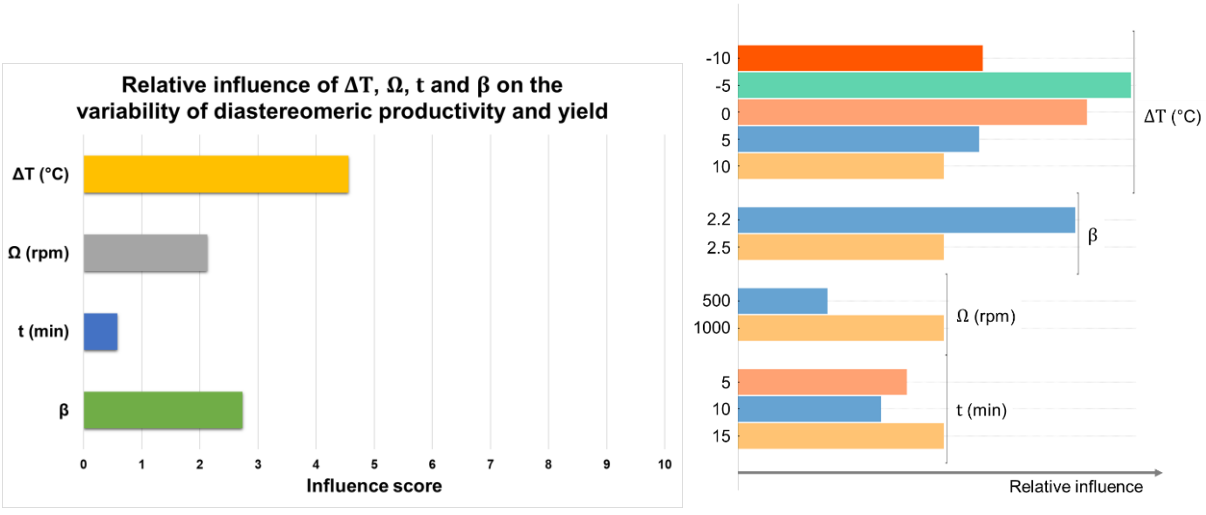

(a) **(b)**

Figure E- 13: Results from Azurad for the standard deviation of the diastereomeric productivity and yield: (a) Relative influence of the temperature difference ΔT, the rotation speed Ω, the residence time t and the supersaturation ratio β on the variability of the diastereomeric productivity and yield. (b) Total effect plot taken from Azurad; for every factor, the bars give the relative effect of each level on the variability of the diastereomeric productivity and yield.

The impact of each factor level on the variability of the diastereomeric productivity and yield can be found in Figure E- 13b. The interpretation should be modulated regarding the influence of each factor discussed in the previous paragraph

The effect of the temperature gradient ΔT on the standard deviation of the diastereomeric productivity and yield is not linear. This factor is probably subject to interaction(s). However, the same trend than that of the standard deviation of the global responses seems to be drawn: a positive gradient, corresponding to the inner cylinder being the hot one, seems to reduce the standard deviation.

The increase of the supersaturation ratio β appears to improve the regularity of the results. Like for the standard deviation of the global responses, this result is surprising, as the medium is more concentrated at higher supersaturation, the system is expected to be less stable.

As observed for the two other standard deviations, regarding the rotation speed Ω, the lowest level seems to limit the standard deviations. The mixing effects are probably less efficient when decreasing the rotation speed, but they also might be less intense, thus more stable.

The effect of the different levels of the residence time t does not seem linear. Nevertheless, its impact being limited, the analysis does not need to go further.

To conclude, the best set of parameters to limit the variability of diastereomeric productivity and yield is: $\Delta T = 10$ °C, $\Omega = 500$ rpm and $\beta = 2.5$. This combination was used in experiment 4 in which indeed the standard deviation of the global responses is low, but not the minimal one. Even if the model statistically seemed significant, a part of the experimental observations is probably not well-explained and would deserve more experiments to refine the conclusions.

Continuous crystallization - Contribution to the implementation of the Pasteurian resolution of racemic Ibuprofen in a Couette-Taylor crystallizer

Abstract

The main objective of the work described in the present manuscript was to implement the chiral resolution of racemic Ibuprofen (rac-Ibu) by diastereomeric salt formation with *S*-αMethylBenzylAmine (*S*-αMBA) in a continuous crystallizer called Couette-Taylor (CT) crystallizer

Firstly, the system to resolve was investigated, which led to the revision of the phase diagram between the two diastereomers since a partial solid solution enriched in *S*-Ibu-*S*-αMBA was evidenced. The crystals of ss-*S*-Ibu-*S*-αMBA exhibit a surprising fibrous aspect, favoring the formation of biphasic fluid inclusions. Investigations on these particles served the formulation of hypotheses around their fibrous nature, and the development of a procedure to limit the occurrence of fluid inclusions.

After a careful design of the continuous set-up, Couette-Taylor experiments were performed through two different designs of experiments (DoE). The continuous mode resulted in lower yield than batch mode, but this can largely be counterbalanced by the outstanding improvement of the productivity of at least 1.5 times, and up to 30 times. Also, the transfer from batch to continuous mode seems to ensure the access to high diastereomeric excesses, in a repeatable manner.

Unfortunately, encrustation issues were encountered during the continuous experiments. The causes and potential solutions were extensively discussed leading to the proposition of an original continuous CT set-up.

Keywords: Continuous chiral resolution by diastereomeric salt formation; Couette-Taylor crystallizer; Ibuprofen; Design of experiments; Fluid inclusions; Fibrous crystals.

Résumé

L'objectif principal du travail décrit dans ce manuscrit est la mise en œuvre du procédé de résolution chirale de l'ibuprofène racémique (rac-Ibu) par formation de sels diastéréoisomères avec la *S*-αMethylBenzylAmine (*S*-αMBA) dans un cristalliseur continu appelé cristalliseur Couette-Taylor (CT).

Dans un premier temps, le système à résoudre a été étudié, ce qui a conduit à la révision du diagramme de phase entre les deux diastéréoisomères puisqu'une solution solide partielle enrichie en *S*-Ibu-*S*-αMBA a été mise en évidence. Les cristaux de ss-*S*-Ibu-*S*-αMBA présentent un aspect fibreux surprenant, favorisant la formation d'inclusions fluides biphasiques. Les investigations sur ces particules ont permis de formuler des hypothèses autour de leur nature fibreuse, et d'élaborer une procédure pour limiter l'apparition d'inclusions fluides.

Après une étude minutieuse du montage, les expériences en continu avec le Couette-Taylor ont été réalisées au travers de deux plans d'expériences (DoE) différents. Le rendement obtenu en mode continu est inférieur à celui obtenu en mode 'batch', mais cela peut être largement contrebalancé par l'amélioration exceptionnelle de la productivité d'au moins 1,5 fois, et jusqu'à 30 fois. De plus, le passage du mode 'batch' au mode continu semble assurer l'accès à des excès diastéréoisomériques élevés, de manière répétable.

Malheureusement, des problèmes d'incrustation ont été rencontrés au cours des expériences en continu. Les causes et les solutions potentielles ont été longuement discutées, ce qui a conduit à la proposition d'un montage en continu original.

Mots-clés : Résolution chirale en continu par formation de sels diastéréoisomères ; Cristalliseur Couette-Taylor ; Ibuprofène ; Plan d'expériences ; Inclusions fluide ; Cristaux fibreux.